2017

Metal-Organic Frameworks: A Versatile Platform For Light Harvesting And Energy Transfer

Derek E. Williams
University of South Carolina

METAL-ORGANIC FRAMEWORKS: A VERSATILE PLATFORM FOR LIGHT HARVESTING AND ENERGY TRANSFER

by

Derek E. Williams

Bachelor of Science
University of Northern Colorado, 2012

Submitted in Partial Fulfillment of the Requirements

For the Degree of Doctor of Philosophy in

Chemistry

College of Arts and Sciences

University of South Carolina

2018

Accepted by:

Natalia Shustova, Major Professor

Richard Adams, Committee Member

Andrew Greytak, Committee Member

Camelia Knapp, Committee Member

Cheryl L. Addy, Vice Provost and Dean of the Graduate School

DEDICATION

This dissertation is dedicated to all those who have pushed me to succeed, and convinced me that I could achieve anything in life that I wished.

ACKNOWLEDGEMENTS

I wholeheartedly thank Dr. Natalia Shustova, for being such a great mentor, advisor, colleague, and friend, and for guiding me for the past four years and not giving up on me. Thank you for teaching me all that I know; it's because of you that I am equipped for the future, and I cannot convey my gratitude enough for everything you have done for me.

My dearest wife, Amanda Williams, and daughter, Ada Williams, and son, Elliot Williams, have been such great motivational factors, and have provided me encouragement throughout my Ph.D. career. I would not have made it without them. I also thank my family, my mother, and father for being there when I needed them the most.

I would also like to thank my fellow colleagues for constantly answering my questions and providing suggestions.

ABSTRACT

The global energy demand is undoubtedly rising at an alarming rate, and as a result, humanity faces the problem of finding alternative energy supplies. Approximately 80 percent of the world's energy currently comes from fossil fuels, and only a small fraction, 10 percent, from renewable energy sources. The study of energy transfer (ET) processes is a rapidly developing area of interest due to the necessity for more efficient photovoltaic devices, which are crucial to meet the growing energy demand. A promising approach to further advance organic photovoltaics is to precisely arrange many light-harvesting chromophores (e.g., porphyrin derivatives), attainable through a self-assembly process, to make a highly ordered network of light-harvesting antennae, much like what is observed in the natural photosystem. The large network of ordered porphyrin-containing derivatives could then funnel the collected energy in a predesigned pathway to a specific location to be stored or used, for instance, for photocatalysis. Metal-organic frameworks (MOFs) can be used as a tool to self-assemble hundreds of chromophores in a large light-harvesting ensemble with high level of precision, similar to the natural photosystem. MOFs are highly modular, and with a plethora of organic linkers and metal choices available, limitless combinations are possible, which allows for a number of topologically different structures, and new ways to tailor the physiochemical properties of the material. Modularity and tunability give MOFs an advantage over traditional materials, because they can be fine-tuned and tailored to meet the specific criteria demanded by various applications.

This work presented within the following five chapters is focused on the design, synthesis, and characterization of MOFs that target the fundamental understanding of ET processes in predesigned pathways. In the first chapter, a brief introduction of ET mechanisms and MOF synthesis are explained. The second chapter describes a photoswitchable MOF that is capable of exhibiting fluorescence modulation through integrated diarylethene photoswitch linkers. The third chapter discusses the photoswitchable properties of diarylethene and spiropyran-based derivatives in the solid-state, solution, and coordinatively immobilized as pillars in a MOF. Chapter four describes how fullerene derivatives were self-assembled with a porphyrin-based compound, creating a highly-ordered donor-acceptor MOF with the capability for ultrafast electron/energy transfer. Lastly, chapter five discusses how MOFs were used as a mimic of the green fluorescent protein (GFP) β-barrel to suppress low energy vibrational modes of a confined chromophore.

We envision that MOFs can be utilized as a unique platform to assemble well-defined, highly-ordered, versatile, modular structural arrays capable of efficient ET. Materials with the ability to precisely control the mutual orientation and organization of ligands could be vital for the advancement of organic photovoltaic or energy storage devices, sensors, or molecular electronics.

TABLE OF CONTENTS

LIST OF TABLES

LIST OF FIGURES

LIST OF SCHEMES

CHAPTER 1

Light Harvesting and Energy Transfer in Metal-Organic Frameworks

Williams, D. E.; Shustova, N. B. *Chem. Eur. J.* **2015**, *21*, 15474-15479.

INTRODUCTION

Demand for energy continues to rise, creating the need for alternative energy sources which are both clean and efficient. Over the past several decades,[1,2] solar power has been increasingly utilized to meet the growing energy demand. However, commercialized photovoltaic devices, which are relatively expensive to produce, lack the efficiency necessary to make them a viable energy substitute to meet those demands. A cheaper alternative that maintains or improves the overall efficiency of photovoltaic devices should be developed so that they can compete with other of energy sources. To develop such a device, it is helpful to look toward the natural photosystem which is capable of both light harvesting and energy transfer (ET) to produce usable fuels. Surprisingly, in nature, a leaf is capable of efficient ET and delivers captured energy to a reaction center with near 100% internal quantum efficiency.[3,4]

In the natural photosystem, an ensemble of antenna chromophore pigment-protein complexes is responsible for photon energy migration to the photosystem reaction centers that yield separated charges, and ultimately, storable fuels. The large network of antennae forms an array that increases the cross-section for light absorption nearly 100-fold, thereby concentrating the excitation energy to the fewer number of reaction centers.[5] To date, natural photosynthetic mimics range from covalently-linked polymer arrays[6] to self-assembled supramolecular systems.[7–10] These artificial light-harvesting ensembles reveal that the overall efficiency of the system is highly dependent on the hierarchically-organized antenna surrounding the reaction center.[5,11–14] MOFs offer the possibility of creating

artificial systems composed of a multitude of highly-ordered chromophores through a self-assembly approach.

MOFs are organic-inorganic, crystalline, ordered materials that are commonly assembled from carboxylic acid- or pyridyl-terminated organic linkers with a metal cation.[15–25] One major advantage of MOFs is the possibility of their characterization by single-crystal X-ray diffraction, which enables us to determine the distances and angles between chromophores, as well as chromophore molecular conformations. Furthermore, MOF structures can be systematically tuned by incorporating various linkers and/or altering the synthetic conditions. [26–30] They are typically assembled via one of three routes: (i) solvothermal synthesis, (ii), insertion, and (iii) solvent-assisted linker exchange (SALE).

Solvothermal synthesis of MOFs involves the careful manipulation of several variables to induce self-assembly. One variable to adjust is the solvent mixture, which frequently contains *N*,*N*-dimethylformamide (DMF) or *N*,*N*-diethylformamide (DEF) as well as a primary alcohol (e.g., methanol or ethanol), and their relative ratios can be varied to alter the polarity or composition of the solution, which may help to promote the MOF growth. The addition of various acids (HCl, HNO_3, HBF_4, HF, etc.) can slow down the process of MOF formation, resulting in single-crystal growth. The solvent, partially decomposed during, heating acts as a weak base to deprotonate the carboxylic acid groups on the MOF linker. The addition of acid increases the number of competing protons, effectively resulting in slower crystallization. Lastly, the heating rate and temperature can play a key role in the topology of the resulting material. Commonly, slower ramping rates during the heating phase can slow down the decomposition of the solvent, which in turn slows down the deprotonation of the MOF linker (vide supra), and can yield larger crystals.

The second method to prepare 3D MOFs is to soak a previously-prepared two-dimensional (2D) crystals containing unsaturated metal sites (e.g. Zn_2(ZnTCPP)),[27] in a solution containing a compound that can act as a pillaring linker capable of insertion between the 2D layers (e.g. 4,4'-bipyridine). The resulting 3D MOF would then contain layers of one organic linker, and pillars of another. This method is particularly useful to make a MOF, where two different linkers have been mutually oriented in the crystalline material, much like a copolymer.

Lastly, the third common method for MOF preparation, solvent-assisted linker exchange (SALE), is to take an existing 3D MOF and soak it in a solution containing the desired linker. This method results in the exchange of the initial pillar with the one that the crystals were soaked in, which is beneficial for obtaining non-interpenetrated structures. For instance, a smaller linker, such as 4,4'-bipyridine,[28,31] can be exchanged with linkers of a larger (or smaller) length.[30,32]

These three methods are certainly not the only routes for MOF preparation.[33–40] It is not uncommon for trials to exceed 100 synthesis attempts to obtain single-crystalline material, and often, attempts using all three syntheses techniques are necessary. Despite this challenge, the availability of various synthetic techniques, along with the vast array of linkers and metals, could result in novel topologies and unrevealed structural patterns. The modular behavior of MOFs allows for combination of a plethora of linkers to form hybrid materials which have properties tailored to specific applications, including gas storage,[41–44] catalysis,[45–48] sensing,[49–52] drug delivery,[53–56] and light harvesting.[23,57–59]

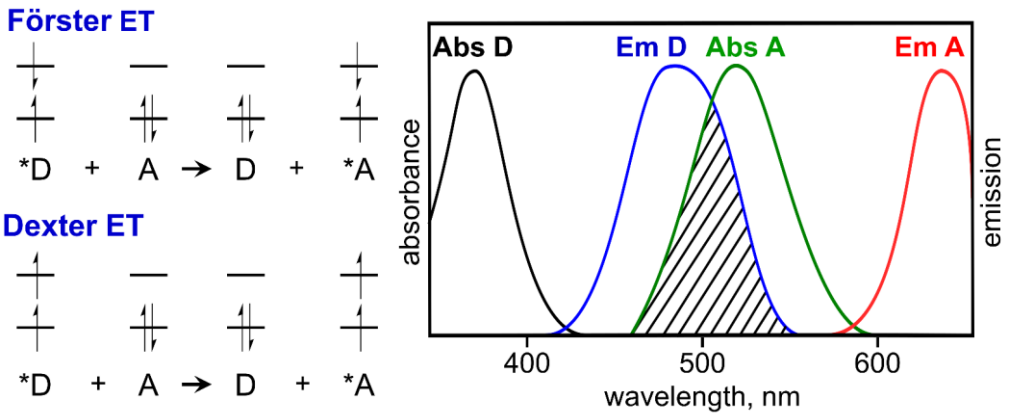

Figure 1.1. A representation of the Förster and Dexter ET mechanisms (*left*) and the absorption and emission profiles of donor and acceptor molecules (*right*). The overlap between the donor emission and acceptor absorption (hashed lines) indicates an opportunity for FRET.

The combination of the modularity and a high-degree of structural order make MOFs excellent candidates to mimic the natural photosystem. Light harvesting and energy transfer process can be systematically studies using a MOF as a versatile platform.[60–64]

Two main types of ET have been studied extensively in MOFs: FRET and Dexter ET mechanisms (Figure 1.1).[23,65–68] In FRET, long-range ET can occur through non-radiative pathways via dipole-dipole interactions.[68,69] The efficiency of FRET relies on: (i) the quantum yield of the fluorophore, which should be emissive in the visible/NIR range for light harvesting applications, (ii) the distance between donor and acceptor ligands should be positioned within a 1-10 nm range, and (iii) the degree of overlap between the absorption spectrum of the acceptor and the emission spectrum of the donor.[68] The rate of ET, *k*, decreases to the power of –6 with increasing donor-acceptor distance:

$$k_{FRET} \propto r^{-6} \qquad \textbf{Equation 1.1}$$

where *r* is the donor-acceptor distance.

The Dexter ET mechanism relies on electronic coupling and intermolecular orbital overlap between the donor and acceptor ligands.[68] The donor and acceptor ligands must be

close for electron exchange to occur (<1 nm) via the Dexter mechanism. The rate of ET decreases exponentially with increasing donor-acceptor distance:

$$(k_{DEX} \propto e^{\frac{-2r}{L}}) \qquad \textbf{Equation 1.2}$$

where r is the donor-acceptor distance, and L is the sum of the van der Waals radii.[68] Due to the larger separation between adjacent linkers, FRET is the prevailing ET mechanism in MOFs. However, some MOFs that rely on the Dexter ET mechanism have been reported previously.[70–75]

To summarize, MOFs are excellent platforms to study and model light-harvesting and ET processes due to their modularity, tunability, and crystallinity. They offer a significant level of control over competitive systems through self-assembly, which could be vital for the advancement of light-harvesting materials with the goal of directional ET. Thus, understanding how MOFs can influence the ET processes in the studies described lays the fundamental groundwork necessary to ultimately tie such structures to reaction centers and/or charge collection interfaces.

REFERENCES

(1) Nocera, D. G. *Acc. Chem. Res.* **2017**, *50* (3), 616–619.
(2) Lewis, N. S.; Nocera, D. G. *Proc. Natl. Acad. Sci. U. S. A.* **2006**, *103* (43), 15729–15735.
(3) Page, C. C.; Moser, C. C.; Dutton, P. L. *Curr. Opin. Chem. Biol.* **2003**, *7* (5), 551–556.
(4) Scholes, G. D.; Fleming, G. R.; Olaya-Castro, A.; van Grondelle, R. *Nat. Chem.* **2011**, *3* (10), 763–774.
(5) Scholes, G. D.; Fleming, G. R.; Olaya-Castro, A.; van Grondelle, R. *Nat. Chem.* **2011**, *3* (10), 763–774.
(6) Aratani, N.; Kim, D.; Osuka, A. *Acc. Chem. Res.* **2009**, *42* (12), 1922–1934.
(7) Patwardhan, S.; Sengupta, S.; Siebbeles, L. D. A.; Würthner, F.; Grozema, F. C. *J. Am. Chem. Soc.* **2012**, *134* (39), 16147–16150.
(8) Li, X.; Sinks, L. E.; Rybtchinski, B.; Wasielewski, M. R. *J. Am. Chem. Soc.* **2004**, *126* (35), 10810–10811.
(9) Kelley, R. F.; Lee, S. J.; Wilson, T. M.; Nakamura, Y.; Tiede, D. M.; Osuka, A.;

Hupp, J. T.; Wasielewski, M. R. *J. Am. Chem. Soc.* **2008**, *130* (13), 4277–4284.
(10) Sengupta, S.; Ebeling, D.; Patwardhan, S.; Zhang, X.; von Berlepsch, H.; Böttcher, C.; Stepanenko, V.; Uemura, S.; Hentschel, C.; Fuchs, H.; Grozema, F. C.; Siebbeles, L. D. A.; Holzwarth, A. R.; Chi, L.; Würthner, F. *Angew. Chemie Int. Ed.* **2012**, *51* (26), 6378–6382.
(11) Kühlbrandt, W.; Wang, D. N.; Fujiyoshi, Y. *Nature* **1994**, *367* (6464), 614–621.
(12) McDermott, G.; Prince, S. M.; Freer, A. A.; Hawthornthwaite-Lawless, A. M.; Papiz, M. Z.; Cogdell, R. J.; Isaacs, N. W. *Nature* **1995**, *374* (6522), 517–521.
(13) Calderon, R. M. K.; Valero, J.; Grimm, B.; Mendoza, J. de; Guldi, D. M. *J. Am. Chem. Soc.* **2014**, *136*, 11436–11443.
(14) Qiao, F.; Zhang, L.; Lian, Z.; Yuan, Z.; Yan, C.-Y.; Zhuo, S.; Zhou, Z.-Y.; Xing, L.-B. *J. Photochem. Photobiol. A Chem.* **2017**, 6–11.
(15) Williams, D. E.; Shustova, N. B. *Chem. - A Eur. J.* **2015**, *21* (44), 15474–15479.
(16) Zhou, H.-C.; Long, J. R.; Yaghi, O. M. *Chem. Rev.* **2012**, *112* (2), 673–674.
(17) Lee, C. Y.; Farha, O. K.; Hong, B. J.; Sarjeant, A. a.; Nguyen, S. T.; Hupp, J. T. *J. Am. Chem. Soc.* **2011**, *133* (40), 15858–15861.
(18) Furukawa, H.; Cordova, K. E.; O'Keeffe, M.; Yaghi, O. M. *Science (80-.).* **2013**, *341* (6149), 1230444–1230444.
(19) Wang, Z.; Cohen, S. M. *Chem. Soc. Rev.* **2009**, *38* (5), 1315.
(20) Li, H.; Eddaoudi, M.; O'Keeffe, M.; Yaghi, O. M. *Nature* **1999**, *402* (6759), 276–279.
(21) O'Keeffe, M.; Yaghi, O. M. *Chem. Rev.* **2012**, *112* (2), 675–702.
(22) Kent, C. a; Liu, D.; Ma, L.; Papanikolas, J. M.; Meyer, T. J.; Lin, W. **2011**, 12940–12943.
(23) Zhang, T.; Lin, W. *Chem. Soc. Rev.* **2014**, 5982–5993.
(24) Kent, C. a.; Mehl, B. P.; Ma, L.; Papanikolas, J. M.; Meyer, T. J.; Lin, W. *J. Am. Chem. Soc.* **2010**, *132* (37), 12767–12769.
(25) Jiang, H.-L.; Feng, D.; Wang, K.; Gu, Z.-Y.; Wei, Z.; Chen, Y.-P.; Zhou, H.-C. *J. Am. Chem. Soc.* **2013**, *135* (37), 13934–13938.
(26) Lee, Y.-R.; Kim, J.; Ahn, W.-S. *Korean J. Chem. Eng.* **2013**, *30* (9), 1667–1680.
(27) Choi, E.-Y.; Wray, C. A.; Hu, C.; Choe, W. *CrystEngComm* **2009**, *11* (4), 553–555.
(28) Burnett, B. J.; Choe, W. *CrystEngComm* **2012**, *14* (19), 6129.
(29) Barron, P. M.; Wray, C. a; Hu, C.; Guo, Z.; Choe, W. *Inorg. Chem.* **2010**, *49* (22), 10217–10219.
(30) Karagiaridi, O.; Bury, W.; Mondloch, J. E.; Hupp, J. T.; Farha, O. K. *Angew. Chem. Int. Ed. Engl.* **2014**, *53* (18), 4530–4540.
(31) Choi, E.-Y.; Barron, P. M.; Novotny, R. W.; Son, H.-T.; Hu, C.; Choe, W. *Inorg. Chem.* **2009**, *48* (2), 426–428.
(32) Karagiaridi, O.; Bury, W.; Tylianakis, E.; Sarjeant, A. a.; Hupp, J. T.; Farha, O. K. *Chem. Mater.* **2013**, *25* (17), 3499–3503.
(33) Jhung, S. H.; Lee, J.-H.; Yoon, J. W.; Serre, C.; Férey, G.; Chang, J.-S. *Adv. Mater.* **2007**, *19* (1), 121–124.
(34) Jung, D.-W.; Yang, D.-A.; Kim, J.; Kim, J.; Ahn, W.-S. *Dalt. Trans.* **2010**, *39* (11), 2883.
(35) Klimakow, M.; Klobes, P.; Thünemann, A. F.; Rademann, K.; Emmerling, F. *Chem. Mater.* **2010**, *22* (18), 5216–5221.

(36) Friščić, T.; Reid, D. G.; Halasz, I.; Stein, R. S.; Dinnebier, R. E.; Duer, M. J. *Angew. Chemie Int. Ed.* **2010**, *49* (4), 712–715.
(37) *Catal. Today* **2012**, *185* (1), 35–40.
(38) Hartmann, M.; Kunz, S.; Himsl, D.; Tangermann, O.; Ernst, S.; Wagener, A. *Langmuir* **2008**, *24* (16), 8634–8642.
(39) Kim, J.; Yang, S.-T.; Choi, S. B.; Sim, J.; Kim, J.; Ahn, W.-S. *J. Mater. Chem.* **2011**, *21* (9), 3070.
(40) Mueller, U.; Schubert, M.; Teich, F.; Puetter, H.; Schierle-Arndt, K.; Pastré, J. *J. Mater. Chem.* **2006**, *16* (7), 626–636.
(41) Czaja, A. U.; Trukhan, N.; Müller, U. *Chem. Soc. Rev.* **2009**, *38* (5), 1284.
(42) Morris, R. E.; Wheatley, P. S. *Angew. Chemie - Int. Ed.* **2008**, *47* (27), 4966–4981.
(43) Ma, S.; Zhou, H.-C. *Chem. Commun.* **2010**, *46* (1), 44–53.
(44) Dietzel, P. D. C.; Besikiotis, V.; Blom, R. *J. Mater. Chem.* **2009**, *19* (39), 7362.
(45) Wang, L.; Sun, J.; Meng, X.; Zhang, W.; Zhang, J.; Pan, S.; Shen, Z.; Xiao, F.-S. *Chem. Commun.* **2014**, *50* (16), 2012.
(46) Aijaz, A.; Xu, Q. *J. Phys. Chem. Lett.* **2014**, *5* (8), 1400–1411.
(47) Roy, S.; George, C. B.; Ratner, M. A. *J. Phys. Chem. C* **2012**, *116* (44), 23494–23502.
(48) Ding, M.; Chen, S.; Liu, X.-Q.; Sun, L.-B.; Lu, J.; Jiang, H.-L. *ChemSusChem* **2017**, *10* (9), 1898–1903.
(49) Hu, Z.; Deibert, B. J.; Li, J. *Chem. Soc. Rev.* **2014**, *43* (16), 5815–5840.
(50) Cui, Y.; Yue, Y.; Qian, G.; Chen, B. *Chem. Rev.* **2012**, *112* (2), 1126–1162.
(51) Kreno, L. E.; Leong, K.; Farha, O. K.; Allendorf, M.; Van Duyne, R. P.; Hupp, J. T. *Chem. Rev.* **2012**, *112* (2), 1105–1125.
(52) Chen, B.; Wang, L.; Zapata, F.; Qian, G.; Lobkovsky, E. B. *J. Am. Chem. Soc.* **2008**, *130* (21), 6718–6719.
(53) Vallet-Regí, M.; Balas, F.; Arcos, D. *Angew. Chemie Int. Ed.* **2007**, *46* (40), 7548–7558.
(54) Horcajada, P.; Serre, C.; Vallet-Regí, M.; Sebban, M.; Taulelle, F.; Férey, G. *Angew. Chemie Int. Ed.* **2006**, *45* (36), 5974–5978.
(55) Horcajada, P.; Chalati, T.; Serre, C.; Gillet, B.; Sebrie, C.; Baati, T.; Eubank, J. F.; Heurtaux, D.; Clayette, P.; Kreuz, C.; Chang, J.-S.; Hwang, Y. K.; Marsaud, V.; Bories, P.-N.; Cynober, L.; Gil, S.; Férey, G.; Couvreur, P.; Gref, R. *Nat. Mater.* **2010**, *9* (2), 172–178.
(56) Horcajada, P.; Gref, R.; Baati, T.; Allan, P. K.; Maurin, G.; Couvreur, P.; Férey, G.; Morris, R. E.; Serre, C. *Chem. Rev.* **2012**, *112* (2), 1232–1268.
(57) Lee, C. Y.; Farha, O. K.; Hong, B. J.; Sarjeant, A. a; Nguyen, S. T.; Hupp, J. T. *J. Am. Chem. Soc.* **2011**, *133* (40), 15858–15861.
(58) Wang, J.-L.; Wang, C.; Lin, W. *ACS Catal.* **2012**, *2* (12), 2630–2640.
(59) Son, H.-J.; Jin, S.; Patwardhan, S.; Wezenberg, S. J.; Jeong, N. C.; So, M.; Wilmer, C. E.; Sarjeant, A. A.; Schatz, G. C.; Snurr, R. Q.; Farha, O. K.; Wiederrecht, G. P.; Hupp, J. T. *J. Am. Chem. Soc.* **2013**, *135* (2), 862–869.
(60) Jin, S.; Son, H.-J.; Farha, O. K.; Wiederrecht, G. P.; Hupp, J. T. *J. Am. Chem. Soc.* **2013**, *135* (3), 955–958.
(61) So, M. C.; Jin, S.; Son, H.-J.; Wiederrecht, G. P.; Farha, O. K.; Hupp, J. T. *J. Am. Chem. Soc.* **2013**, *135* (42), 15698–15701.

(62) Leong, K.; Foster, M. E.; Wong, B. M.; Spoerke, E. D.; Van Gough, D.; Deaton, J. C.; Allendorf, M. D. *J. Mater. Chem. A* **2014**, *2* (10), 3389–3398.
(63) Lee, D. Y.; Shinde, D. V.; Yoon, S. J.; Cho, K. N.; Lee, W.; Shrestha, N. K.; Han, S.-H. *J. Phys. Chem. C* **2014**, *118* (30), 16328–16334.
(64) Joyce, J. T.; Laffir, F. R.; Silien, C. *J. Phys. Chem. C* **2013**, *117* (24), 12502–12509.
(65) Lin, J.; Hu, X.; Zhang, P.; Van Rynbach, A.; Beratan, D. N.; Kent, C. A.; Mehl, B. P.; Papanikolas, J. M.; Meyer, T. J.; Lin, W.; Skourtis, S. S.; Constantinou, M. *J. Phys. Chem. C* **2013**, *117* (43), 22250–22259.
(66) Yang, W.; Zhang, G.; Weng, W.; Qiu, B.; Guo, L.; Lin, Z.; Chen, G. *RSC Adv.* **2014**, *4* (102), 58852–58857.
(67) So, M. C. *Chem. Commun.* **2015**, *51*, 3501–3510.
(68) J. R. Lakowicz. *Principles of Fluorescence Spectroscopy*; Springer: Heidelberg, 2007.
(69) Valeur, B. *Molecular Fluorescence: Principles and Applications*; Wiley-VCH: Weinheim, 2001.
(70) Lin, J.; Hu, X.; Zhang, P.; Van Rynbach, A.; Beratan, D. N.; Kent, C. A.; Mehl, B. P.; Papanikolas, J. M.; Meyer, T. J.; Lin, W.; Skourtis, S. S.; Constantinou, M. *J. Phys. Chem. C* **2013**, *117* (43), 22250–22259.
(71) Kent, C. A.; Liu, D.; Ito, A.; Zhang, T.; Brennaman, M. K.; Meyer, T. J.; Lin, W. *J. Mater. Chem. A* **2013**, *1* (47), 14982.
(72) Kent, C. A.; Liu, D.; Ma, L.; Papanikolas, J. M.; Meyer, T. J.; Lin, W. *J. Am. Chem. Soc.* **2011**, *133* (33), 12940–12943.
(73) Breu, J.; Kratzer, C.; Yersin, H. *J. Am. Chem. Soc.* **2000**, *122* (11), 2548–2555.
(74) Devenney, M.; Worl, L. A.; Gould, S.; Guadalupe, A.; Sullivan, B. P.; Caspar, J. V.; Leasure, R. L.; Gardner, J. R.; Meyer, T. J. *J. Phys. Chem. A* **1997**, *101* (25), 4535–4540.
(75) Park, Y. S.; Wu, Q.; Nam, C.-Y.; Grubbs, R. B. *Angew. Chemie* **2014**, *126* (40), 10867–10871.

CHAPTER 2

Diarylethene-Based Metal-Organic Frameworks

Williams, D. E.; Rietman, J. A.; Maier, J. M.; Tan, R.; Greytak, A. B.; Smith, M. D.; Krause, J. A.; Shustova, N. B. *J. Am. Chem. Soc.* **2014**, *136* (34), 11886–11889.

INTRODUCTION

As the demand for energy continues to rise, the need to modify the existing energy and material landscape is paramount. To address the current energy challenges, development of materials with efficient and directional energy transfer (ET) could be beneficial. Metal-organic frameworks (MOFs)[1–6] are materials assembled from organic linkers and inorganic metal nodes, and exhibit crystallinity, porosity, tunability, and a high surface area, and can be used as a tool to direct ET in a predesigned pathway.[7] One of the major benefits that MOFs can offer to study and model ET processes is that the angles and distances between chromophores as well as the molecular conformations can be assessed by single-crystal X-ray crystallography. The modularity of MOFs allows us to systematically tune the physiochemical properties of MOFs with a nearly limitless combination of organic linkers and metals. ET in a predesigned pathway has previously been studied,[8] however a concept missing from the natural and artificial photosystems is the ability to control ET processes.

Photochromic compounds are a class of organic molecules that can switch between two discrete states when irradiated with UV or visible light, and are capable of controlling the photophysical properties of the molecules coupled to them.[9,10] For example, a molecular dyad system which contained a photochromic derivative (acceptor, A) was coupled to a chromophore (donor, D), and the photochromic compound could control the photophysical response depending on the photoswitch form, open or closed.[11] This type of ET, from D to A in close proximity, can be classified as the Förster Resonance Energy

Transfer (FRET) mechanism, which relies on the transfer of excitation energy in a non-radiative fashion through long range dipole-dipole interactions in distances up to 10 nm.[12,13] Using those works as an inspiration, we sought to develop a MOF which exhibits a fluorescence response when irradiated with UV light, as well as contain metal nodes that will allow for linker installation. Then, after photoswitchable linker installation, modulation of the fluorescence response of the framework (donor) via FRET with the photochromic linker (acceptor) using incident light could be possible. This strategy, which is summarized in Scheme 2.1, provides the possibility of dynamic control of ET in extended light-harvesting matrices.

There are several classes of photochromic molecules, with the more explored among them being diarylethene, spiropyran, and azobenzene derivatives.[14–18] Diarylethene was chosen for immobilization inside the MOF matrix due to its fatigue-resistant photochromic performance, high thermal stability, and a rapid photoisomerization response in the solid state.[11] Diarylethene photochromic compounds contain a 1,3,5-hexatriene moiety (colorless open form) that, when irradiated with UV light, undergo a 6π electrocyclization to form a, less-stable hexadiene (colored closed form).[19,20] The reverse reaction (cycloreversion) to reform the 1,3,5-hexatriene is allowed both photochemically and thermally according to the Woodward-Hoffman π-orbital symmetry rules,[21] but the ability for the molecule to undergo thermal cycloreversion is strongly governed by the steric hindrance of the substituents at the reactive carbons and aryl groups that the photoswitch is comprised of.[22] Several studies have been reported in the literature regarding the photochromic and thermochromic behavior of diarylethene compounds.[19,22–29] These studies conclude that if the aryl groups are thiophene, benzothiophene, or furan

heterocycles, the molecule will remain in either the open or closed isomer in temperatures exceeding 100 °C. However, if the aryl groups are composed of phenyl, pyrrolyl, or indolyl groups, it is not thermally stable and will display switchable behavior with heating. Diarylethene was chosen as the photochromic molecule for our MOF primarily because of its capability for fast photoisomerization in the solid state, as well as the ability to tailor it for thermal stability.

To incorporate a photoswitch into the MOF, a diarylethene-based core was modified with two pyridyl arms to facilitate installation into the framework (Scheme 2.1). The detailed procedure will be discussed in Section 2.2. The MOF containing the diarylethene photoswitch should have an emission profile that overlaps the absorption profile of the photoswitch, as well as possess accessible metal sites for photoswitch immobilization. The two-dimensional (2D) framework, Zn_2(ZnTCPP),[30] has open metal

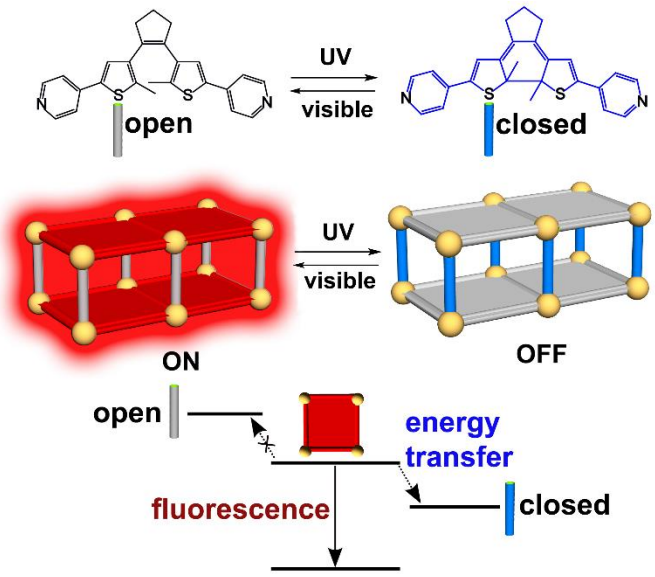

Scheme 2.1. The MOF consists of light harvesting blocks ( ) and photoswitches ( ) in ON and OFF states depending on the wavelength of the incident light (*top*). This simplified diagram demonstrates the transitions responsible for fluorescence and energy transfer in the designed material (*bottom*).

centers for the coordination of pyridyl-based compounds, and also exhibits an emission response in the visible region, therefore the criteria listed above are satisfied.

In this chapter, we report the synthesis of a MOF capable of efficient ET in a predesigned pathway through integration of diarylethene-based photoswitch inside a MOF. This chapter contains three main sections: (i) the synthesis and characterization of the diarylethene-based linker, (ii) the synthesis and characterization of the diarylethene-containing MOF, and (iii) elucidation of the photophysical properties of the prepared MOF.

2.1. Synthesis and Characterization of the Diarylethene Derivative

The diarylethene-based photoswitch, bis(5-pyridyl-2-methyl-3-thienyl)cyclopentene (BPMTC) was prepared using the four-step synthesis as shown in Scheme 2.2.[33] To prepare 2-chloro-5-methylthiphene (**2**), 2-methylthiophene (**1**) underwent a chlorination reaction using N-chlorosuccinimide.[33] Friedel-Crafts acylation was used to produce 1,5-bis(5-chloro-2-methylthien-3-yl)pentane-1,5-dione (**3**),[33] which

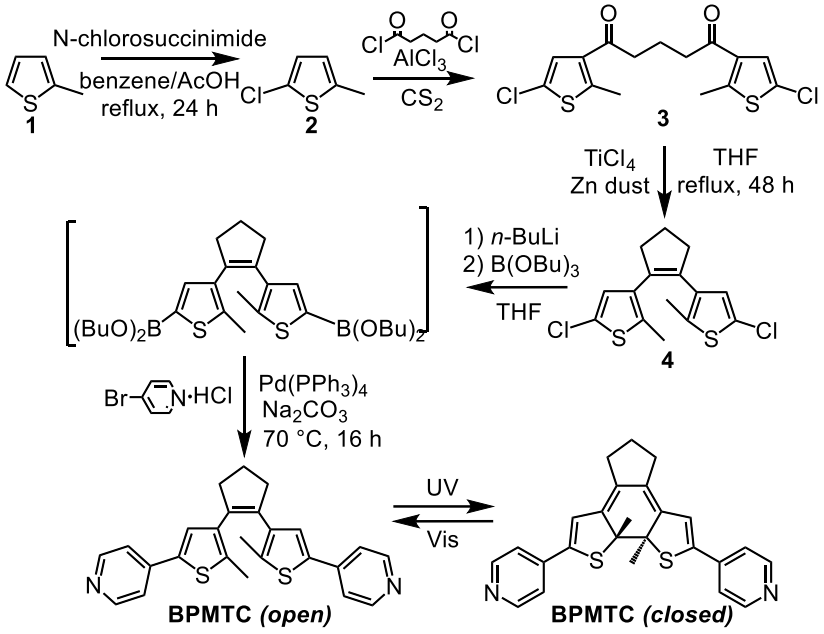

Scheme 2.2. Synthesis scheme of bis(5-pyridyl-2-methyl-3-thienyl)cyclopentene (BPMTC).

was then converted to 1,2-bis(5-chloro-2-methylthien-3-yl)cyclopentene (**4**) by the McMurry coupling reaction.[33] Lastly, BPMTC, was prepared from **4** by a lithium-halogen exchange, followed by a palladium-catalyzed Suzuki coupling reaction with 4-bromopyridine·HCl.[33] Once BPMTC was obtained, it was heated gently (50 °C) under high vacuum for at least 24 hours to remove any trace of solvents, which resulted in a grey powder with a yield of 66%. BPMTC was structurally characterized using ^{1}H and ^{13}C NMR, Fourier-transform infrared (FT-IR), and diffuse reflectance spectroscopies as well as single-crystal X-ray diffraction. Detailed synthetic and characterization techniques are listed in the experimental section. The ^{1}H NMR spectrum of pure BPMTC in the open form is shown in Figure 2.1. To determine the pyridyl-pyridyl distance (from N···N), single crystal X-ray data were obtained on colorless crystals of BPMTC, which were obtained by slowly evaporating a concentrated solution of BPMTC in acetone and hexanes. The structure of BPMTC is shown in Figure 2.2.

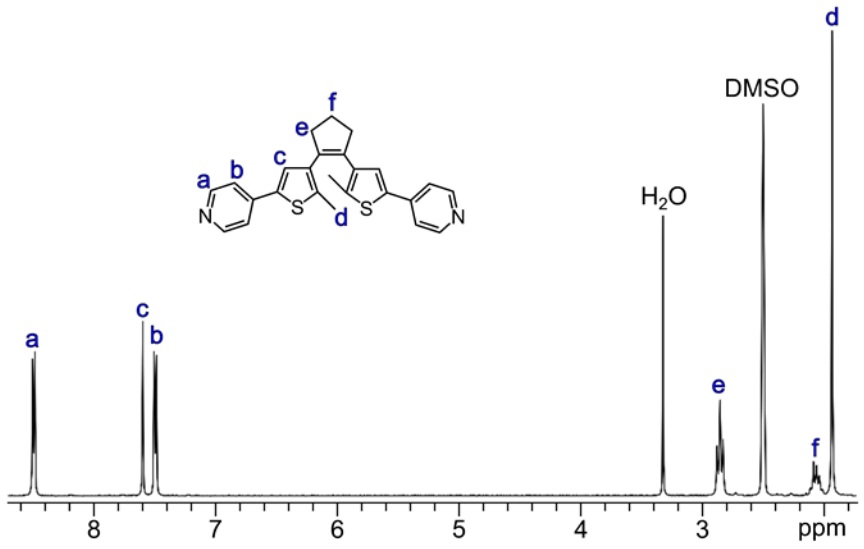

Figure 2.1. The ^{1}H NMR spectrum of BPMTC in DMSO-d_6.

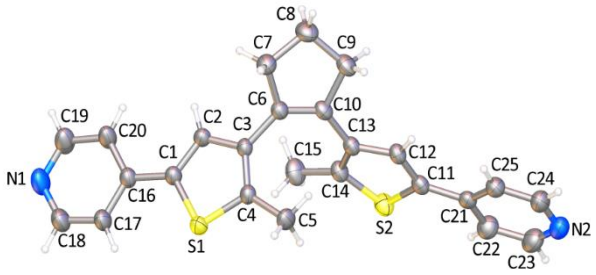

Figure 2.2. Single crystal X-ray structure of BPMTC. Displacement ellipsoids drawn at the 30% probability level. Blue, yellow, gray, and white spheres represent N, S, C, and H atoms, respectively.

To probe the photophysical properties of BPMTC in the solid state, a high-power UV LED (λ = 365 nm) was used in conjunction with a JAZ portable spectrophotometer equipped with an integrating sphere (see the experimental section for more details). It was found that BPMTC changes colorless to blue when irradiated at 365 nm, which indicates conversion of from the open to the closed form (Scheme 2.2). When irradiated with UV light, a large band appears in the absorption profile, with a λ_{max} = 590 nm, which is not observed in the spectrum of the colorless form (Figure 2.3). However, when the sample is irradiated at λ_{ex} = 590 nm with a high-powered LED, the absorption profile starts to drop in intensity, until the sample reaches its original, colorless form. At this point, there is no absorption observed in the visible range. To determine whether FRET could occur, the emission spectrum of a prepared porphyrin-based MOF (vide infra) was overlayed with the absorption profile of BPMTC (Figure 2.3). If BPMTC is in the closed form, an overlap between the absorption spectrum of BPMTC and the emission spectrum of the porphyrin MOF occurs, but there is no overlap when it is in the open form. This lead us to hypothesize that the ET can occur between the porphyrin-containing MOF layers and BPMTC.

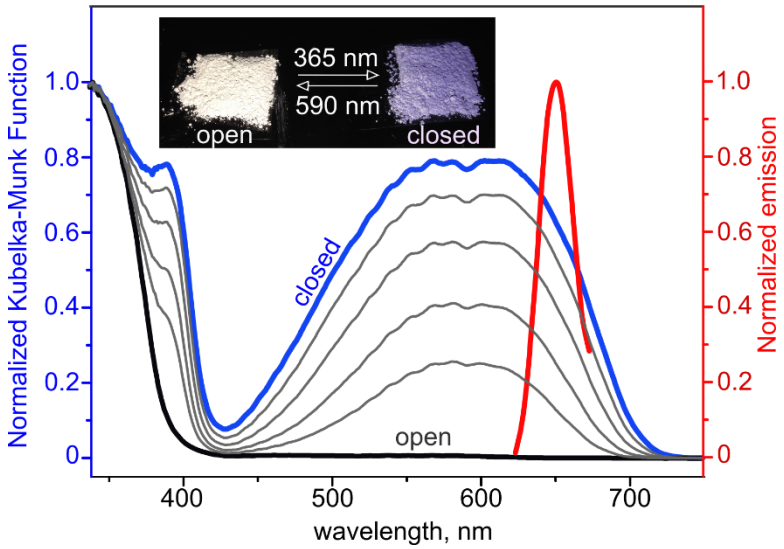

Figure 2.3. Normalized diffuse reflectance spectrum of open (*black line*) and closed (*blue line*) BPMTC, and the emission overlay of the porphyrin-based MOF (red). Gray lines correspond to the intermediate absorption profiles between the open and closed forms. Inset shows shows a photograph of BPMTC after 365 nm and 590 nm irradiation.

2.2. Synthesis and Characterization of MOF 1

The photoswitchable MOF (**1**), was prepared using commercially available H_4TCPP (Figure 2.4), *N*,*N*-diethylformamide (DEF), ethanol (EtOH), $Zn(NO_3)_2 \cdot 6H_2O$, and as-synthesized BPMTC (Section 1.1). They were subjected to solvothermal synthesis at 80 °C for 14 h in a programmable oven, and produced red plate crystals in 24 % yield after cooling (see the experimental section for full synthetic details).

To evaluate the structure and composition, single crystals of **1** were subjected to X-ray analysis, and due to their small size of (<5 μm thick), data collection was performed at the Advanced Light Source, Lawrence Berkeley National Laboratory, Beamline 11. 3.1. Details of data collection and structural solution can be found in the experimental section. Based on the crystallographic data shown in Figure 2.4, we found that **1** is composed of stacked porphyrin layers which are interconnected between zinc paddlewheel secondary

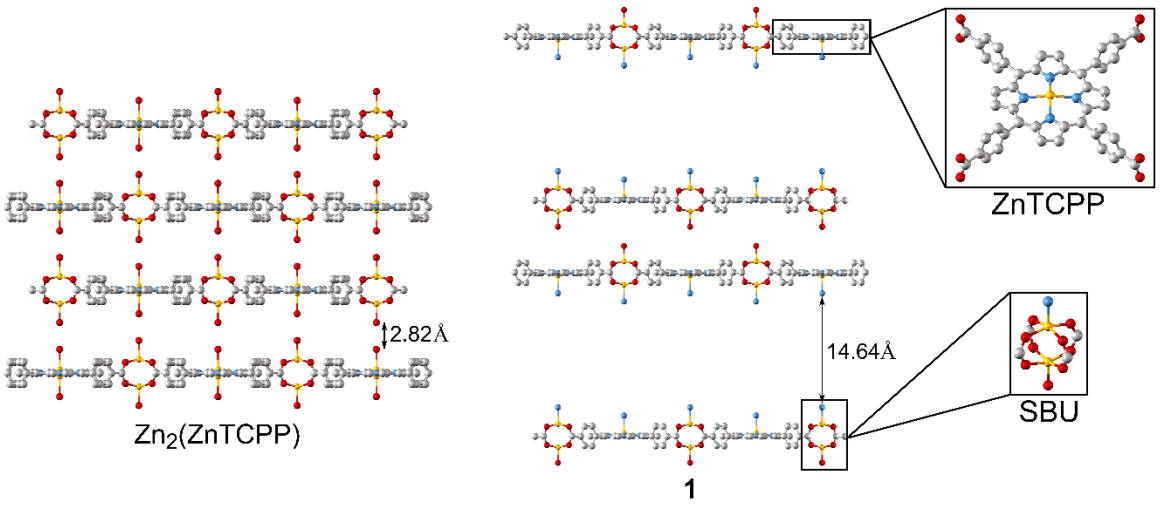

Figure 2.4. The X-ray crystal structures of Zn_2(ZnTCPP)[30] (*left*) and **1** (*middle*). The porphyrin subunit of the MOF (*top right*). Zinc paddlewheel SBU (*bottom right*). Orange, red, blue, and gray spheres represent Zn, O, N, and C atoms, respectively. Hydrogen atoms are omitted for clarity.

building units (SBUs). Furthermore, the 2D porphyrin layers ($C_{48}H_{30}N_4O_{11}Zn_3$, Zn_2(ZnTCPP)) are separated by a substantial distance, which is in line with the length of BPMTC. The residual electron density between the porphyrin layers could not be assigned due to severe disorder, which can be attributed to the photoswitchable nature of BPMTC, as well as partial linker installation. In comparison, layers of Zn_2(ZnTCPP) in the 2D MOF without installed photoswitches are separated by a distance of 2.82 Å. In contrast, interlayer distance in **1** is 14.64 Å. Therefore, interlayer expansion can only be attributed to the successful installation of BPMTC. The nitrogen-nitrogen distances from the pyridyl groups in other diarylethene derivatives are in the range of 14.46 Å to 15.41 Å,[34–36] which is consistent with the observed interlayer distances in **1**.

The PXRD pattern of bulk **1** matched the simulated pattern from the single-crystal X-ray structure. Moreover, the interlayer expansion led to a shift to lower 2θ angles in the powder X-ray spectrum of **1** when compared to Zn_2(ZnTCPP), as shown in Figure 2.5. To determine the percent installation of BPMTC and overall composition of **1**, it was digested

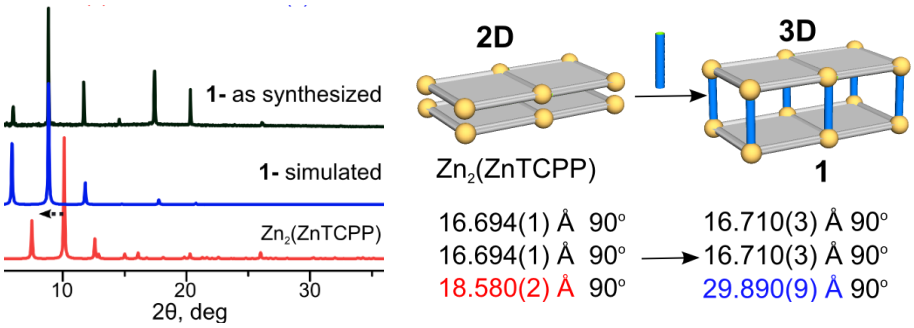

Figure 2.5. The PXRD patterns of **1** and simulated Zn_2(ZnTCPP)[30] (*left*) The 2D→3D transformations from BPMTC insertion (*right*). The dashed arrow indicates the changes in the PXRD profile associated with increase of interlayer distance.

(destroyed in the presence of acid) to utilize solution-based ^{1}H NMR spectroscopy. This procedure is necessary since MOFs are insoluble, and thereby must be characterized either using solid-state methods, or digested in order to employ conventional methods, including NMR analysis in solution. For digestion, crystals of **1** (7 mg) were soaked in fresh DMF, which was replaced twice a day for three days to eliminate the residual linker adsorbed on the MOF surface, filtered, and dried under vacuum overnight at 50 °C. DMSO-d_6 (500 mL) and concentrated hydrochloric acid (3.5 μL) were added and the vial was sonicated for several minutes prior to NMR analysis. To perform mass spectrometry analysis, the digestion procedure was slightly modified, and instead of DMSO-d_6, 500 μL of chloroform and 3.5 μL of concentrated hydrochloric acid were added to washed crystals of **1** and sonicated for several minutes. Once dissolved, the sample was dried for 48 hours with gentle heating (50 °C) under high vacuum before being submitted for mass spectrometry analysis. As seen from Figure 2.6, both ^{1}H NMR spectroscopy and mass spectrometry show clear evidence that BPMTC and TCPP are present in **1**. The relative integrations of H_4TCPP to BPMTC are 1:0.85 in the ^{1}H NMR spectrum of **1**, which corresponds to 48% installation of BPMTC between 2D layers of **1**.

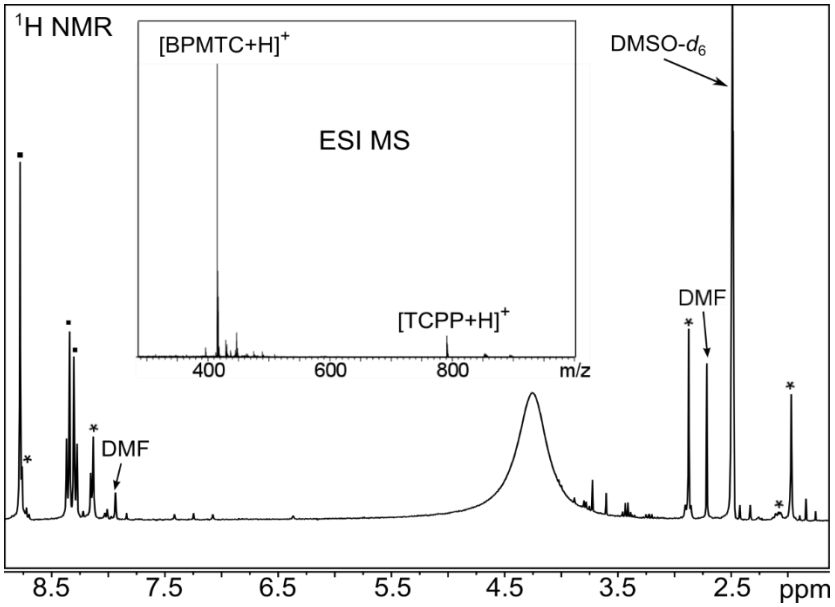

Figure 2.6. The ^{1}H NMR spectrum of digested **1**. The peaks corresponding to H_4TCPP(■**)** and BPMTC (∗) are labeled. The inset shows the electrospray ionization mass-spectrum of digested **1**.

To further probe the composition of **1**, the bulk sample was analyzed using energy-dispersive X-ray (EDX)spectroscopy and elemental analysis. Single crystals of **1** were sonicated for 10 minutes, followed by vigorous stirring in a 20 mL vial containing ethanol for several days. Daily, the suspension was centrifuged and the ethanol was replaced to remove residual BPMTC adsorbed on the surface of the MOF. The final wash was checked using UV-Vis spectroscopy to confirm that all nonbonded BPMTC had been removed from the MOF. EDX spectra were collected on a TESCAN Vega-3 SBU scanning electron microscope equipped with a backscattered electron detector. Results showed the presence of sulfur, nitrogen, zinc, and oxygen in **1**, which could be attributed to BPMTC and porphyrin linkers, as well as metal inside the metal nodes in **1**, as shown in Figure 2.7.

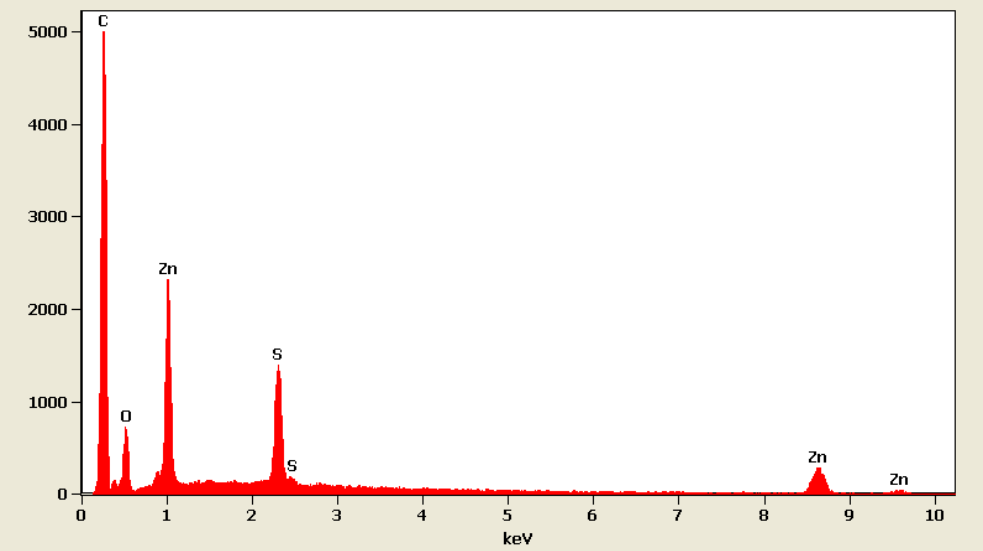

Figure 2.7. The EDX spectrum of as-synthesized **1**.

Another characterization method that can be performed in the solid-state without MOF degradation is FT-IR spectroscopy. Data was obtained on samples of BPMTC, H_4TCPP, and **1**, and determined the presence of both the donor and acceptor in **1** (Figure 2.8).

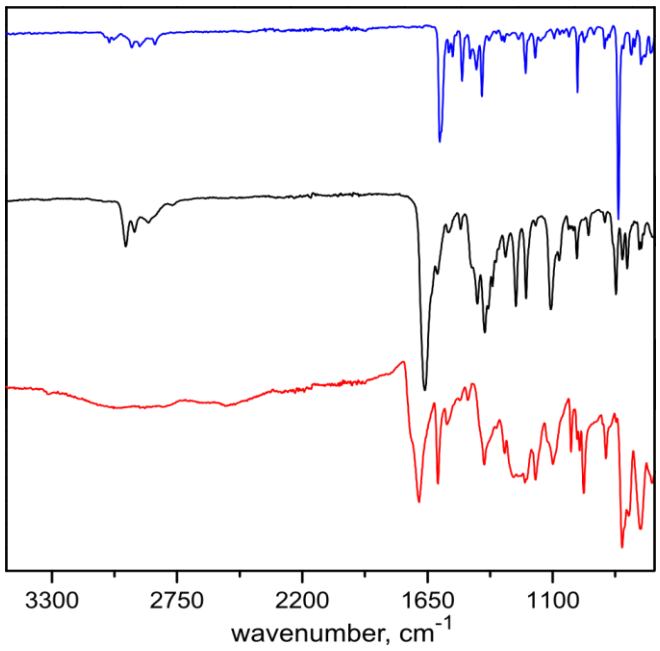

Figure 2.8. The FT-IR spectra of as-synthesized **1** (black), BPMTC (blue), and H_4TCPP (red).

2.3. Photophysical Properties of MOF 1

MOF photophysical properties were elucidated using diffuse reflectance, steady state, and time-resolved fluorescence spectroscopies. To test whether the BPMTC photoswitch could preserve the ability to isomerize after coordinative immobilization and affect the photophysical properties of **1**, the emission intensity of **1** was monitored while irradiating it with UV light. Irradiation of **1** at 365 nm resulted in the suppression of the fluoresence signal caused by the BPMTC photoisomerization from the initially open form to the closed form. We found that the fluorescence intensity could then be restored after irradiation with 590 nm excitation (Figure 2.9), which is attributed to the BPMTC photoisomerization back to the open form. As a control experiment, the fluorescence response from the 2D Zn_2(ZnTCPP) MOF, which does not contain BPMTC, was monitored while irradiated at 365 nm. We found that there was no attenuation in the signal from

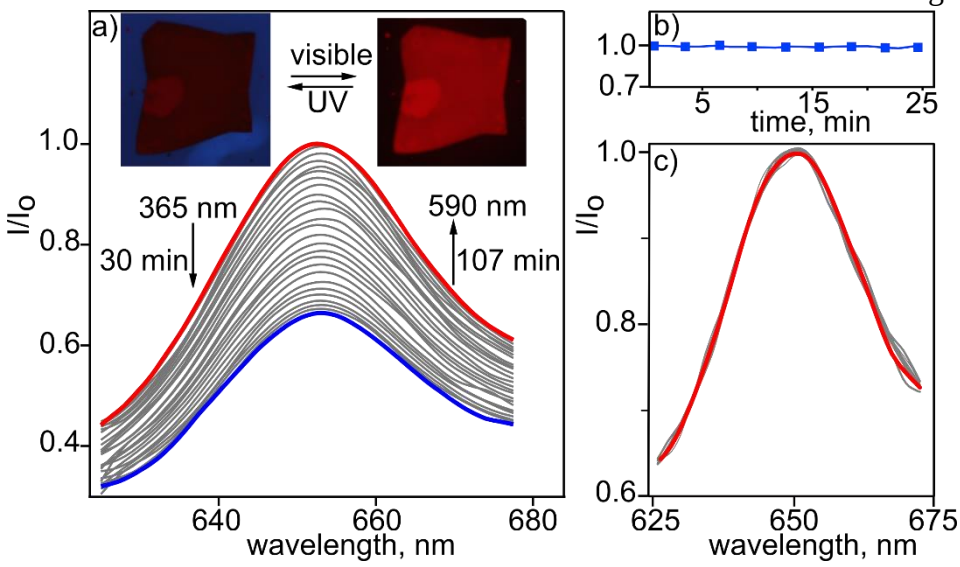

Figure 2.9. a) Emission spectra recorded for **1**, scaled such that the peak intensity I_o = 1.0 on the first scan at λ_{ex} = 590 nm. The inset shows the epifluorescence microscopy images of a crystal of **1** at λ_{ex} = 370 nm (left) and 530 nm (right). b) Time-dependent fluorescence responses of Zn_2(ZnTCPP) irradiated at 365 nm for 25 min. c) Emission spectra recorded for Zn_2(ZnTCPP) (λ_{ex} = 590 nm) analogous to **1**. The first emission spectrum of Zn_2(ZnTCPP) is highlighted in red.

Zn_2(ZnTCPP) over 30 minutes. The intensity attenuation as a function of time shows no fluorescence decay in Zn_2(ZnTCPP) MOF, due to the absence of BPMTC.

During the fluorescence measurements, we observed that the process of closing the photoswitches within the MOF is much faster than opening. As shown in Figure 2.9, 60% modulation depth was achieved after 30 minutes, however it took nearly four times as long to recover the fluorescence intensity using 590 nm excitation. This fact is consistent with the photoisomerization rates which were observed for a non-coordinated BPMTC in the solid-state. Indeed, the conversion of BPMTC from the closed to open form at 590 nm irradiation is much slower than the reverse process.

For the evaluation of the switching capabilities of **1**, the bulk sample was irradiated at 365 nm, followed by 590 nm for 5 consecutive cycles (Figure 2.10). We found that the fluorescence modulation in **1** is consistently reversible, and in each case, the initial fluorescence intensity was recovered. Therefore **1** can maintain its photoswitchable behavior while preserving its crystallinity (Figure 2.12). The rate constant of fluorescence

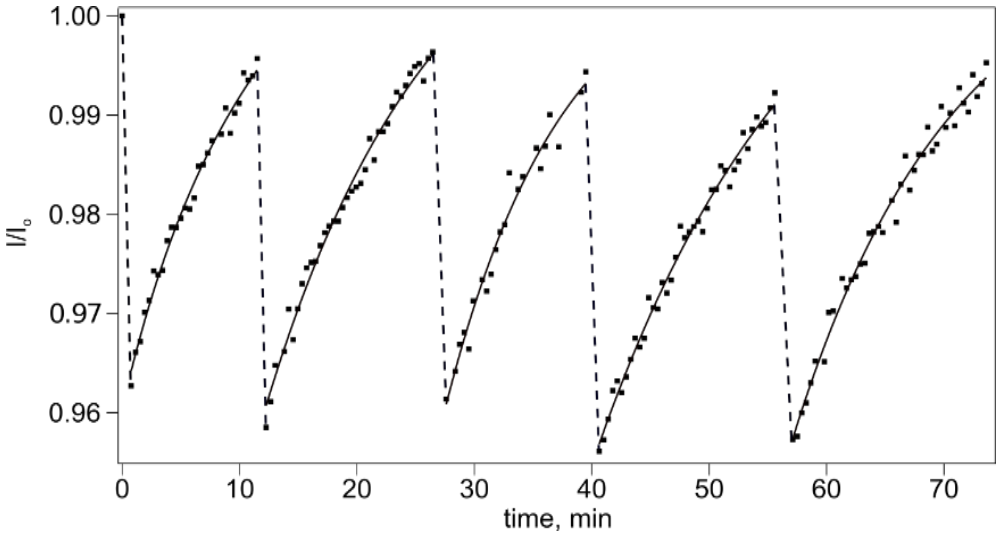

Figure 2.10. Optical cycling (I/I_o vs. time) of **1** by alternative irradiation at 365 (- - -) and 590 (—) nm.

I/I_o decay (I_o – maximum of emission intensity at 653 nm) was calculated by fitting the decay with a monoexponential function, and was found to be 1×10^{-3} s^{-1} (Figure 2.11). To rule out MOF degradation as a cause for fluorescence modulation, the crystallinity of the sample was evaluated by PXRD before and after fluorescence measurements. Crystals of **1** from the bulk sample were placed into a 4 mm quartz sample cell, and the crystals were dried slightly (i.e. not all the DMF was removed). Notably, MOFs containing zinc paddlewheel nodes are typically susceptible to degradation after prolonged dryness or exposure to water.[37] Fluorescence measurements were performed, and then the crystals were then transferred to a zero background plate for PXRD analysis. As shown in Figure 2.12, **1** remained intact after 75 min of optical cycling and 90 min of 365 nm irradiation, ruling out degradation as a cause for fluorescence modulation.

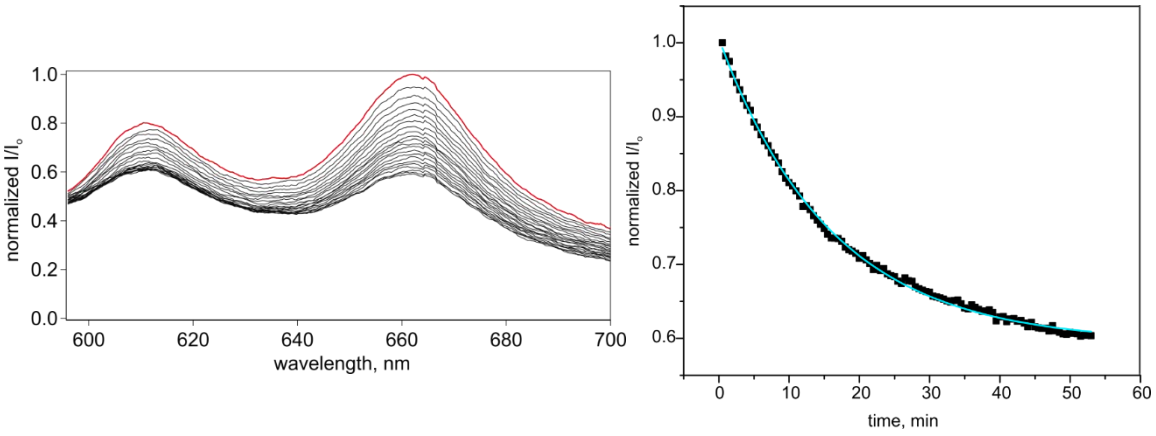

Figure 2.11. (*left*) Emission spectra of **1** during irradiation at 365 nm using a high-power LED. The excitation power was held constant and the spectra are scaled such that the maximum fluorescence intensity $I = I_o$ after the first 30-sec scan. (*right*) Time-dependence of the maximum intensity at ~660 nm. The blue solid line is a fit of the experimental data with the monoexponential function $y = y_o + B_1 \exp(-t/c_1)$ ($B_1 = 0.41$, $c_1 = 15.96$ min).

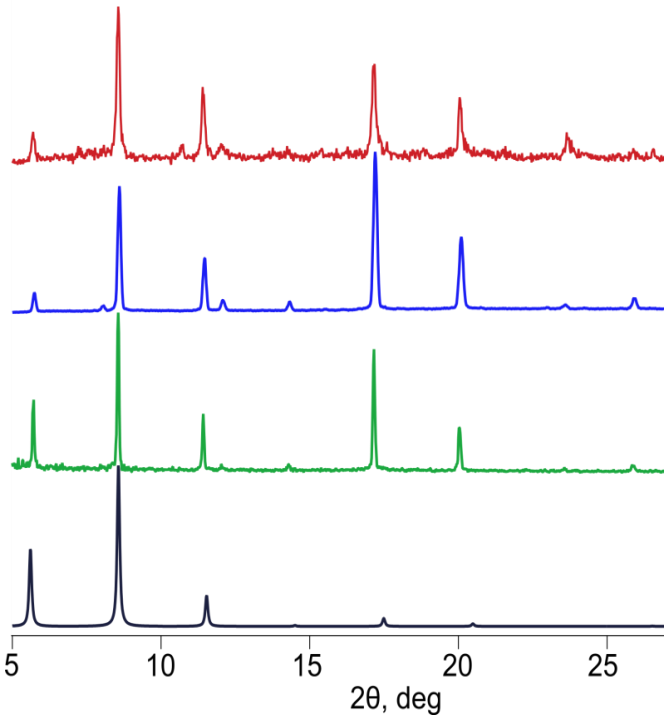

Figure 2.12. PXRD patterns of **1**: simulated with preferential orientation along 00l direction (black), as-synthesized (green), after optical cycling for 75 min (blue), and after irradiation at 365 nm for 90 min (red).

Fitting of Fluorescence Decays. Energy Transfer Efficiency, Φ_e.

To describe quantitatively the ET processes occurring in **1**, the ET efficiency, Φ_e, was estimated based on experimentally found lifetimes of Zn_2(ZnTCPP) and **1** (Equation 2.1). The fluorescence lifetimes for **1** and Zn_2(ZnTCPP) were acquired (λ_{ex} = 360 nm) by fitting the fluorescence decays with a triexponential function (Equation 2.2 and 2.3). In Figure 2.13, analysis of the decay curves clearly demonstrates that fluorescence decay of **1** is more rapid in comparison to Zn_2(ZnTCPP). This fact is consistent with experimentally found amplitude-weighted average lifetime values for Zn_2(ZnTCPP) and **1**, which are 1.46 and 1.24 ns, respectively (Table 2.1), corresponding to a Φ_e of 15%. The corresponding energy transfer constant, k_e, was estimated to be 1.2×10^{10} s^{-1}.

$$\Phi_e = k_e / (k_r + k_{nr} + k_e) = k_e / (k_o + k_e)$$ **Equation 2.1.**

where k_r, k_{nr}, and k_e = radiative decay, non-radiative decay, and ET constants, respectively. The k_o and k_e values were found from the lifetimes for Zn_2(ZnTCPP) and **1**, which are $\tau_{2D} = 1/k_o$ and $\tau_{3D} = 1/(k_o + k_e)$, respectively.

$$I(t) = \int_0^t IRF(t') \cdot \left(C + \sum_{i=1}^{3} A_i \exp\left(-\frac{t - t'}{\tau_i} \right) \right) dt'$$ **Equation 2.2.**

where τ and A are lifetime and amplitude, respectively.

The weighted average fluorescence lifetimes were calculated based on Equation. 2.3.

$$\tau_{av} = (A_{w1}\tau_1 + A_{w2}\tau_2 + A_{w3}\tau_3)/(A_{w1} + A_{w2} + A_{w3})$$ **Equation 2.3.**

where $A_{wi} = A_i / \Sigma A_i$.

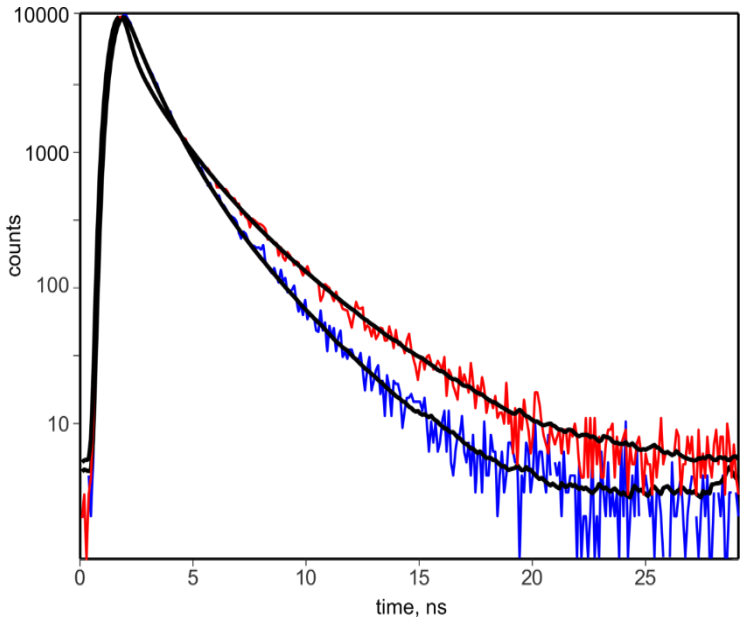

Figure 2.13. Fluorescence decays of **1** (blue) and Zn_2(ZnTCPP) (red). Black solid lines are fits of decays according to Equation 2.1.

Table 2.1. Amplitudes and weighted lifetimes of Zn_2(ZnTCPP) and **1**.

	A_{w1}	τ_1, ns	A_{w2}	τ_2, ns	A_{w3}	τ_3, ns	τ_{av}, ns
1	0.20	0.39	0.57	1.04	0.22	2.52	1.24
Zn_2(ZnTCPP)	0.35	0.20	0.41	1.41	0.24	3.34	1.46

To summarize all three sections, the data indicate that the synthesized BPMTC photoswitch was successfully immobilized between 2D MOF layers, which produced **1**. By coordinatively immobilizing the BPMTC photoswitches into a MOF, we achieved a system which exhibited solid-state photoisomerization, while at the same time, directed the PL response.

The prepared MOF underwent comprehensive structural and photophysical characterization. Based on single-crystal X-ray data, we observed a significant increase in interlayer distance in **1** when compared with the parent 2D MOF, from 2.82 Å to 14.64 Å in Zn_2(ZnTCPP) and **1**, respectively. In addition to single-crystal X-ray data, we employed seven characterization techniques including elemental analysis, PXRD, MS as well as EDX, NMR, and IR spectroscopy for confirmation of BPMTC installation. The results obtained from all applied characterization techniques clearly indicated that BPMTC pillars were successfully immobilized inside the rigid framework **1**.

To study the effect of BPMTC photoisomerization on the photophysical properties of the framework, we used fluorescence spectroscopic studies to show that the photoluminescence response from **1** could be attenuated by alternation of the excitation wavelengths. To ensure that the integrity of **1** was not affected, and the observed fluorescence decays were not caused by MOF degradation, we confirmed the MOF integrity by PXRD analysis. We have also found that **1** could undergo a series of optical

cycles restoring its emission. To quantify the energy transfer processes occurring in **1**, we estimated ET quantum efficiency based on the lifetimes of **1** and Zn_2(ZnTCPP), which were found to be 1.46 and 1.24 ns, respectively. Based on time resolved photoluminescence studies, the ET quantum efficiency was found to be 15%.

Conclusion

We have demonstrated the diarylethene photoswitch, BPMTC, is capable of retaining its photochromic properties after coordinative immobilization inside of a rigid, porous scaffold. The reversible photoisomerization of BPMTC within the PL scaffold allowed for the emission properties of the framework to be controlled through the activation of ET processes. The presented MOF is capable of light harvesting and ET due to the spectral overlap between the BPMTC photoswitches and porphyrin chromophores. The integrity of MOFs allows for the system to retain structural integrity after multiple optical cycles. Photoswitchable ligands can be used as a tool to direct the photophysical properties of the parent MOF, thereby directing the chromophore behavior in large light-harvesting ensembles.

EXPERIMENTAL SECTION

Materials.

$Zn(NO_3)_2 \cdot 6H_2O$ (technical grade, Ward's Science), tetrakis(4-carboxyphenyl)porphyrin (97%, Frontier Scientific), 2-methylthiophene (98%, Matrix Scientific), *n*-chlorosuccinimide (98%, Sigma-Aldrich), glutaryl dichloride (97%, Acros Organics), $TiCl_4$ (99%, Alfa Aesar), zinc dust (95%, Macron), 4-bromopyridine hydrochloride (98%, Matrix Scientific), tri-*n*-butylborate (98%, Strem Chemicals), glacial

acetic acid (ACS grade, BDH), *N,N*-diethylformamide (> 99%, TCI America), *N,N*-dimethylformamide (ACS grade, BDH), *n*-butyllithium solution (2.5 M in hexanes, Sigma-Aldrich), benzene (ACS grade, Fischer Scientific), CS_2 (99.9%, Sigma-Aldrich), ethylene glycol (HPLC grade, Amresco), $Pd(PPh_3)_4$ (99.8%, Alfa Aesar), hexanes (ACS certified, Fischer Scientific), HNO_3 (ACS grade, Fischer Scientific), ethyl ether (ACS grade, J. T. Baker® Chemicals), ethyl acetate (HPLC grade, EMD Chemicals), CH_2Cl_2 (ACS grade, BDH), $CDCl_3$ (Cambridge Isotopes), and DMSO-d_6 (Cambridge Isotopes) were used as received.

Synthesis.

The compounds **1-4**[33], BPMTC[33] and Zn_2(ZnTCPP)[38] were prepared according to the reported procedures.

*Synthesis of 2-chloromethylthiophene (**1**)*

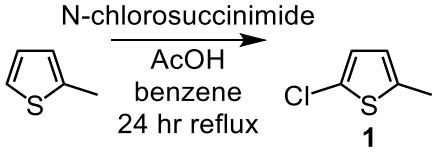

Scheme 2.3. Synthesis of 2-chloromethylthiophene **(1)**.

Benzene (120 mL) and acetic acid (120 mL) were degassed in a 500 mL Schlenk flask by bubbling nitrogen through the solution for two hours. After degassing, *n*-chlorosuccinimide (32.0 g, 0.240 mol) and 2-methylthiophene (21.5 g, 0.219 mol) were added and the solution was degassed for an additional hour before heating to reflux under nitrogen. After the solution was heated at reflux overnight, the reaction mixture was cooled and 150 mL ice cold water was added to the solution and stirred. The reaction mixture was extracted with DCM (3 × 150 mL) and the combined organic layers were washed with

water (3 × 200 mL), dried over Na_2SO_4, and then evaporated under vacuum which yielded a brown oil. The oil was distilled under high vacuum and **1** was obtained as a colorless oil (14.7 g, 0.150 mol) in 54% yield. ^{1}H NMR ($CDCl_3$, ppm): δ = 6.73-6.12 (1H, d, J = 2.2 Hz), 6.56-6.55 (1H, m), and 2.44(3H, s).

*Synthesis of 1,5-Bis(5-chloro-2-methylthien-3-yl)pentane-1,5-dione (**2**)*

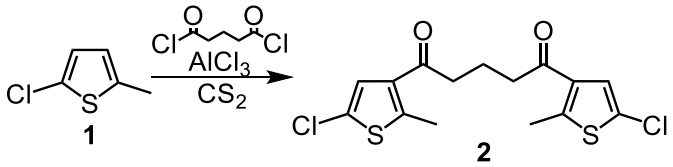

Scheme 2.4. Synthesis of 1,5-Bis(5-chloro-2-methylthien-3-yl)pentane-1,5-dione (**2**).

After a solution of **1** (5.76 g, 43.6 mmol), glutaryl dichloride (3.67 g, 21.7 mmol), and 50 mL CS_2 were stirred in an ice bath for 30 minutes, $AlCl_3$ (7.00 g, 52.5 mmol) was slowly added. The solution was stirred in a nitrogen atmosphere for 24 hours before adding 100 mL ice cold water. The slurry was stirred for 20 minutes, or until the black tar on the walls of the flask were dissolved, the mixture was extracted with DCM (3 × 150 mL) and the combined organic layers were washed with water (3 × 200 mL), dried over Na_2SO_4, and then evaporated under vacuum to yield a black solid. The solid was purified using column chromatography (silica, hexane/diethyl ether 9:1), to afford a pale yellow powder (7.62 g) in 73 % yield. ^{1}H NMR ($CDCl_3$, ppm): δ = 2.02-2.11 (2H, p, J = 6.9 Hz), 2.66 (6H, s), 2.86 (4H, t, J = 6.9), and 7.19 (2H, s).

*Synthesis of 1,2-Bis(5-chloro-2-methylthien-3-yl)cyclopentene (**3**)*

$TiCl_4$ (3.20 mL, 9.77 mmol) was added dropwise to a cold solution of **2** (3.00 g, 8.30 mmol) and THF (100 mL), followed by the addition of Zn dust (3.45, 52.7 mmol). The solution was stirred for two hours in an ice bath and then heated to reflux under a nitrogen atmosphere for 48 hours. The solution was cooled to room temperature before 100

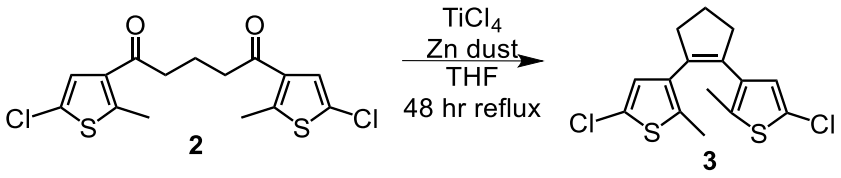

Scheme 2.5. Synthesis of 1,2-Bis(5-chloro-2-methylthien-3-yl)cyclopentene (**3**).

mL of 10% K_2CO_3 was added, and the solution was stirred for an additional five minutes. Hexane was added to the flask, stirred for one minute, and decanted into a separatory funnel. This was repeated several times until the decanted hexane became colorless, then the combined organic layers were washed with water (3 × 100 mL), dried over Na_2SO_4, and the solvent evaporated under vacuum to yield to afford a yellow oil, which crystallizes overnight after placing it in the refrigerator. The yellow crystals were further purified by column chromatography (silica, hexane) to afford a white solid (1.62 g) in 59 % yield. ^{1}H NMR (DMSO-d_6, ppm): δ = 1.85 (6H, s), 1.92-2.02 (2H, p, J = 7.5), 2.69-2.74 (4H, t, J = 7.64), and 6.84 (2H, s).

*Synthesis of 1,2-bis(2-methyl-5-(pyridin-4-yl)thiophen-3-yl)cyclopentene (**BPMTC**)*

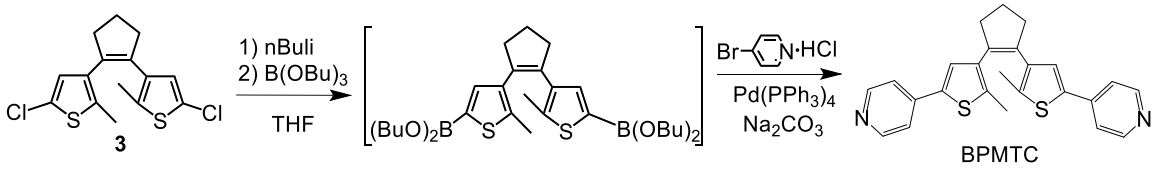

Scheme 2.6. Synthesis of 1,2-bis(2-methyl-5-(pyridin-4-yl)thiophen-3-yl)cyclopentene (BPMTC).

N-butyllithium (2.5 M in hexanes, 5.04 mL, 12.6 mmol) was added to an ice-cooled solution of **3** (1.88 g, 5.71 mmol) in 15 mL dry THF. After 15 minutes of stirring, tri-butylborate (4.62 mL, 17.1 mol) was added, and flask was removed from the ice bath and allowed to warm up to room temperature while stirring. The solution was stirred for 1 hour after removing it from the ice bath. Meanwhile, a second flask was prepared by heating

$Pd(PPH_3)_4$ in 20 mL dry of THF to 70 °C in a two-neck flask. After 15 minutes, 25 mL of 2 M K_2CO_3, ethylene glycol (10 drops), and 4-bromopyridine·HCl (2.43 g, 12.5 mol) were added. Then the solution from the initial flask was transferred via cannula in one portion. The combined mixture was heated to 70 ° for 16 hours. The solution was then cooled to room temperature, and 20 mL water was added. Then the mixture was extracted several times with diethyl ether. The combined organic layers were washed with water and brine and the solvent was evaporated under vacuum, yielding a brown oil. The oil was purified using column chromatography (silica, ethyl acetate/hexane 4:1) and the product was afforded as a purple oil. The oil appeared pure by ^{1}H NMR, however it was further purified by sonicating in hexane and collecting the grey precipitate. After repeating this procedure numerous times, a gray powder was obtained in 66% yield. The powder was made white by irradiating the bulk of the sample with a 590 nm LED with occasional stirring. ^{1}H NMR ($CDCl_3$, ppm): 2.02 (6H, s), 2.11 (2H, q, J = 7.1), 2.85 (4H, t, J = 7.1), 7.21 (2H, s), 7.34 (4H, dd, J = 1.4 Hz, 4.6 Hz), 8.53 (4h, dd, J = 1.4 Hz, 4.6 Hz). IR (neat, cm^{-1}): 3048, 2949, 2914, 2848, 1596, 1556, 1540, 1498, 1463, 1435, 1411, 1380, 1324, 1312, 1250, 1219, 1177, 1154, 1094, 1069, 1028, 991, 761, 919, 872, 822, 754, 740, 712, 670 (Figure 2.8). The single-crystal structure of BPMTC is shown in Figure 2.2.

For the synthesis of **1**, $Zn(NO_3)_2·6H_2O$ (17 mg, 58 μmol) and H_4TCPP (7.9 mg, 10 μmol) were placed in a 1-dram vial and dissolved in 2.1 mL DEF and 0.5 mL EtOH, followed by sonication for 10 min. To the solution, BPMTC (6.2 mg, 15 μmol) in 0.16 mL DEF and 30 μL of HNO_3 (1 M solution in EtOH) were added. The resulting solution was sonicated for 10 min and then heated at 80 °C for 14 hours in an isothermal oven. After 14 h of heating, the reaction mixture was cooled down to room temperature at 0.5 °C/min.

Red square-plate crystals of **1** (7.7 mg, 3.7 μmol) were isolated in 24% yield. IR (neat, cm^{-1}): 2975, 2937, 2876, 1661, 1606, 1556, 1504, 1431, 1398, 1383, 1364, 1307, 1262, 1217, 1175, 1108, 1071, 1030, 1009, 994, 943, 871, 822, 794, 773, 720, 711 (Figure 2.8).

Single Crystal X-ray Data.

BPMTC·0.5(C_3H_6O) ($C_{25}H_{22}N_2S_2$·0.5(C_3H_6O)), ***BPMTC***

X-ray intensity data from a colorless plate crystal of BPMTC were collected at 296(2) K using a Bruker SMART APEX diffractometer (Mo Kα radiation, λ = 0.71073 Å).[39] The raw area detector data frames were reduced using the SAINT+ program.[39] Final unit cell parameters were determined by least- squares refinement of 7127 reflections from the data set. The structure was solved by direct methods with SHELXS.[40] Subsequent difference Fourier calculations and full-matrix least-squares refinement against F^2 were performed with SHELXL-2014/1[40] using OLEX2.[41] The compound crystallizes in the monoclinic space group $P2_1/n$ as determined by the pattern of systematic absences in the intensity data. The asymmetric unit consists of one $C_{25}H_{22}N_2S_2$ molecule and half of one acetone molecule, which is disordered across an inversion center. The acetone is further disordered within the asymmetric unit over two independent sites with refined occupancies 0.267(8) / 0.233(8) (constrained to the sum of 0.5). Non-hydrogen atoms were refined with anisotropic displacement parameters except for disordered atoms of the acetone solvate (isotropic). Hydrogen atoms were placed in geometrically idealized positions and included as riding atoms. The largest residual electron density peak in the final difference map is 0.37 e/$Å^3$, located among the disordered acetone molecules. The crystallographic data for BPMTC·0.5(C_3H_6O) are shown in Table 2.2.

*[Zn(ZnTCPP)(BPMTC)$_{0.85}$(DEF)$_{1.15}$]·(DEF)$_{5.15}$(H$_2$O)$_{7.25}$ (Zn$_3$C$_{100.75}$H$_{126.5}$N$_{12}$O$_{21.55}$S$_{1.7}$, **1**).*

X-ray intensity data from a dark red plate of **1** were collected at 150 K on a D8 goniostat equipped with a Bruker APEXII CCD detector at Beamline 11.3.1 at the Advanced Light Source (Lawrence Berkeley National Laboratory) using synchrotron radiation tuned to λ = 1.0333 Å. For data collection, frames were measured for a duration of 3-s at 0.3º intervals of ω. The data frames were collected using the program APEX2 and processed using the SAINT program routine within APEX2. The data were corrected for absorption and beam corrections based on the multi-scan technique as implemented in SADABS.[42] The structures were solved by direct methods using SHELXS[40]shelds and refined against F^2 on all data by full-matrix least squares as implemented in S4 SHELXL-97.[43] The Zn, C, and N atoms in Zn$_2$(ZnTCPP) layers were refined anisotropically. Hydrogen atoms attached to the ligand were included in the model at geometrically calculated positions using a riding model. Due to partial occupancy of BPMTC and the disorder of the solvent molecules, which is very common in MOF structures,[44,45] the large amount of spatially delocalized electron density in the pores of the lattice was observed. The acceptable refinement values could not be obtained for this electron density (maximum and minimum of residual density were 0.73 and −0.89 e/Å^3, respectively), and therefore, the best residual indices were obtained from a model for which the program SQUEEZE[46] was used to account for the electron density in regions of high disorder. Part of the extended structure is shown in Figure 2.4, and the refinement data are given in Table 2.2.

Fluorescence spectroscopy.

Steady-state emission spectra were acquired on a Perkin Elmer LS55 fluorescence spectrometer equipped with a pulsed high-energy xenon source for excitation. Emission

measurements on solid samples were collected in front-face mode on the single crystals of the appropriate materials placed inside the 6-mm quartz sample holder that, in case of MOFs, prevented rapid solvent loss from the framework. The emission response was also detected using an Ocean Optics JAZ spectrometer. In this case, mounted high-power 365 and 590 nm LEDs (M365L2, M590L3, Thorlabs) were used as an excitation source. Fluorescence lifetimes were measured using a Mini-τ lifetime spectrometer equipped with a 360-nm picosecond-pulsed-light-emitting diode.

Other physical measurements.

FT-IR spectra were obtained on a Perkin-Elmer Spectrum 100. NMR spectra were collected on a Varian Mercury 300 and 400 MHz NMR spectrometers. ^{13}C and ^{1}H spectra were referenced to natural abundance ^{13}C peaks and residual ^{1}H peaks of deuterated solvents, respectively. Powder X-ray diffraction patterns were recorded on a Rigaku Miniflex II diffractometer with accelerating voltage and current of 30 kV and 15 mA, respectively. Thermogravimetric analysis (TGA) was performed on a SDT Q600 Thermogravimetric Analyzer using an aluminum boat as a sample holder at a heating rate of 1 °C/min. The Waters QTOF-I quadrupole time-of-flight mass-spectrometer was used to record the electrospray ionization mass-spectra. Diffuse reflectance spectra were collected on a Perkin Elmer Lambda 45 UV/Vis spectrometer referenced to Spectralon®. The energy dispersive X-ray (EDX) spectra were collected on a TESCAN Vega-3 SBU scanning electron microscope equipped with a backscattered electron detector and EDX capability. The epifluorescence microscopy images were collected on the Olympus BX51 microscope with a 120 W mercury vapor short arc excitation light source.

Table 2.2. X-ray structure refinement data for BPMTC[a] and **1**[b].

compound	**BPMTC**	**1**
formula	$C_{25}H_{22}N_2S_2{\cdot}0.5(C_3H_6O)$	$Zn_3C_{48}H_{24}N_6O_9$[c]
FW	443.60	1024.84
T, K	296(2)	150(2)
crystal system, space group	monoclinic, P 2_1/n	tetragonal, P4/nmm
Z	4	2
a, Å	10.3059(6)	16.710(3)
b, Å	12.9893(7)	16.710(3)
c, Å	17.9870(10)	29.890(9)
α, °	90	90
β, °	98.5160(10)	90
γ, °	90	90
V, Å^3	2381.3(2)	8346(3)
d_{calc}, g/cm^3	1.237	0.408
μ, mm^{-1}	0.242	1.188
F(000)	936.0	1032.0
crystal size, mm	0.460×0.400×0.100	0.130 × 0.030 × 0.005
theta range	3.88 to 50.15	1.98 to 31.39
index ranges	$-12 \le h \le 12$	$-16 \le h \le 16$
	$-15 \le k \le 15$	$-16 \le k \le 16$
	$-21 \le l \le 21$	$-28 \le l \le 29$
refl. collected	31145	30876
data/restrains/parameters	4229 / 24 / 296	2539 /103 /0
GOF on F^2	0.950	0.904
large peak/hole, e/Å^3	0.37/−0.16	0.314/−0.421
R_1 (wR_2), %, [I>2sigma(I)][d]	0.0511 (0.1438)	5.36 (15.79)

[a] Mo-Kα (λ = 0.71073 Å) radiation; [b] synchrotron radiation (λ = 1.0333Å)
[c] Formula is given based on single-crystal X-ray data and does not include BPMTC ligands or solvent molecules (complete formula was determined based on elemental analysis and ^{1}H NMR spectroscopy (vide supra)
[d] $R_1 = \Sigma||F_o| - |F_c||/ \Sigma |F_o|$, $wR_2 = \{ \Sigma [w(F_o^2-F_c^2)^2]/ \Sigma [w(F_o^2)^2]\}^{1/2}$

REFERENCES

(1) Zhang, T.; Lin, W. *Chem. Soc. Rev.* **2014**, 5982–5993.
(2) Kent, C. a.; Mehl, B. P.; Ma, L.; Papanikolas, J. M.; Meyer, T. J.; Lin, W. *J. Am. Chem. Soc.* **2010**, *132* (37), 12767–12769.
(3) So, M. C. *Chem. Commun.* **2015**, *51*, 3501–3510.
(4) Farha, O. K.; Hupp, J. T. *Acc. Chem. Res.* **2010**, *43* (8), 1166–1175.
(5) Zhou, H.-C.; Long, J. R.; Yaghi, O. M. *Chem. Rev.* **2012**, *112* (2), 673–674.
(6) Furukawa, H.; Cordova, K. E.; O'Keeffe, M.; Yaghi, O. M. *Science (80-.).* **2013**, *341* (6149), 1230444–1230444.
(7) Lee, C. Y.; Farha, O. K.; Hong, B. J.; Sarjeant, A. a; Nguyen, S. T.; Hupp, J. T. *J. Am. Chem. Soc.* **2011**, *133* (40), 15858–15861.
(8) Lee, C. Y.; Farha, O. K.; Hong, B. J.; Sarjeant, A. a.; Nguyen, S. T.; Hupp, J. T. *J. Am. Chem. Soc.* **2011**, *133* (40), 15858–15861.
(9) Hou, L.; Zhang, X.; Pijper, T. C.; Browne, W. R.; Feringa, B. L. *J. Am. Chem. Soc.* **2014**, *136* (3), 910–913.
(10) Fukaminato, T.; Sasaki, T.; Kawai, T.; Tamai, N.; Irie, M. *J. Am. Chem. Soc.* **2004**, *126* (45), 14843–14849.
(11) Irie, M. *Photochem. Photobiol. Sci.* **2010**, *9* (12), 1535–1542.
(12) J. R. Lakowicz. *Principles of Fluorescence Spectroscopy*; Springer: Heidelberg, 2007.
(13) Valeur, B. *Molecular Fluorescence: Principles and Applications*; Wiley-VCH: Weinheim, 2001.
(14) Tanaka, S.; Itoh, S.; Kurita, N. *Chem. Phys.* **2001**, *272* (2–3), 171–184.
(15) Kobatake, S.; Takami, S.; Muto, H.; Ishikawa, T.; Irie, M. *Nature* **2007**, *446* (7137), 778–781.
(16) Klajn, R. *Chem. Soc. Rev.* **2014**, *43* (1), 148–184.
(17) Irie, M.; Ogilby, P. R.; Ceroni, P.; Credi, A.; Venturi, M.; Balzani, V.; Phillips, D. **2010**.
(18) Whalley, A. C.; Steigerwald, M. L.; Guo, X.; Nuckolls, C. *J. Am. Chem. Soc.* **2007**, *129* (42), 12590–12591.
(19) Nakamura, S.; Irie, M. *J. Org. Chem.* **1988**, *53* (26), 6136–6138.
(20) Nakayama, Y.; Hayashi, K.; Irie, M. *J. Org. Chem.* **1990**, *55* (9), 2592–2596.
(21) Woodward, R. B.; Hoffmann, R. *The Conservation of Orbital Symmetry*, 1st ed.; Verlag Chemie, GmbH: Weinheim, 1970.
(22) Irie, M.; Fukaminato, T.; Matsuda, K.; Kobatake, S. *Chem. Rev.* **2014**, *114* (24), 12174–12277.
(23) Shigekazu Kawai; Takuya Nakashima; Kazuhiko Atsumi; Toshiyuki Sakai; Miki Harigai; Yasushi Imamoto; Hironari Kamikubo; Mikio Kataoka, and; Kawai*, T. **2007**.
(24) Kobatake, S.; Uchida, K.; Tsuchida, E.; Irie, M. *Chem. Lett.* **2000**, *29* (11), 1340–1341.
(25) Gilat, S. L.; Kawai, S. H.; Lehn, J.-M. *Chem. - A Eur. J.* **1995**, *1* (5), 275–284.
(26) Masahiro Irie, *,†; Thorsten Lifka, †; Seiya Kobatake, † and; Kato‡, N. **2000**.
(27) Kobatake, S.; Irie, M. *Chem. Lett.* **2003**, *32* (11), 1078–1079.
(28) Patel, P. D.; Masunov, A. E. *J. Phys. Chem. C* **2011**, *115* (20), 10292–10297.

(29) Gurke, J.; Quick, M.; Ernsting, N. P.; Hecht, S. *Chem. Commun.* **2017**, *53*, 2150–2153.
(30) Choi, E.-Y.; Wray, C. A.; Hu, C.; Choe, W. *CrystEngComm* **2009**, *11* (4), 553–555.
(31) Szaciłowski, K. *Chem. Rev.* **2008**, *108* (9), 3481–3548.
(32) Leong, K.; Foster, M.; Wong, B.; Spoerker, E.; Van Gough, D.; Deaton, J.; Allendorf, M. *J. Mater. Chem. A* **2014**, *2* (10), 3389–3398.
(33) Tam, E. S.; Parks, J. J.; Shum, W. W.; Zhong, Y.-W.; Santiago-Berríos, M. B.; Zheng, X.; Yang, W.; Chan, G. K.-L.; Abruña, H. D.; Ralph, D. C. *ACS Nano* **2011**, *5* (6), 5115–5123.
(34) Matsuda, K.; Takayama, K.; Irie, M. *Chem. Commun.* **2001**, No. 4, 363–364.
(35) Matsuda, K.; Shinkai, Y.; Yamaguchi, T.; Nomiyama, K.; Isayama, M.; Irie, M. *Chem. Lett.* **2003**, *32* (12), 1178–1179.
(36) Qin, B.; Yao, R.; Tian, H. *Inorganica Chim. Acta* **2004**, *357* (11), 3382–3384.
(37) Tan, K.; Nijem, N.; Canepa, P.; Gong, Q.; Li, J.; Thonhauser, T.; Chabal, Y. J. *Chem. Mater.* **2012**, *24* (16), 3153–3167.
(38) Burnett, B. J.; Choe, W. *CrystEngComm* **2012**, *14* (19), 6129.
(39)
(40) Sheldrick, G. M. *Acta Crystallogr. A.* **2008**, *64* (Pt 1), 112–122.
(41) Oleg V. Dolomanov, Luc J. Bourhis, Richard J. Gildea, J. A. K. H. and; Puschmann, H. *J. Appl. Crystallogr.* **2009**, *42*, 339–341.
(42) Sheldrick, G. M. *SADABS —A Program for Area Detector Absorption Corrections*; 2004.
(43) Sheldrick, G. M. *Acta Crystallogr. Sect. A* **1990**, *46*, 467.
(44) Stoeck, U.; Krause, S.; Bon, V.; Senkovska, I.; Kaskel, S. *Chem. Commun.* **2012**, *48* (88), 10841.
(45) Yang, R.; Li, L.; Xiong, Y.; Li, J.-R.; Zhou, H.-C.; Su, C.-Y. *Chem. - An Asian J.* **2010**, *5* (11), 2358–2368.
(46) Spek, T. *SQUEEZE; PLATON: Spek, A. L.*; 1999.

CHAPTER 3

Flipping the Switch: Fast Photoisomerization in a Confined Environment

---

Williams, D. E.; Martin, C. M.; Godfrey, D. C.; Pellechia, P. J.; Smith, M. D.; Shustova, N. B. *manuscript in preparation*

INTRODUCTION

Photochromic molecules can switch between two distinct states, each with inherently different physiochemical properties upon excitation with incident light.[1–6] The ability to cycle between each isomer with the use of external stimuli, such as light, makes them valuable for applications such as smart windows,[7] transition lenses,[8] photo-optic switches,[9-9] or controlled drug delivery systems.[10–12] Popular classes of photochromic compounds that have undergone extensive examination are azobenzenes,[13–15] fulgides,[16–18] diarylethenes,[19–21] and spiropyrans.[22–25] Of these photoswitches, the latter two were of particular interest for our studies. For example, diarylethene photoswitches are capable of rapid, reversible, solid-state photoisomerization,[1,26,27] whereas only a few examples of reversible solid-state photoisomerization exist in the case of spiropyran.[28–30] Diarylethene can be derivatized to have a high thermal stability, and will remain in either isomeric state for an extended period of time,[1,3,31,32] whereas spiropyran relaxes back to its original form within minutes.[33,34] Nonetheless, it was recently found that once spiropyran was introduced into a porous system, it was capable of reversible photoisomerization in the solid state,[35,36] which could warrant its use in the aforementioned systems. However, there are very few reports to date which study coordinatively immobilized diarylethene- and spiropyran-based photoswitchable ligands in three-dimensional extended networks.[35,37–41]

For the development of specialized applications, some of which were mentioned above, it is crucial to build on the fundamental understanding of solid state and solution-based photoisomerization of spiropyran and diarylethene photoswitches. Therefore, we

were interested in studying the fundamental behavior of diarylethene and spiropyran photoswitches in solution, solid, and while coordinatively immobilized in a porous scaffold.

In this chapter, we report the preparation and photophysical studies of four different photochromic materials. For that, two novel spiropyran-containing derivatives were prepared. Typically, spiropyran-derivatives have limited reversibility in the solid state, but we envision that by immobilization in a porous network through a rigid backbone, the steric hindrance will provide rotational freedom for spiropyran linkers inside the MOF pores.

The photophysical properties of the two spiropyran-based derivatives were studied in the solid state, solution, and coordinatively immobilized inside of porous MOFs. We prepared two diarylethene-based MOFs to compare their photophysical properties with the spiropyran-based frameworks. Thus, the rates of diarylethene photoisomerization could be compared with spiropyran-based systems, as well as in solution and the solid state. The comparison of the two photoswitches in various environments could allow us to tailor the systems for more specific applications, such as gas vapor sensing and photoresponsive coatings. This chapter covers the synthesis and characterization of the photoswitches and photoswitch-containing MOFs, and consists of four main sections: (i) the synthesis and characterization of the photochromic linkers, (ii) the photophysical characterization of the photochromic linkers, (iii) the synthesis and characterization of the corresponding MOFs, and (iv) photophysical studies of the prepared photoswitch linkers and MOFs.

3.1 Synthesis and Characterization of the Photochromic Linkers

For clarity purposes, the names of the linkers are defined here, and will be referred to by their acronyms for the remainder of the chapter: BPMTC = bis(5-pyridyl-2-methyl-

3-thienyl)cyclopentene (Scheme 3.1); H_2BCMTC = 4,4'-(cyclopent-1-ene-1,2-diyl)bis(5-methylthiophene-2-carboxylic acid (Scheme 3.2); TNDS = 1',3',3'-trimethyl-6-nitro-4',7'-di(pyridin-4-yl)spiro[chromene-2,2'-indoline] (Scheme 3.3); and HDDB = 1',1''',3',3',3''',3'''-hexamethyl-6,6''-dinitro-4',4'''-di(pyridin-4-yl)-7',7'''-bispiro[chromene-2,2'-indoline] (Scheme 3.4).

Two diarylethene and two spiropyran-based linkers were prepared to study their photoisomerization rates. To do so, their cores were modified with terminal pyridyl or carboxylic groups, which are necessary for incorporation into a MOF scaffold. Using the prepared linkers, we attempted to measure the photoisomerization rate of pyridyl-based derivatives of diarylethene and spiropyran in solution, solid-state, and in MOFs.

3.1.1 Synthesis and Characterization of BPMTC

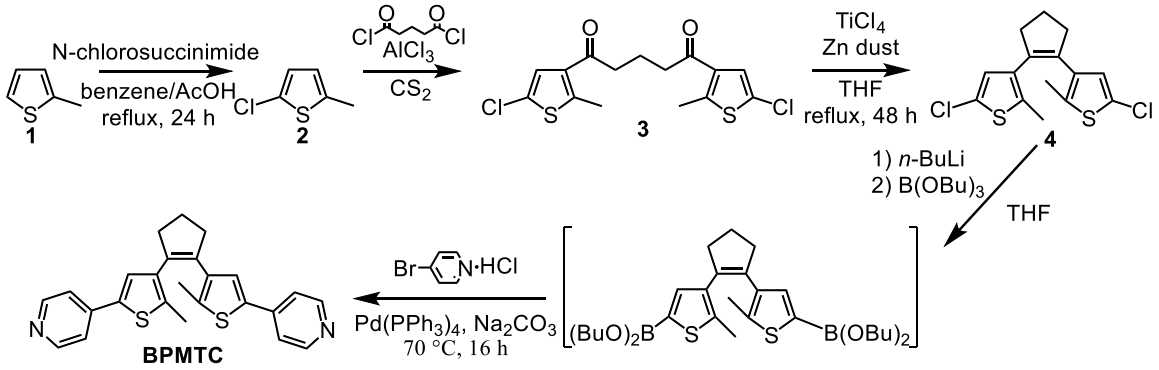

Scheme 3.1. Synthesis scheme of bis(5-pyridyl-2-methyl-3-thienyl)cyclopentene, BPMTC.

For the synthesis of BPMTC, a diarylethene core was modified with terminal pyridyl groups to coordinate to the Zn-containing metal nodes between 2D MOF layers. It was prepared using a modified literature procedure.[42] A detailed synthetic procedure has already been described in Chapter 2. The synthesis scheme of BPMTC is shown in Scheme 3.1. BPMTC was structurally characterized using ^{1}H NMR, ^{13}C NMR, and Fourier-

transform infrared (FT-IR) spectroscopies, as well as single crystal X-ray diffraction (see Chapter 2).

3.1.2 Synthesis and Characterization of H_2BCMTC

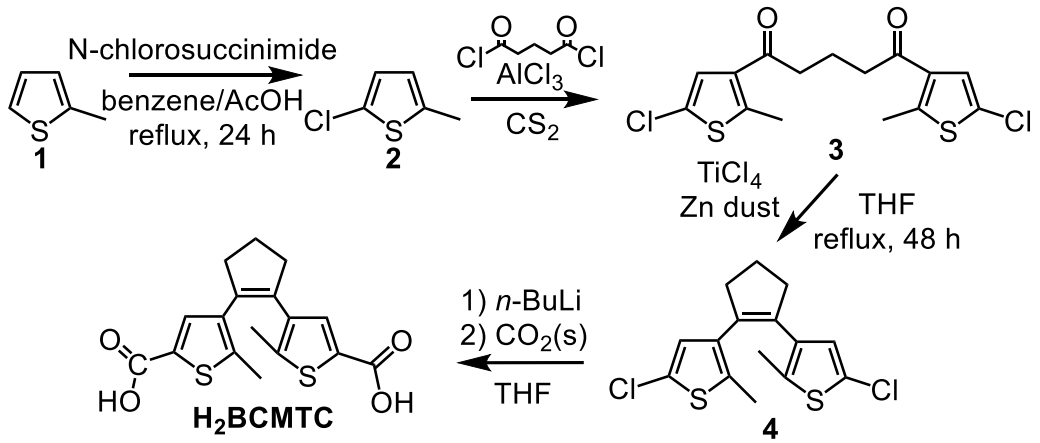

Scheme 3.2 Synthesis scheme of 4,4'-(cyclopent-1-ene-1,2-diyl)bis(5-methylthiophene-2-carboxylic acid), H_2BCMTC.

For the synthesis of H_2BCMTC, a diarylethene core was modified with terminal carboxylic acid groups to attach to the Zr-based secondary building unit (SBU) of PCN-700 (vide infra).[43] It was prepared using a similar scheme to BPMTC, however instead of a palladium-catalyzed Suzuki-coupling reaction on **4**, it underwent a carbonation reaction to form the terminal carboxylic acid groups (Scheme 3.2) using a previously-reported literature procedure.[44]

3.1.3 Synthesis and Characterization of TNDS

The TNDS derivative was synthesized via a six-step procedure as shown in Scheme 3.3. The last step in this scheme was a palladium-catalyzed Suzuki coupling reaction which was performed on the brominated precursor, MSP6, in the presence of 4-pyridyl boronic acid, which yielded the novel bis(pyridyl) spiropyran derivative, TNDS (Scheme 3.3). The TNDS photoswitch was structurally characterized using ^{1}H NMR, ^{13}C NMR, and FT-IR

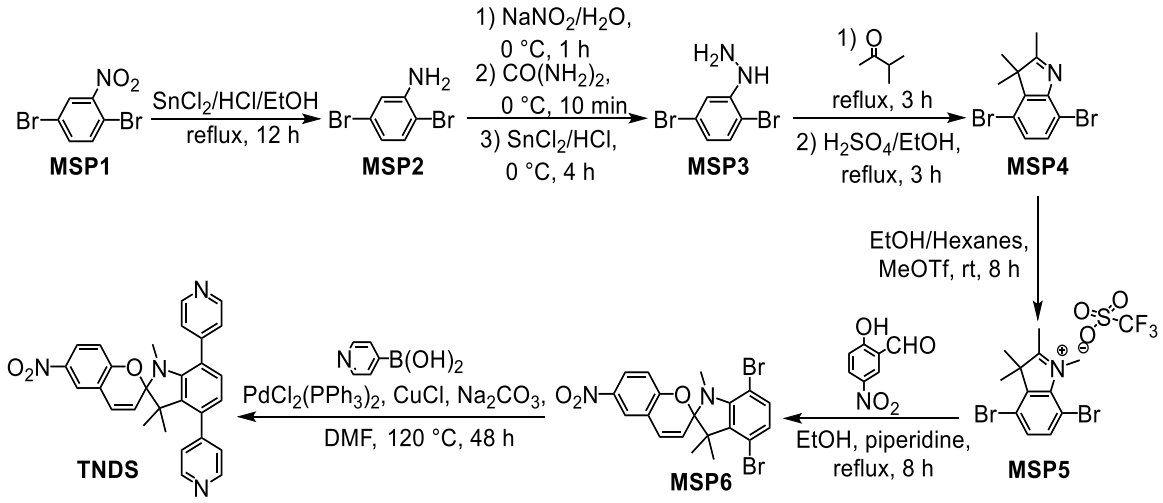

Scheme 3.3. Synthesis scheme of 1',3',3'-trimethyl-6-nitro-4',7'-di(pyridin-4-yl)spiro[chromene-2,2'-indoline] (TNDS).

spectroscopies, as well as single crystal X-ray diffraction and mass spectrometry (Figures 3.10, 3.17, 3.13, and 3.12, respectively). Full synthetic details for MSP5, MSP6, and TNDS can be found in the experimental section (Schemes 3.5, 3.6, and 3.7, respectively).

3.1.4 Synthesis and Characterization of HDDB

The HDDB compound was synthesized via a seven-step procedure as shown in Scheme 3.4. The last step (similar to TNDS) was a palladium-catalyzed Suzuki coupling reaction performed on the brominated precursor, BSP6, in the presence of 4-pyridyl boronic acid. HDDB was characterized using ^{1}H NMR, ^{13}C NMR, ^{13}C CP-MAS NMR, and FT-IR spectroscopies, as well as single crystal X-ray diffraction and mass spectrometry (Figures 3.11, 3.17, 3.16, and 3.15, respectively). Full synthetic details for BSP5, BSP6, and HDDB can be found in the experimental section (Schemes 3.8, 3.9, and 3.10, respectively).

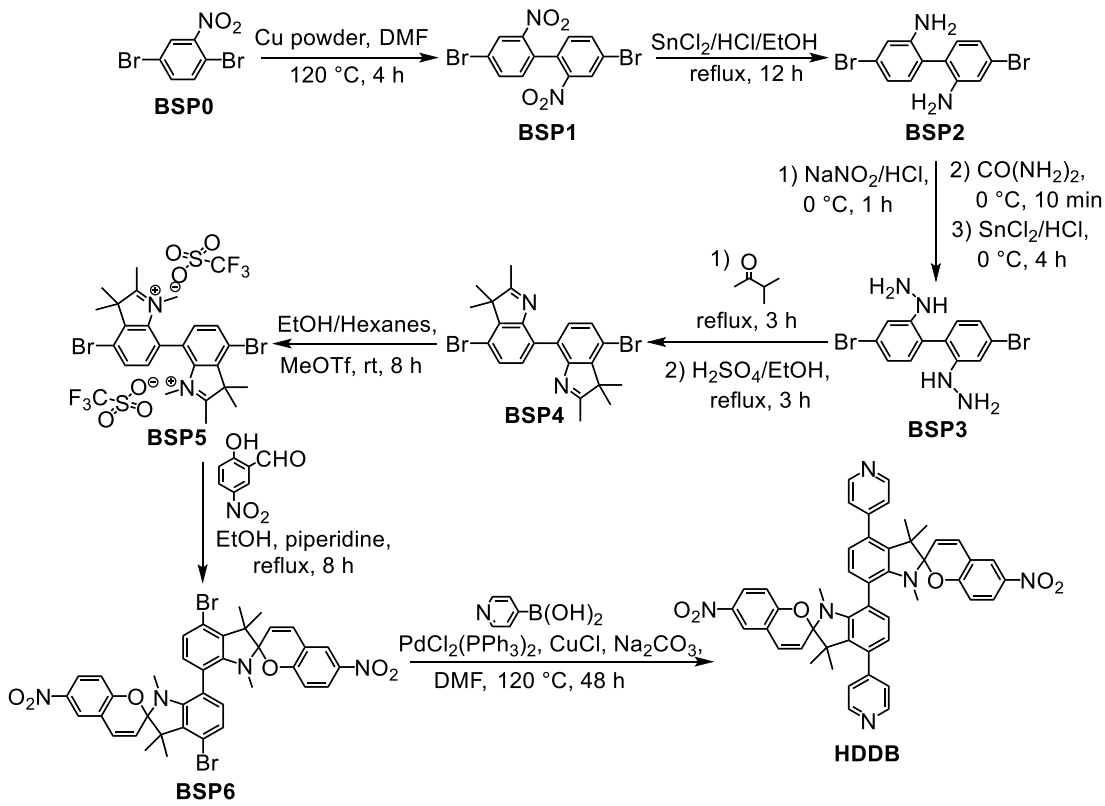

Scheme 3.4. Synthesis scheme of 1',1''',3',3',3''',3'''-hexamethyl-6,6''-dinitro-4',4'''-di(pyridin-4-yl)-7',7'''-bispiro[chromene-2,2'-indoline] (HDDB).

3.1.4.1 Enantiomerization of HDDB: $HDDB_{in\text{-}in}$, $HDDB_{in\text{-}out}$, and $HDDB_{out\text{-}out}$

HDDB, containing two spiropyran groups, can exist as three unique diastereomers ($HDDB_{in\text{-}in}$, $HDDB_{in\text{-}out}$, and $HDDB_{out\text{-}out}$), and each of which has unique NMR shifts (Figure 3.1). We were able to collect a pure ^{1}H NMR spectrum of the $HDDB_{in\text{-}in}$ isomer (Figure 3.11) by crystallizing it from a solution of acetone (purification technique is described in detail in the experimental section below, Scheme 3.10). We were interested in studying the transformation of $HDDB_{in\text{-}in}$ to $HDDB_{in\text{-}out}$ and $HDDB_{out\text{-}out}$, inspired by similar work conducted by Klajn, et al.[45] To study the isomerization, we introduced crystalline $HDDB_{in\text{-}in}$ into an NMR tube that contained cold methylene chloride-d_2, and measured the ^{1}H NMR spectrum over several days (Figure 3.1). After only 9 hours at 25 °C, 32% of the $HDDB_{in\text{-}in}$ isomer converted into a mixture of diastereomers, 50% after 25

hours. We obtained single crystals of $HDDB_{in\text{-}out}$ by dissolving a mixture of isomers in a vial with 50% ethyl acetate/hexanes and then stored at 0 °C for several days (Figure 3.11). From the combination of the ^1H NMR spectra of $HDDB_{in\text{-}in}$ and $HDDB_{in\text{-}out}$, we were able to deduce the resonances of all three diastereomers in the final, equilibrated spectrum.

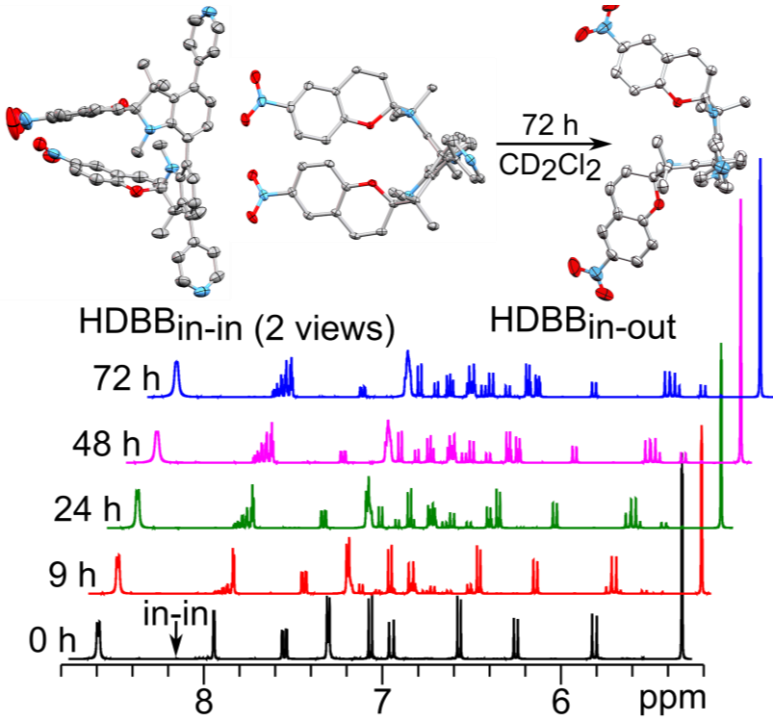

Figure 3.1. Single crystal X-ray structures of $HDDB_{in\text{-}in}$ and $HDDB_{in\text{-}out}$ (*top*). The ^1H NMR spectra showing the conversion of $HDDB_{in\text{-}in}$ to the other isomers, $HDDB_{in\text{-}out}$ and $HDDB_{out\text{-}out}$ after three days (*bottom*).

3.2 Photophysical Characterization of BPMTC, H_2BCMTC, TNDS, and HDDB.

In general, spiropyran consists of two groups, indoline and chromene, linked together through a single sp^3 "spiro" chiral carbon (Figure 3.2). Once the photoswitch is irradiated with UV light (λ_{max} ~ 365 nm), the compound undergoes a cyclization reaction and generates a planar, highly colored, zwitterionic form of the photoswitch (merocyanine), shown in Figure 3.2. The isomerization of the compound from the

spiropyran to the merocyanine form is accompanied with a large structural change, and therefore can severely impact the photoisomerization rates.

Diarylethene photoswitches also have two isomeric forms, colorless (open) and colored (closed.) The colorless form of diarylethene can be irradiated with UV light, which causes it to undergo a 6π-electron electrocyclic reaction and form a bond between the two heterocyclic thiophene moieties, generating the colored diarylethene form. The diarylethene-based derivative, unlike spiropyran, is thermally stable in either form, and does not undergo such a drastic structural change during photoisomerization.

To study spiropyran and diarylethene photoisomerization rates, we initially performed photophysical measurements on the two classes of photoswitches in solution and solid state. For solution studies, a 3 mM solution of the respective photoswitch was loaded into a 8 mm × 1 mm front-facing quartz sample cell. For solid-state studies, 4 μmol of photoswitch was mixed with 100 mg KBr, which was then pressed into the 8 mm sample cell. All samples were excited to an absorbance value of 0.05 a.u. Photochromic diarylethene and spiropyran-based derivatives typically display first-order decays during the photoisomerization process,[13,31,46–48] and their rate constant, k, is extracted from the negative slope of the absorption plot of ln A versus time (A = absorbance.)

We found that photoisomerization of BPMTC and H_2BCMTC were fully reversible in solution and the solid state. The BPMTC compound isomerized rapidly in the solid state, and after only 35 seconds showed 100% photoconversion to the colorless form at a rate of 0.20 s^{-1} (Table 3.1, Figure 3.5). For solution, BPMTC took approximately 6 minutes to fully switch at a rate of 1.0×10^{-2} s^{-1}. With similar behavior, H_2BCMTC took three minutes to isomerize at a rate of 4.8×10^{-2} s^{-1} as a solid, and two minutes at a rate of 2.6×10^{-2} s^{-1}

in solution. The H_2BCMTC photoswitch was not responsive with UV irradiation due to interactions with the DMF solvent, and could not reach the desired absorption value of 0.05 a.u., so the rate in solution was measured in MeOH. The photoisomerization rates of TNDS and HDDB were conducted in an analogous manner to BPMTC and H_2BCMTC. It is evident that the solid form of spiropyran is not fully reversible, and even after 5 minutes of irradiation with visible light, it only displayed 90% conversion to the colorless form (Figure 3.2). However, in solution, complete reversion of TNDS was achieved in 30 seconds at a rate of 0.122 s^{-1} (Table 3.1, Figure 3.5.) In comparison with TNDS, HDDB also showed limited photoconversion after five minutes (Figure 3.5), but showed 100% conversion in solution after one minute with a rate of 0.064 s^{-1}. The slower photoisomerization of HDDB can be attributed to the bulky core, which impedes the photoisomerization in solution and in the solid state. Fitting the experimental data was not successful, and therefore no reliable photoisomerization rates for HDDB and TNDS were determined in the solid state. The solid-state photoisomerization process may be hindered due to mechanical strain,[50] decomposition,[51] photo- and thermal degradation,[13,52,53] as well as π-π stacking interactions.[36] In fact, crystalline spiropyran is not considered reversible due to the highly organized and densely packed molecules. As an amorphous powder there is a small degree of conformational freedom due to the loose packing, which gives rise to poorly responsive and non-reversible photoisomerization. However, our results indicate that, in solution, spiropyran switches have significantly faster photoisomerization rates than diarylethene. The photoisomerization rates of spiropyran in solution are attractive, however any applications which require the use of solid-state materials must exclude spiropyran as an

option, due to their setback in nonreversible solid-state photoisomerization. We envisioned that the introduction of the spiropyran compounds into a porous environment would remove impeding intermolecular interactions, π-π stacking, and steric hindrance during isomerization while maintaining uniform chromophore arrangement. We anticipated that this would accelerate the photoisomerization rates of spiropyran in the solid state. However, the same method for immobilizing diarylethene through the structural core could

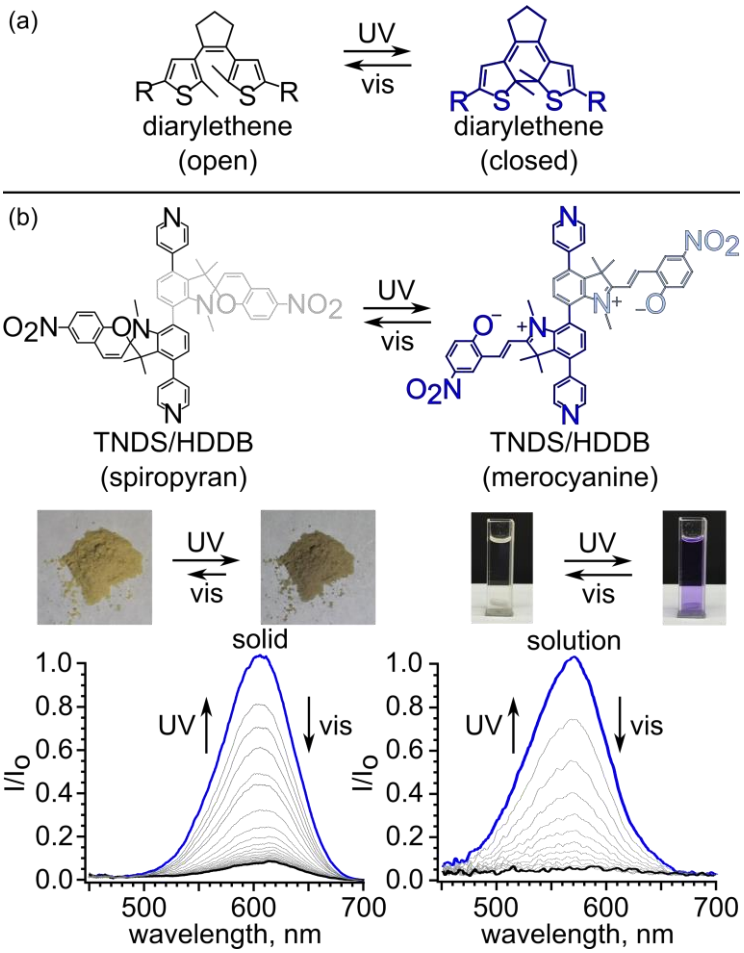

Figure 3.2. Photoisomerization of the diarylethene (*top*) and spiropyran (*middle*) derivatives. Pictures of TNDS as a solid, and in solution, before and after UV irradiation, as well as normalized diffuse reflectance and UV-vis spectra of TNDS during isomerization from the colored to colorless form (*bottom*).

impede the photoisomerization rate by restricting its movement in a confined environment. Therefore, we decided to probe how the prepared derivatives would behave while coordinatively immobilized in porous environments.

3.3 Synthesis and Characterization of 1, 2, 3, and 4 MOFs

It was shown previously that MOFs can drastically change the photophysical properties of the confined molecules by suppressing low-energy vibrational modes,[54] and could also be used to isolate high energy chromophore conformations.[55] For those reasons, we developed two strategies to integrate the photochromic molecules inside of porous

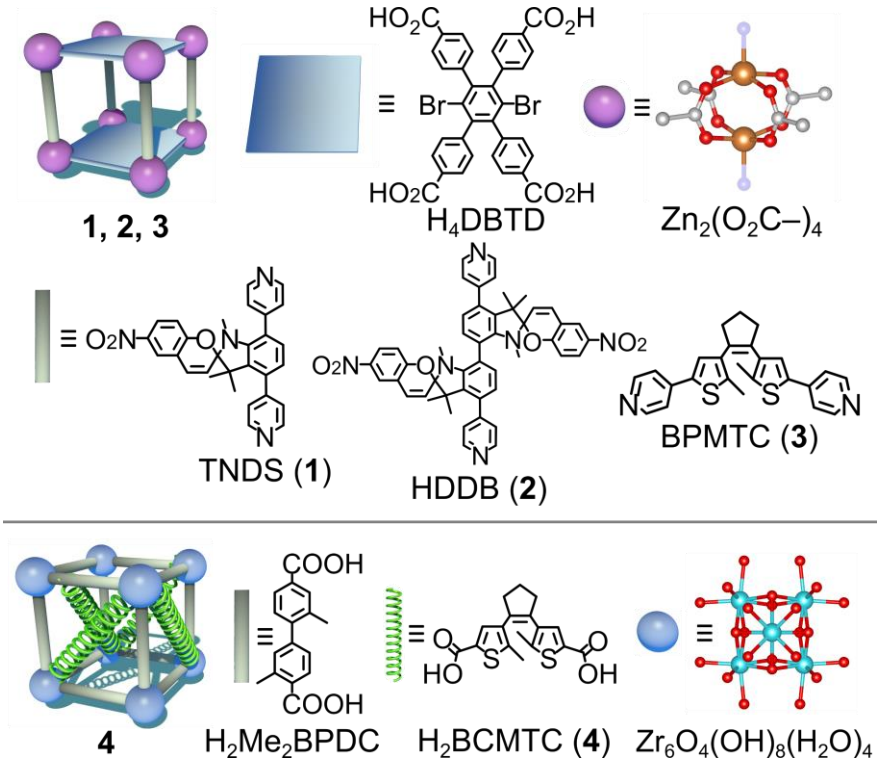

Figure 3.3. The TNDS, HDDB, and BPMTC linkers were used to synthesize **1**, **2**, and **3**, respectively, in the presence of H_4DBTD (*top*). The linker, H_2BCMTC, was installed as a capping linker into an existing MOF framework, PCN-700,[43] to make **4** (*bottom*). Orange, red, blue, teal, and white spheres correspond to zinc, oxygen, nitrogen, zirconium, and hydrogen atoms, respectively.

frameworks, through coordinative immobilization and capping linker installation. The three ligands BPMTC, TNDS, and HDDB were designed with terminal pyridyl groups, which makes them suitable for incorporation between 2D MOF layers (Figure 3.3). The tetracarboxylate MOF linker (3',6'-dibromo-4',5'-bis(4-carboxyphenyl)-1[1,1':2',1''-tetraphenyl]-4,4''-dicarboxylic acid, H_4DBTD, Figure 3.3) has previously been shown to form transparent two-dimensional layers of $DBTD^{4-}$ anchored together through zinc-containing paddlewheel SBUs.[56] The MOF contains unsaturated metal sites for incorporation of pyridyl linkers, to form a 3D scaffold. In fact, the BPMTC derivative has been previously utilized as pillars in a MOF which contains 2D layers of $DBTD^{4-}$.[57] We anticipated that our spiropyran analogues would bind axially to the zinc SBUs in the same way as a literature-reported structure of BPMTC with $DBTD^{4-}$,[57] resulting in two novel photochromic MOFs, **1** and **2**, with similar topology. For TNDS, HDDB, and BPMTC, a one-pot synthesis was performed in an isothermal oven with the prepared MOF linker H_4DBTD,[58] and $Zn(NO_3)_2 \cdot 6H_2O$ in DMF to obtain single crystals of **1**, **2**, and **3**, respectively.

Both MOFs **1** and **2** crystallize in the P*mmm* space group of the orthorhombic crystal system. The **1** and **2** frameworks consist of layers of $DBTD^{4-}$ with a pillar backbone with three and four six-membered rings that are anchored to the axial positions of the SBUs with two-fold disorder. The interlayer distance (defined here as distance from nitrogen to nitrogen along the structural backbone) measured ~11.4 Å and ~15.7 Å for **1** and **2**, respectively, which match the c-axis in our crystal structures, 11.4 Å and 15.6 Å for TNDS and HDDB, respectively. The crystallographic data shows 100% incorporation of the photochromic linkers, however the electron density within the pores could not be assigned

due to severe disorder. The bulk samples of **1** and **2** were also characterized using PXRD and showed good agreement with their simulated patterns (Figure 3.4). The ^{1}H NMR spectra of digested **1** and **2** showed the presence of both TNDS and HDDB pillars in their respective MOF structures (Figure 3.12 and 3.15, respectively). The FT-IR spectra of **1** and **2** are shown in Figures 3.13 and 3.16, respectively.

Similar to **1** and **2**, the framework **3** contains the BPMTC linker coordinatively anchored between the axial zinc paddlewheel SBUs and 2D layers of $DBTD^{4-}$.[57] The BPMTC photoswitch was not resolved between the layers of $DBTD^{4-}$ in the crystallographic data, but was shown to have 100% incorporation based on the relative

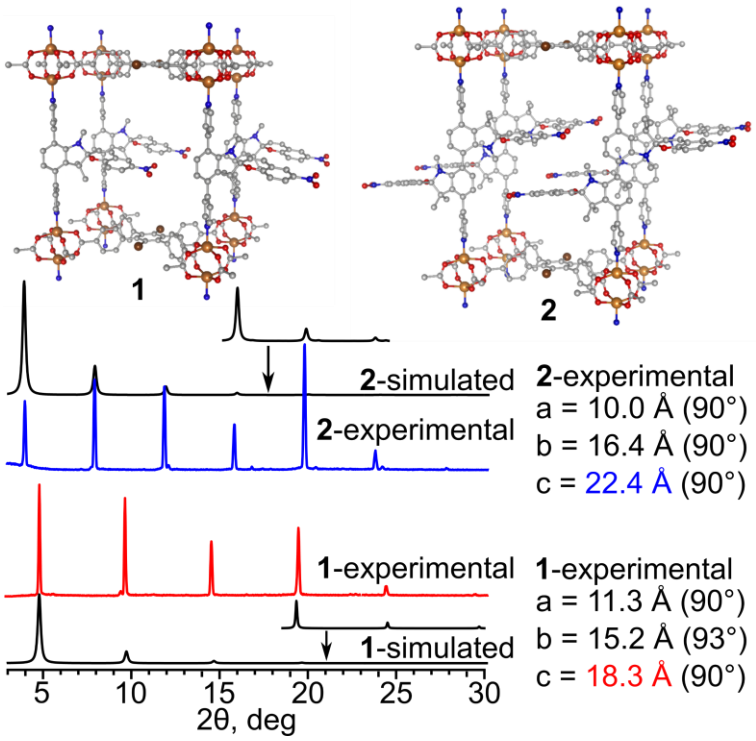

Figure 3.4. *(top)* Structures of **1** and **2** with the immobilized TNDS and HDDB, respectively. *(bottom)* The simulated and experimental PXRD patterns of MOFs **1** (red) and **2** (blue) The colored text shows the c-expansion of each MOF with respect to linker size.

integrations of H_4DBTD and BPMTC in the ^{1}H NMR spectrum of the digested MOF (Figure 3.19). The PXRD pattern of the bulk sample of **3** was in good agreement with the simulated pattern (Figure 3.18).[57]

As shown in previous studies and tested herein, BPMTC immobilized between $DBTD^{4-}$ layers exhibits slow photoisomerization from the colored to colorless state, due to the rigid nature of MOFs.[57] We envisioned that photoisomerization rate of the diarylethene photoswitch could be enhanced if it was installed into a flexible MOF. Therefore, we prepared a dicarboxylic acid derived diarylethene photoswitch, H_2BCMTC, for insertion between the $Zr_6O_4(OH)_8(H_2O)_4$ SBU clusters of the flexible PCN-700 MOF.[43] The structure of PCN-700 consists of eight 2,2′-dimethylbiphenyl-4,4′-dicarboxylate $(Me_2BPDC)^{2-}$ linkers coordinated to its zirconium-based SBU above and below the equatorial planes.[43] It was shown previously that PCN-700 contains three sites for the incorporation of dicarboxylic acid linkers. By installing the linkers into the equatorial sites, the MOF is capable of changing the shape of its porous environment through expansion in the axial direction, depending on the size of the linker.[59] Crystals of **4** were obtained by soaking crystals of prepared PCN-700 (see the experimental section for full synthetic details) in a solution of H_2BCMTC in DMF through a single-crystal to single-crystal transformation. The $BCMTC^{2-}$ molecules occupy the four equatorial sites surrounding the SBU, which fully saturate the node into a stable 12-coordinate SBU. The powder pattern of prepared PCN-700 was in good agreement with simulated pattern,[43] and the crystallinity was retained after incorporation of $BCMTC^{2-}$ (Figure 3.20). The installation of $BCMTC^{2-}$ into **4** was quantified at 50% by washing the MOF for several days in DMF, digesting it in

the presence of acid, and integrating the respective H_2Me_2BPDC and H_2BCMTC resonances in the ^1H NMR spectrum (Figure 3.21).

3.4 Photophysics of 1, 2, 3, and 4 MOFs

The photophysical properties of **1, 2, 3,** and **4** MOFs were studied using the sample experimental setup similar to that used for the ligands. In the 8 mm quartz sample cell, the MOFs were loaded, and the crystals were dried slightly (i.e., not all the DMF was removed.) An absorption value of ~0.05 a.u. was obtained by irradiating the sample with a 365 nm LED *in-situ* before the LED source was turned off, and the resulting absorption intensity was monitored until the photoisomerization was deemed complete. Remarkably, we found that once TNDS was coordinatively immobilized in a porous environment, it demonstrated solution-like photoisomerization, even as a crystalline solid. MOF **1** showed a 100% conversion from merocyanine to spiropyran, which was achieved after only 30 seconds (Figure 3.5). From the first order plot of ln A versus time (vide supra), a rate of 0.16 s^{-1} was found. However, in the case of HDDB with the bulky substituents, we observe that the photoisomerization is completely hindered. This behavior could be attributed to intermolecular interactions occurring between the spiropyran groups on adjacent linkers. The crystals of **1** and **2** are also fluorescent, which has been previously observed for solution-based spiropyran derivatives,[5] and we attribute it to the presence of surface-bound photoswitches (Figure 3.22). It has been previously shown that surface-bound photoswitches are capable of isomerization,[32,35,46,60] and in the case of HDDB, any surface-bound ligands could still undergo photoisomerization where it was restricted inside the MOF.

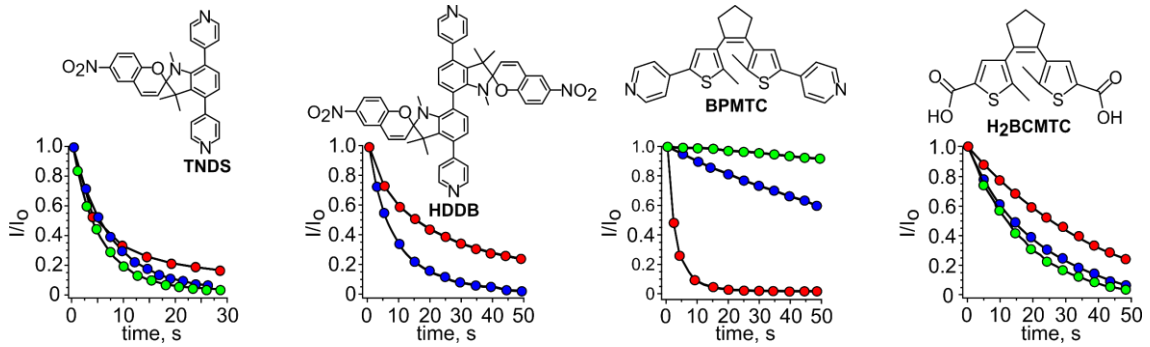

Figure 3.5. Normalized decay plots of TNDS, HDDB, BPMTC, and H_2BCMTC in the solid state(red), solution (blue), and immobilized in a MOF (green) when irradiated with a tungsten-halogen lamp.

The MOF **3** showed contrasting behavior compared to **1** and **2**. Through rational design, the BPMTC pyridyl arms were tethered between the two-dimensional layers of $DBTD^{4-}$, and as expected, the photoisomerization rate was severely impacted. A dramatic change in the isomerization rate of MOF **3** was observed in comparison with BPMTC in solution and the solid state. For the MOF **3**, an excessive 30 minutes of irradiation was required to achieve photoconversion from the colored to colorless form, with a rate of 2.8×10^{-3} s^{-1}, nearly two orders of magnitude less than its solid-state photoisomerization rate (Figure 3.5, Table 3.1). Our results indicate that the installation of BPMTC between 2D MOF layers heavily impacts the photoisomerization rate, which we attribute to the isomerization occurring through the structural core. However, we found that when the diarylethene-based MOF linker, $BCMTC^{2-}$, is immobilized in a flexible framework (**4**), solution-like photoisomerization rates are observed. The MOF **4** exhibited complete photoconversion after 1.5 minutes, with a rate of 4.1×10^{-2} s^{-1} (Figure 3.5). Once the MOF is exposed to UV or visible light, the $BCMTC^{2-}$ linker is capable of unrestricted photoisomerization because the framework easily can accommodate the change in linker size. This fact is supported by Zhou and coworkers, where the pores of PCN-700 (used in

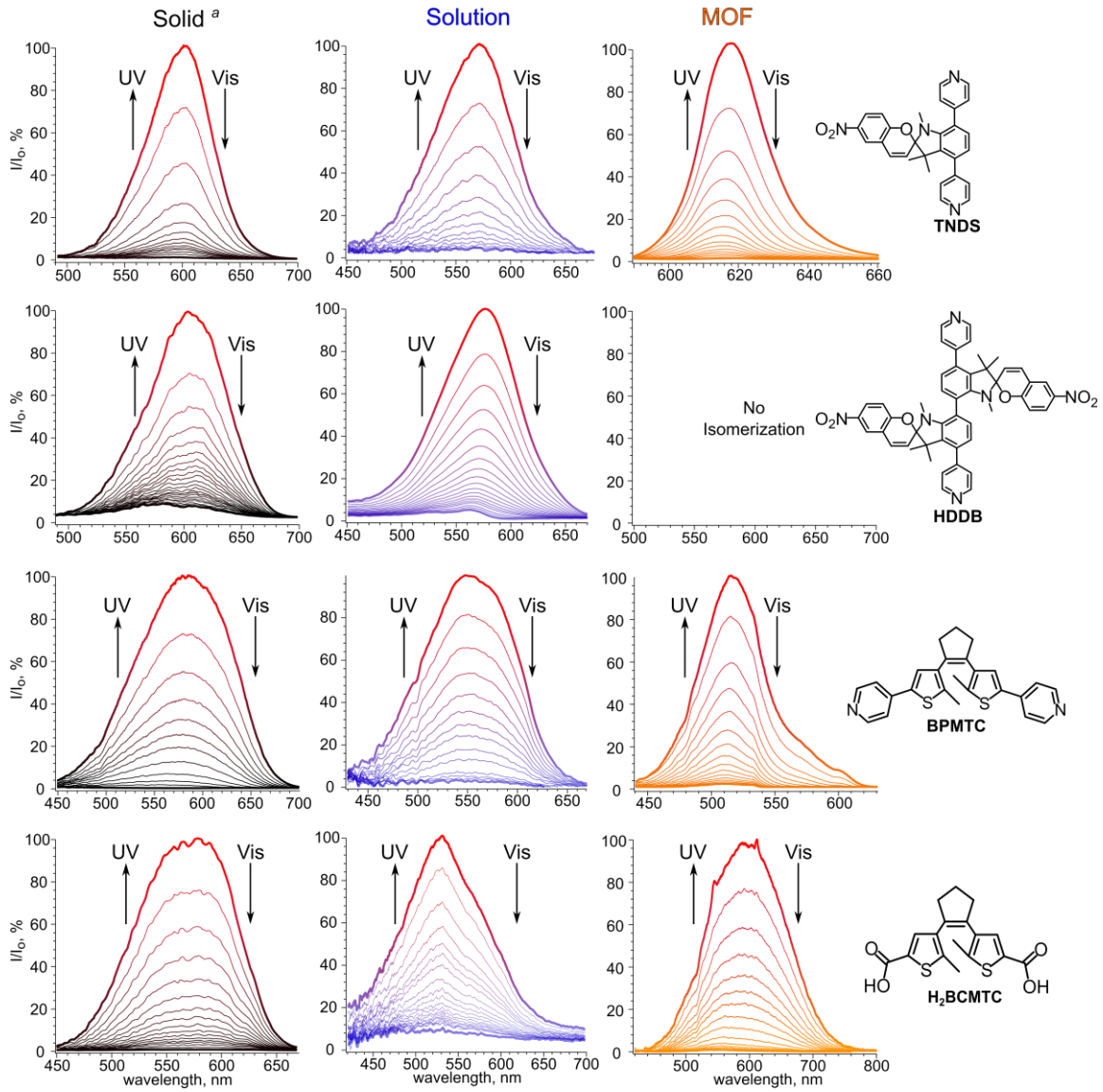

Figure 3.6. Normalized absorption plots of TNDS, HDDB, BPMTC, H_2BCMTC, as a solid, solution, and in the MOF during UV and visible irradiation. [a] The solids of TNDS and HDDB did not exhibit reversible photoisomerization, and did not follow zero, first, or second order rate laws.

our studies) were engineered with various ditopic linkers, ranging in lengths from 9.1 Å to 18.9 Å, while MOF crystallinity was preserved.[59]

We found that the introduction of the spiropyran-based TNDS liner into a confined environment (**1**) indeed accelerated the photoisomerization behavior in respect to our

prepared solutions. However, in the case of **2**, the bulky HDDB linker restricted photoisomerization almost completely. MOF **3** consists of BPMTC anchored between rigid two-dimensional MOF layers, and showed drastically reduced photoisomerization. However, MOF **4**, which contained $BCMTC^{2-}$ installed into a flexible MOF, was capable of rapid photoisomerization with solution-like behavior. The photoisomerization rates of all the ligands are summarized in Table 3.1. A summary of the photoisomerization decay

Table 3.1. Photoisomerization rates of TNDS, HDDB, BPMTC, and H_2BCMTC, in the solid-state, solution, and coordinatively immobilized in a MOF (**1**, **2**, **3**, and **4**, respectively).

	solid state (s^{-1})	**solution** (s^{-1})	**MOF** (s^{-1})
TNDS (**1**)	n/a [a]	0.12 [b]	0.16
HDDB (**2**)	n/a [a]	6.0×10^{-2} [b]	8.1×10^{-2}
BPMTC (**3**)	0.20	1.0×10^{-2} [b]	2.8×10^{-3}
H_2BCMTC (**4**)	4.8×10^{-2}	2.6×10^{-2} [c]	4.1×10^{-2}

[a] Fitting the experimental data was not successful, and therefore no reliable rate could be determined
[b] 3 mM in DMF
[c] 3 mM in MeOH

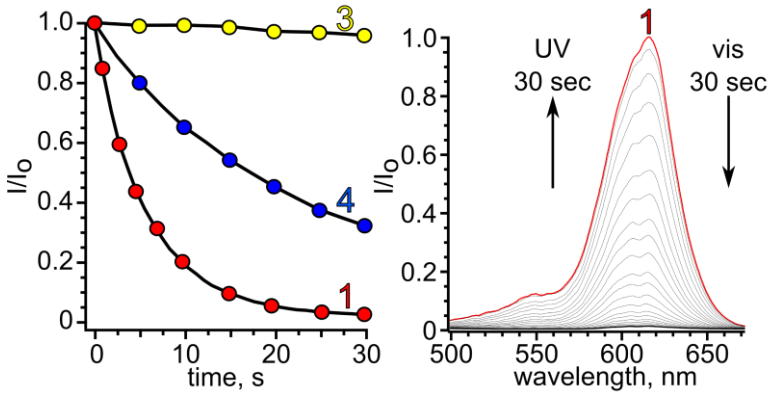

Figure 3.7 Normalized decay plots comparing the decays of MOFs **1**, **3**, and **4** (left). MOF **1** shows rapid photoisomerization of the photoswitch from merocyanine to spiropyran while immobilized in the MOF (right).

plots for **1**, **3**, and **4** MOFs are shown in Figure 3.7, showing that **1** demonstrates the fastest photoisomerization of the installed photochromic compound, TNDS.

Conclusion

In this work, we investigated the photophysical properties of two novel spiropyran-based photochromic compounds, TNDS and HDDB, and two diarylethene compounds, BPMTC and H_2BCMTC in the solid state, solution, and immobilized inside a MOF. We found that the TNDS and HDDB spiropyran moieties demonstrated photoisomerization in solution, much like the diarylethene photoswitches. However in the solid state, BPMTC demonstrated faster photoisomerization than TNDS and HDDB. Once MOFs were employed as a tool to covalently confine the spiropyran moieties, we witnessed rapid isomerization inside the framework for TNDS with solution-like behavior, whereas photoisomerization of HDDB was restricted in the MOFs due to their close proximity. In contrast, the diarylethene-based analog, BPMTC, showed a significant decrease in isomerization efficiency once immobilized, due to the strain of the rigid MOF matrix. The BCMTC photoswitch, on the other hand, showed a comparable photoisomerization rate to that of solution when covalently immobilized in a flexible MOF system. We envision that MOFs can be used as a tool to covalently anchor photochromic linkers for applications.

EXPERIMENTAL SECTION

Materials.

Zinc(II) nitrate, hexahydrate (technical grade, Ward's Science), tin(II) chloride, anhydrous (98%, Beantown Chemicals), copper(I) chloride, anhydrous (97%, Strem Chemicals), bis(triphenylphosphine)palladium(II) dichloride (96%, Oakwood Chemicals),

copper powder (99.9%, Alfa Aesar), sodium carbonate (ACS grade, Ameresco), magnesium sulfate, anhydrous (USP, Chem-Implex, International Inc.), sodium sulfate, anhydrous (99.5%, Oakwood Chemicals), sodium hydroxide (ACS, Oakwood Chemicals), 2,5-dibromonitrobenzene (99%, Oakwood Chemicals), sodium nitrite (98%, Oakwood Chemicals), 3-methyl-2-butanone (98%, Beantown Chemicals), methyl trifluoromethanesulfonate (97%, Matrix Scientific), 2-hydroxy-5-nitrobenzaldehyde (98%, Oakwood Chemicals), pyridine-4-boronic acid (95%, Matrix Scientific), hexabromobenzene (>99%, TCI America), *p*-tolylmagnesium bromide (0.5 M in diethyl ether, Acros Organics), hydrochloric acid (ACS, Fisher Chemical), sulfuric acid (ACS grade, Fisher Chemical), nitric acid (ACS reagent, Sigma-Aldrich), fluoroboric acid (48%, Oakwood Chemicals), ethanol (200 poof, Decon Laboratories, Inc), methanol (ACS grade, Fischer Scientific), methylene chloride (99.9%, Fisher Chemical), acetone (ACS grade, Sigma Aldrich), ethyl acetate (99.9%, Fisher Chemical), chloroform (99.9%, Fisher Chemical), diethyl ether (ACS grade, J. T. Baker® Chemicals), hexanes (ACS, BDH), *N*,*N*-dimethylformamide (ACS grade, Oakwood Chemicals), piperidine (99%, Sigma-Aldrich), carbon tetrachloride (99.9%, Sigma-Aldrich), bromine(99.8%, Acros-Organic), tetrahydrofuran (HPLC grade, Beantown Chemicals), chloroform-*d* (Cambridge Isotopes), acetone-d_6 (Cambridge Isotopes), methylene chloride-d_2 (Cambridge Isotopes), dimethyl sulfoxide-d_6 (Cambridge Isotopes) were used as received.

Synthesis.

The compounds **MSP1**-**MSP4** (Scheme 3.3),[61] **BSP1**-**BSP4** (Scheme 3.4),[35] and PCN-700[62] were prepared according to their slightly modified literature procedures.

*Synthesis of [4,7-dibromo-1,2,3,3-tetramethyl-3H-indol-1-ium][trifluoromethanesulfonate] **(MSP5)***

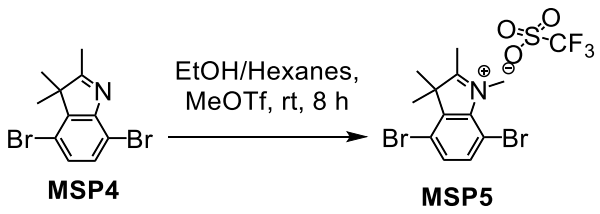

Scheme 3.5. Synthesis of*[4,7-dibromo-1,2,3,3-tetramethyl-3H-indol-1-ium][trifluoromethanesulfonate] (**MSP5**).*

Methyl trifluoromethanesulfonate (4.13 g, 25.2 mmol) was added to synthesized **MSP4** (2.00 g, 6.31 mmol) in 120 mL of diethyl ether and 80 mL of hexanes. After the resulted mixture was stirred vigorously overnight at room temperature, a pale pink powder was collected by filtration and washed with diethyl ether (3 × 10 mL). After drying under vacuum, **MSP5** (2.70 g, 5.61 mmol) was isolated in 89% yield and used without further purification.

*Synthesis of 4',7'-dibromo-1',3',3'-trimethyl-6-nitrospiro[chromene-2,2'-indoline] **(MSP6)***

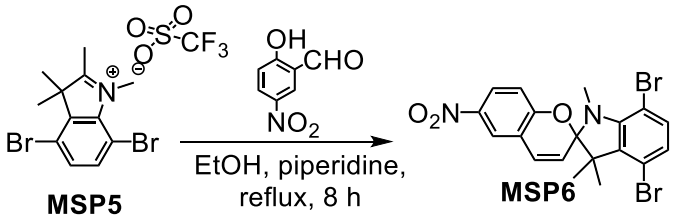

Scheme 3.6. Synthesis of 4',7'-dibromo-1',3',3'-trimethyl-6-nitrospiro[chromene-2,2'-indoline] (**MSP6**).

Under a nitrogen atmosphere, piperidine (1.41 g, 16.6 mmol) was added to a solution of **MSP5** (2.00 g, 4.15 mmol) and 2-hydroxy-5-nitrobenzaldehyde (1.25 g, 7.47 mmol) in 80 mL of ethanol and heated at reflux for 8 h. After cooling to 0 °C, the resulting

light-yellow precipitate was filtered and washed with cold ethanol. After drying under vacuum, **MSP6** (0.971 g, 2.02 mmol) was isolated in 48% yield. The detailed description for the data collection and refinement details are given below. Table 3.2 contains the crystallographic refinement data. The single crystal X-ray structure of **MSP6** is shown in Figure 3.8. ^{1}H NMR ($(CD_3)_2CO$-d_6, 300 MHz): δ = 1.27 (3H, s), 1.49 (3H, s), 3.17 (3H, s), 6.00-6.04 (1H, d, J = 10.4 Hz), 6.92-6.95 (1H, d, J = 8.55 Hz), 6.96-6.99 (1H, d, J = 9.00), 7.26-7.29 (1H, d, J = 8.62 Hz), 7.30-7.33 (1H, d, J = 10.4 Hz), 8.09-8.13 (1H, dd, J = 2.83, 8.96 Hz) ppm. (Figure 3.9). ^{13}C NMR ($(CD_3)_2CO$-d_6, 400 MHz): δ = 20.61, 22.46, 32.91, 54.59, 101.14, 108.00, 116.27, 118.15, 119.49, 121.36, 123.81, 126.69, 126.75, 130.59, 135. 93, 136.86, 142.31, 147.37, 160.18 ppm (Figure 3.9). FT-IR (neat, cm^{-1}): 3076, 2968, 2934, 2868, 2545, 2162, 2041, 1980, 1910, 1736, 1654, 1614, 1577, 1510, 1478, 1466, 1443, 1396, 1379, 1361, 1331, 1272, 1255, 1228, 1175, 1145, 1127, 1088, 1061, 1017, 955, 927, 915, 904, 877, 834, 811, 792, 771, 745, 717, 703, 666 (Figure 3.13). HRMS (ESI, m/z) calculated for $C_{19}H_{16}Br_2N_2O_3$ $[M+H]^+$ 478.9601, found 478.9600 (Figure 3.9).

*Synthesis of 1',3',3'-trimethyl-6-nitro-4',7'-di(pyridin-4-yl)spiro[chromene-2,2'-indoline] (**TNDS**)*

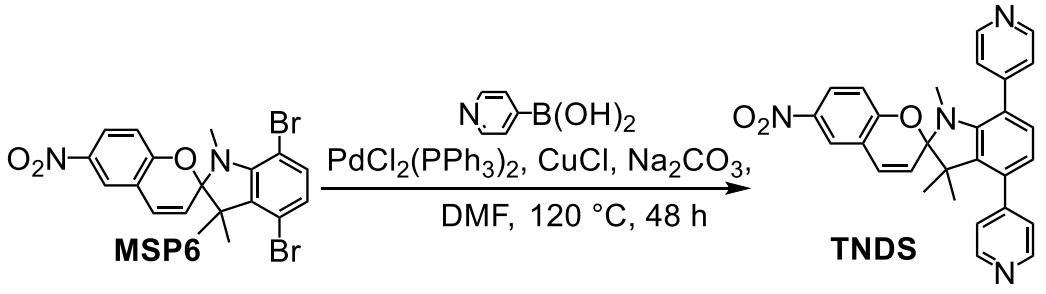

Scheme 3.7. Synthesis of 1',3',3'-trimethyl-6-nitro-4',7'-di(pyridin-4-yl)spiro[chromene-2,2'-indoline] (**TNDS**).

Under a nitrogen atmosphere, 25 mL of dry DMF was added to a flask containing **MSP6** (300 mg, 0.624 mmol), Na_2CO_3 (240 mg, 2.26 mmol), $PdCl_2(PPh_3)_2$ (88.0 mg, 0.125 mmol), CuCl (134 mg, 1.35 mmol), and pyridine-4-boronic acid (460 mg, 3.74 mmol) which stirred for three days at 120 °C. The contents of the reaction vessel were placed in a 250 mL separatory funnel, following dilution with deionized water (75 mL). The product was then extracted with ethyl acetate (3 × 50 mL) and the combined organic layers were washed with brine, dried over sodium sulfate, followed by solvent removal under vacuum. Impurities were removed from the resulting brown oil via several recrystallizations in ethyl acetate and hexanes. The solvent from the combined filtrates were removed under vacuum. The resulting orange powder was dissolved in ethyl acetate (20 mL) and hexanes (30 mL) and the ethyl acetate was removed under vacuum which resulted in a suspension. The suspension was filtered to collect a light-yellow powder. After drying on vacuum, TNDS (44.0 mg, 93.8 µmol) was isolated in 17% yield. The detailed description for the data collection and refinement details are given below. Table 3.2 contains the crystallographic refinement data. The single crystal X-ray structure of TNDS is shown in Figure 3.12. ^{1}H NMR ($(CD_3)_2CO$-*d*$_6$, 400 MHz): δ = 0.81 (3H, s), 1.33 (3H, s), 2.43 (3H, s), 6.00-6.03 (1H, d, *J* = 10.5 Hz), 6.69-6.71 (1H, d, *J* = 7.9 Hz), 6.85-6.88 (1H, d, *J* = 9.0 Hz), 7.12-7.14 (1H, d, *J* = 7.9 Hz), 7.18-7.22 (1H, d, *J* = 10.6 Hz), 7.39-7.45 (1H, m), 8.01-8.05 (1H, dd, *J* = 2.8 Hz and 9.0 Hz), 8.08 (1H, d, *J* = 2.8 Hz), 8.64 (4H, m). ^{13}C NMR ($(CD_3)_2CO$-*d*$_6$ 400 MHz): δ = 20.61, 22.46, 32.91, 54.59, 101.14, 108.00, 116.27, 118.15, 119.49, 121.36, 123.81, 126.74, 130.59, 135.93, 136.86, 142.31, 147.37, 160.18 ppm (Figure 3.10). FT-IR (neat, cm^{-1}): 3746, 2965, 2344, 2163, 2049, 1981, 1596, 1543, 1522, 1494, 1464, 1438, 1392, 1363, 1337, 1286, 1253, 1216, 1145, 1129, 1072, 1055, 1011, 980, 939, 905, 873,

827, 803, 749, 729, 681 (Figure 3.13). HRMS (ESI, m/z) calculated for $C_{29}H_{24}N_4O_3$ $[M+H]^+$ 477.1918, found 477.1921. (Figure 3.10).

*Synthesis of [4,4'-dibromo-1,1',2,2',3,3,3',3'-octamethyl-3H,3'H-[7,7'-biindole]-1,1'-diium]bis[trifluoromethanesulfonate] (**BSP5**)*

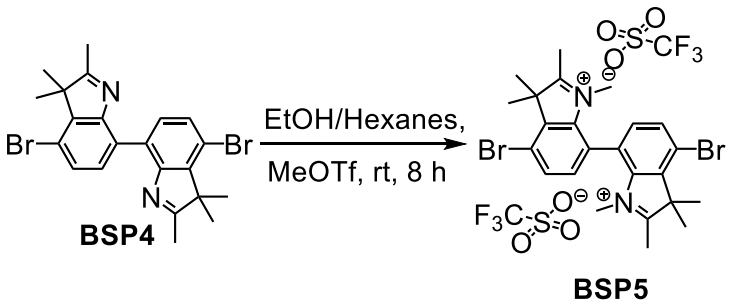

Scheme 3.8. Synthesis of [4,4'-dibromo-1,1',2,2',3,3,3',3'-octamethyl-3H,3'H-[7,7'-biindole]-1,1'-diium]bis[trifluoromethanesulfonate] (**BSP5**).

Methyl trifluoromethanesulfonate (1.50 g, 10.1 mmol) was added to a solution of **BSP4** (1.00 g, 2.11 mmol) in 90 mL of diethyl ether and 60 mL of hexanes. The mixture was stirred vigorously overnight at room temperature, and the resulting pale pink powder was collected by filtration and washed with diethyl ether (3 × 10 mL). After drying under vacuum, **BSP5** (1.57g, 1.96 mmol) was isolated in 93% yield and used without further purification.

*4',4'''-dibromo-1',1''',3',3',3''',3'''-hexamethyl-6,6''-dinitro-7',7'''-bispiro[chromene-2,2'-indoline] (**BSP6**)*

Using sensitive air techniques, distilled piperidine (713 mg, 8.37 mmol) was added to a solution of **BSP5** (1.50 g, 1.87 mmol) and 2-hydroxy-5-nitrobenzaldehyde (706 mg, 4.38 mmol) in 60 mL of ethanol and heated at reflux for eight hours. After cooling to 0 °C, the resulting light-yellow precipitate was filtered and washed with cold ethanol. After

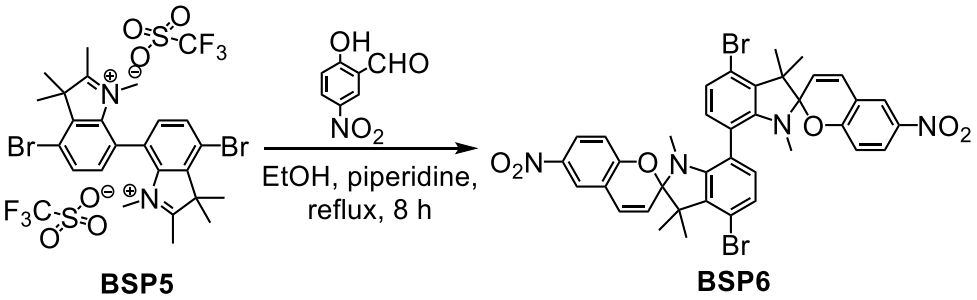

Scheme 3.9. Synthesis of 4',4'''-dibromo-1',1''',3',3',3''',3'''-hexamethyl-6,6''-dinitro-7',7'''-bispiro[chromene-2,2'-indoline] (**BSP6**).

drying under vacuum, **BSP6** (761 mg, 948 µmol) was isolated in 51% yield. The detailed description for the data collection and refinement details are given below. Table 3.3 contains the crystallographic refinement data for $HDDB_{in\text{-}in}$ and $HDDB_{in\text{-}out}$. The single crystal X-ray structure of $HDDB_{in\text{-}in}$ and $HDDB_{in\text{-}out}$ are shown in Figure 3.15. ^{1}H NMR ($(CD_3)_2CO$-d_6, 400 MHz): δ = 1.30 (6H, s), 1.43 (6H, s), 2.59 (6H, s), 5.96-5.99 (2H, d, J = 10.4 Hz), 6.34-6.37 (2H, d, J = 9.00 Hz), 6.87-6.90 (2H, d, J = 8.18 Hz), 6.97-7.00 (2H, d, J = 8.25 Hz), 7.24-7.28 (2H, d, J = 10.4 Hz), 7.59-7.54 (2H, dd, J = 2.77 Hz and 9.01 Hz), 8.10 (2H, d, J = 2.73 Hz). FT-IR (neat, cm^{-1}): 3556, 3076, 2976, 2934, 2873, 2258, 2162, 2040, 1980, 1895, 1654, 1614, 1572, 1513, 1473, 1447, 1435, 1397, 1363, 1336, 1274, 1255, 1232, 1179, 1148, 1126, 1088, 1062, 1022, 1001, 950, 923, 905, 863, 823, 799, 766, 747, 709, 697.

*Synthesis of 1',1''',3',3',3''',3'''-hexamethyl-6,6''-dinitro-4',4'''-di(pyridin-4-yl)-7',7'''-bispiro[chromene-2,2'-indoline] (**HDDB**)*

Using air and water sensitive techniques, 20 mL of dry DMF was added to a flask containing **BSP6** (336 mg, 420 µmol), Na_2CO_3 (84.0 mg, 793 µmol), $PdCl_2(PPh_3)_2$ (47.0 mg, 670 µmol), CuCl (168 mg, 1.69 mmol), and pyridine-4-boronic acid (206 mg, 1.68 mmol) and stirred for two days at 120 °C. The contents of the reaction vessel were placed

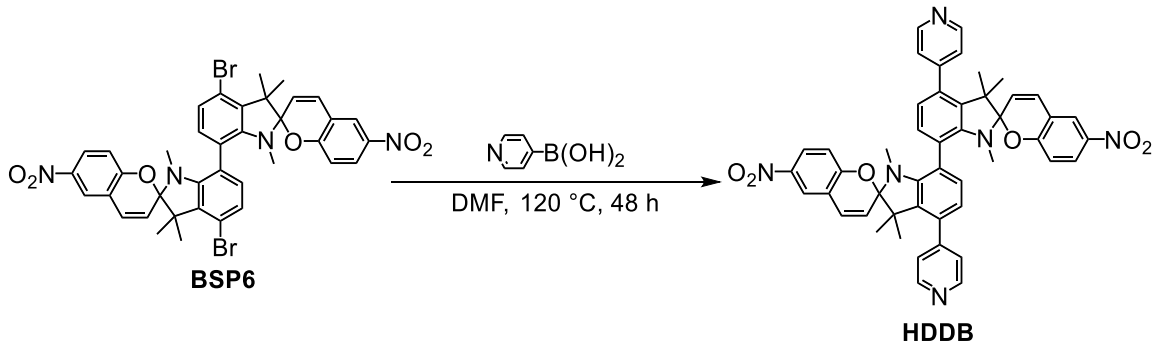

Scheme 3.10. Synthesis of 1',1''',3',3',3''',3'''-hexamethyl-6,6''-dinitro-4',4'''-di(pyridin-4-yl)-7',7'''-bispiro[chromene-2,2'-indoline] (**HDDB**).

in a 250 mL separatory funnel, following dilution with deionized water (75 mL). The product was then extracted with ethyl acetate (3 × 50 mL), and the combined organic layers were washed with brine, dried over sodium sulfate, followed by solvent removal under vacuum. Impurities were removed from the resulting brown oil via several recrystallizations in ethyl acetate and hexanes, and the solvent from the combined filtrates were removed under vacuum. The resulting orange powder was dissolved in ethyl acetate (20 mL) and hexanes (30 mL) and the ethyl acetate was removed under vacuum which resulted in a suspension. The suspension was filtered to collect a light-yellow powder. After drying under vacuum, HDDB (50.0 mg, 62.8 μmol) was isolated in 15% yield. Single crystals of $HDDB_{in\text{-}in}$ were obtained after subjecting an equilibrated mixture of HDDB isomers to preparatory TLC (DCM/MeOH 95:5). The dark yellow band (R_f = 0.7) turned deep purple when irradiated with UV light. It was scraped and extracted with distilled acetone, followed by removal of the solvent under reduced pressure. To the resulting oil, 0.5 mL of distilled acetone was added, the solution was transferred to a 5 mm NMR tube, and the solution evaporated over two days, which produced single crystals of $HDDB_{in\text{-}in}$. Single crystals of $HDDB_{in\text{-}out}$ were obtained by dissolving a mixture of isomers in a vial with 50% ethyl acetate/hexanes, followed by cooling at 0 °C for several days. The detailed

description for the data collection and refinement details are given in the experimental section, and Table 3.3 contains the crystallographic refinement data. The single crystal X-ray structures of $HDDB_{in\text{-}in}$ and $HDDB_{in\text{-}out}$ are shown in Figure 3.15. ^{1}H NMR (CD_2Cl_2-d_2, 400 MHz): δ = 0.74 (1H, s), 1.24 (6H, s), 2.58 (6H, s), 5.79-5.83 (2H, d, J = 10.5 Hz), 6.23-6.26 (2H, d, J = 9.06 Hz), 6.55-6.58 (2H, d, J = 7.81 Hz), 6.93-6.96 (2H, d, J = 10.7 Hz), 7.05-7.08 (2H, d, J = 7.91 Hz), 7.29-7.31 (4H, d, J = 5.81 Hz), 7.52-7.57 (2H, dd, J = 2.70, 8.99 Hz), 7.94-7.95 (2H, d, J = 2.69 Hz), 8.58-8.60 (2H, d, J = 5.23 Hz) (Figure 3.11). ^{13}C NMR ($(CD_3)_2CO$-d_6, 400 MHz): δ = 21.00, 25.65, 31.66, 52.51, 108.23, 114.92, 118.80, 120.65, 120.89, 121.17, 122.99, 125.13, 125.64, 129.69, 131.38, 132.90, 136,40, 141.08, 145.72, 149.54, 160.00 ppm (Figure 3.11). FT-IR (neat, cm^{-1}): 3327, 2972, 2934, 2364, 2343, 2288, 2191, 2150, 2043, 1984, 1920, 1648, 1613, 1594, 1576, 1519, 1467, 1386, 1340, 1282, 1230, 1180, 1149, 1125, 1090, 1074, 1059, 1020, 951, 928, 906, 833, 803, 747, 706, 682, 661 (Figure 3.16). HRMS (ESI, m/z) calculated for $C_{48}H_{40}N_6O_6$ $[M+H]^+$ 797.3088, found 797.3094. (Figure 3.11).

*Synthesis of **1***

In a one-dram vial, $Zn(NO_3)_2 \cdot 6H_2O$ (18 mg, 59 µmol), H_4DBTD (5.4 mg, 7.5 µmol), and TNDS (5.0 mg, 10.5 µmol) were dissolved in 0.8 mL of a prepared stock solution of 10 mL DMF and one drop of HCl. The resulting solution was sonicated, and then placed in a preheated oven at 80 °C for 24 hours, then cooled down to room temperature over two hours. Red almond-shaped crystals of **1** (13 mg, 9.4 µmol) were isolated in 90% yield. The detailed description for the data collection and refinement details are given in the experimental section, and Table 3.4 contains the crystallographic refinement data. The determined structure of **1** is shown in Figure 3.12. FT-IR (neat, cm^{-}

^{1}): 1460, 1435, 1385, 1338, 1275, 1255, 1220, 1178, 1151, 1092 (Figure 3.13). The PXRD pattern of **1** is shown in Figure 3.13. The ^{1}H NMR spectrum and ESI MS of digested **1** are shown in Figure 3.14.

*Synthesis of **2***

In a one-dram vial, $Zn(NO_3)_2 \cdot 6H_2O$ (8.8 mg, 30 µmol), H_4DBTD (2.5 mg, 3.5 µmol) and HDDB (4.8 mg, 6.0 µmol) were dissolved in one mL from a prepared stock solution of two mL DMF and one drop of HBF_4, followed by sonication. The resulting solution was placed in a preheated oven at 85 °C for 18 hours, then cooled down to room temperature over two hours. Deep red oval plate crystals of **2** (9.6 mg, 5.8 µmol) isolated in 97% yield. The detailed description for the data collection and refinement details are given in the experimental section, and Table 3.4 contains the crystallographic refinement data. The determined structure of **2** is shown in Figure 3.15. FT-IR (neat, cm-1): 1463, 1436, 1385, 1337, 1316, 1274, 1255, 1221, 1178, 1152, 1090 (Figure 3.16). The ^{13}C CP-MAS NMR spectrum and PXRD pattern of **2** are shown in Figures 2.17 and 2.16, respectively.

*Synthesis of **3***

In a one-dram vial, $Zn(NO_3)_2 \cdot 6H_2O$ (35 mg, 120 µmol), H_4DBTD (10 mg, 14 µmol), and BPMTC (9.0 mg, 22 µmol) were dissolved in a solution of two mL DMF and one drop of HBF_4, followed by sonication. The resulting solution was placed in a preheated oven at 85 °C for 18 hours, then cooled down to room temperature over two hours. Colorless plate crystals of **3** (13 mg, 10 µmol) were isolated in 75% yield. FT-IR (neat, cm^{-1}): 1435, 1385, 1255, 1222, 1177, 1150, 1091. The simulated and as-synthesized PXRD

patterns of **3** is shown in Figure 3.18. The ^{1}H NMR spectrum of digested **3** is shown in Figure 3.19.

*Synthesis of **4***

Crystals of PCN-700 (30 mg, 16 μmol) were added to H_2BCMTC (42 mg, 0.12 mmol) and 4 mL DMF in a one-dram vial. The vial was placed in a preheated oven at 75 °C for 24 hours, then cooled to room temperature over two hours. Colorless crystals of **4** (35 mg, 14 μmol) were isolated in 64% yield. FT-IR (neat, cm^{-1}): 1411, 1384, 1255, 1208, 1139, 1091. The experimental and as-synthesized PXRD patterns of **4** are shown in Figure 3.20. The ^{1}H NMR spectrum of digested **4** is shown in Figure 3.21.

Fluorescence Spectroscopy.

Steady-state emission spectra were acquired on an Edinburgh FS5 fluorescence spectrometer equipped with a 150 W Continuous Wave Xenon Lamp source for excitation. Emission measurements on solid samples were collected on the powders of the appropriate materials placed inside a 0.5 mm quartz sample holder using the front-facing module. The Ocean Optics JAZ spectrometer was also used for absorbance and diffuse reflectance measurements. An Ocean Optics ISP-REF integrating sphere was connected the spectrometer using a 450 μm SMA fiber optic cable. A 400 nm long pass filter was placed between an 8.0 mm quartz sample cell with cover and the integrating sphere to filter any UV light from the internal tungsten-halogen lamp. An Ocean Optics WS-1 Spectralon® reflectance standard was placed on the sample cell throughout the measurement. A mounted high-power LED (M365L2, Thorlabs) was used for *in situ* irradiation of the samples.

^{13}C CP-MAS NMR Spectroscopy.

Solid-state NMR spectra (^{13}C CP-MAS) were collected on a Bruker Avance III-HD 500 MHz spectrometer fitted with a 1.9 mm MAS probe. $^{13}C\{^{1}H\}$ CP-MAS NMR spectra (125.79 MHz) were collected at ambient temperature with a sample rotation rate of 20 kHz. For cross polarization, 1.5 ms contact time with linear ramping on the ^{1}H channel and 62.5 kHz field on the ^{13}C channel were used. ^{1}H dipolar decoupling was performed with SPINAL64 modulation and 147 kHz field strength. Free induction decays (512–2048 transients) were collected with a 27 ms acquisition time over a 300 ppm spectra width with a relaxation delay of 2.0 s.

Other Physical Measurements.

FT-IR spectra were obtained on a Perkin-Elmer Spectrum 100. NMR spectra were collected on Bruker Avance III-HD 300 and Bruker Avance III 400 MHz NMR spectrometers. ^{13}C and ^{1}H NMR spectra were referenced to natural abundance ^{13}C peaks and residual ^{1}H peaks of deuterated solvents, respectively. Powder X-ray diffraction patterns were recorded on a Rigaku Miniflex II diffractometer with accelerating voltage and current of 30 kV and 15 mA, respectively. The Waters QTOF-I quadrupole time-of-flight and Thermo Scientific Orbitrap Velos Pro mass-spectrometers were used to record the mass-spectra of the prepared compounds.

Single Crystal X-ray Data.

$C_{19}H_{16}Br_2N_2O_3$, ***MSP6***

X-ray intensity data from a pale-yellow parallelogram-shaped plate were collected at 100(2) K using a Bruker D8 QUEST diffractometer equipped with a PHOTON-100 CMOS area detector and an Incoatec microfocus source (Mo K_α radiation, $\lambda = 0.71073$ Å).

The raw area detector data frames were reduced and corrected for absorption effects using the Bruker APEX3, SAINT+ and SADABS programs.[63,64] Final unit cell parameters were determined by least-squares refinement of 9121 reflections taken from the data set. The structure was solved with SHELXT.[65,66] Subsequent difference Fourier calculations and full-matrix least-squares refinement against F^2 were performed with SHELXL-2016[65] using OLEX2.[67]

The compound crystallizes in the monoclinic system. The pattern of systematic absences in the intensity data was consistent with the space group $P2_1/c$. The structure solution revealed two apparent crystallographically independent, chemically similar molecules in the asymmetric unit. One is fully ordered and refines normally. This molecule was given atom label suffixes "A". The second independent molecule shows similar geometry, but if refined with a single position shows highly elongated anisotropic displacement parameters and large residual electron density peaks among the atoms. This second molecule exhibits whole-molecule disorder. Obtaining a satisfactory disorder model was difficult owing to the large number of atoms which appear nearly superimposed and only a relative few which are not. Eventually a disorder model consisting of three discrete components was successfully refined. The components were given atom label suffixes B, C, and D. The total site population was constrained to sum to 100%, and the disorder populations fractions refined to B/C/D = 0.366(3)/0.276(3)/0.358(3). A large array of geometric restraints was necessary for stability and chemical reasonableness. The 1,2- and 1-3-distances of all three disorder components were restrained to be similar to those of molecule "A" using SHELX SAME restraints. The planar parts of the molecule were further restrained with FLAT instructions (C3-C8 and N2/C12-C19). The anisotropic

displacement parameters of atoms which are nearly superimposed in the asymmetric unit (*e.g.* C1 B-D) were held equal, and some triplets of atoms were further restrained with an isotropic approximation restraints (SHELX ISOR instructions, atoms C19 B/C/D and C3C/C8B/C8D). All non-hydrogen atoms were refined with anisotropic displacement parameters. Hydrogen atoms bonded to carbon were located in Fourier difference maps before being placed in geometrically idealized positions and included as riding atoms with d(C-H) = 0.95 Å and U_{iso}(H) = 1.2U_{eq}(C) for aromatic hydrogen atoms and d(C-H) = 0.98 Å and U_{iso}(H) = 1.5U_{eq}(C) for methyl hydrogens. The methyl hydrogens were allowed to rotate as a rigid group to the orientation of maximum observed electron density. The largest residual electron density peak in the final difference map is 0.66 e^-/Å^3, located 0.73 Å from Br2A. Trial refinement models in alternative space groups such as $P2_1$, Pc, $P2/c$ and also in $P1$ also showed similar whole-molecule disorder, and it is therefore concluded that the crystal is best described as having a disordered structure in space group $P2_1/c$ as described above. The refinement data are given in Table 3.2.

$C_{29}H_{24}N_4O_3$, ***TNDS***

X-ray intensity data from a colorless plate were collected at 100(2) K using a Bruker D8 QUEST diffractometer equipped with a PHOTON-100 CMOS area detector and an Incoatec microfocus source (Mo K_α radiation, λ = 0.71073 Å). The raw area detector data frames were reduced and corrected for absorption effects using the Bruker APEX3, SAINT+ and SADABS programs.[63,64] Final unit cell parameters were determined by least-squares refinement of 9170 reflections taken from the data set. The structure was solved with SHELXT.[65,66] Subsequent difference Fourier calculations and full-matrix least-squares refinement against F^2 were performed with SHELXL-2016[65] using OLEX2.[67]

The compound crystallizes in the triclinic system. The space group *P*-1 (No. 2) was confirmed by structure solution. The asymmetric unit consists of one molecule. All non-hydrogen atoms were refined with anisotropic displacement parameters. Hydrogen atoms bonded to carbon were located in Fourier difference maps before being placed in geometrically idealized positions and included as riding atoms with d(C-H) = 0.95 Å and U_{iso}(H) = 1.2U_{eq}(C) for aromatic hydrogen atoms and d(C-H) = 0.98 Å and U_{iso}(H) = 1.5U_{eq}(C) for methyl hydrogens. The methyl hydrogens were allowed to rotate as a rigid group to the orientation of maximum observed electron density. The largest residual electron density peak in the final difference map is 0.28 $e^-/Å^3$, located 0.78 Å from C14. The refinement data are given in Table 3.2.

$C_{48}H_{40}N_6O_6$, ***HDDB$_{in\text{-}in}$***

X-ray intensity data from a pale green tablet were collected at 100(2) K using a Bruker D8 QUEST diffractometer equipped with a PHOTON-100 CMOS area detector and an Incoatec microfocus source (Mo K_α radiation, λ = 0.71073 Å). The raw area detector data frames were reduced and corrected for absorption effects using the Bruker APEX3, SAINT+ and SADABS programs.[63,64] Final unit cell parameters were determined by least-squares refinement of 9008 reflections taken from the data set. The structure was solved with SHELXT.[65] Subsequent difference Fourier calculations and full-matrix least-squares refinement against F^2 were performed with SHELXL-2016[3] using OLEX2.[67]

The compound crystallizes in the monoclinic system. The pattern of systematic absences in the intensity data was consistent with the space group $P2_1/c$, which was confirmed by structure solution. The asymmetric unit consists of one molecule. All non-hydrogen atoms were refined with anisotropic displacement parameters. Hydrogen atoms

bonded to carbon were located in Fourier difference maps before being placed in geometrically idealized positions and included as isotropically refined riding atoms with *d*(C-H) = 0.95 Å for aromatic and *d*(C-H) = 0.98 Å for methyl hydrogens. The methyl hydrogens were allowed to rotate as a rigid group to the orientation of maximum observed electron density. The largest residual electron density peak in the final difference map is 0.27 $e^-/Å^3$, located 0.76 Å from C22. The refinement data are given in Table 3.3

$C_{48}H_{40}N_6O_6$·0.5($C_4H_8O_2$)·unknown solvate, ***HDDB$_{in\text{-}out}$***

Crystals of the compound grew as densely intergrown light brown aggregations. Difficulty was encountered in cleaving apart a predominantly single domain of suitable size for intensity measurements. Eventually a fragment giving a diffraction pattern largely free of multiple maxima and diffuse streaking was found. X-ray intensity data were collected at 100(2) K using a Bruker D8 QUEST diffractometer equipped with a PHOTON-100 CMOS area detector and an Incoatec microfocus source (Mo Kα radiation, λ = 0.71073 Å). Strong low-angle peaks were observed, but reflection intensity decreased rapidly with θ. No appreciable scattering was observed above $2\theta_{max}$ of ~46°. Longer scan times (>60s/°) simply increased the number of low-angle reflections which were beyond the measurement range of the area detector and thereby required a higher speed re-scan. Analysis of the intensity statistics using the Bruker XPREP program showed the mean reflection $I/\sigma(I)$ fell below 2.0 in the *d* = 0.90-0.88 Å shell, where also the $R(\sigma)$ value rose to greater than 0.50 ($R(\sigma) = \Sigma[\sigma (F_{obs}^2)]/\Sigma[F_{obs}^2]$). Data were truncated at 2θ = 0.90 Å ($2\theta_{max}$ = 46.5°) for this reason. The raw area detector data frames were reduced and corrected for absorption effects using the Bruker APEX3, SAINT+ and SADABS programs.[63,64] Final unit cell parameters were determined by least-squares refinement of 9672 reflections taken from the data set.

The structure was solved with SHELXT.[65] Subsequent difference Fourier calculations and full-matrix least-squares refinement against F^2 were performed with SHELXL-2016[65] using OLEX2.[67]

The compound crystallizes in the monoclinic system. The pattern of systematic absences in the intensity data was consistent with the space group $P2_1/c$, which was verified by structure solution. The asymmetric unit consists of two crystallographically independent $C_{48}H_{40}N_6O_6$ molecules, one ethyl acetate molecule and a region of disordered and unidentified solvent peaks. The two $C_{48}H_{40}N_6O_6$ molecules were numbered identically except for label suffixes A or B. Efforts to model the solvent disorder were unsuccessful. Some solvents peaks are relatively isolated, suggesting a mixture of water molecules and ethyl acetate. The Squeeze program in PLATON was used to account for these species.[68,69] The solvent-accessible volume was calculated to be 398 $Å^3$ per unit cell (5% of the total cell volume), containing the equivalent of 80 electrons per unit cell. The scattering contribution of this electron density was added to the structure factors computed from the known part of the structure during refinement. For comparison, the residual factors were R_1/wR_2 = 0.085/0.245 for the best disorder model, and R_1/wR_2 = 0.0813/0.2322 after Squeeze. The reported crystal density and *F.W.* are calculated from the known part of the structure only. All non-hydrogen atoms were refined with anisotropic displacement parameters. Hydrogen atoms bonded to carbon were located in Fourier difference maps before being placed in geometrically idealized positions and included as riding atoms with d(C-H) = 0.95 Å and U_{iso}(H) = 1.2U_{eq}(C) for aromatic hydrogen atoms, d(C-H) = 0.99 Å and U_{iso}(H) = 1.2U_{eq}(C) for methylene hydrogen atoms, and d(C-H) = 0.98 Å and U_{iso}(H) = 1.5U_{eq}(C) for methyl hydrogens. The methyl hydrogens were allowed to rotate as a rigid

group to the orientation of maximum observed electron density. The largest residual electron density peak in the final difference map is 0.68 $e^-/Å^3$, located 0.62 Å from H4SB, near the ethyl acetate molecule. The refinement data are given in Table 3.3

Zn_2(DBTD)(TNDS), $C_{50}H_{24}Br_2N_2O_8Zn_2$, **1**

X-ray intensity data from a red almond-shaped plate were collected at 220(2) K using a Bruker D8 QUEST diffractometer equipped with a PHOTON-100 CMOS area detector and an Incoatec microfocus source (Mo K_α radiation, λ = 0.71073 Å). The crystals develop cracks and lose crystallinity in air and under oil. Diffraction pattern quality at 100 K was inferior to those at higher temperatures, showing broader maxima and stronger diffuse streaking. Diffraction intensities fell off rapidly with θ. The dataset was truncated at d = 0.98 Å, at which point the mean reflection $I/\sigma(I)$ was less than 2.0. The raw area detector data frames were reduced and corrected for absorption effects using the Bruker APEX3, SAINT+ and SADABS programs.[63,64] Final unit cell parameters were determined by least-squares refinement of 2965 reflections taken from the data set. The structure was solved with SHELXT.[65,66] Subsequent difference Fourier calculations and full-matrix least-squares refinement against F^2 were performed with SHELXL-2017[65] using OLEX2.[67]

The compound crystallizes in the space group P*mmm* of the orthorhombic system. It is structurally similar to previously reported compounds.[70] The asymmetric unit consists of ¼ of a Zn atom, ¼ of one $C_{34}H_{16}Br_2O_8$ cross-linking ligand, ¼ of one $C_{29}H_{24}N_4O_3$ pillar ligand and a large volume of unidentified disordered solvent guest molecules. The unique pyridyl ring and the central phenyl ring of the $C_{29}H_{24}N_4O_3$ pillar are disordered across mirror planes. The -$C_{13}H_{14}N_2O_3$ substituent of the central phenyl ring of the pillar could not be crystallographically located. It is presumably bonded to C15/C15*

and is therefore disordered over four symmetry-equivalent positions and contributes too weakly to the structure factors to be reasonably located. The largest electron density peak in this region was 0.43 $e^-/Å^3$, located 1.97 Å from C15, and could not be modeled as part of the -$C_{13}H_{14}N_2O_3$ substituent. For the final refinement cycles, C15 was left 'naked', with no substituent. Enhanced rigid-bond restraints were applied to the U_{ij} values of all atoms (SHELX RIGU). Additional spherical restraints (ISOR) were applied to the displacement ellipsoids of atoms C6 and C7. The disordered interstitial solvent species could not be reasonably modeled. Their contribution to the structure factors was accounted for using the Squeeze technique. The contribution of the unlocated -$C_{13}H_{14}N_2O_3$ substituent atoms was also accounted for with Squeeze.[68,69] The solvent-accessible volume was calculated to be 2394 $Å^3$ (73% of the total unit cell volume), containing the scattering equivalent of 420 electrons per unit cell. The reported formula and F.W. reflect the expected framework atoms with the complete $C_{29}H_{24}N_4O_3$ pillar but not the unknown solvent content. All non-hydrogen atoms were refined with anisotropic displacement parameters. Hydrogen atoms bonded to carbon were placed in geometrically idealized positions and included as riding atoms with d(C-H) = 0.95 Å and U_{iso}(H) = 1.2U_{eq}(C). The largest residual electron density peak in the final difference map is 0.73 $e^-/Å^3$, located 1.20 Å from Zn1. The refinement data are given in Table 3.4.

(Zn_2(DBTD)(HDDB), $C_{82}H_{56}N_6O_{14}Zn_2Br_2$), ***2***

X-ray intensity data from a deep red oval plate were collected at 220(2) K using a Bruker D8 QUEST diffractometer equipped with a PHOTON-100 CMOS area detector and an Incoatec microfocus source (Mo K_α radiation, λ = 0.71073 Å). The raw area detector data frames were reduced and corrected for absorption effects using the Bruker APEX3,

SAINT+ and SADABS programs. The diffraction pattern was characterized by broad maxima and pronounced diffuse streaking. Diffraction intensities fell off rapidly with θ. The dataset was truncated at d = 0.98 Å, at which point the mean reflection $I/\sigma(I)$ was less than 1.7. Final unit cell parameters were determined by least-squares refinement of 5853 reflections taken from the data set. The structure was solved with SHELXT.[65,66] Subsequent difference Fourier calculations and full-matrix least-squares refinement against F^2 were performed with SHELXL-2017[65] using OLEX2.[67]

The compound crystallizes in the space group P*mmm* of the orthorhombic system. It is structurally similar to previously reported compounds.[71] The asymmetric unit consists of ¼ of a Zn atom, ¼ of one $C_{34}H_{16}Br_2O_8$ cross-linking ligand, ¼ of one $C_{48}H_{40}N_6O_6$ pillar ligand and a large volume of unidentified disordered solvent guest molecules. The unique pyridyl ring and the central phenyl ring of the $C_{48}H_{40}N_6O_6$ pillar are disordered across mirror planes. The two -$C_{13}H_{14}N_2O_3$ substituents of the two central phenyl rings of the pillar could not be crystallographically located. They are presumably attached at carbon atom sites C15/C16 and are therefore each disordered over four symmetry-equivalent positions. The substituents apparently contribute too weakly to the structure factors to be reasonably located. The largest electron density peak in this region was 0.25 $e^-/Å^3$, located > 2 Å from C16, and could not be modeled as part of a -$C_{13}H_{14}N_2O_3$ substituent. For the final refinement cycles, C15 and C16 were left 'naked', with no substituent. Appropriate C-C and C-N distance (DFIX) restraints were applied to the disordered groups. The independent parts of the disordered pyridyl and phenyl rings were restrained with a FLAT instruction. Disordered carbon atoms were refined isotropically. All other non-hydrogen atoms were refined with anisotropic displacement parameters. Spherical

restraints (ISOR) were applied to the displacement ellipsoids of atoms C5, C6 and C7. The disordered interstitial solvent species could not be reasonably modeled. The contribution of these diffusely scattering species to the structure factors was accounted for using the Squeeze technique.[68,69] The contribution of the two unlocated -$C_{13}H_{14}N_2O_3$ substituent groups was also accounted for with Squeeze. The solvent-accessible volume was calculated to be 3031 $Å^3$ (76% of the total unit cell volume), containing the scattering equivalent of 453 electrons per unit cell. The reported formula and F.W. reflect the expected framework atoms with the complete di-substituted $C_{48}H_{40}N_6O_6$ pillar but not the unknown solvent content. Hydrogen atoms were placed in geometrically idealized positions and included as riding atoms d(C-H) = 0.95 Å and U_{iso}(H) = 1.2U_{eq}(C). The largest residual electron density peak in the final difference map is 1.12 $e^-/Å^3$, located 1.24 Å from Zn1. The refinement data are given in Table 3.4.

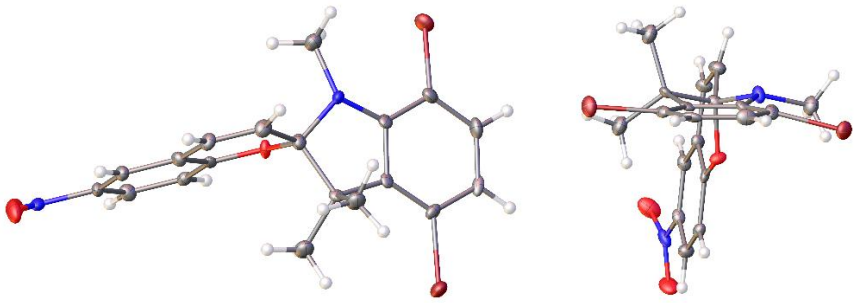

Figure 3.8. The single crystal X-ray structure of **MSP6**. Displacement ellipsoids are drawn at the 50% probability level. Blue, brown, red, gray, and white spheres represent N, Br, O, C, and H atoms, respectively.

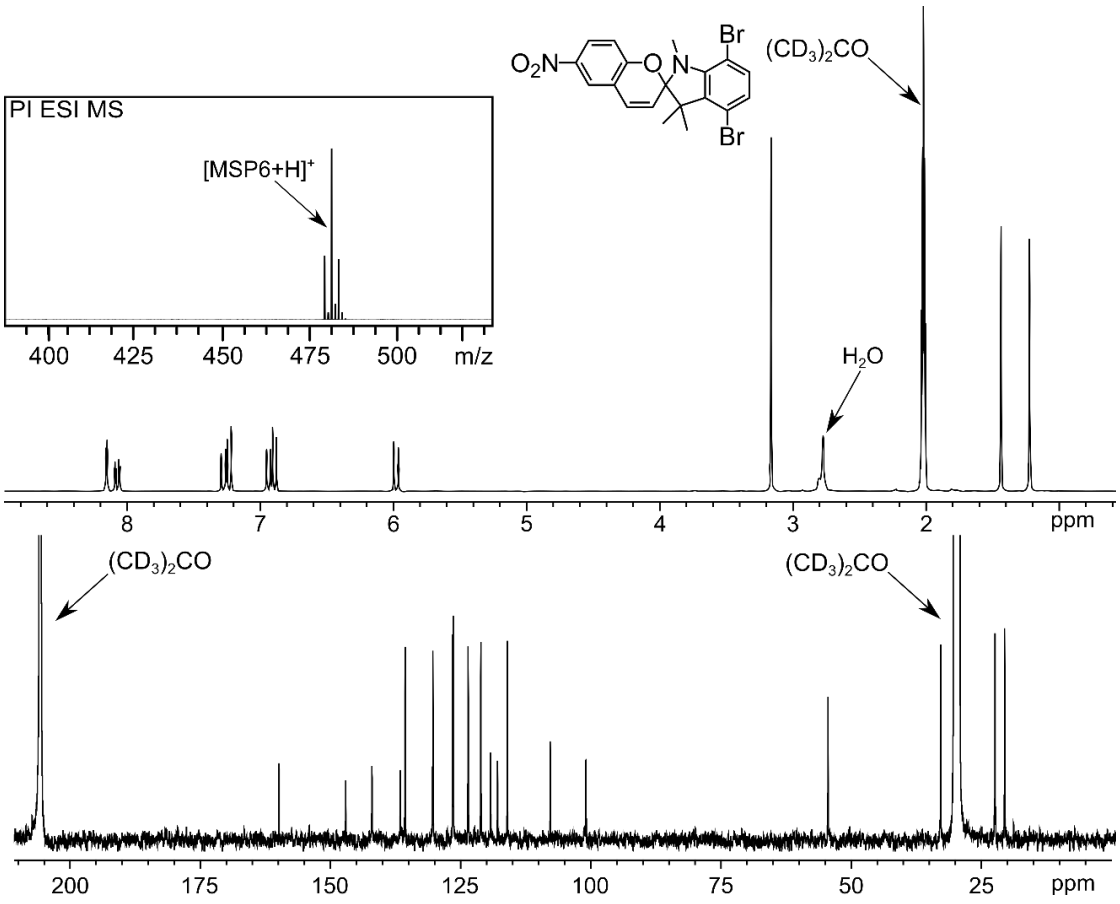

Figure 3.9. The ^{1}H NMR (*top*) and ^{13}C NMR (*bottom*) spectra of **MSP6** in $(CD_3)_2CO$-d_6. The inset shows the positive ion electrospray mass spectrum.

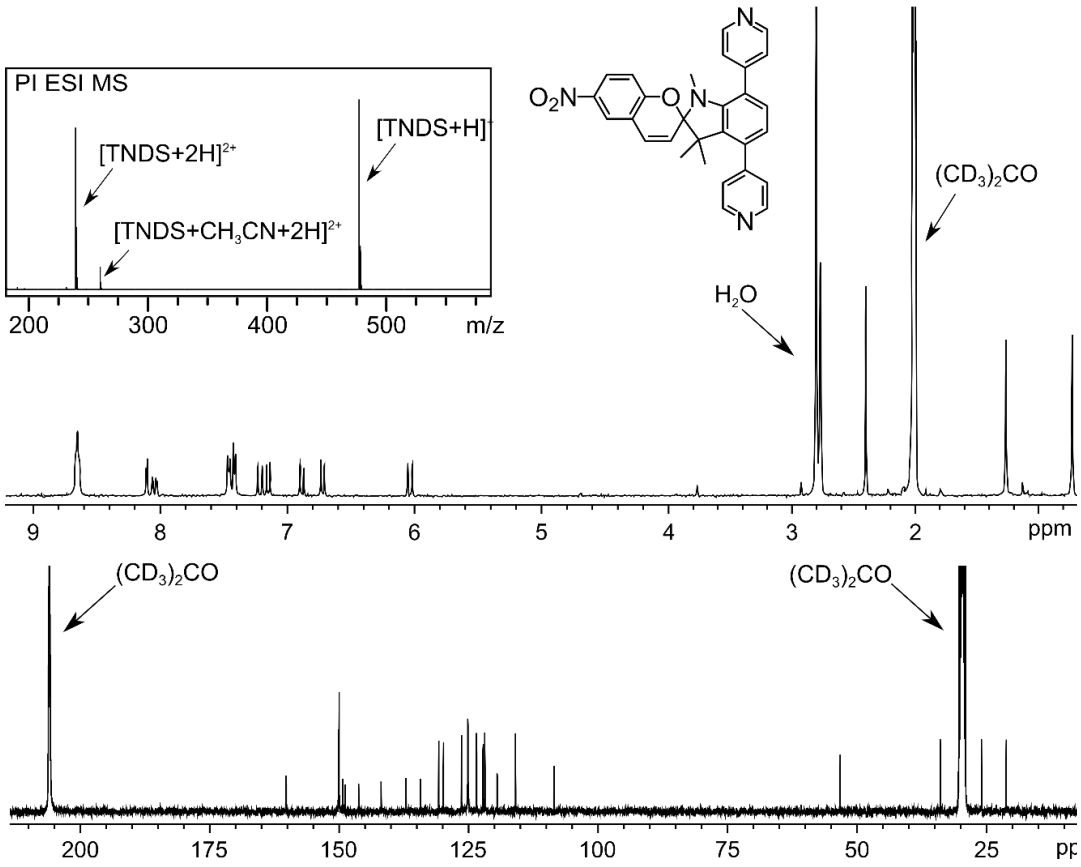

Figure 3.10. The ^{1}H NMR (*top*) and ^{13}C NMR (*bottom*) spectra of TNDS in $(CD_3)_2CO$-d_6. The inset shows the positive ion electrospray mass spectrum.

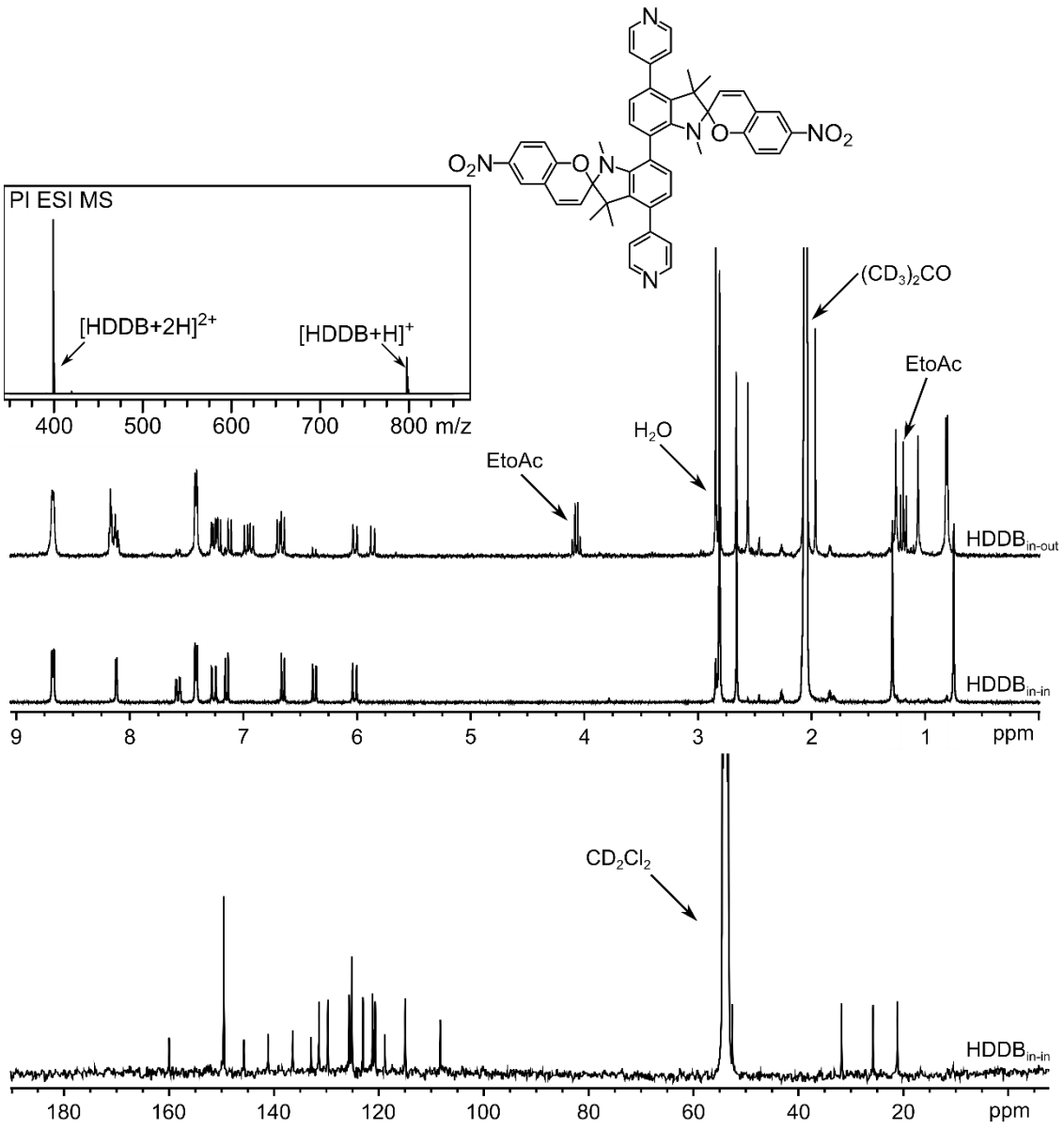

Figure 3.11. The ^{1}H NMR spectra of $HDDB_{in\text{-}out}$ (*top*), and $HDDB_{in\text{-}in}$ (*middle*) and ^{13}C NMR spectrum of $HDDB_{in\text{-}in}$ (*bottom*). The inset shows the positive ion electrospray mass spectrum.

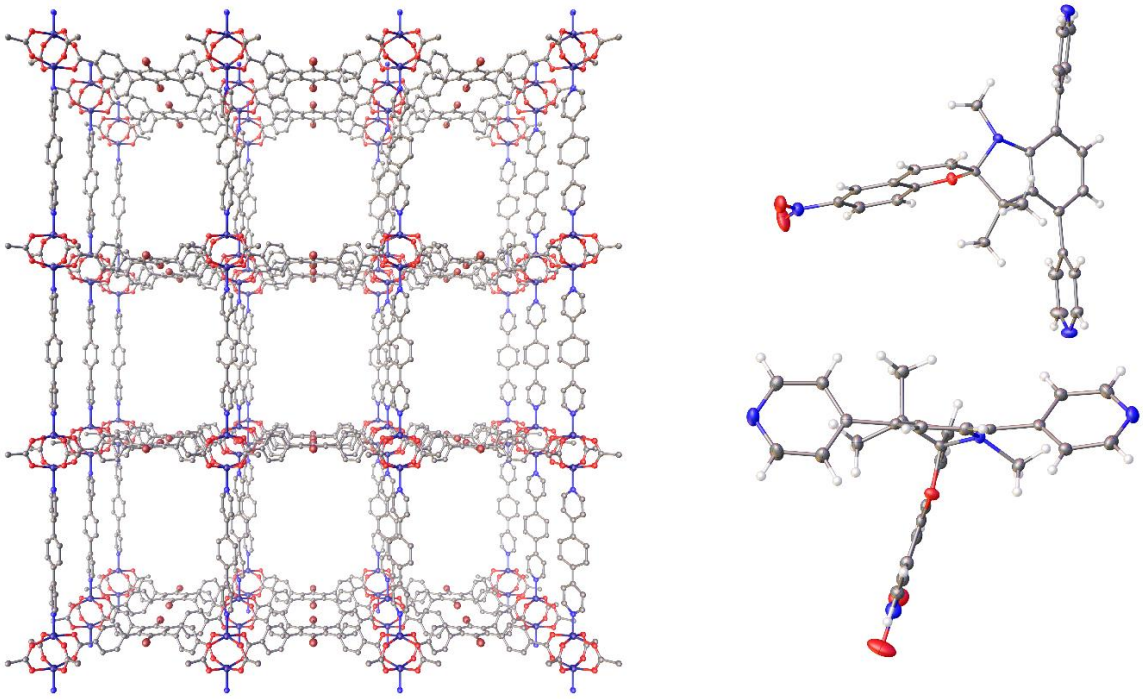

Figure 3.12. The single crystal X-ray structure of **1** (*left*). Solvent, hydrogens, and disordered molecules are omitted for clarity. The single-crystal structure of TNDS (*right*). Displacement ellipsoids are drawn at the 50% probability level. Blue, brown, red, gray, and white spheres represent N, Br, O, C, and H atoms, respectively.

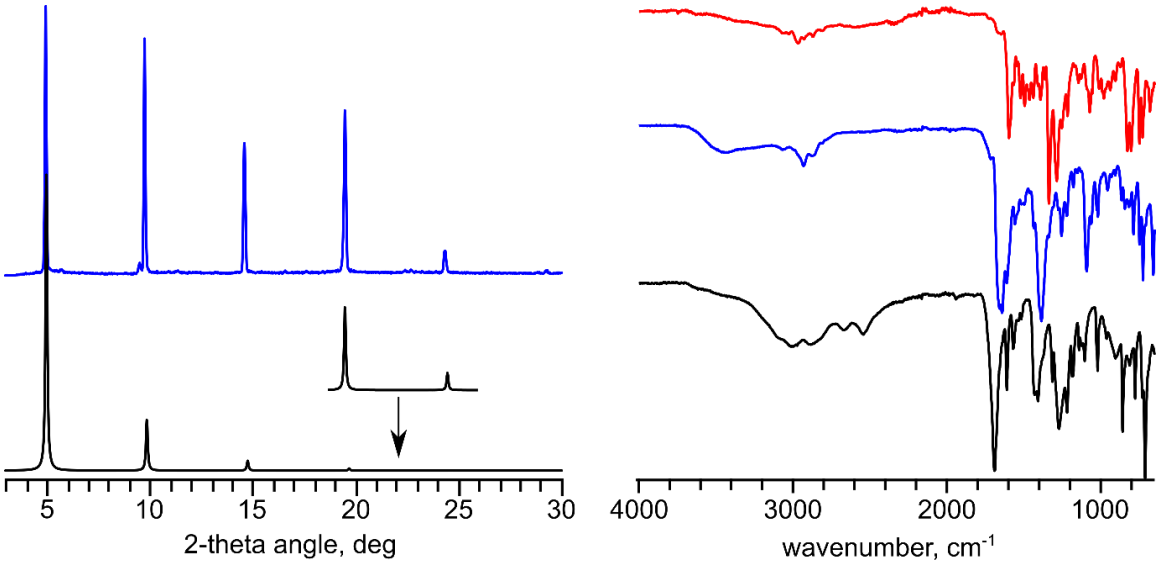

Figure 3.13. Simulated (black) and as-synthesized (blue) PXRD patterns **1** (*left*). FT-IR spectra (*right*) of TNDS (red), **1** (blue) H_4DBTB (black).

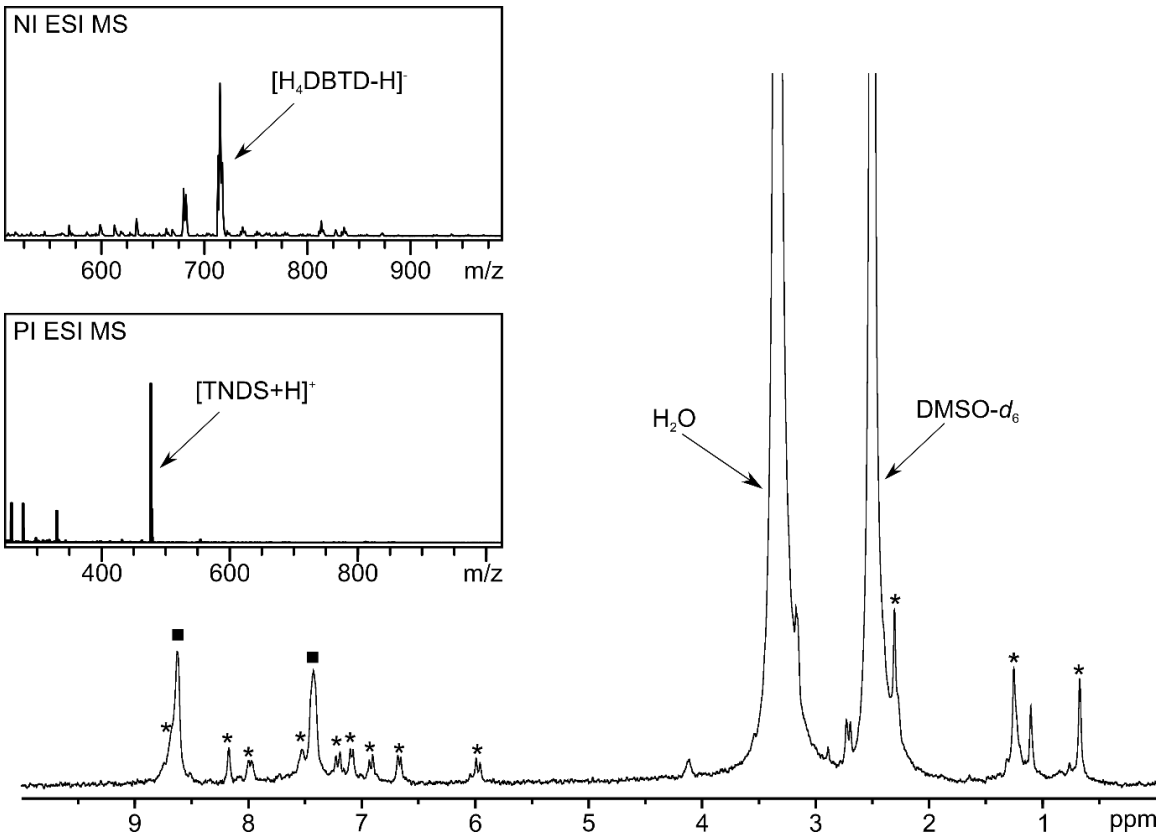

Figure 3.14. ^{1}H NMR spectrum of digested **1** in DMSO-d_6. The peaks corresponding to H_4DBTB (■) and TNDS (*) are labeled. The inset (*top*) shows the negative ion electrospray mass spectrum and the inset (*bottom*) shows the positive ion electrospray mass spectrum.

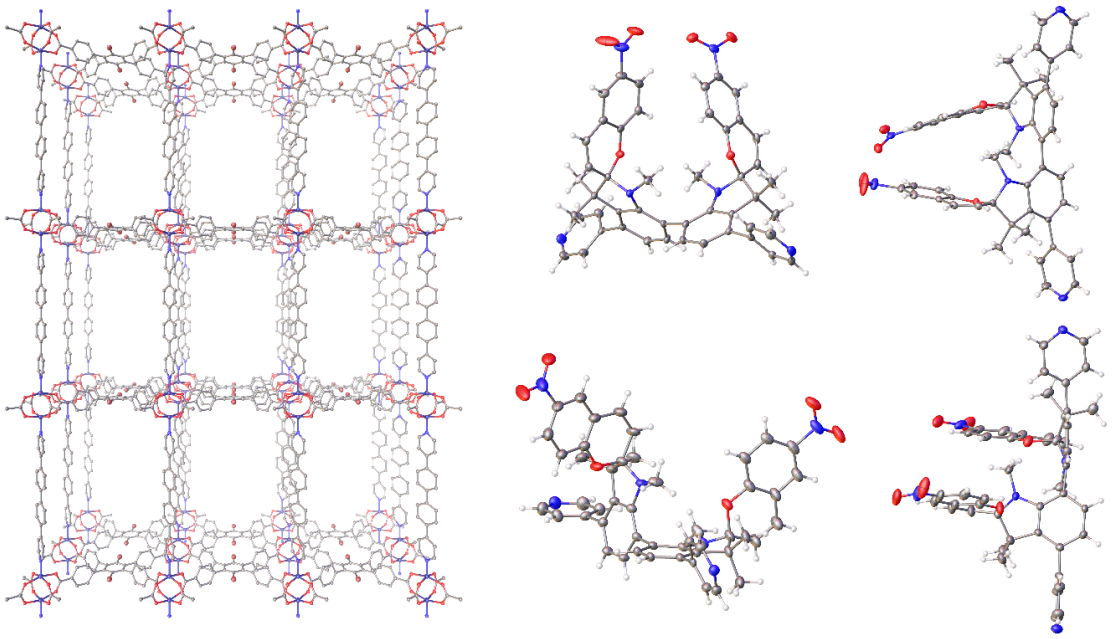

Figure 3.15. The single crystal X-ray structure of **2** (*left*). Solvent, hydrogens, and disordered molecules are omitted for clarity. The single-crystal structure of $HDDB_{in\text{-}in}$ (*top middle and top right*). Displacement ellipsoids are drawn at the 50% probability level. The single-crystal structure of $HDDB_{in\text{-}out}$ (*bottom middle and bottom right*). Displacement ellipsoids are drawn at the 30% probability level. Blue, brown, red, gray, and white spheres represent N, Br, O, C, and H atoms, respectively.

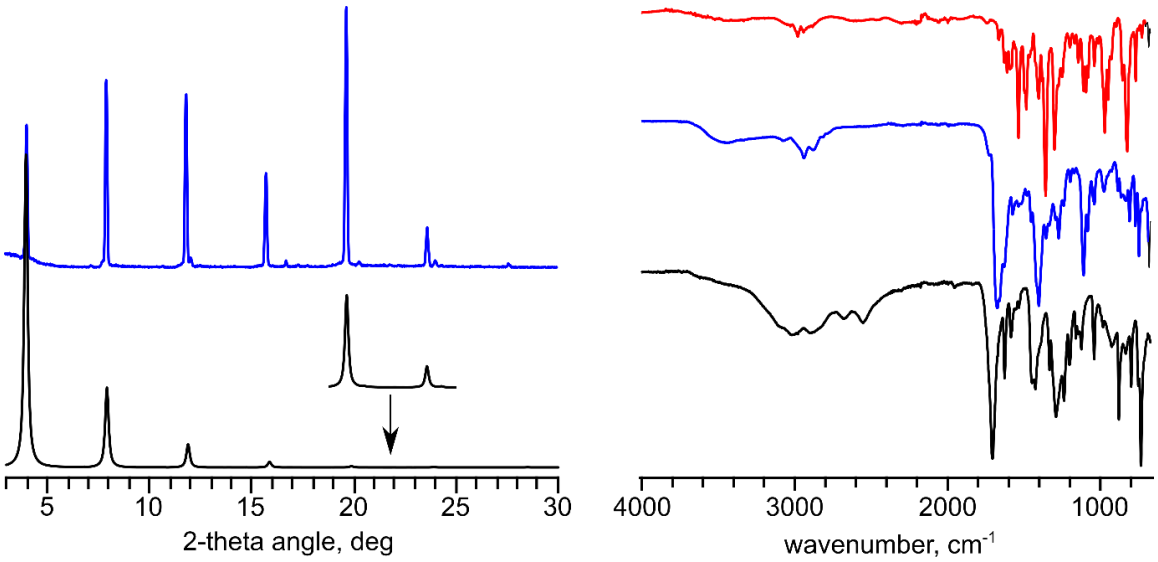

Figure 3.16. Simulated (black) and as-synthesized (blue) PXRD patterns **2** (*left*). FT-IR spectra (*right*) of HDDB (red), **2** (blue), and H_4DBTB (black).

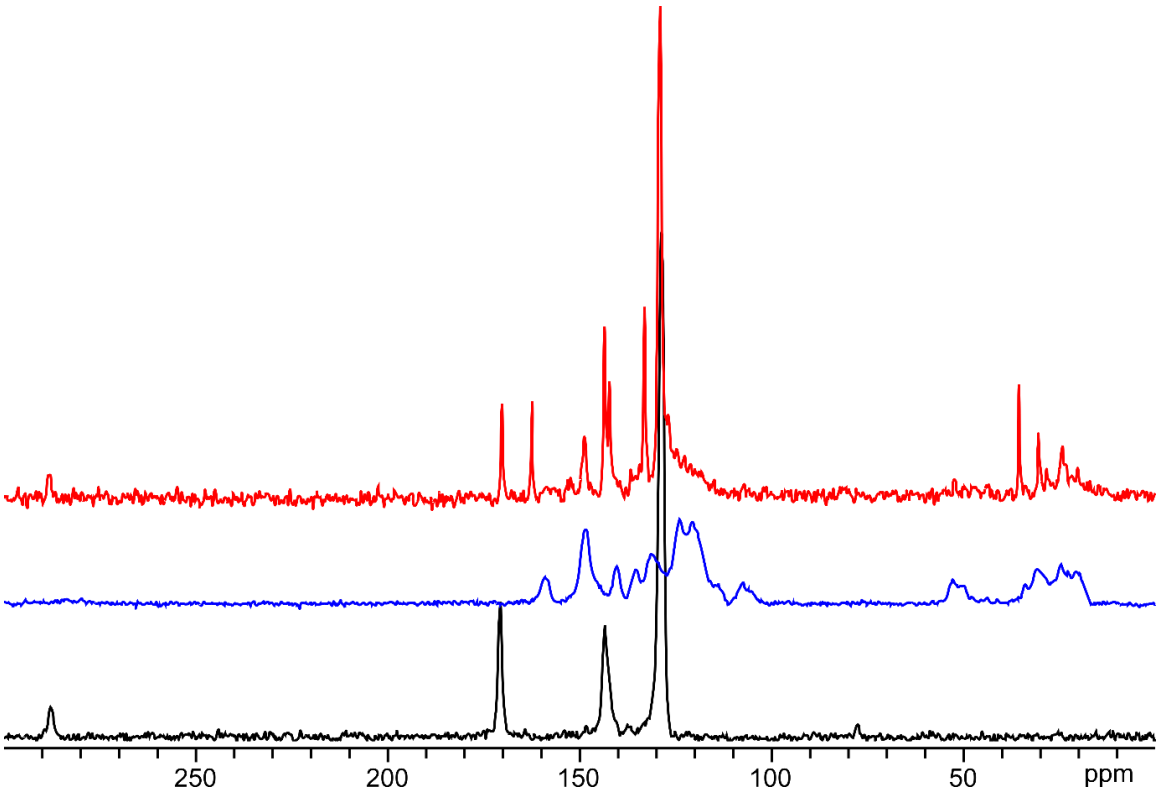

Figure 3.17. ^{13}C CP-MAS NMR spectra of **2** (red), HDDB (blue), and H_4DBTB (black).

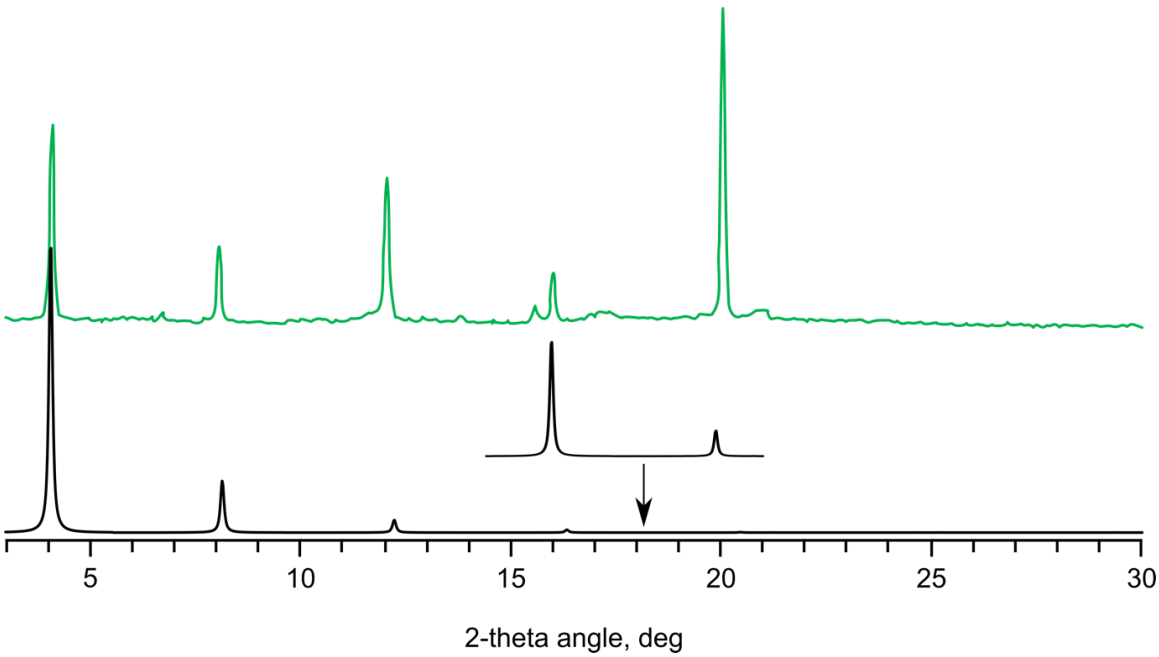

Figure 3.18. PXRD patterns of simulated (black) and as-synthesized (green) **3**.

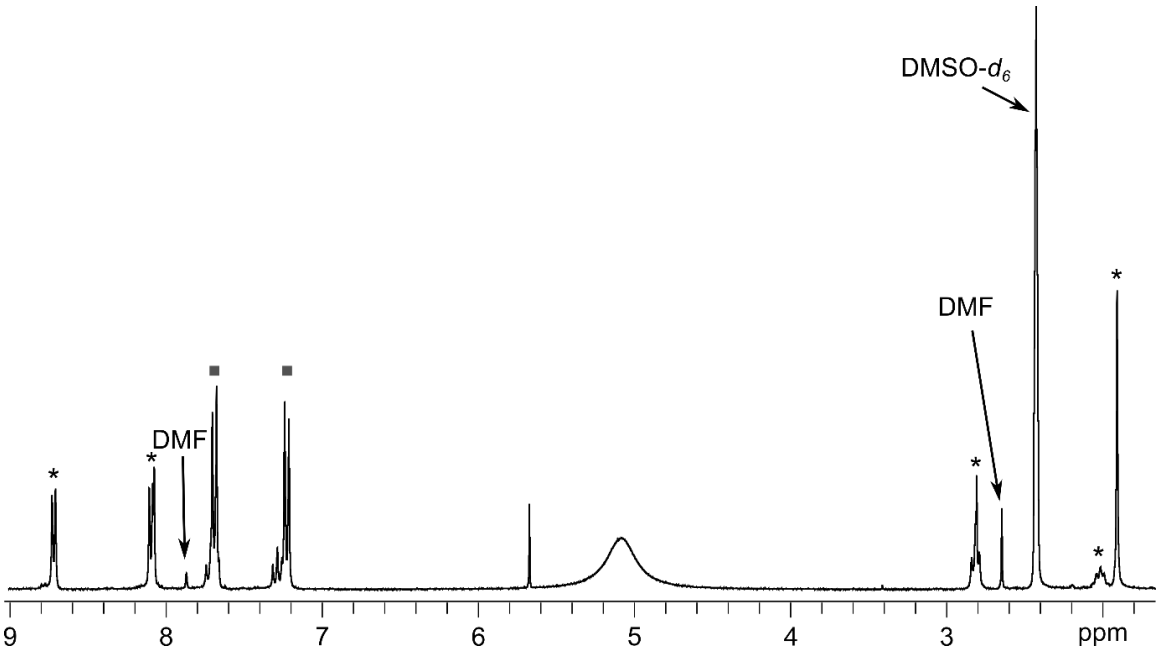

Figure 3.19. ^{1}H NMR spectrum of digested **3**. The peaks corresponding to H_4DBTB (■) and BPMTC (*) are labeled.

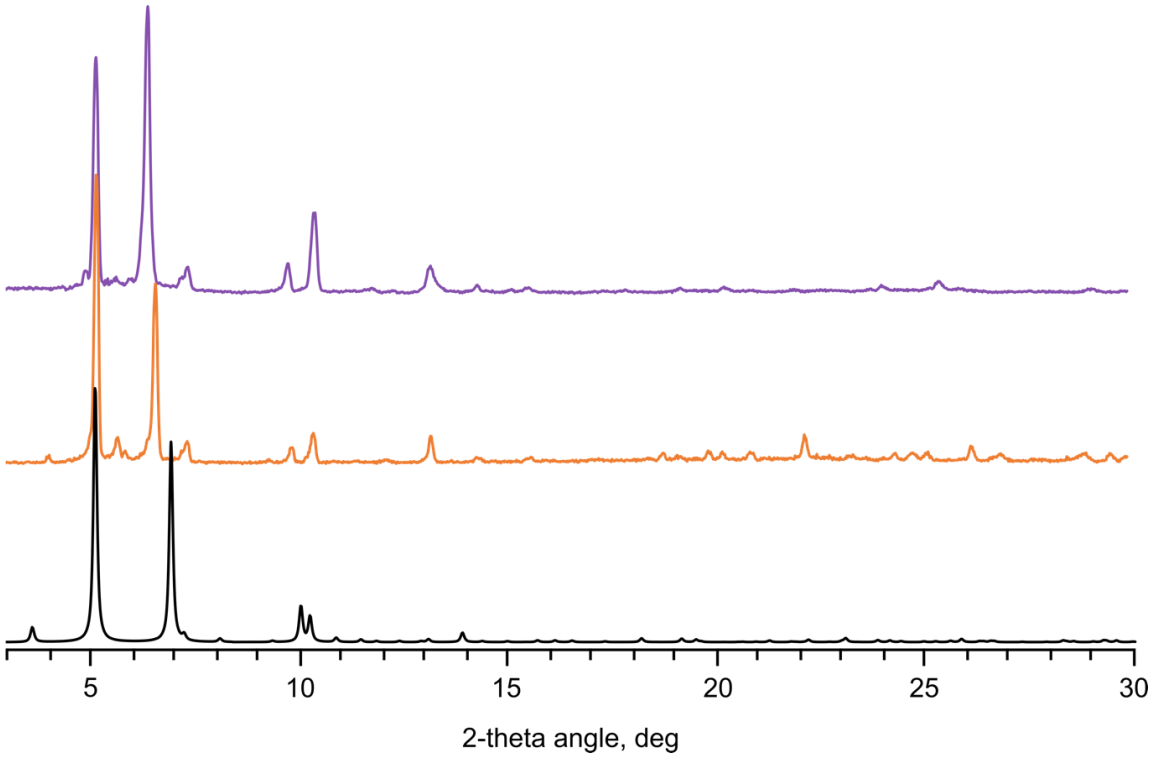

Figure 3.20. PXRD patterns of simulated PCN-700 (black)[62], as-synthesized PCN-700 (orange), and PCN-700 after $BCMTC^{2-}$ insertion (**4**) (purple).

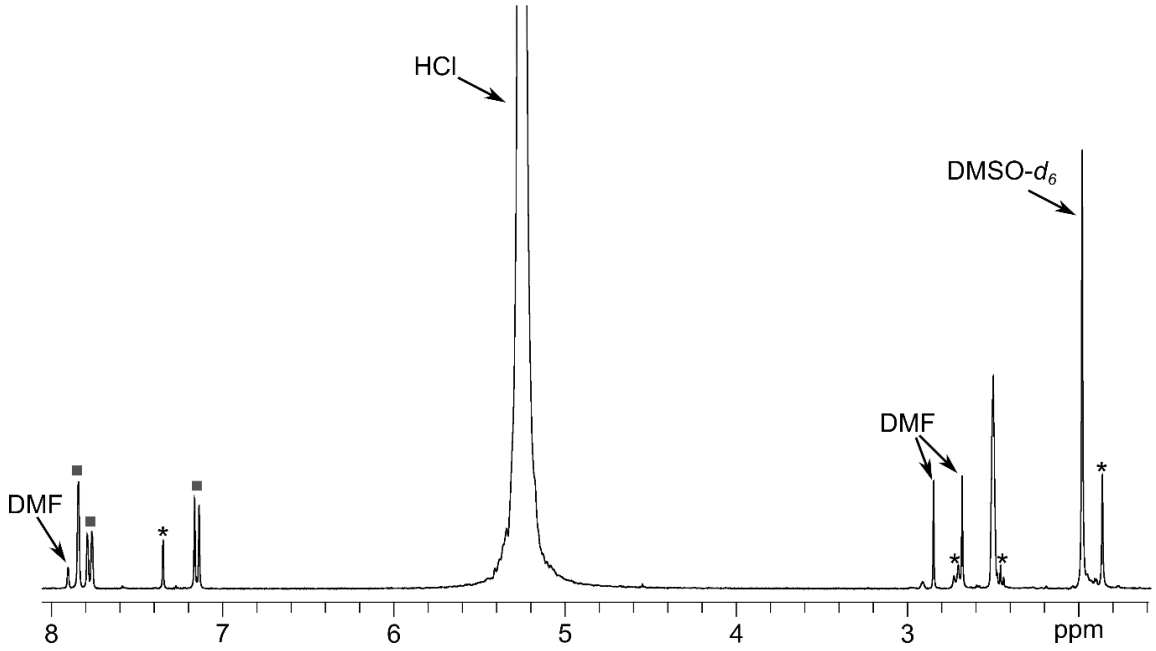

Figure 3.21. ^{1}H NMR spectrum of digested **4**. The peaks corresponding to H_4DBTB (■) and H_2BCMTC (*) are labeled.

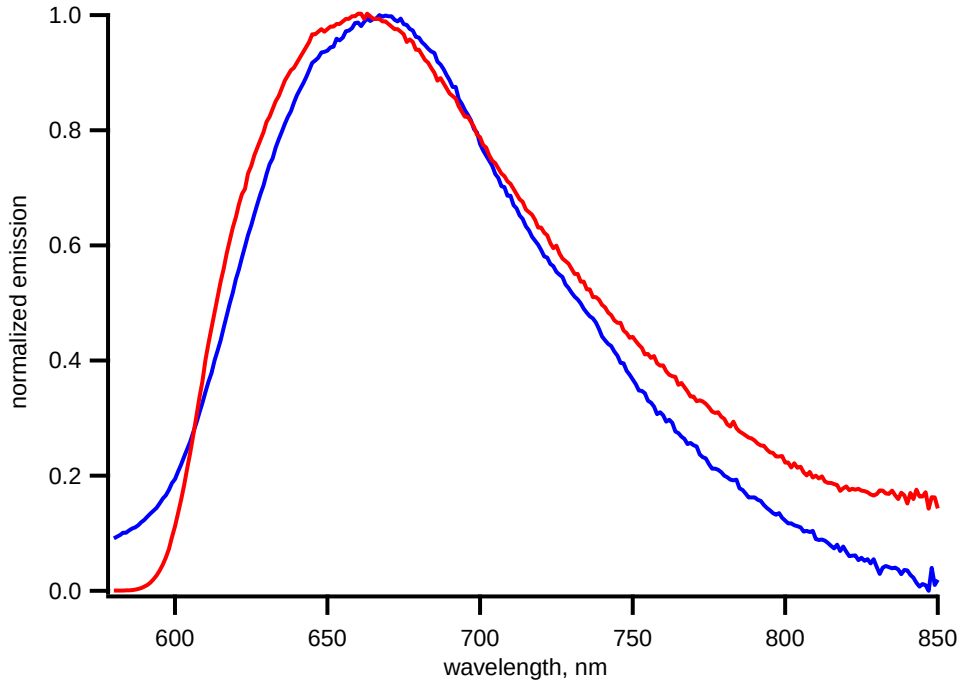

Figure 3.22. Emission spectra of TNDS (red) and HDDB (blue) in DMF, λ_{ex} = 365 nm.

Table 3.2. X-ray structure refinement data for **MSP6** and TNDS.[a]

compound	**MSP6**	**TNDS**
formula	$C_{19}H_{16}N_2O_3Br_2$[b]	$C_{29}H_{24}N_4O_3$[b]
FW	480.16	476.52
T, K	100(2)	100(2)
crystal system	Monoclinic	triclinic
space group	$P2_1/c$	P-1
Z	8	2
a, Å	9.3937(3)	8.9034(3)
b, Å	33.5488(13)	10.0040(4)
c, Å	11.4358(4)	15.0137(6)
α, °	90	92.4060(10)
β, °	92.7950(10)	105.7170(10)
γ, °	90	113.9040(10)
V, Å^3	3599.7(2)	1159.22(8)
$d_{calc,}$ g/cm^3	1.772	1.365
μ, mm^{-1}	1.008	0.090
F(000)	1904.0	500.0
crystal size/mm^3	0.26 × 0.2 × 0.15	0.18 × 0.08 × 0.05
theta range	4.314 to 60.424	4.522 to 52.85
index ranges	$-13 \le h \le 13$	$-11 \le h \le 11$
	$-47 \le k \le 47$	$-12 \le k \le 12$
	$-16 \le l \le 16$	$-18 \le l \le 18$
refl. collected	177181	33010
data/restraints/parameters	10644/516/653	4759/0/329
GOF on F^2	1.329	1.005
Largest peak/hole, e/Å^3	0.67 /–1.01	0.28/–0.20
R_1 (wR$_2$), %, [I ≥ 2sigma(I)][c]	5.53 (11.17)	4.30 (8.94)

[a] Mo-K$_\alpha$ (λ = 0.71073 Å) radiation

[b] Formula is given based on single crystal X-ray data and does not include disordered solvent molecules

[c] $R_1 = \Sigma||F_o| - |F_c||/ \Sigma |F_o|$, $wR_2 = \{\Sigma [w(F_o^2-F_c^2)^2]/ \Sigma [w(F_o^2)^2]\}^{1/2}$

Table 3.3. X-ray structure refinement data for $HDDB_{in\text{-}in}$ and $HDDB_{in\text{-}out}$.[a]

compound	$HDDB_{in\text{-}in}$	$HDDB_{in\text{-}out}$
formula	$C_{48}H_{40}N_6O_6$[b]	$C_{50}H_{44}N_6O_7$[b]
FW	796.86	840.91
T, K	100(2)	100(2)
crystal system	monoclinic	monoclinic
space group	$P2_1/c$	$P2_1/c$
Z	4	8
a, Å	17.2113(8)	15.7656(10)
b, Å	9.6042(4)	22.9720(15)
c, Å	25.5421(12)	23.9458(15)
α, °	90	90
β, °	109.466(2)	94.083(2)
γ, °	90	90
V, Å^3	3980.8(3)	8650.4(10)
$d_{calc,}$ g/cm^3	1.330	1.291
μ, mm^{-1}	0.089	0.088
F(000)	1672.0	3536.0
crystal size/mm^3	0.22 × 0.14 × 0.06	0.36 × 0.18 × 0.16
theta range	4.566 to 52.742	4.392 to 46.706
index ranges	$-21 \le h \le 21$	$-17 \le h \le 17$
	$-12 \le k \le 12$	$-25 \le k \le 25$
	$-31 \le l \le 31$	$-26 \le l \le 26$
refl. collected	154012	237374
data/restraints/parameters	8112/0/587	12536/0/1150
GOF on F^2	1.051	1.058
Largest peak/hole, e/Å^3	0.27/–0.26	0.68/–0.68
R_1 (wR$_2$), %, [I ≥ 2sigma(I)][c]	4.51 (9.52)	8.13 (21.15)

[a] Mo-K_α (λ = 0.71073 Å) radiation

[b] Formula is given based on single crystal X-ray data and does not include disordered solvent molecules

[c] $R_1 = \Sigma||F_o| - |F_c||/ \Sigma |F_o|$, $wR_2 = \{\Sigma [w(F_o^2-F_c^2)^2]/ \Sigma [w(F_o^2)^2]\}^{1/2}$

Table 3.4. X-ray structure refinement data for **1** and **2**.[a]

compound	**1**	**2**
formula	$C_{63}H_{40}N_4O_{11}Zn_2Br_2$[b]	$C_{82}H_{56}N_6O_{14}Zn_2Br_2$[b]
FW	1319.55	1639.88
T, K	220(2)	220(2)
crystal system	orthorhombic	orthorhombic
space group	P*mmm*	P*mmm*
Z	1	4
a, Å	11.291(4)	11.149(2)
b, Å	15.799(5)	15.869(3)
c, Å	18.292(6)	22.608(5)
α, °	90	90
β, °	90	90
γ, °	90	90
V, Å^3	3263.0(18)	4000.1(13)
$d_{calc,}$ g/cm^3	0.672	2.723
μ, mm^{-1}	1.008	3.327
F(000)	664.0	3328.0
crystal size/mm^3	0.46 × 0.2 × 0.18	0.4 × 0.36 × 0.2
theta range	4.434 to 42.596	4.424 to 42.52
index ranges	-11 ≤ h ≤ 11	-11 ≤ h ≤ 11
	-14 ≤ k ≤ 16	-16 ≤ k ≤ 16
	-18 ≤ l ≤ 18	-23 ≤ l ≤ 23
refl. collected	12712	23134
data/restraints/parameters	2089/84/103	2555/28/90
GOF on F^2	1.027	1.039
Largest peak/hole, e/Å^3	0.76/–0.53	1.12/–0.94
R_1 (wR_2), %, [I ≥ 2sigma(I)][c]	5.71 (14.31)	6.97 (19.34)

[a] Mo-K$_\alpha$ (λ = 0.71073 Å) radiation
[b] Formula is given based on single crystal X-ray data and does not include disordered solvent molecules (complete formula was determined based on elemental analysis)
[c] $R_1 = \Sigma||F_o| - |F_c||/ \Sigma |F_o|$, $wR_2 = \{\Sigma [w(F_o^2-F_c^2)^2]/ \Sigma [w(F_o^2)^2]\}^{1/2}$

REFERENCES

(1) Kobatake, S.; Takami, S.; Muto, H.; Ishikawa, T.; Irie, M. *Nature* **2007**, *446* (7137), 778–781.
(2) Wei, M.; Gao, Y.; Li, X.; Serpe, M. J. *Polym. Chem.* **2017**, *8* (1), 127–143.
(3) Irie, M. *Photochem. Photobiol. Sci.* **2010**, *9* (12), 1535–1542.
(4) Tomizaki, K.; Mihara, H. *J. Mater. Chem.* **2005**, *15* (27–28), 2732.
(5) Wagner, K.; Byrne, R.; Zanoni, M.; Gambhir, S.; Dennany, L.; Breukers, R.; Higgins, M.; Wagner, P.; Diamond, D.; Wallace, G. G.; Officer, D. L. *J. Am. Chem. Soc.* **2011**, *133* (14), 5453–5462.
(6) Chen, J.; Zeng, F.; Wu, S. *ChemPhysChem* **2010**, *11* (5), 1036–1043.

(7) Wilkinson, M.; Kafizas, A.; Bawaked, S. M.; Obaid, A. Y.; Al-Thabaiti, S. A.; Basahel, S. N.; Carmalt, C. J.; Parkin, I. P. *ACS Comb. Sci.* **2013**, *15* (6), 309–319.
(8) Liou, J.-C.; Teng, M.-C.; Tsai, Y.-S.; Lin, E.-C.; Chen, B.-Y. *Mol. Vis.* **2015**, *21*, 846–856.
(9) Wu, Y.; Xie, Y.; Zhang, Q.; Tian, H.; Zhu, W.; Li, A. D. Q. *Angew. Chemie - Int. Ed.* **2014**, *53* (8), 2090–2094.
(10) Xing, Q. J.; Li, N. J.; Chen, D. Y.; Sha, W. W.; Jiao, Y.; Qi, X. X.; Xu, Q. F.; Lu, J. M. *J. Mater. Chem. B* **2014**, *2*, 1182–1189.
(11) Cotí, K. K.; Belowich, M. E.; Liong, M.; Ambrogio, M. W.; Lau, Y. A.; Khatib, H. A.; Zink, J. I.; Khashab, N. M.; Stoddart, J. F. *Nanoscale* **2009**, *1* (1), 16.
(12) *Prog. Polym. Sci.* **2008**, *33* (11), 1088–1118.
(13) Whelan, J.; Abdallah, D.; Buncel, E. **2010**, 5727–5735.
(14) Hu, X. G.; Li, X.; Yang, S. I. *Chem. Commun.* **2015**, *51* (53), 10636–10639.
(15) Beharry, A. A.; Woolley, G. A. *Chem. Soc. Rev.* **2011**, *40* (8), 4422.
(16) Yokoyama*, Y. **2000**.
(17) Weerasekara, R. K.; Uekusa, H.; Hettiarachchi, C. V. *Cryst. Growth Des.* **2017**, *17* (6), 3040–3047.
(18) Harada, J.; Taira, M.; Ogawa, K. *Cryst. Growth Des.* **2017**, *17* (5), 2682–2687.
(19) Pariani, G.; Quintavalla, M.; Colella, L.; Oggioni, L.; Castagna, R.; Ortica, F.; Bertarelli, C.; Bianco, A. *J. Phys. Chem. C* **2017**, acs.jpcc.7b04848.
(20) Maeda, N.; Hirose, T.; Yokoyama, S.; Matsuda, K. *J. Phys. Chem. C* **2016**, *120* (17), 9317–9325.
(21) Lucotti, A.; Bertarelli, C.; Zerbi, G. *Chem. Phys. Lett.* **2004**, *392* (4–6), 549–554.
(22) Berkovic, G.; Krongauz, V.; Weiss, V. *Chem. Rev.* **2000**, *100* (5), 1741–1754.
(23) Mondal, B.; Ghosh, A. K.; Mukherjee, P. S. *J. Org. Chem.* **2017**, *82* (15), 7783–7790.
(24) Yamaguchi, T.; Maity, A.; Polshettiwar, V.; Ogawa, M. *J. Phys. Chem. A* **2017**, *121* (42), 8080–8085.
(25) Halbritter, T.; Kaiser, C.; Wachtveitl, J.; Heckel, A. *J. Org. Chem.* **2017**, *82* (15), 8040–8047.
(26) He, J.; He, J.; Wang, T.; Zeng, H. *J. Mater. Chem. C* **2014**, *2* (36), 7531.
(27) Morimoto, M.; Irie, M. **2005**, No. Scheme 1, 3895–3905.
(28) Florea, L.; Scarmagnani, S.; Benito-Lopez, F.; Diamond, D. *Chem. Commun.* **2014**, *50* (8), 924–926.
(29) Harada, J.; Kawazoe, Y.; Ogawa, K. *Chem. Commun.* **2010**, *46* (15), 2593.
(30) Bénard, S.; Yu, P. *Adv. Mater.* **2000**, *12* (1), 48–50.
(31) Shoji, H.; Kitagawa, D.; Kobatake, S. *New J. Chem.* **2014**, *38* (3).
(32) Szaciłowski, K. *Chem. Rev.* **2008**, *108* (9), 3481–3548.
(33) Kinashi, K.; Nakamura, S.; Imamura, M.; Ishida, K.; Ueda, Y. *J. Phys. Org. Chem.* **2012**, *25* (6), 462–466.
(34) Klajn, R. *Chem. Soc. Rev.* **2014**, *43* (1), 148–184.
(35) Kundu, P. K.; Olsen, G. L.; Kiss, V.; Klajn, R. *Nat. Commun.* **2014**, *5*, 1–9.
(36) Schwartz, H. A.; Olthof, S.; Schaniel, D.; Meerholz, K.; Ruschewitz, U. *Inorg. Chem.* **2017**, acs.inorgchem.7b01908.

(37) Williams, D. E.; Rietman, J. A.; Maier, J. M.; Tan, R.; Greytak, A. B.; Smith, M. D.; Krause, J. A.; Shustova, N. B. *J. Am. Chem. Soc.* **2014**, *136* (34), 11886–11889.
(38) Park, J.; Feng, D.; Yuan, S.; Zhou, H.-C. *Angew. Chemie Int. Ed.* **2014**, n/a-n/a.
(39) Walton, I. M.; Cox, J. M.; Mitchell, T. B.; Bizier, N. P.; Benedict, J. B. *CrystEngComm* **2016**, *18* (41), 7972–7977.
(40) Patel, D. G. (Dan); Walton, I. M.; Cox, J. M.; Gleason, C. J.; Butzer, D. R.; Benedict, J. B. *Chem. Commun.* **2014**, *50* (20), 2653–2656.
(41) Walton, I. M.; Cox, J. M.; Benson, C. A.; Patel, D. (Dan) G.; Chen, Y.-S.; Benedict, J. B. *New J. Chem.* **2016**, *40* (1), 101–106.
(42) Tam, E. S.; Parks, J. J.; Shum, W. W.; Zhong, Y.-W.; Santiago-Berríos, M. B.; Zheng, X.; Yang, W.; Chan, G. K.-L.; Abruña, H. D.; Ralph, D. C. *ACS Nano* **2011**, *5* (6), 5115–5123.
(43) Yuan, S.; Lu, W.; Chen, Y.-P.; Zhang, Q.; Liu, T.-F.; Feng, D.; Wang, X.; Qin, J.; Zhou, H.-C. *J. Am. Chem. Soc.* **2015**, *137* (9), 3177–3180.
(44) Lucas, L. N.; Jong, J. J. D. de; Esch, J. H. van; Kellogg, R. M.; Feringa, B. L. *European J. Org. Chem.* **2003**, *2003* (1), 155–166.
(45) Leitus, G.; Klajn, R. **2014**.
(46) Udayabhaskararao, T.; Kundu, P. K.; Ahrens, J.; Klajn, R. **2016**, *76100*, 1805–1809.
(47) Florea, L.; McKeon, A.; Diamond, D.; Benito-Lopez, F. *Langmuir* **2013**, *29* (8), 2790–2797.
(48) Metelitsa, A. V.; Nikolaeva, O. G.; Cheprasov, A. S.; Karlutova, O. Y.; Burtseva, A. A.; Dubonosov, A. D.; Bren, V. A.; Minkin, V. I. *J. Photochem. Photobiol. A Chem.* **2016**, *321*, 12–18.
(49) Yokoyama, S.; Hirose, T.; Matsuda, K. *Chem. - A Eur. J.* **2015**, *21* (39), 13569–13576.
(50) Harada, J.; Kawazoe, Y.; Ogawa, K. *Chem. Commun.* **2010**, *46* (15), 2593.
(51) Zhang, F.; Zou, X.; Feng, W.; Zhao, X.; Jing, X.; Sun, F.; Ren, H.; Zhu, G. *J. Mater. Chem.* **2012**, *22* (48), 25019.
(52) Chimica, D.; Inorganica, C.; Chimica, D. *New J. Chem.* **2004**, *i*, 379–386.
(53) Bénard, S.; Yu, P. *Adv. Mater.* **2000**, *12* (1), 48–50.
(54) Williams, D. E.; Dolgopolova, E. A.; Pellechia, P. J.; Palukoshka, A.; Wilson, T. J.; Tan, R.; Maier, J. M.; Greytak, A. B.; Smith, M. D.; Krause, J. A.; Shustova, N. B. *J. Am. Chem. Soc.* **2015**, *137* (6), 2223–2226.
(55) Shustova, N. B.; Cozzolino, A. F.; Dincă, M. *J. Am. Chem. Soc.* **2012**, *134* (48), 19596–19599.
(56) So, M. C. *Chem. Commun.* **2015**, *51*, 3501–3510.
(57) Park, J.; Feng, D.; Yuan, S.; Zhou, H.-C. *Angew. Chem. Int. Ed. Engl.* **2015**, *54* (2), 430–435.
(58) Lee, C. Y.; Farha, O. K.; Hong, B. J.; Sarjeant, A. a.; Nguyen, S. T.; Hupp, J. T. *J. Am. Chem. Soc.* **2011**, *133* (40), 15858–15861.
(59) Yuan, S.; Chen, Y.-P.; Qin, J.-S.; Lu, W.; Zou, L.; Zhang, Q.; Wang, X.; Sun, X.; Zhou, H.-C. *J. Am. Chem. Soc.* **2016**, *138* (28), 8912–8919.
(60) Han, J.; Maekawa, M.; Suenaga, Y.; Ebisu, H.; Nabei, A.; Kuroda-sowa, T.; Munakata, M. **2007**, *46* (8), 3537–3540.
(61) Benniston, A. C.; Harriman, A.; Howell, S. L.; Li, P.; Lydon, D. P. *J. Org. Chem.* **2007**, *72* (3), 888–897.

(62) Yuan, S.; Lu, W.; Chen, Y.-P.; Zhang, Q.; Liu, T.-F.; Feng, D.; Wang, X.; Qin, J.; Zhou, H.-C. *J. Am. Chem. Soc.* **2015**, *137* (9), 3177–3180.
(63) APEX3 Version 2016.5-0 and SAINT+ Version 8.37A. Bruker AXS, Inc., Madison, Wisconsin, USA, 2016. .
(64) SADABS-2016: Krausa, L., Herbst-Irmer, R., Sheldrick G.M., S. D. *J. Appl. Crystallogr.* **2015**, *48*, 3–10.
(65) Sheldrick, G. M. *Acta Crystallogr. Sect. A Found. Adv.* **2015**, *71* (1), 3–8.
(66) Sheldrick, G. M. *Acta Crystallogr. A.* **2008**, *64* (Pt 1), 112–122.
(67) Oleg V. Dolomanov, Luc J. Bourhis, Richard J. Gildea, J. A. K. H. and; Puschmann, H. *J. Appl. Crystallogr.* **2009**, *42*, 339–341.
(68) van der Sluis, P.; Spek, A. L. *Acta Crystallogr. Sect. A Found. Crystallogr.* **1990**, *46* (3), 194–201.
(69) PLATON SQUEEZE: Spek, A. L. *Acta Crystallogr. Sect.* **2015**, *C71*, 9–18.
(70) Vermeulen, N. A.; Karagiaridi, O.; Sarjeant, A. A.; Stern, C. L.; Hupp, J. T.; Farha, O. K.; Stoddart, J. F. *J. Am. Chem. Soc.* **2013**, *135* (40), 14916–14919.
(71) Farha, O. K.; Malliakas, C. D.; Kanatzidis, M. G.; Hupp, J. T. *J. Am. Chem. Soc.* **2010**, *132* (3), 950–952.

CHAPTER 4

Highly-Ordered Fulleretic Metal-Organic Frameworks

Williams, D. E.; Dolgopolova, E. A; Godfrey, D. C.; Ermolaeva, E. D.; Pellechia, P. J.; Greytak, A. B.; Smith, M. D.; Avdoshenko, S. M.; Popov, A. A.; Shustova, N. B. *Angew. Chemie Int. Ed.* **2016**, *55*, 9070–9074

INTRODUCTION

Fullerene derivatives have been a valuable tools in the development of organic photovoltaics and molecular electronics[1,2] due to their unique electron-accepting properties and ultrafast electron/energy transfer.[3–5] The efficiency of exciton transport is highly dependent on the morphology and mutual alignment of the donors and acceptors.[6] For example, device performance is dependent on the donor-acceptor interface (i.e. bulk heterojunction versus bilayer morphology) and the exciton diffusion length.[7] Fullerene derivatives are excellent acceptors used in organic photovoltaic devices,[8] and can be mutually oriented with the donor molecules through several routes: covalent bonding,[9–13] insertion into porous matrices,[14–16] or co-crystallized.[17,18] Fullerene derivatives can be coordinated with donor molecules via the self-assembly approach, which resulted in an increase of device performance.[19] However, there are few reports of self-assembled fullerene derivatives which are covalently coordinated to metal ions to form a well-defined extended structure.[20–23] Moreover, there are no know reports regarding the development of a crystalline metal-donor-acceptor framework that focus on the precise control of the donor-fullerene mutual orientation through covalent bonding, which is the approach demonstrated herein (Scheme 4.1).

Self-assembled systems, such as covalent-organic frameworks (COFs) or metal-organic frameworks (MOFs), can be utilized for donor-acceptor alignment possessing long-range ordering, and have received much interest in recent years.[24–36] What sets MOFs apart from other materials is that they are crystalline, hybrid, porous, rigid materials that

are assembled from organic linkers anchored to one another through metal nodes. They exhibit high crystallinity; therefore, the distances and angles between donor and acceptor ligands, as well as their molecular conformation may be determined using single-crystal X-ray diffraction.

A common donor molecule capable of ET/charge transfer to fullerene is porphyrin. Porphyrin and fullerene derivatives are often paired in molecular dyad and triad systems because of the ability for photoinduced electron transfer from the porphyrin donor to the fullerene acceptor.[37–40] In our studies, porphyrin was selected as a donor molecule because the porphyrin derivative, tetrakis(4-carboxyphenyl)porphyrin (H_4TCPP), has an exceptional ability to form rigid two- and three-dimensional, crystalline, and modular MOFs.[41–44] The modularity of the MOF could allow for the insertion of a fullerene-derived acceptor between two-dimensional layers of the porphyrin MOF, thereby controlling the porphyrin-fullerene (donor-acceptor) mutual orientation. This method could be particularly useful to obtain a highly-ordered, three-dimensional, donor-acceptor fulleretic extended structure.

In this chapter, a novel approach is presented for the self-assembly of a crystalline porphyrin-fullerene extended structure while controlling the mutual orientation through metal coordination, as shown in Scheme 4.1. This chapter covers the synthesis of the fullerene derivative and fulleretic MOF, along with their structural and photophysical characterizations, and it consists of three main sections: (i) the design, synthesis, and characterization of the pyridyl-terminated fulleretic linker (ii) the synthesis and structural characterization of the donor-fullerene MOF, and (iii) elucidation of the fulleretic MOF photophysical properties.

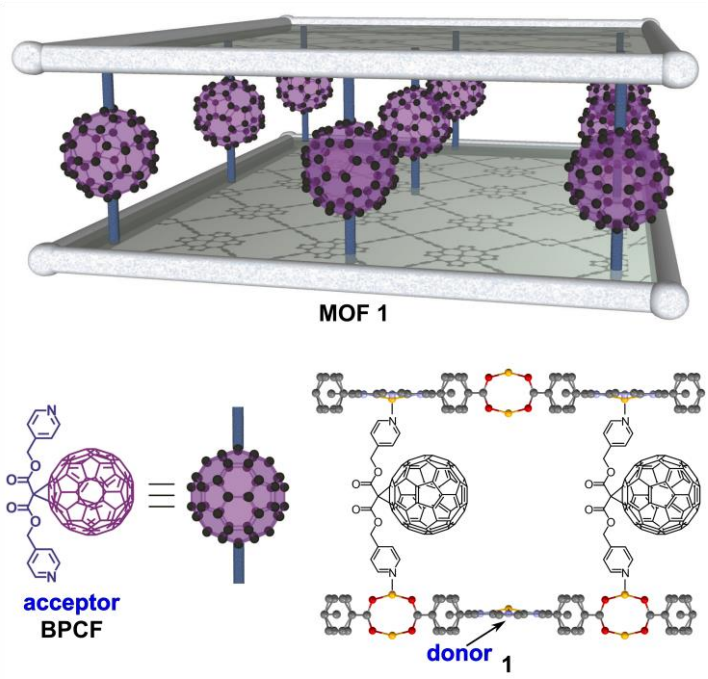

Scheme 4.1. A schematic representation of porphyrin-based donors and fullerene-based acceptors in the hybrid crystalline scaffold (**1**) through ligand-metal coordination.

4.1. Synthesis and Characterization of the Fullerene-based MOF Linker.

To incorporate fullerene into the MOF covalently rather than through π-π interactions,[15,45–47] modification of the fullerene core was necessary. Functionalization of fullerene with pyridyl-terminated groups provides the capability for it to be coordinatively immobilized into 2D MOFs with open metal centers.[41] Moreover, it was necessary to

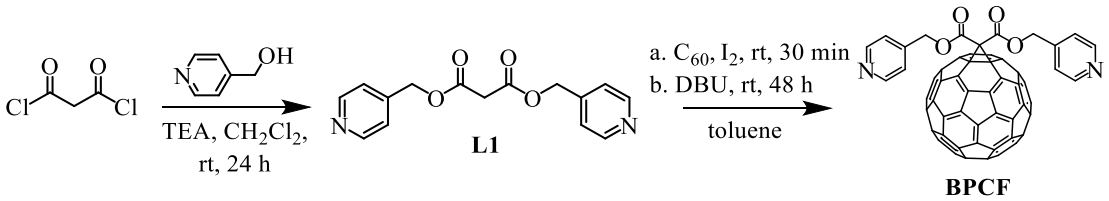

Scheme 4.2. Synthetic scheme of BPCF

prepare the fullerene derivative in gram-scale quantities for MOF synthesis. Therefore, we chose to prepare the known fullerene compound, bis(pyridin-4-ylmethyl)-*3'H*-cyclopropa-

[1,2](C_{60}-*I*$_h$)[5,6]fullerene-3',3'-dicarboxylate (BPCF, Scheme 4.2),[48] because: (i) through pyridyl groups, BPCF can be incorporated inside the MOF, and (ii) the BPCF compound could be prepared in gram quantities without the use of labor-intensive high performance liquid chromatography (HPLC) methods.[49,50]

The MOF linker, BPCF, was prepared through a Bingel cyclopropanation reaction by stirring bis(pyridine-4-ylmethyl)malonate (**L1**) and C_{60} at 25 °C in the presence of 1,8-diazabicyclo(5.4.0)undec-7-ene (DBU) and iodine in toluene for two days (Scheme 4.2). The crude reaction mixture was evaporated, loaded onto a silica column, and flushed with toluene to remove unreacted C_{60}, and the product was eluted with $CHCl_3$/acetone (7:3, v/v). Solvent removal under reduced pressure produced BPCF as a dark brown powder with a yield of 19%. It was characterized using ^{1}H NMR, ^{13}C NMR, ^{13}C cross-polarization magic angle spinning (CP-MAS) NMR, Fourier-transform infrared (FT-IR), and diffuse reflectance (DR) spectroscopies, mass spectrometry (MS), as well as single crystal X-ray diffraction. The ^{1}H NMR spectrum of BPCF is shown in Figure 4.1. To assess the structure of BPCF and determine the pillar length, it was crystallized from a concentrated toluene

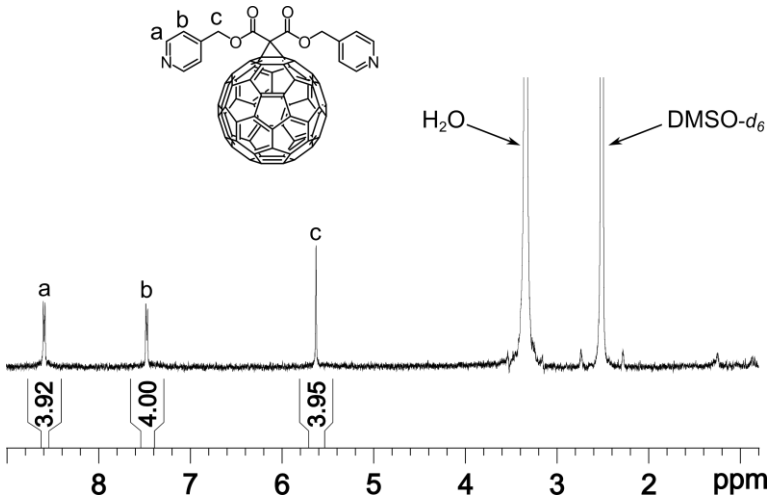

Figure 4.1. The ^{1}H NMR spectrum of BPCF in DMSO-*d*$_6$.

solution by slow evaporation over several days, yielding several dark clusters of flat needles. This was necessary so that, once synthesized, the MOF interlayer distance could be estimated based on the length of the linker. Therefore, crystals of $Ag_2(BPCF)_2(PF_6)_2$ and $Ag(BPCF)_2(PF_6)$ were grown by layering BPCF in benzene over $AgPF_6$ in MeOH/benzonitrile and acetonitrile in a 5 mm NMR tube, respectively (Figure 4.2).

The absorption profile of BPCF was measured using diffuse reflectance spectroscopy so that we could estimate the degree of absorption-emission overlap between BPCF (acceptor) and the expected porphyritic MOF host (donor), and therefore determine if Förster Resonance Energy Transfer (FRET, see Chapter 1) could be possible in the prepared scaffold (vide infra, see Section 4.3). As shown in Figure 4.3, BPCF exhibits a panchromatic absorption profile, and when overlaid with the emission profile of the 2D

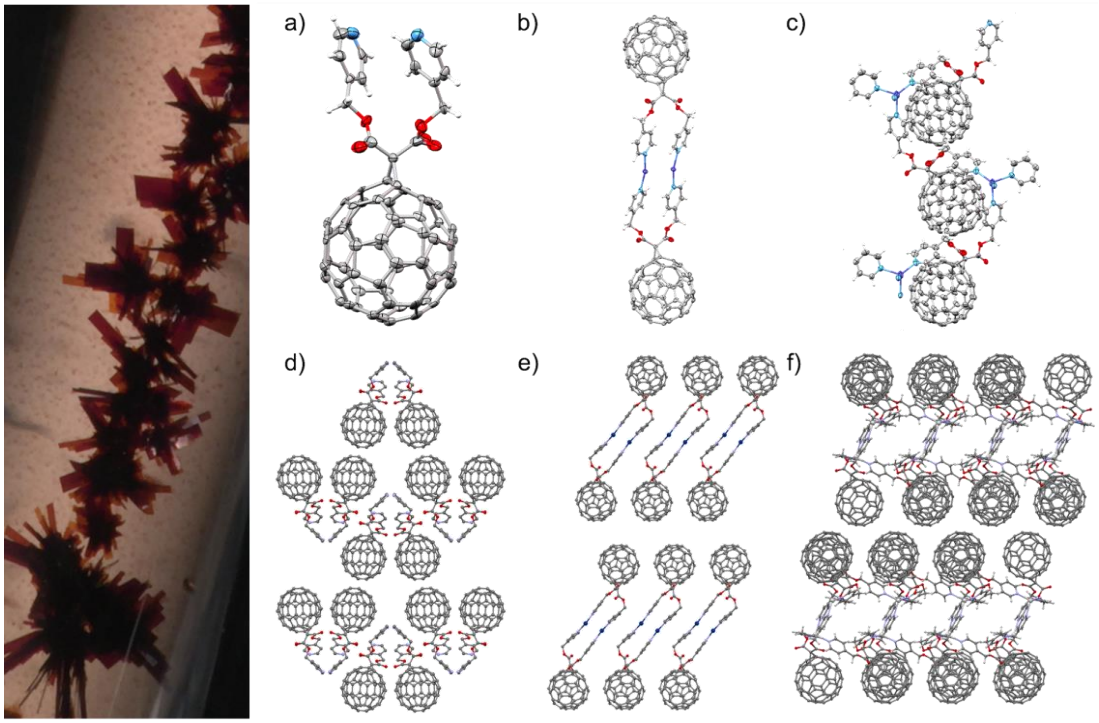

Figure 4.2. Single crystal X-ray structures of fullerene-based precursors are shown. A photograph of the crystalline silver molecular complex $Ag(BPCF)_2(PF_6)$ (*left*). Crystal structures of the fullerene-based precursor (a and d) and the silver molecular complexes (b and e, c and f) were utilized to simulate the PXRD pattern of **1** (*right*).

porphyritic MOF, Zn_2(ZnTCPP),[41] a large amount of overlap is observed, which portends to the possibility of FRET as a viable pathway for ET. Due to the electron-accepting properties of fullerene-derived materials, it is possible that the system exhibits charge transfer (CT, see Section 4.3) in addition to FRET, and is further discussed in detail in the experimental section (Figures 4.13-4.16).

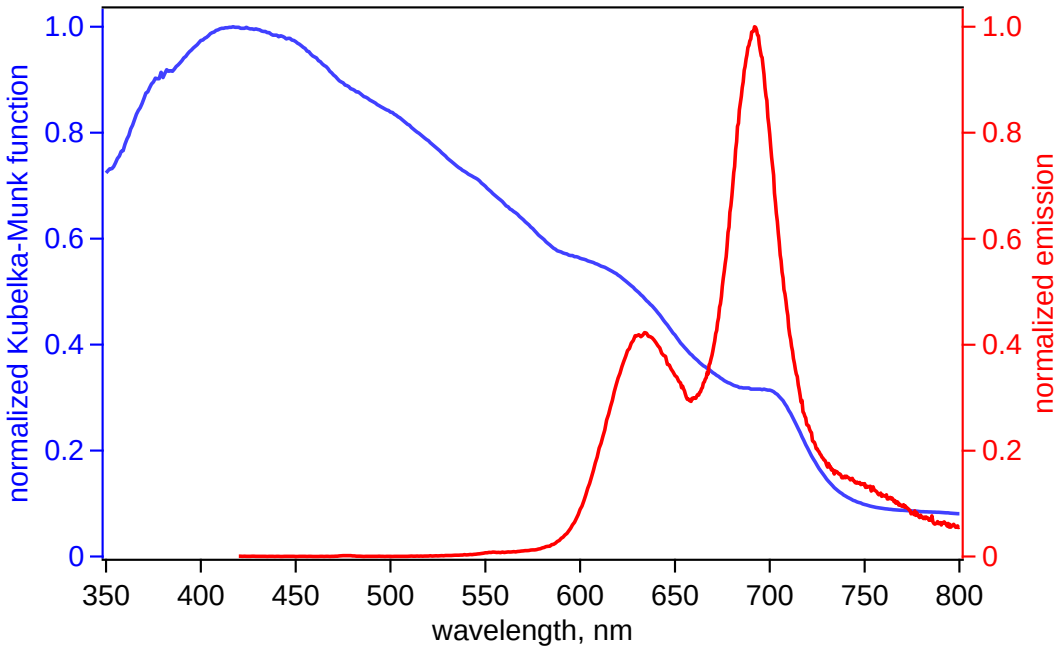

Figure 4.3. Normalized diffuse reflectance spectrum of BPCF (blue line, left axis) and normalized emission spectrum of a 2D porphyritic MOF (red line, right axis).

4.2. Synthesis and Characterization of MOF 1

The porphyrin-fullerene MOF (**1**) was obtained by heating a mixture of $Zn(NO_3)_2 \cdot 6H_2O$, H_4TCPP, and BCPF in DMF/EtOH in a ramping oven at 80 °C for 16 h, followed by cooling over 1 h, which yielded dark red crystals of **1** in 33% yield (Figure 4.21). The composition of **1** was comprehensively analyzed using DR, ^{13}C CP-MAS NMR, ^{1}H NMR, and FT-IR spectroscopies, as well as PXRD, elemental and thermogravimetric analysis. The prepared MOF **1** was digested (decomposed in the presence of acid) to utilize

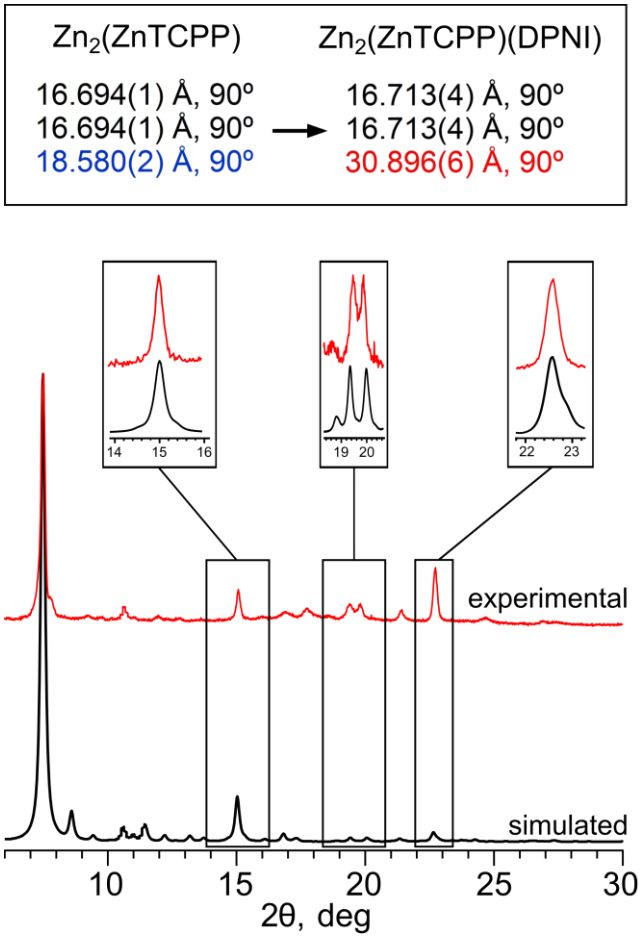

Figure 4.4. The simulated and experimental PXRD pattern from Zn_2(ZnTCPP)(DPNI) in the *110* direction and **1**, respectively. The inset shows the unit cell expansion from two-dimensional Zn_2(ZnTCPP) and simulated **1**.

solution-based ^{1}H NMR spectroscopic and mass spectrometric experiments. The bulk sample was washed thoroughly with DMF several times over two days and stored in DMF prior to analysis to remove residual linker adsorbed onto the MOF surface and in the pores.

Single crystal X-ray data collection was performed at the Advanced Light Source, Lawrence Berkeley National Laboratory, Beamline 11.3.1 but no structure could be determined with the obtained data. The most likely cause is from the poor crystallinity of the MOF, therefore, we had to rely on multiple characterization techniques to confirm the

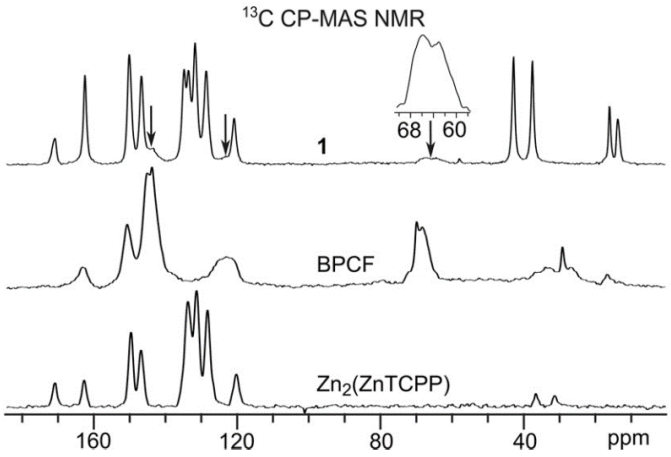

Figure 4.5. The solid-state ^{13}C CP-MAS spectra of two-dimensional Zn_2(ZnTCPP), BPCF, and **1**. The arrows on the spectrum of **1** show resonances from BPCF.

composition of **1**. We found that the PXRD of **1** was shifted to lower 2θ angles from that of 2D Zn_2(ZnTCPP), which could indicate a substantial expansion of the 2D layers, which is common for 2D systems involving Zn_2(ZnTCPP).[51–53] Therefore to determine the interlayer distance of **1**, the PXRD data of **1** was compared with a MOF that contained a linker with similar length to BPCF, *N,N'*-di-(4-pyridyl)-1,4,5,8-naphthalenetetracarboxydiimide (DPNI).[51] The DPNI linker has a length (measured from nitrogen to nitrogen in the pyridyl groups) of 15.5 Å while BPCF measures 15.8 Å, which was averaged between the three structures shown in Figure 4.2. The simulated PXRD pattern of the MOF that contained DPNI was in good agreement with the experimental PXRD pattern of **1** (Figure 4.4). Structural analysis revealed that the interlayer distance, which is measured from the apically bound atom at the $Zn_2(O_2C)$- SBU to the apically bound atom at the metalated porphyrin center of the next layer, had expanded from 2.82 Å, observed for a 2D porphyrin-based framework without fullerene linkers,[41] to 15.4 Å in **1** containing BPCF linkers, which is in line with the length of the pyridyl arms calculated

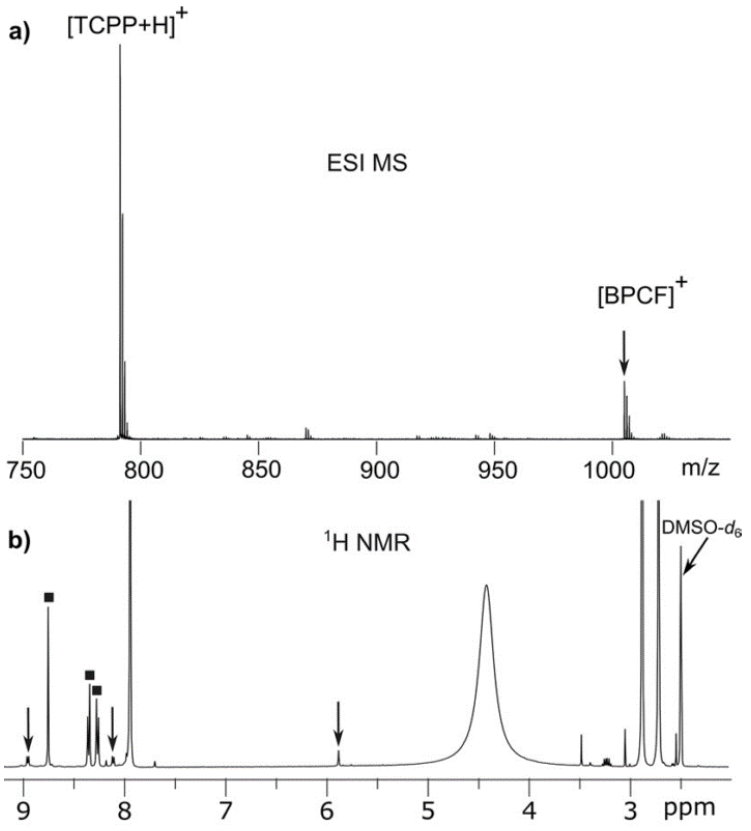

Figure 4.6. a) Mass spectrum (ESI-MS) of digested **1**. b) ^{1}H NMR of digested **1** in DMSO-d_6. Corresponding resonances of BPCF are indicated with arrows, and H_4TCPP (■) with black boxes.

from the single-crystal structure of BPCF (Figures 4.2 and 4.4). A schematic representation of BPCF installation between two-dimensional porphyrin layers is shown in Figure 4.21.

To further analyze the MOF in the solid-state, ^{13}C CP-MAS NMR spectroscopy was employed for the compositional analysis of **1**. Washed crystals of **1** were dried under high vacuum for one hour at 50 °C and then transferred to a zirconium sample rotor for further measurements. For comparison, ^{13}C CP-MAS NMR spectra were collected on Zn_2(ZnTCPP) and BPCF to assign the resonances belonging to BPCF and therefore, confirm BPMTC installation between 2D Zn_2(ZnTCPP) layers (Figure 4.5).

The composition of **1** was studied using ^{1}H NMR spectroscopy and mass spectrometry. For that, washed crystals of **1** were collected by filtration and dried under vacuum overnight at 50 °C. To the prepared sample, 500 µL DMSO-d_6 and 3.5 µL concentrated hydrochloric acid were added, and the resulting mixture sonicated for 10 minutes. Using ^{1}H NMR spectroscopy, BPCF incorporation was confirmed and found to be 23% based on the peak integrations of H_4TCPP and BPCF (Figure 4.6). For mass-spectrometry analysis, washed/dried crystals of **1** were digested in 500 µL DMSO, followed by the addition of 3.5 µL concentrated hydrochloric acid. After sonication, the vial was placed under high vacuum and heated at 50 °C overnight to remove any residual acid. The ESI MS results of **1** are shown in Figure 4.6.

FT-IR spectroscopy was used in conjunction with NMR spectroscopy and MS to further confirm BPCF installation between 2D layers of Zn_2(ZnTCPP) in **1**. A washed sample of **1** was placed on a piece of filter paper and allowed to dry for one hour before

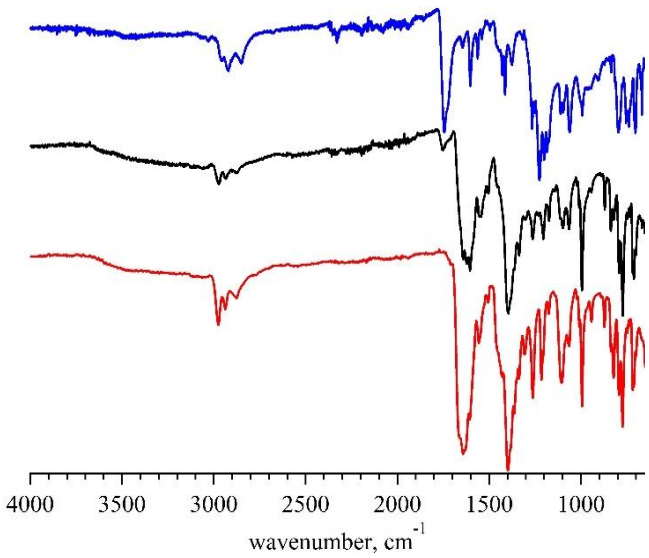

Figure 4.7. The FT-IR spectrum of Zn_2(ZnTCPP) (red), **1** (black), and BPCF (blue).

placing it onto the sample stage of the FT-IR spectrometer. The FT-IR spectra in Figure 4.7 confirm the incorporation of BPCF inside **1**.

Attempts were made to prepare a fulleretic MOF with integrated C_{60} inside its pores, and resulted in an amorphous powder, which could be attributed to the lack of pyridyl-functionalization of C_{60}, which is necessary for successfully incorporation of it into the MOF.

4.3. Photophysical Properties of MOF 1

The photophysical properties of the as-synthesized MOF were elucidated using UV/Vis, DR, fluorescence, and time-resolved photoluminescence spectroscopy. Prior to analysis, crystals of **1** were soaked in DMF, which was refreshed daily, for three days. No residual BPCF remained in the DMF solution, which was verified by UV-Vis spectroscopy.

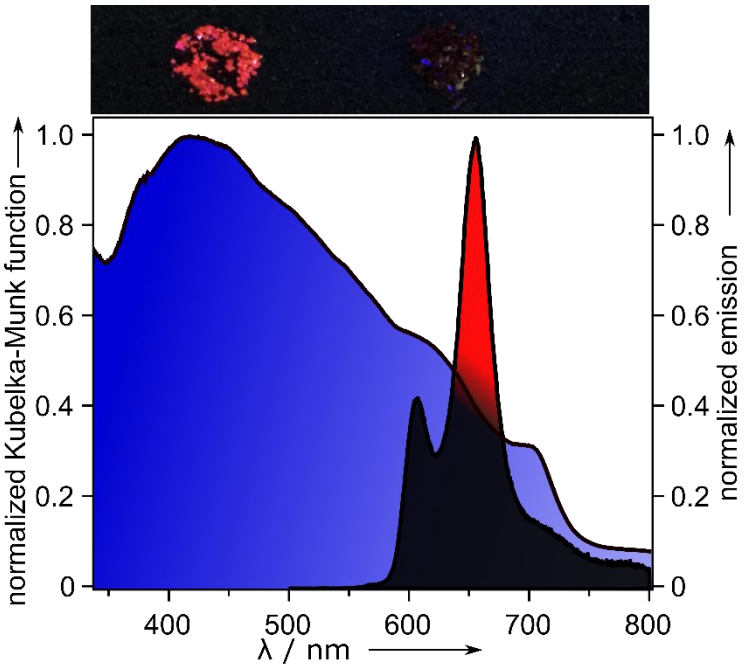

Figure 4.8. *(top)* Image of two-dimensional Zn_2(ZnTCPP) (*left)* and **1** *(right)* under 365 nm UV excitation. *(bottom)* Diffuse reflectance and fluorescence overlay of BPCF and Zn_2(ZnTCPP), respectively.

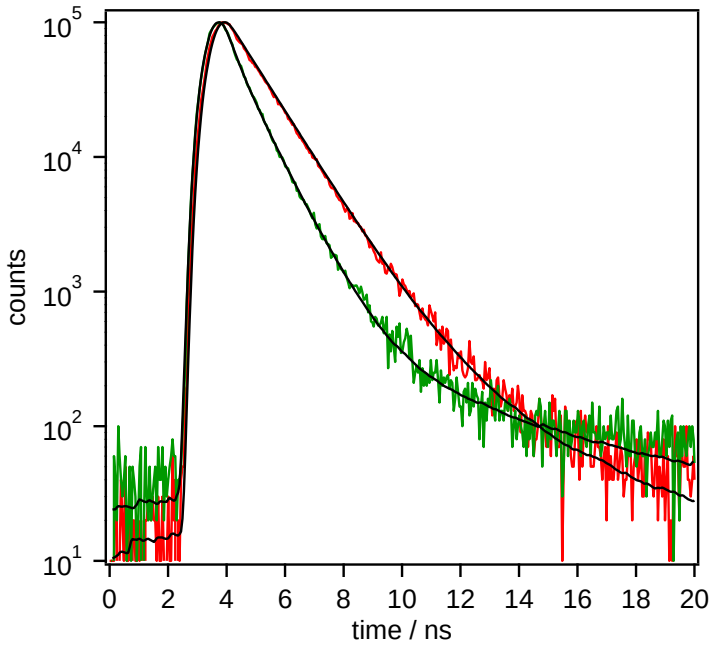

Figure 4.9. Fluorescence decays of Zn_2(ZnTCPP) (red line) and **1** (green line). Black solid lines are fits of the decays.

Even after extensive soaking, the crystals of **1** appeared very dark red in color, and very little fluorescence response was observed. In contrast, Zn_2(ZnTCPP) (in the absence of BPCF linkers) exhibits bright red remission after the same washing procedure (Figure 4.8). These changes in the emission profile can be attributed to the ET between the BPCF donor and Zn_2(ZnTCPP acceptor within the MOF. Analysis of the time-resolved data supported triexponential decays, which indicated a shortened amplitude-weighted average lifetime of **1** (0.54 ns) in comparison with Zn_2(ZnTCPP) 1.07 ns (Figure 4.9).

The fluorescence decays were fit with the triexponential function, Equation 4.1:

$$I(t) = \int_0^t IRF(t')\,(C + \sum_{i=1}^{n}(B_i e^{\left[-\frac{t-t'}{\tau_i}\right]})dt' \qquad \textbf{Equation 4.1.}$$

where τ_i and B_i are lifetimes and amplitudes of each component, respectively.

The amplitude-weighted average fluorescence lifetimes were calculated based on Equation 4.2:

$$\langle \tau_{\mathrm{av}} \rangle = \frac{B_1\tau_1 + B_2\tau_2 + B_3\tau_3}{B_1 + B_2 + B_3}$$ **Equation 4.2.**

To estimate the energy transfer efficiency of the system, it was necessary to calculate the spectral overlap function (*J*) from the experimental donor emission and acceptor absorption spectra, using Equation 4.3 below.

$$J = \int f(\lambda) d\lambda, f(\lambda) = F(\lambda)\varepsilon(\lambda)\,\lambda^4$$ **Equation 4.3**

where *F(λ)* is the donor emission spectrum normalized to unit area and $\varepsilon(\lambda)$ is the molar extinction spectrum of the acceptor (Figure 4.10). The calculated overlap function was used to estimate the corresponding Förster critical radius (R_o, the distance at which Φ_{ET} is 50%) in Equation 4.4:

$$R_{\mathrm{o}}(\mathrm{cm}) = (8.79 \times 10^{-25} \times \kappa^2 n^{-4} Q_d J)^{\frac{1}{6}}$$ **Equation 4.4.**

where $Q_d = k_r \times \tau_D$ (k_r = donor radiative decay rate constant), κ is an orientation factor and *n* is the refractive index. The overlap function is given by $f(\lambda) = F(\lambda)\varepsilon(\lambda)\lambda^4$ *with F(λ)*. Where $\varepsilon(\lambda)$ is the molar extinction of BPCF in CS_2 (Figure 4.10). The spectral overlap integral $J = \int f(\lambda) d(\lambda)$, was used to determine the energy transfer rate k_{ET}. The ET efficiency was

Table 4.1. Lifetime data of Zn_2(ZnTCPP) and **1**.

	B_1	τ_1, ns	B_2	τ_2, ns	B_3	τ_3, ns	$<\tau_{av}>$, ns
Zn_2(ZnTCPP)	0.23	0.32	0.76	1.29	0.00	4.20	1.07
1	0.69	0.31	0.31	1.01	0.00	7.08	0.54

determined to be 49.5% with a radiative decay rate constant of 9.18×10^8 s^{-1}. From the information obtained from Förster analysis, FRET could be responsible for the shortened

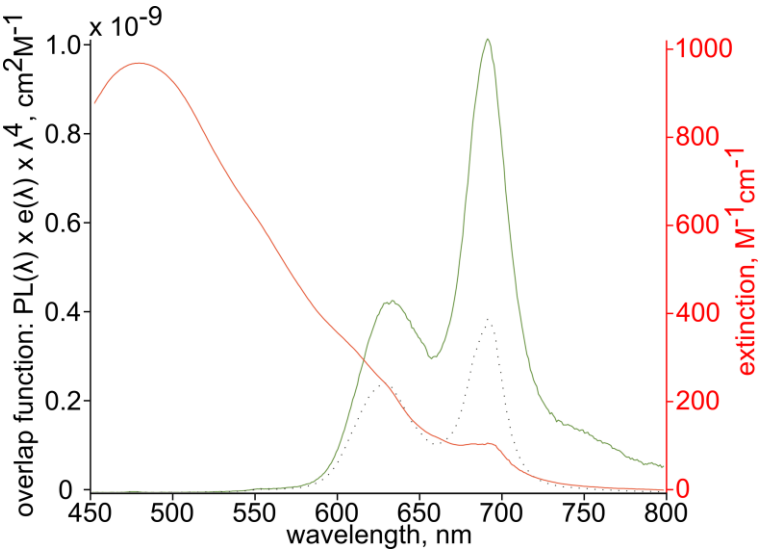

Figure 4.10. Förster analysis of **1**. BPCF acceptor absorption (red line) in CS_2, Zn_2(ZnTCPP) emission (green line), and the overlap function (dashed line, left vertical axis).

lifetime.[54,55] Förster analysis of **1** and calculation of the spectral overlap function, $J = 2.34 \times 10^{-15}$ cm^3 M^{-1}, between the donor and acceptor, revealed the critical radius, R_o to be 18.8 Å, which is beyond the distance approximated from the structural data.

The data and Förster analysis of **1** suggest that FRET is a possible mechanism for ET, however charge transfer (CT) could also be responsible for the observed change in the photophysical response. There is a large number of porphyrin-fullerene systems in which CT is reported.[56–66] Therefore, to elucidate the mechanism, we collaborated with Dr. Avdoshenko and Dr. Popov from Leibniz Institute for Solid State and Materials Research, Dresden, Germany to perform theoretical calculations on our system. The time-dependent density functional theory (TD-DFT) calculations revealed that the CT excitation of the truncated porphyrin-fullerene model (Figure 4.15, see the experimental) has a similar energy to that of C_{60}-based excitations, which indicates that CT is viable in **1**. The *computational details* subsection in the experimental section below contains detailed

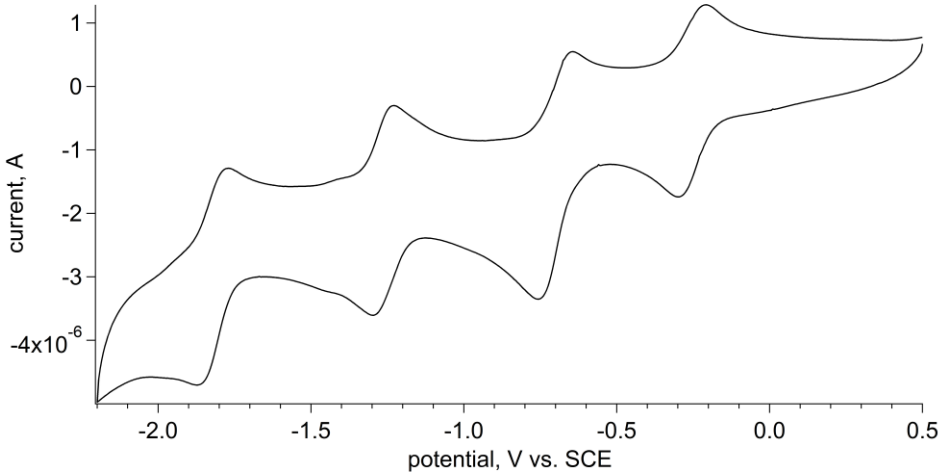

Figure 4.11. Cyclic voltammogram of BPCF in 0.1 *M* tetrabutylammonium hexaflourophosphate in DMF.

explanations of the data obtained from DFT calculations. In addition, cyclic voltammetry (CV) was performed on BPCF and **1**. The CV results for BPCF show four distinct reversible reduction and oxidation peaks of at $E_{1/2}$ = -0.29 V, $E_{1/2}$ = -0.75 V, $E_{1/2}$ = -1.30 V, and $E_{1/2}$ = -1.87 V (Figure 4.11). The cyclic voltammogram of **1** showed two of the four

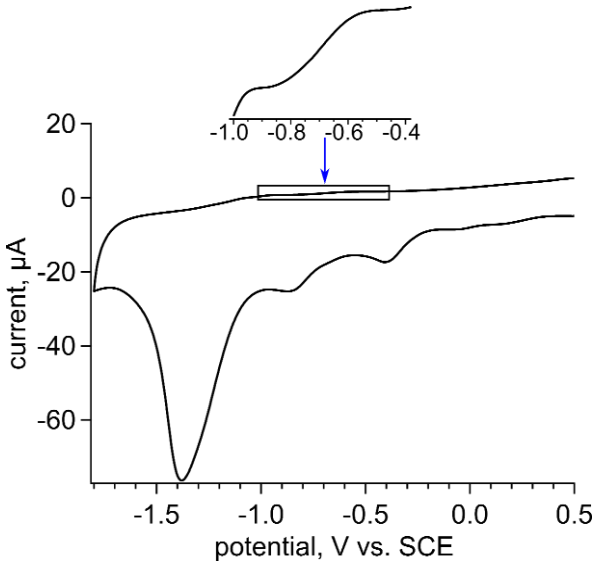

Figure 4.12. Cyclic voltammogram of **1** in 0.1 *M* tetrabutylammonium hexaflourophosphate in DMF, suspended with Nafion. The expansion shows the oxidation curves from immobilized BPCF.

reversible reduction peaks, E_p = -0.40 V and -0.87 V (Figure 4.12). However, there is a large irreversible reduction at E_p = -1.38 V, which could be attributed to the reduction of Zn in the MOF SBUs.

Conclusion

The fullerene-derivative, BPCF, was comprehensively characterized using single-crystal X-ray diffraction, ^{1}H and ^{13}C CP-MAS NMR, and IR spectroscopy. Two crystal structures of BPCF were obtained through metal coordination and their structures characterized by single-crystal X-ray and powder X-ray diffraction, as well as FT-IR spectroscopy. The exceptional mutual alignment of a porphyrin donor and fullerene acceptor, BPCF, in an extended three-dimensional, porous, crystalline, hybrid metal-organic scaffold was achieved. Photophysical studies were performed on the prepared fulleretic-porphyrin scaffold, and the energy and charge transfer properties elucidated using steady-state and time-resolved fluorescence spectroscopy. In conjunction with the photophysical studies, theoretical calculations were employed to demonstrate that both FRET and CT could occur in **1**. We have shown that MOFs can be used as a tool to mutually organize a large number of donor and acceptor molecules, which could significantly improve development of applications in the area of photovoltaic and molecular electronics

EXPERIMENTAL SECTION

Materials.

Malonyl dichloride (97%, Acros Organics), 4-pyridylcarbinol (98%, Matrix Scientific), tetrakis(4-carboxyphenyl)porphyrin (97%, Frontier Scientific), silver hexafluorophosphate (99%, Strem Chemicals Inc.), benzene (ACS grade, EMD

Chemicals), methanol (ACS grade, BDH), acetonitrile (HPLC grade, Fisher Scientific), benzonitrile (99%, Alfa Aesar), triethylamine (reagent grade, Fisher Scientific), anhydrous sodium sulfate (ACS grade, Amresco), acetone (ACS grade, Fisher Scientific), C_{60} (>99.5%, Solaris Chemicals), iodine (ACS grade, EMD Chemicals), toluene (ACS grade, Oakwood Chemicals), DBU (1,8-diazabicyclo[5.4.0]undec-7-ene, 98%, Acros Organics), chloroform (ACS grade, Macron Chemicals), $Zn(NO_3)_2 \cdot 6H_2O$ (technical grade, Ward's Science), ethanol (Decon Laboratories, Inc.), *N*,*N*-diethylformamide (>99%, TCI America), tetrahydrofuran (ACS grade, EMD Chemicals), dichloromethane (ACS grade, BDH), and DMSO-d_6 (Cambridge Isotopes) were used as received.

Synthesis.

The compounds bis(pyridin-4-ylmethyl)malonate (**L1**) and BPCF were prepared according to the reported procedure (Scheme 4.2).[48]

Synthesis of Bis(pyridin-4-ylmethyl) malonate (**L1**)

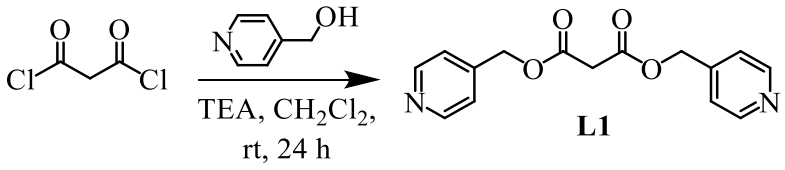

Scheme 4.3. Synthesis of **L1**.

To a stirred solution of pyridine-4-ylmethanol (7.7 g, 71 mmol) and trimethylamine (5 mL) in dichloromethane (100 mL), malonyl dichloride (5.0 g, 35 mmol) in dichloromethane (50 mL) was added dropwise using an addition funnel, and the mixture stirred overnight. The resulting residue was washed with water (3 × 75 mL), and the organic layer dried over Na_2SO_4, and then the solvent removed under reduced pressure. The brown oil was purified using column chromatography (silica, pure acetone), which after evaporation, resulted in

L1 (4.13 g) as a brown oil in 25% yield. ^{1}H NMR ($CDCl_3$, ppm): δ = 8.57 (4H, m), 7.36 (4H, m), 5.26 (4 H, s), 3.85 (2H, s).

Synthesis of bis(pyridin-4-ylmethyl)-3'H-cyclopropa-[1,2](C60-Ih)[5,6]fullerene-3',3'-dicarboxylate (BPCF)

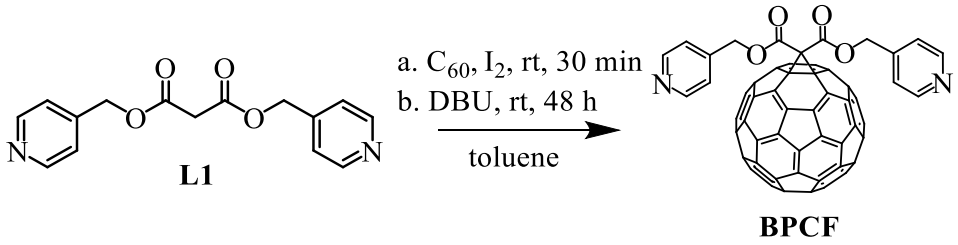

Scheme 4.4. Synthesis of BPCF.

Iodine (70 mg, 0.28 mmol) was added to a stirred solution of C_{60} (200 mg, 0.28 mmol) in toluene (400 mL), followed by the dropwise addition of **L1** (80 mg, 0.28 mmol). After the solution was stirred for 30 minutes, DBU (0.042 g, 0.28 mmol) was added dropwise and the solution was stirred for 2 days. The crude reaction mixture was evaporated, loaded onto a silica column, and flushed with toluene (200 mL) to remove unreacted C_{60}, and the product (brown band) was eluted with $CHCl_3$/acetone (7:3, v/v). The solvent was removed under reduced pressure, and BPCF was recovered as a dark brown powder (53 mg, 52.7 μmol) with a yield of 19%. ^{1}H NMR (DMSO, ppm) δ = 8.58-8.60 (4H, dd, *J* = 1.6 Hz, 4.4 Hz), 7.46-7.48 (4H, dd, *J* = 1.6 Hz, 4.4 Hz), 5.62 (4H, s). IR (neat, cm^{-1}): 3381, 3030, 2922, 2850, 2331, 2190, 2078, 1744, 1644, 1603, 1563, 1428, 1414, 1377, 1318, 1266, 1226, 1200, 1184, 1110, 1062, 993, 835, 796, 740, 703, 671 (Figure 4.7).

Single crystals of BPCF were obtained by slow evaporation of a concentrated toluene solution from a one-dram vial (Figure 4.2a). Single crystals of $C_{210}H_{84}Ag_2F_{12}N_4O_8P_2$

($Ag_2(BPCF)_2(PF_6)_2$) were obtained by layering a solution of BPCF in benzene over $AgPF_6$ in MeOH/benzonitrile in a 5 mm NMR tube (Figure 4.2b,e). Single crystals of $C_{180}H_{54}AgF_6N_4O_8$ ($Ag(BPCF)_2(PF_6)$) were obtained by layering a solution of BPCF in benzene over $AgPF_6$ in acetonitrile in a 5 mm NMR tube (Figure 4.2c,f). Single crystals of each compound were obtained over several days.

MOF Synthesis.

Zn_2(ZnTCPP) was prepared according to the reported literature procedure.[41]

Synthesis of $[Zn_2(ZnTCPP)(BPCF)_{0.23}\cdot(DEF)_{0.77}]\cdot 2EtOH\cdot 0.2H_2O$, $Zn_3C_{73.1}H_{47.6}N_{5.23}O_{11.9}$, **1**)

To synthesize **1**, $Zn(NO_3)_2\cdot 6H_2O$ (3.6 mg, 12 μmol), H_4TCPP (3.3 mg, 4.2 μmol), and BPCF (4.3 mg, 4.3 μmol) were sonicated in 0.85 mL DEF/EtOH (3:1), followed by filtration through a pasteur pipet, plugged with a glass microfiber filter, into a one-dram vial. The vial was placed into an isothermal oven and heated at 2 °C/minute and held at 80 °C for 16 h. After cooling to room temperature at 2 °C/minute, dark red crystals of **1** (1.9 mg, 1.4 μmol) were isolated in 33% yield. IR (neat, cm^{-1}): 2975, 1694, 1601, 1538, 1382, 1265, 1204, 1176, 1098, 1067, 994, 870, 824, 793, 773, 715 (Figure 4.7).

Fluorescence Spectroscopy.

Emission spectra were acquired on an Edinburgh FS5 fluorescence spectrometer equipped with a 150 W Continuous Wave Xenon Lamp source for excitation. Emission measurements on solid samples were collected on the powders of the appropriate materials placed inside a 0.5 mm quartz sample holder using the front-facing module.

An emission response was also obtained using an Ocean Optics JAZ spectrometer. In this case, a mounted high-power 365 nm LED (M365L2, Thorlabs) was used as an excitation source. Fluorescence lifetimes were measured using a Mini-τ lifetime spectrometer from Edinburgh Instruments equipped with a 365-nm picosecond-pulsed light-emitting diode (EPLED 365).

^{13}C CP-MAS NMR Spectroscopy.

Solid-state NMR spectra (^{13}C CP-MAS) were collected on a Bruker Avance III-HD 500 MHz spectrometer fitted with a 1.9 mm MAS probe. $^{13}C\{^{1}H\}$ CP-MAS NMR spectra (125.79 MHz) were collected at ambient temperature with a sample rotation rate of 20 kHz. For cross polarization, 1.5 ms contact time with linear ramping on the ^{1}H channel and 62.5 kHz field on the ^{13}C channel were used. ^{1}H dipolar decoupling was performed with SPINAL64 modulation and 147 kHz field strength. Free induction decays (512–2048 transients) were collected with a 27 ms acquisition time over a 300 ppm spectrum width with a relaxation delay of 2.0 s. Data was processed after appropriate shifting of the echoes using Bruker Topspin 3.2.

X-ray Crystal Structure Determination.

Single Crystal X-ray structure of $C_{75}H_{12}N_2O_4$ (BPCF)

Crystals of the compound grew as dark clusters composed of many intergrown flat needles. All larger crystals examined were multiply twinned. Eventually a single-domain specimen was located, which was reddish-brown in color. Single crystals are exceedingly thin, *ca*. 0.01 mm and the diffraction intensity is correspondingly weak. A scan time of 90 s per 0.5° frame was used for data collection. Despite this, no intensity was observed at higher angles. The dataset was truncated at $2\theta_{max}$ = 40.4° (d = 1.03 Å) at which point the

mean $I/\sigma(I)$ of the reflection data fell below 2.0. Data was collected at 100(2) K using a Bruker D8 QUEST diffractometer equipped with a PHOTON 100 CMOS area detector and an Incoatec microfocus source (Mo K_α radiation, λ = 0.71073 Å).[69] The raw area detector data frames were reduced and corrected for absorption effects using the SAINT+ and SADABS programs.[69] Final unit cell parameters were determined by least-squares refinement of 3792 reflections taken from the data set. The structure was solved by direct methods with SHELXT.[70] Subsequent difference Fourier calculations and full-matrix least-squares refinement against F^2 were performed with SHELXL-2014[70] using OLEX2.[71]

The compound crystallizes in the orthorhombic system. The pattern of systematic absences in the intensity data was uniquely consistent with the space group *Pbca*. The asymmetric unit consists of one $C_{75}H_{12}N_2O_4$ molecule and an essentially continuous one-dimensional ribbon of disordered electron density running along the crystallographic *b* axis and centered near *x*,*z* = ¼,¼ and symmetry-equivalent locations. Carbonyl oxygen O3 of the $C_{75}H_{12}N_2O_4$ molecule is disordered equally over two positions and were refined with half-occupancy. Their displacement parameters were held equal and additionally restrained to approximate a spherical shape (SHELX ISOR). A rigid-bond restraint (SHELX RIGU instruction) was applied to all atoms of the C_{60} cage, to prevent some displacement ellipsoids from becoming unrealistically flattened (three became 'non-positive definite') along the cage surface. All non-hydrogen atoms were refined with anisotropic displacement parameters. Hydrogen atoms were placed in geometrically idealized positions and included as riding atoms. The disordered interstitial species could not be modeled reasonably, and their contribution to the structure factors was accounted for during refinement using the Squeeze program.[72,73] Squeeze calculated the volume occupied

by these atoms to be 1382 $Å^3$, and they were calculated to contribute 332 electrons per unit cell to the scattering. This value corresponds to *ca*. 6.6 toluene molecules per cell, or 0.83 per $C_{72}H_{12}N_2O_4$ molecule. The final reported *F.W.*, *d*(calc) and *F*(000) refer to known species only. The largest residual electron density peak in the final difference map is 0.43 $e^-/Å^3$, located 1.53 Å from C2. The refinement data is given in Table 4.2.

Single crystal X-ray structure of $Ag_2(C_{75}H_{12}N_2O_4)_2(PF_6)_2 \cdot 10(C_6H_6)$ ($Ag_2(BPCF)_2(PF_6)_2$).

The compound crystallized as aggregations of thin brown parallelogram-shaped plates, with visually evident lamellar (plate-upon-plate) twinning. Numerous crystals were screened, most of which produced broad diffraction peaks with multiple maxima. The best crystal had no obvious peak splitting or pronounced streaking in the area detector images. Autoindexing routines gave the reported triclinic unit cell, but also suggested a *C*-centered monoclinic cell with a fair figure of merit (*a* = 13.2 Å, *b* = 67.2 Å, c = 10.0 Å, β = 130.8°, α, γ ~ 90.2°). The crystal was eventually determined to be a pseudo-merohedral twin emulating the apparent monoclinic symmetry in the latter stages of the refinement (see below). X-ray intensity data covering the full sphere of reciprocal space were collected at 100(2) K using a Bruker D8 QUEST diffractometer equipped with a PHOTON 100 CMOS area detector and an Incoatec microfocus source (Mo K_α radiation, λ = 0.71073 Å).[69] One phi and three omega scans of width 0.5° and a scan time of 50 s per image were collected at a crystal-to-detector distance of 60 mm. The raw area detector data frames were reduced and corrected for absorption effects using the SAINT+ and SADABS programs.[69] Final unit cell parameters were determined by least-squares refinement of 9962 reflections taken from the data set. The structure was solved by direct methods with SHELXS.[70] Subsequent

difference Fourier calculations and full-matrix least-squares refinement against F^2 were performed with SHELXL-2014[70] using OLEX2.[71]

The compound crystallizes in the triclinic system. The space group *P*-1 (No. 2) was confirmed by structure solution. The asymmetric unit consists of half of one $Ag_2(C_{75}H_{12}N_2O_4)_2^{2+}$ cation, which is located on a crystallographic inversion center, one PF_6^- anion and five benzene molecules of crystallization. All non-hydrogen atoms were refined with anisotropic displacement parameters (ADPs), however a free and unrestrained refinement resulted in 10 carbon atoms adopting physically senseless ("non-positive definite") displacement parameters. These atoms were located in the C_{60} cage and in the pyridyl ligand arms. To maintain physically reasonable ADPs, an enhanced rigid bond restraint (SHELX RIGU) was applied to the U_{ij} values of the ligand atoms. An additional spherical ISOR restraint was necessary for pyridyl ring atom C7. In total, 993 displacement parameter restraints were used. The reason for this is likely the moderate crystallinity and twinning of the available samples. Hydrogen atoms bonded to carbon were located in Fourier difference maps before being placed in geometrically idealized positions included as riding atoms with d(C-H) = 0.95 Å and U_{iso}(H) = 1.2U_{eq}(C) for arene hydrogen atoms and d(C-H) = 0.99 Å and U_{iso}(H) = 1.2U_{eq}(C) for methylene hydrogens. The pseudo-merohedral twin law emulating the apparent monoclinic symmetry (R_{int}, monoclinic C = 0.18) was derived using the TwinRotMat program in PLATON.[73] The twin law is (-1 0 0 / 0 -1 0 / 1 1 1), corresponding to a 180° rotation perpendicular to the (001) plane. The refined major twin component volume fraction refined to 0.623(2). The largest residual

electron density peak in the final difference map is 1.61 e-/Å^3, located 1.09 Å from Ag1, and is not chemically significant.

Single-crystal X-ray structure of Ag($C_{75}H_{12}N_2O_4)_2$](PF_6)·5(C_6H_6) (Ag(BPCF)$_2$(PF_6)).
X-ray intensity data from a dark brown tablet were collected at 100(2) K using a Bruker D8 QUEST diffractometer equipped with a PHOTON 100 CMOS area detector and an Incoatec 'high-brilliance' microfocus source (Mo K_α radiation, λ = 0.71073 Å).[69] The raw area detector data frames were reduced and corrected for absorption effects using the SAINT+ and SADABS programs.[69] Final unit cell parameters were determined by least-squares refinement of 9354 reflections taken from the dataset. The structure was solved by direct methods with SHELXS.[70] Subsequent difference Fourier calculations and full-matrix least-squares refinement against F^2 were performed with SHELXL-2014[70] using OLEX2.[71]

The compound crystallizes in the monoclinic system. The pattern of systematic absences in the intensity data was consistent with the space group $P2_1/c$, which was confirmed by structure solution. The asymmetric unit consists of one silver atom, one PF_6^- anion, two independent $C_{75}H_{12}N_2O_4$ ligands, four complete benzene molecules and half each of two additional benzene molecules located on crystallographic inversion centers. Refinement precision was limited by disorder of one C_{60} cage and three -$CC(O)OCH_2C_5H_4N$ arms from the two independent $C_{75}H_{12}N_2O_4$ ligands. Further, a pattern of small residual electron density peaks (< 0.5 e-/Å^3) among atoms of the other C_{60} cage (C101–C160) suggests minor disorder of this cage also, but a stable disorder model could not be attained because of the apparent low disorder faction (trial occupancies << 10%). The disordered C_{60} cage was refined with two independent orientations, C201–C260 and C301–C360. Both were restrained to be geometrically similar to the ordered C_{60} ball

(C101–C160) using SHELX SAME instructions. The disorder extends into both ligand arms attached to this cage. These were also modeled with two orientations (C16–C17, O5 A/B and C24–C30, O7, O8, N2 A/B). The major disorder fraction of this ligand refined to 0.638(3). Disorder of ligand arm C9–C15, N2, O3, O4 was also modeled with two components A/B with a major group occupancy of 0.626(6). Appropriate 1,2- and 1,3-distance restraints were applied to atom pairs of the ligand arms. Displacement parameters for nearly superimposed atoms were held equal. Most non-hydrogen atoms were refined with anisotropic displacement parameters, the exception being disordered benzene molecules with fractional occupancies ≤ 0.5, which were refined isotropically. Enhanced rigid-bond (RIGU) restraints were applied to the ligand arm and disordered C_{60} atoms (C201–C260 and C301–C360) atoms to maintain physically reasonable anisotropic displacement parameters. Benzene molecules C421–C426 and C451-C453 were restrained to adopt a similar geometry as the best-behaved benzene C401–C406. Disordered and partially occupied benzene molecules C441-C446 and C421-C426/C521-C526 were refined as rigid hexagons. Hydrogen atoms placed in geometrically idealized positions included as riding atoms with d(C-H) = 0.95 Å and U_{iso}(H) = 1.2U_{eq}(C) for benzene and pyridyl ring hydrogen atoms and d(C-H) = 0.99 Å and U_{iso}(H) = 1.2U_{eq}(C) for methylene hydrogens. The largest residual electron density peak in the final difference map is 0.73 e-/Å^3, located 1.43 Å from C453. This suggests further minor disorder of this group, though trial modeling efforts were not stable and did not improve the refinement.

Computational Details.

DFT calculations were employed to elucidate the structural and electronic properties at the PBE/DZVP level of theory.[74] The interlayer distance of **1** was predicted

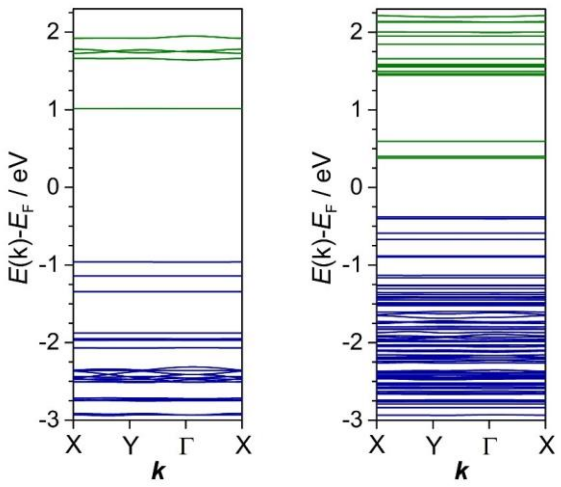

Figure 4.13. Band structure calculations of Zn_2(ZnTCPP) (*left*) and **1** (*right*), which also shows flat lines indicating a localized system. Green and blue lines are conductance and valence bands, respectively.

using Γ-point optimization (CP2K code)[75–77] assuming a tetragonal lattice, and was predicted to be 19.4 Å, which corresponds nicely with PXRD data. The GPAW code[78,79] used to calculate the band structure of optimized **1** shows that the charge transfer bands near the Fermi level are flat (Figure 4.13), which indicates localized nature of the frontier orbitals (shown in Figure 4.15). Moreover, the calculated band structure of **1** is significantly more populated than Zn_2(ZnTCPP) (Figure 4.14). This localized nature of the frontier orbitals allows the program to perform calculations on the molecular ZnTCPP-BPCF dyad, as opposed to an extended network, which can be very time and computationally demanding. The calculations were performed of the exciton migration for the dyad, where BPCF was coordinated through the pyridyl arm to the Zn metal in the ZnTCPP porphyrin center. We determined that the charge-transfer excitation of the truncated model displayed similar energy to that of C_{60}-based systems (Figure 4.14d) when TD-DFT calculations were performed at the CAM-B3LYP/DZP level of theory (Gamess-

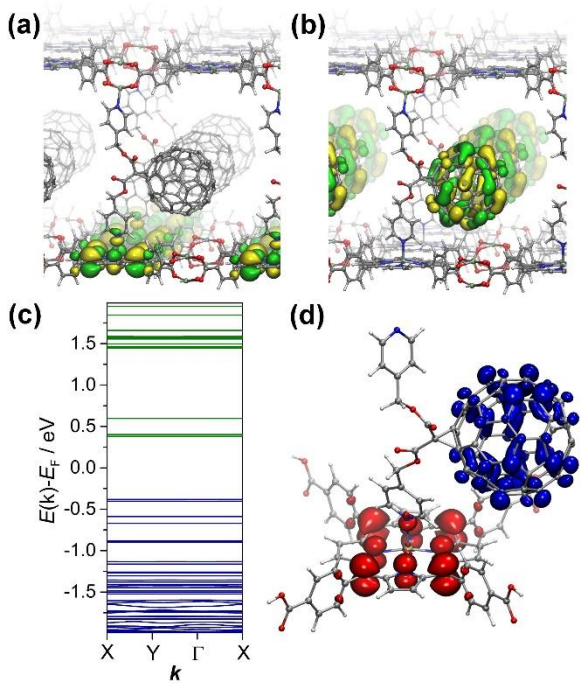

Figure 4.14. Predicted HOMO *(a)* and LUMO *(b)* of **1** at the Γ-point optimization. The band structure and difference density map for the charge-transfer excitation of the molecular dyad are shown in *(c)* and *(d)*, respectively.

US code).[80,81] Figure 4.15 shows a frontier MO diagram of the BPCF-ZnTCPP dyad. HOMO and HOMO-1 of the model are localized on the ZnTCPP moiety and show two-fold degenerate HOMO of ZnTCPP. At lower energies follow 5 C_{60}- localized MOs resembling the 5-fold degenerate HOMO of C_{60}. LUMO, LUMO+1, and LUMO+2 of BPCF–ZnTCPP resemble the 3-fold degenerate LUMO of C_{60}, whereas LUMO+3 and LUMO+4 are similar to the 2-fold degenerate LUMO of ZnTCPP. In this model, three types of excitations may have comparable energies: excitations in the ZnTCPP moiety (denoted as ZnTCPP*), excitations in the BPCF moiety (denoted as BPCF*), and charge-transfer excitations between ZnTCPP-localized HOMOs and C_{60}-based LUMOs (denoted

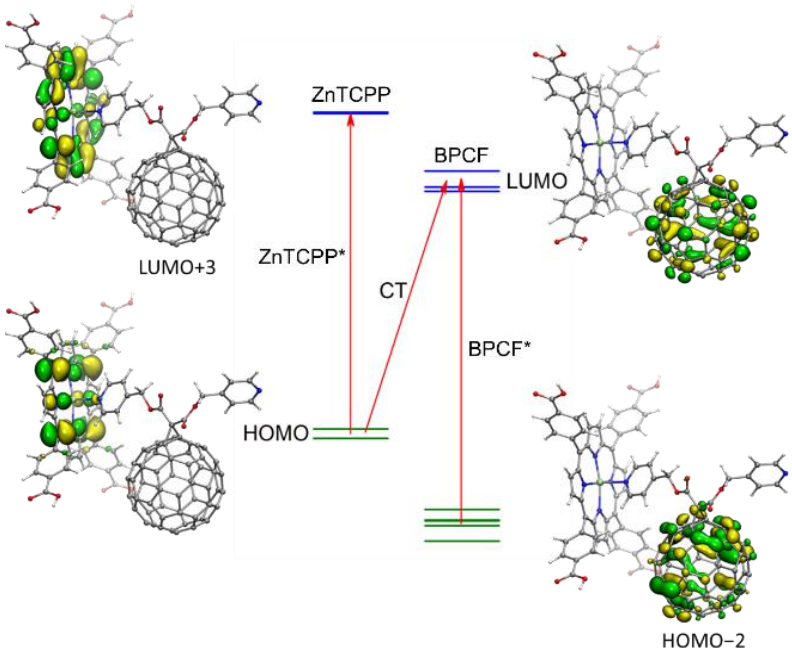

Figure 4.15. Energies of the frontier molecular orbitals of the BPCF-TCPP molecular dyad.

as CT). Difference densities for three types of excitations obtained in TD-DFT calculations are shown in Figure 4.16.

Optimization of the molecular and periodic structures was performed at PBE/DZVP level of theory using CP2K code[75–77,82] with Γ-point approximation for solid state. Single point band structure calculations were performed at the PBE/DZ level of theory with the GPAW code.[78,79,82] The electron density was converged with k-mesh 4×4×1 for Zn_2(ZnTCPP) and 2×2×1 for **1**. The Harris calculation for the bands was performed with a resolution of 100 grid-points along X-Y-Γ-X lines, implying the orthorhombic cell with *a* = *b* parameters. Time-dependent DFT calculations were performed using long-range corrected CAM-B3LYP functional and DZVP-quality basis set implemented in the GAMESS-US code.[80,81] The CAM-B3LYP is known to have much better reliability in

prediction of CT excitations. In TD-DFT calculations, only a fragment comprising BPCF linked to ZnTCPP was used (Figure 4.14).

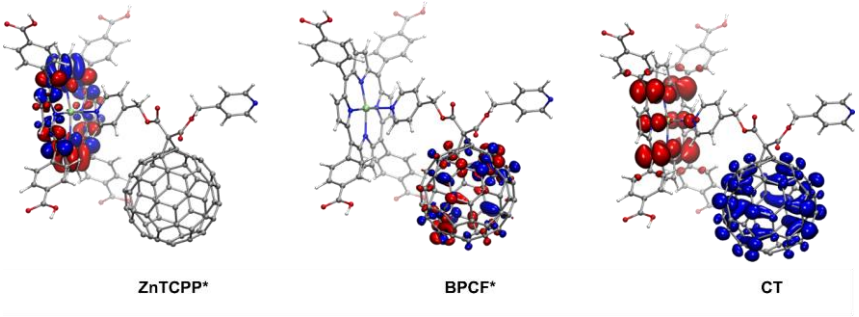

Figure 4.16. Difference density for three types of excitations in the BPCF-ZnTCPP dyad.

Other Physical Measurements.

All FT-IR spectra were obtained on a Perkin-Elmer Spectrum 100. The NMR spectra were collected on Bruker Avance III-HD 300 and Bruker Avance III 400 MHz NMR spectrometers. The ^{13}C and ^{1}H NMR spectra were referenced to natural abundance ^{13}C peaks and residual ^{1}H peaks of deuterated solvents, respectively. Powder X-ray diffraction patterns were recorded on a Rigaku Miniflex II diffractometer with accelerating voltage and current of 30 kV and 15 mA, respectively. Thermogravimetric analysis was performed on an SDT Q600 Thermogravimetric Analyzer using an alumina boat as a sample holder. The Waters QTOF-I quadrupole time-of-flight mass spectrometer was used to record the mass spectra of the prepared compounds. Diffuse reflectance spectra were collected on a Perkin Elmer Lambda 45 UV-vis spectrometer referenced to Spectralon®.

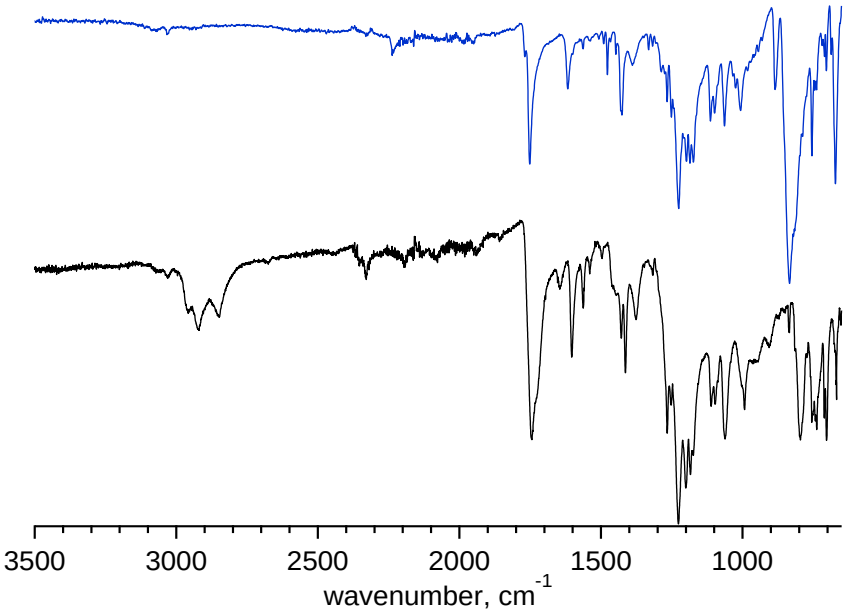

Figure 4.17. The FT-IR spectra of BPCF (black) and the $Ag_2(BPCF)_2(PF_6)_2$ molecular complex (blue).

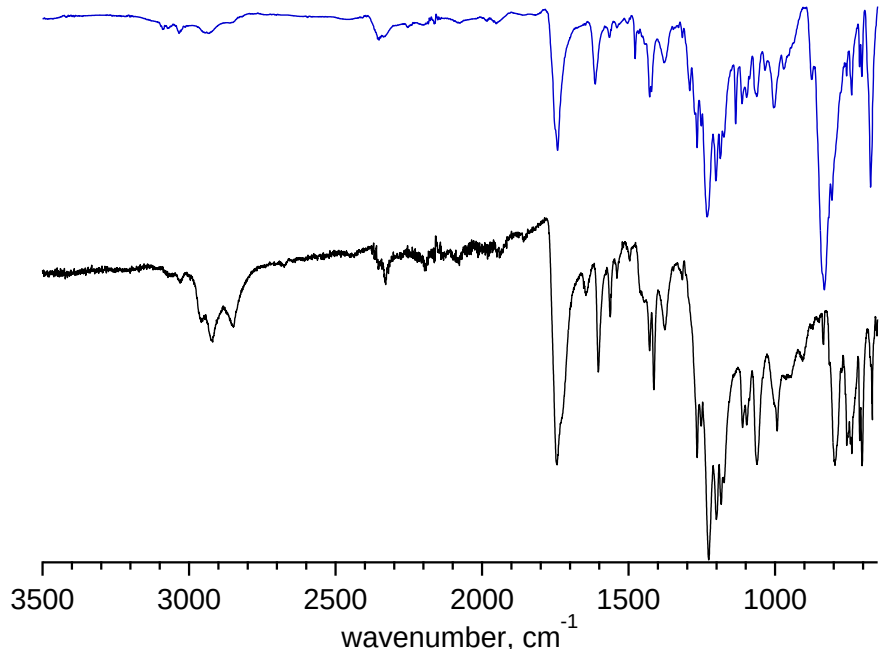

Figure 4.18. The FT-IR spectra of BPCF (black) and the $Ag(BPCF)_2(PF_6)_2$ molecular complex (blue).

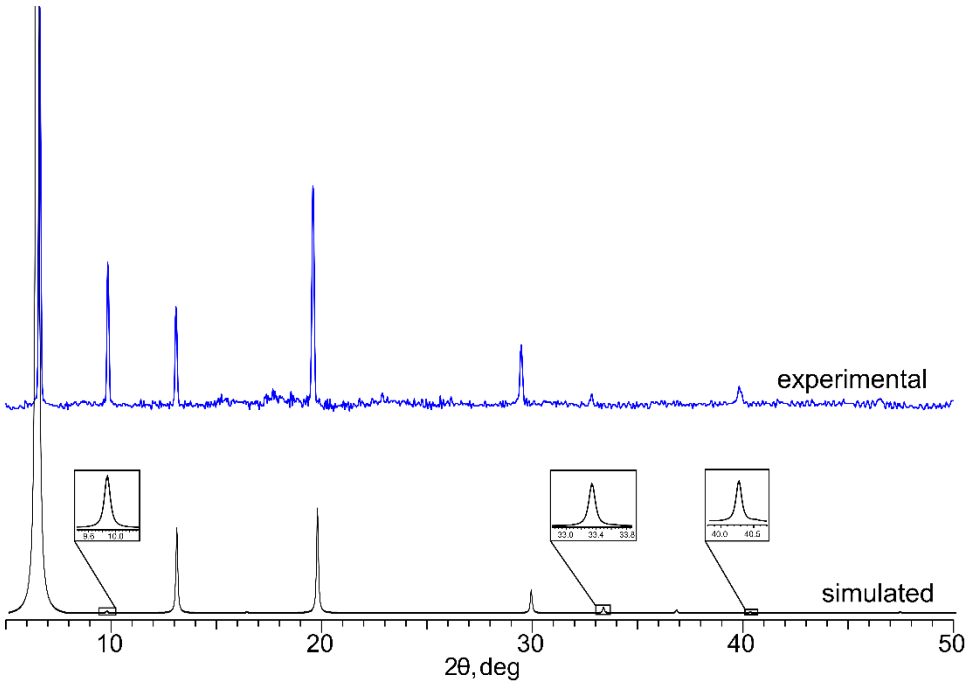

Figure 4.19. The simulated (black) and experimental (blue) PXRD patterns of $Ag(BPCF)_2(PF_6)$.

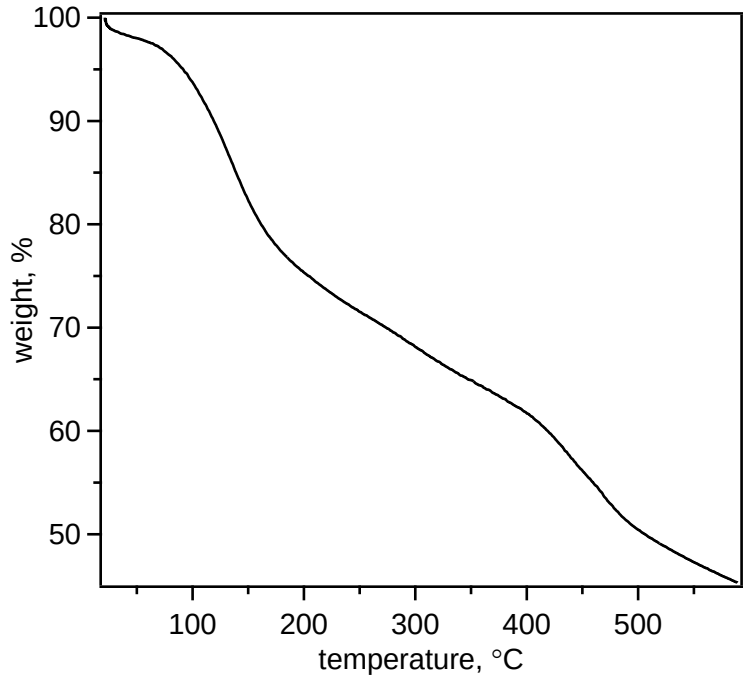

Figure 4.20. Thermogravimetric analysis plot of as-synthesized **1**.

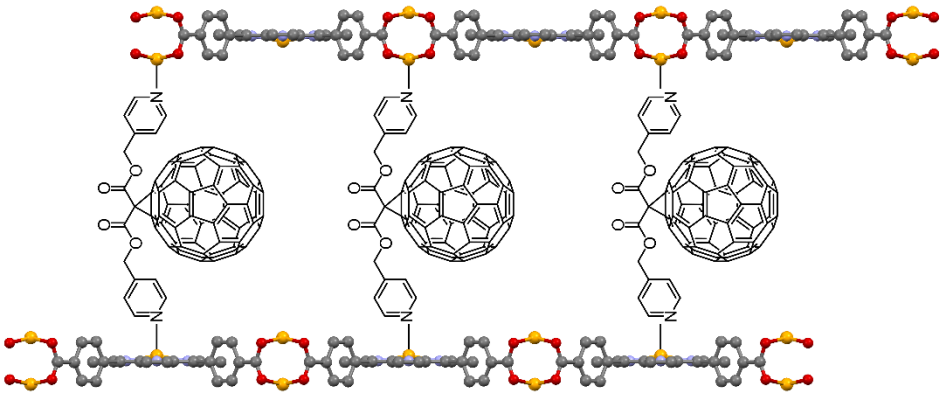

Figure 4.21. A schematic representation of BPCF installation between two-dimensional Zn_2(ZnTCPP) layers.

Table 4.2. X-ray structure refinement data for BPCF,[a] $Ag_2(BPCF)_2(PF_6)_2$,[a] and $Ag_2(BPCF)_2(PF_6)_2$.[a]

compound	**BPCF**	**$Ag_2(BPCF)_2(PF_6)_2$**	**$Ag(C_{75}H_{12}N_2O_4)_2(PF_6)$**
formula	$C_{75}H_{12}N_2O_4$	$C_{210}H_{84}Ag_2F_{12}N_4O_8P_2$	$C_{180}H_{54}AgF_6N_4O_8P$
FW	1004.87	3296.49	2653.11
T, K	100(2)	100(2)	100(2)
crystal system	orthorhombic	triclinic	monoclinic
space group	Pbca	P-1	$P2_1/c$
Z	8	1	4
a, Å	20.741(2)	9.9693(17)	27.5312(16)
b, Å	9.8500(11)	10.037(17)	20.3038(11)
c, Å	42.484(4)	34.229(6)	20.0238(12)
α, °	90	97.239(4)	90
β, °	90	96.966(4)	102.7850(15)
γ, °	90	98.030(4)	90
V, $Å^3$	8679.6(16)	3330.7(10)	10915.6(11)
d_{calc}, g/cm^3	1.538	1.643	1.614
μ, mm^{-1}	0.096	0.413	0.290
F(000)	4064.0	1668.0	5367.0
crystal size/mm^3	0.26 × 0.04 × 0.01	0.44 × 0.12 × 0.02	0.2 × 0.2 × 0.05
theta range	4.308 to 40.36	4.482 to 50.146	4.172 to 50.192
index ranges	$-20 \le h \le 20$ $-9 \le k \le 9$ $-41 \le l \le 41$	$-11 \le h \le 11$ $-11 \le k \le 11$ $-40 \le l \le 40$	$-32 \le h \le 32$ $-24 \le k \le 24$ $-23 \le l \le 23$
refl. collected	59842	44251	259533
data/restraints/parameters	4155/825/734	11494/993/1073	19385/3030/2414
GOF on F^2	1.086	1.041	1.115
Largest peak/hole, $e/Å^3$	0.43/–0.32	1.61/-1.64	0.72/-1.23
R_1 (wR_2), %, $[I \ge 2sigma(I)]$[b]	7.96 (19.10)	8.62 (19.18)	7.13 (14.14)

[a] Mo-K_α (λ = 0.71073 Å) radiation
[b] $R_1 = \Sigma||F_o| - |F_c||/ \Sigma |F_o|$, $wR_2 = \{\Sigma [w(F_o^2-F_c^2)^2]/ \Sigma [w(F_o^2)^2]\}^{1/2}$

REFERENCES

(1) Cravino, A.; Sariciftci, N. S. *Nat. Mater.* **2003**, *2* (6), 360–361.
(2) Seok, J.; Shin, T. J.; Park, S.; Cho, C.; Lee, J.-Y.; Yeol Ryu, D.; Kim, M. H.; Kim, K. *Sci. Rep.* **2015**, *5* (Dcm), 8373.
(3) Sukegawa, J.; Schubert, C.; Zhu, X.; Tsuji, H.; Guldi, D. M.; Nakamura, E. *Nat. Chem.* **2014**, *6* (10), 899–905.
(4) Li, C.-Z.; Yip, H.-L.; Jen, A. K.-Y. *J. Mater. Chem.* **2012**, *22* (10), 4161–4177.
(5) Nakanishi, R.; Nogimura, A.; Eguchi, R.; Kanai, K. *Org. Electron.* **2014**, *15* (11), 2912–2921.
(6) Graham, K. R.; Cabanetos, C.; Jahnke, J. P.; Idso, M. N.; El Labban, A.; Ngongang Ndjawa, G. O.; Heumueller, T.; Vandewal, K.; Salleo, A.; Chmelka, B. F.; Amassian, A.; Beaujuge, P. M.; McGehee, M. D. *J. Am. Chem. Soc.* **2014**, *136* (27), 9608–9618.
(7) Deibel, C.; Dyakonov, V. *Rep. Prog. Phys.* **2010**, *73* (2010), 96401.
(8) Popescu, M. *Fullerene based Organic Solar Cells*; 2008.
(9) Peng, P.; Li, F.-F.; Neti, V. S. P. K.; Metta-Magana, A. J.; Echegoyen, L. *Angew. Chemie* **2014**, *126* (1), 164–167.
(10) Fan, J.; Wang, Y.; Blake, A. J.; Wilson, C.; Davies, E. S.; Khlobystov, A. N.; Schröder, M. *Angew. Chemie* **2007**, *119* (42), 8159–8162.
(11) Pierrat, P.; Réthoré, C.; Muller, T.; Bräse, S. *Synlett* **2008**, *2008* (11), 1706–1710.
(12) Schwenninger, R.; Müller, T.; Kräutler, B. *J. Am. Chem. Soc.* **1997**, *119* (39), 9317–9318.
(13) Hirsch, A.; Lamparth, I.; Groesser, T.; Karfunkel, H. R. *J. Am. Chem. Soc.* **1994**, *116* (20), 9385–9386.
(14) Leong, K.; Foster, M.; Wong, B.; Spoerker, E.; Van Gough, D.; Deaton, J.; Allendorf, M. *J. Mater. Chem. A* **2014**, *2* (10), 3389–3398.
(15) Constable, E. C.; Zhang, G.; Housecroft, C. E.; Zampese, J. A. *CrystEngComm* **2012**, *14* (5), 1770–1774.
(16) Chae, H. K.; Siberio-Pérez, D. Y.; Kim, J.; Go, Y.; Eddaoudi, M.; Matzger, A. J.; O'Keeffe, M.; Yaghi, O. M. *Nature* **2004**, *427* (6974), 523–527.
(17) Boyd, P. D. W.; Hodgson, M. C.; Rickard, C. E. F.; Oliver, A. G.; Chaker, L.; Brothers, P. J.; Bolskar, R. D.; Tham, F. S.; Reed, C. A. *J. Am. Chem. Soc.* **1999**, *121* (45), 10487–10495.
(18) Olmstead, M. M.; Costa, D. A.; Maitra, K.; Noll, B. C.; Phillips, S. L.; Van Calcar, P. M.; Balch, A. L. *J. Am. Chem. Soc.* **1999**, *121* (30), 7090–7097.
(19) Kennedy, R. D.; Ayzner, A. L.; Wanger, D. D.; Day, C. T.; Halim, M.; Khan, S. I.; Tolbert, S. H.; Schwartz, B. J.; Rubin, Y. *J. Am. Chem. Soc.* **2008**, *130* (51), 17290–17292.
(20) Fagan, P. J.; Calabrese, J. C.; Malone, B. *J. Am. Chem. Soc.* **1991**, *113* (24), 9408–9409.
(21) Kc, C. B.; Lim, G. N.; D'Souza, F. *Nanoscale* **2015**, *7* (15), 6813–6826.
(22) Peng, P.; Li, F.-F.; Bowles, F. L.; Neti, V. S. P. K.; J Metta-Magana, A.; Olmstead, M. M.; Balch, A. L.; Echegoyen, L. *Chem. Commun.* **2013**, *49* (31), 3209–3211.

(23) Habicher, T.; Nierengarten, J.-F.; Gramlich, V.; Diederich, F. *Angew. Chemie Int. Ed.* **1998**, *37* (13–14), 1916–1919.
(24) Wang, Z.; Cohen, S. M. *J. Am. Chem. Soc.* **2007**, *129* (41), 12368–12369.
(25) Ma, S.; Sun, D.; Simmons, J. M.; Collier, C. D.; Yuan, D.; Zhou, H.-C. *J. Am. Chem. Soc.* **2008**, *130* (3), 1012–1016.
(26) Farha, O. K.; Yazaydın, A. Ö.; Eryazici, I.; Malliakas, C. D.; Hauser, B. G.; Kanatzidis, M. G.; Nguyen, S. T.; Snurr, R. Q.; Hupp, J. T. *Nat. Chem.* **2010**, *2* (11), 944–948.
(27) Colson, J. W.; Woll, A. R.; Mukherjee, A.; Levendorf, M. P.; Spitler, E. L.; Shields, V. B.; Spencer, M. G.; Park, J.; Dichtel, W. R. *Science* **2011**, *332* (6026), 228–231.
(28) Wu, C. De; Hu, A.; Zhang, L.; Lin, W. *J. Am. Chem. Soc.* **2005**, *127* (25), 8940–8941.
(29) Kumar, D. K.; Filatov, A. S.; Napier, M.; Sun, J.; Dikarev, E. V; Petrukhina, M. A. *Inorg. Chem.* **2012**, *51* (8), 4855–4861.
(30) Williams, D. E.; Rietman, J. A.; Maier, J. M.; Tan, R.; Greytak, A. B.; Smith, M. D.; Krause, J. A.; Shustova, N. B. *J. Am. Chem. Soc.* **2014**, *136* (34), 11886–11889.
(31) Dolgopolova, E. A.; Williams, D. E.; Greytak, A. B.; Rice, A. M.; Smith, M. D.; Krause, J. A.; Shustova, N. B. *Angew. Chemie Int. Ed.* **2015**, *54* (46), 13639–13643.
(32) Williams, D. E.; Dolgopolova, E. A.; Pellechia, P. J.; Palukoshka, A.; Wilson, T. J.; Tan, R.; Maier, J. M.; Greytak, A. B.; Smith, M. D.; Krause, J. A.; Shustova, N. B. *J. Am. Chem. Soc.* **2015**, *137* (6), 2223–2226.
(33) Fellows, W. B.; Rice, A. M.; Williams, D. E.; Dolgopolova, E. A.; Vannucci, A. K.; Pellechia, P. J.; Smith, M. D.; Krause, J. A.; Shustova, N. B. *Angew. Chem. Int. Ed.* **2016**, *55* (6), 2195–2199.
(34) Williams, D. E.; Shustova, N. B. *Chem. - A Eur. J.* **2015**, *21* (44), 15474–15479.
(35) Bon, V.; Kavoosi, N.; Senkovska, I.; Müller, P.; Schaber, J.; Wallacher, D.; Többens, D. M.; Mueller, U.; Kaskel, S. *Dalt. Trans.* **2016**, *45* (10), 4407–4415.
(36) Zhai, Q.-G.; Bu, X.; Mao, C.; Zhao, X.; Feng, P. *J. Am. Chem. Soc.* **2016**, *138*, 2524–2527.
(37) Liddell, P. A.; Kodis, G.; Andre, J.; Garza, L. De; Bandyopadhyay, S.; Mitchell, R. H.; Moore, T. A.; Moore, A. L.; Gust, D.; Vw, C. **2004**, No. 22, 4803–4811.
(38) Szaciłowski, K. *Chem. Rev.* **2008**, *108* (9), 3481–3548.
(39) Zeng, Y.; Fu, Z.; Chen, H.; Liu, C.; Liao, S.; Dai, J. *Chem. Commun.* **2012**, *48* (65), 8114.
(40) Mishra, A.; Ma, C. Q.; Bäuerle, P. *Chem. Rev.* **2009**, *109* (3), 1141–1176.
(41) Choi, E.-Y.; Wray, C. A.; Hu, C.; Choe, W. *CrystEngComm* **2009**, *11* (4), 553–555.
(42) Barron, P. M.; Wray, C. a; Hu, C.; Guo, Z.; Choe, W. *Inorg. Chem.* **2010**, *49* (22), 10217–10219.
(43) Verduzco, J. M.; Chung, H.; Hu, C.; Choe, W. *Inorg. Chem.* **2009**, *48* (19), 9060–9062.
(44) Burnett, B. J.; Choe, W. *CrystEngComm* **2012**, *14* (19), 6129.

(45) Andrzej Sygula, *,†; Frank R. Fronczek, ‡; Renata Sygula, †; Peter W. Rabideau, † and; Olmstead§, M. M. **2007**.
(46) Sawamura, M.; Kawai, K.; Matsuo, Y.; Kanie, K.; Kato, T.; Nakamura, E. *Nature* **2002**, *419* (6908), 702–705.
(47) Sun, D.; Tham, F. S.; Reed, C. A.; Boyd, P. D. W. *Proc. Natl. Acad. Sci. U. S. A.* **2002**, *99* (8), 5088–5092.
(48) Fan, J.; Wang, Y.; Blake, A. J.; Wilson, C.; Davies, E. S.; Khlobystov, A. N.; Schröder, M. *Angew. Chem. Int. Ed.* **2007**, *46* (42), 8013–8016.
(49) Diederich, F.; Ettl, R.; Rubin, Y.; Whetten, R. L.; Beck, R.; Alvarez, M.; Anz, S.; Sensharma, D.; Wudl, F.; Khemani, K. C.; Koch, A. *Science (80-.).* **1991**, *252* (5005), 548–551.
(50) Kikuchi, K.; Nakahara, N.; Wakabayashi, T.; Suzuki, S.; Shiromaru, H.; Miyake, Y.; Saito, K.; Ikemoto, I.; Kainosho, M.; Achiba, Y. *Nature* **1992**, *357* (6374), 142–145.
(51) Chung, H.; Barron, P. M.; Novotny, R. W.; Son, H.-T.; Hu, C.; Choe, W. *Cryst. Growth Des.* **2009**, *9* (7), 3327–3332.
(52) Burnett, B. J.; Barron, P. M.; Choe, W. *CrystEngComm* **2012**, *14* (11), 3839.
(53) Choi, E.-Y.; Barron, P. M.; Novotny, R. W.; Son, H.-T.; Hu, C.; Choe, W. *Inorg. Chem.* **2009**, *48* (2), 426–428.
(54) So, M. C. *Chem. Commun.* **2015**, *51*, 3501–3510.
(55) Zhang, T.; Lin, W. *Chem. Soc. Rev.* **2014**, 5982–5993.
(56) Kuciauskas, D.; Lin, S.; Seely, G. R.; Moore, A. L.; Moore, T. A.; Gust, D.; Drovetskaya, T.; Reed, C. A.; Boyd, P. D. W. *J. Phys. Chem.* **1996**, *100* (39), 15926–15932.
(57) Ciammaichella, A.; Dral, P. O.; Clark, T.; Tagliatesta, P.; Sekita, M.; Guldi, D. M. *Chemistry* **2012**, *18* (44), 14008–14016.
(58) D'Souza, F.; Chitta, R.; Gadde, S.; Zandler, M. E.; McCarty, A. L.; Sandanayaka, A. S. D.; Araki, Y.; Ito, O. *J. Phys. Chem. A* **2006**, *110* (13), 4338–4347.
(59) Krokos, E.; Spänig, F.; Ruppert, M.; Hirsch, A.; Guldi, D. M. *Chemistry* **2012**, *18* (5), 1328–1341.
(60) D'Souza, F.; Ito, O. *Coord. Chem. Rev.* **2005**, *249* (13–14), 1410–1422.
(61) Basurto, L.; Amerikheirabadi, F.; Zope, R.; Baruah, T. *Phys. Chem. Chem. Phys.* **2015**, *17* (8), 5832–5839.
(62) Vail, S. A.; Krawczuk, P. J.; Guldi, D. M.; Palkar, A.; Echegoyen, L.; Tomé, J. P. C.; Fazio, M. A.; Schuster, D. I. *Chemistry* **2005**, *11* (11), 3375–3388.
(63) Imahori, H.; Tkachenko, N. V.; Vehmanen, V.; Tamaki, K.; Lemmetyinen, H.; Sakata, Y.; Fukuzumi, S. *J. Phys. Chem. A* **2001**, *105* (10), 1750–1756.
(64) Imahori, H. *Org. Biomol. Chem.* **2004**, *2* (10), 1425–1433.
(65) Das, S. K.; Song, B.; Mahler, A.; Nesterov, V. N.; Wilson, A. K.; Ito, O.; D'Souza, F. *J. Phys. Chem. C* **2014**, *118* (8), 3994–4006.
(66) Scholes, G. D.; Fleming, G. R.; Olaya-Castro, A.; van Grondelle, R. *Nat. Chem.* **2011**, *3* (10), 763–774.
(67) Bendikov, M.; Wudl, F.; Perepichka, D. F. *Tetrathiafulvalenes, oligoacenenes, and their buckminsterfullerene derivatives: The brick and mortar of organic electronics*; 2004; Vol. 104.

(68) Fellows, W. B.; Rice, A. M.; Williams, D. E.; Dolgopolova, E. A.; Vannucci, A. K.; Pellechia, P. J.; Smith, M. D.; Krause, J. A.; Shustova, N. B. *Angew. Chemie Int. Ed.* **2016**, *55* (6), 2195–2199.
(69) APEX2 Version 2014.9-0, SAINT+ Version 8.34A and SADABS Version 2014/4. Bruker Analytical X-ray Systems, Inc., Madison, Wisconsin, USA, 2014. .
(70) Sheldrick, G. M. *Acta Crystallogr. A.* **2008**, *64* (Pt 1), 112–122.
(71) Oleg V. Dolomanov, Luc J. Bourhis, Richard J. Gildea, J. A. K. H. and; Puschmann, H. *J. Appl. Crystallogr.* **2009**, *42*, 339–341.
(72) van der Sluis, P.; Spek, A. L. *Acta Crystallogr. Sect. A Found. Crystallogr.* **1990**, *46* (3), 194–201.
(73) Spek, A. L. *J. Appl. Crystallogr.* **2003**, *36* (1), 7–13.
(74) Perdew, J. P.; Ernzerhof, M.; Burke, K. *J. Chem. Phys.* **1996**, *105* (22), 9982–9985.
(75) Hutter, J., Iannuzzi, M., Schiffmann, F., VandeVondele, J. *Wiley Interdiscip. Rev. Comput. Mol. Sci* **2014**, *4*, 15–25.
(76) Hartwigsen, C., Goedecker, S., Hutter, J. *Phys. Rev. B* **1998**, *58*, 3641–3662.
(77) VandeVondele, J.; Hutter, J. *J. Chem. Phys.* **2007**, *127* (11), 114105.
(78) Bahn, S. R.; Jacobsen, K. W. *Comput. Sci. Eng.* **2002**, *4* (3), 56–66.
(79) Larsen, A. H.; Vanin, M.; Mortensen, J. J.; Thygesen, K. S.; Jacobsen, K. W. *Phys. Rev. B* **2009**, *80* (19), 195112.
(80) Yanai, T.; Tew, D. P.; Handy, N. C. *Chem. Phys. Lett.* **2004**, *393* (1–3), 51–57.
(81) Schmidt, M. W.; Baldridge, K. K.; Boatz, J. A.; Elbert, S. T.; Gordon, M. S.; Jensen, J. H.; Koseki, S.; Matsunaga, N.; Nguyen, K. A.; Su, S.; Windus, T. L.; Dupuis, M.; Montgomery, J. A. *J. Comput. Chem.* **1993**, *14* (11), 1347–1363.
(82) Perdew, J. P.; Burke, K.; Ernzerhof, M. *Phys. Rev. Lett.* **1996**, *77* (18), 3865–3868.

CHAPTER 5

Mimic of the Green Fluorescent Protein β-barrel using Metal-Organic Frameworks

---

Williams, D. E.; Dolgopolova, E. A.; Pellechia, P. J.; Palukoshka, A.; Wilson, T. J.; Tan, R.; Maier, J. M.; Greytak, A. B.; Smith, M. D.; Krause, J. A.; Shustova, N. B. *J. Am. Chem. Soc.* **2015**, *137* (6), 2223–2226

INTRODUCTION

Materials with tunable photoluminescence (PL) properties can potentially be utilized in solid-state optoelectronics, sensors, and light-harvesting applications.[1–7] The PL response of chromophores can be tuned as a function of their surrounding environment,[8] (for instance, the fluorophore, 4-hydroxybenzylidene imidazolinone (HBI) exhibits intense green fluorescence due to interactions between HBI and the green fluorescent protein (GFP) β-barrel). The unconfined HBI chromophores are virtually non-emissive, (i.e., its emission response is suppressed by four orders of magnitude). Therefore, by tailoring the surrounding chromophore environment and inhibiting the vibrational and rotational behavior of the HBI chromophore, fluorescence may become the main pathway for energy release.[10,11]

Attempts have been made to replicate the emission response observed with the natural GFP-based systems, however artificial mimics are poor substitutes due to their strong π-π stacking interactions between adjacent molecules,[12–14] and the inability to restrict chromophore conformation,[15,16] which results in a suppressed emission response. Utilization of an artificial scaffold, such as a metal-organic framework (MOF) could confine the HBI chromophore, and thereby, suppress low frequency vibrational modes.

In this chapter, the preparation of a novel, artificial porous scaffold which can mimic the GFP β-barrel behavior is described. Immobilization of a chromophore, such as benzylidene imidazolinone, within the MOF can restrict rotational and vibrational

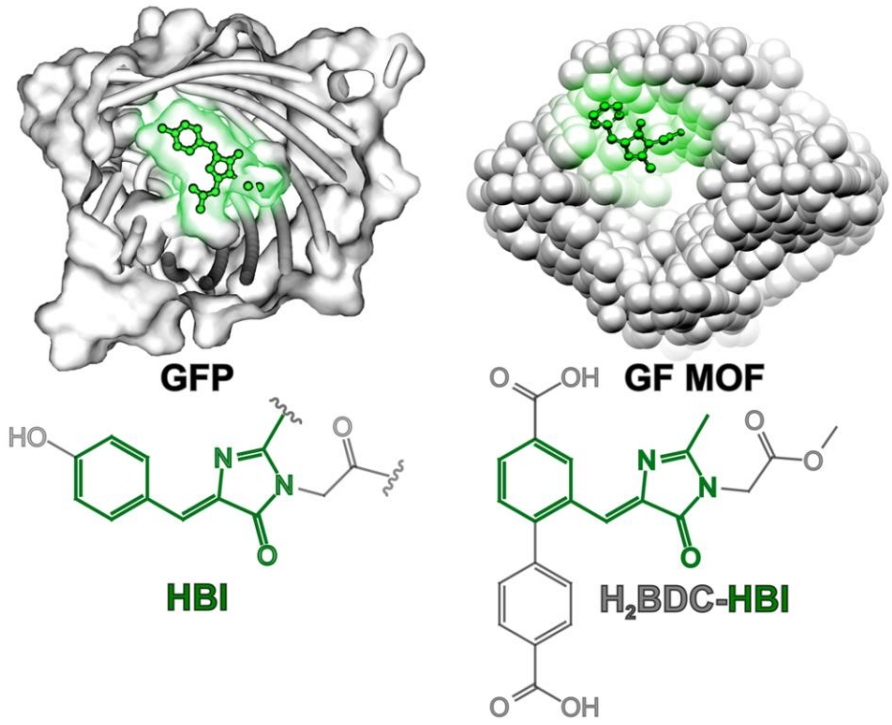

Scheme 5.1. (*left*) GFP with the HBI chromophore. (*right*) A green fluorescent MOF (GF MOF) constructed from HBI-based analogue, H_2BDC-HBI, using solvothermal synthesis or post-synthetic modification procedures.

relaxations (Scheme 5.1). Inspirations from previous works on chromophore emission recovery in molecular[17–20] and hybrid HBI-based systems[21–24] have demonstrated that control of the intermediate environment could be viable with the utilization of MOFs.[25–30] The incorporation of HBI into a modular and tunable MOF could allow us to study photoluminescence of HBI analogues.

We developed two strategies to integrate a HBI-based chromophore within a MOF: (i) through post-synthetic modification (i.e., utilization of reactive sites within the pores of for in-situ chromophore formation), and (ii) through direct solvothermal synthesis by utilization of the HBI analogue as a linker (Scheme 5.3)

This chapter covers the synthesis and characterization of the HBI-based linker and the HBI-containing MOFs. It has been divided into three main sections: (i) the synthesis and characterization of the HBI-containing chromophores, (ii) the synthesis and characterization of the HBI-containing MOFs, and (iii) analysis of the MOF photophysical properties and chromophore dynamics inside the framework.

5.1. Synthesis and Characterization of the MOF Linkers

Synthesis and Characterization of H_2BDC-CHO

The linker, 2-formyl-[1,1'-biphenyl]-4,4'-dicarboxylic acid (H_2BDC-CHO, Scheme 5.2),[31] was prepared as a linker for MOF synthesis because it contains a reactive aldehyde group, which can easily be utilized for in situ formation of HBI-analogues inside the MOF through post-synthetic modification. The MOF linker, H_2BDC-CHO, was prepared according to the four-step procedure shown in Scheme 5.1. Initially, methyl-4-bromo-3-methylbenzoate (**L1**) was oxidized to form (2-bromo-5-(methoxycarbonyl)phenyl)methylene diacetate (**L2**), followed by deprotection to produce methyl 4-bromo-3-formylbenzoate (**L3**). The compound, **L3,** was hydrolyzed into 4-bromo-3-formylbenzoic acid (**L4**), which was then subjected to a palladium-catalyzed Suzuki coupling reaction with 4-carboxyphenylboronic acid, which yielded the final compound, H_2BDC-CHO as a white powder with an 80% yield. The ^{1}H NMR spectrum of H_2BDC-CHO was in good agreement with the spectrum reported in the literature.[31]

Synthesis and Characterization of H_2BDC-HBI

Prior to 2-((1-(2-methoxy-2-oxoethyl)-2-methyl-5-oxo-1,5-dihydro-4H-imidazol-4-ylidene)methyl)-[1,1′-biphenyl]- 4,4′-dicarboxylic acid (H_2BDC-HBI, Scheme 5.2) synthesis, the precursor, methyl-2-((1-ethoxyethylidene)amino)acetate, was prepared

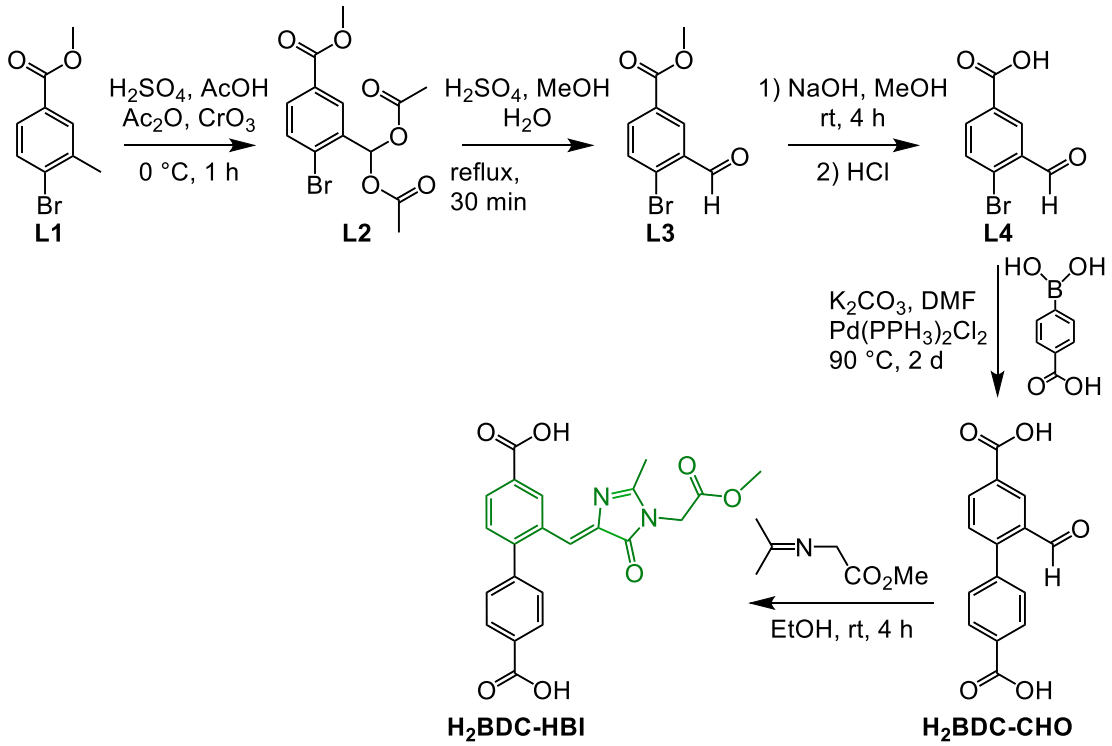

Scheme 5.2. Synthesis of the MOF linkers H_2BDC-CHO and H_2BDC-HBI.

according to the reported literature procedure.[32] A cyclization reaction was performed on H_2BDC-CHO with neat methyl-2-((1-ethoxyethylidene)amino)acetate for four hours. Deionized water was added and the resulting suspension was collected by filtration, washed with water, dichloromethane, and hexane, which produced H_2BDC-HBI as a pale-yellow powder with a yield of 64%. H_2BDC-HBI was comprehensively characterized using ^{1}H NMR, ^{13}C NMR, and ^{13}C cross-polarization magic angle spinning (CP-MAS) NMR, and FT-IR spectroscopies (Figure 5.1, 5.4, and 5.18, respectively), as well as high resolution mass spectrometry (HRMS). Full synthetic details of H_2BDC-HBI can be found in the experimental section.

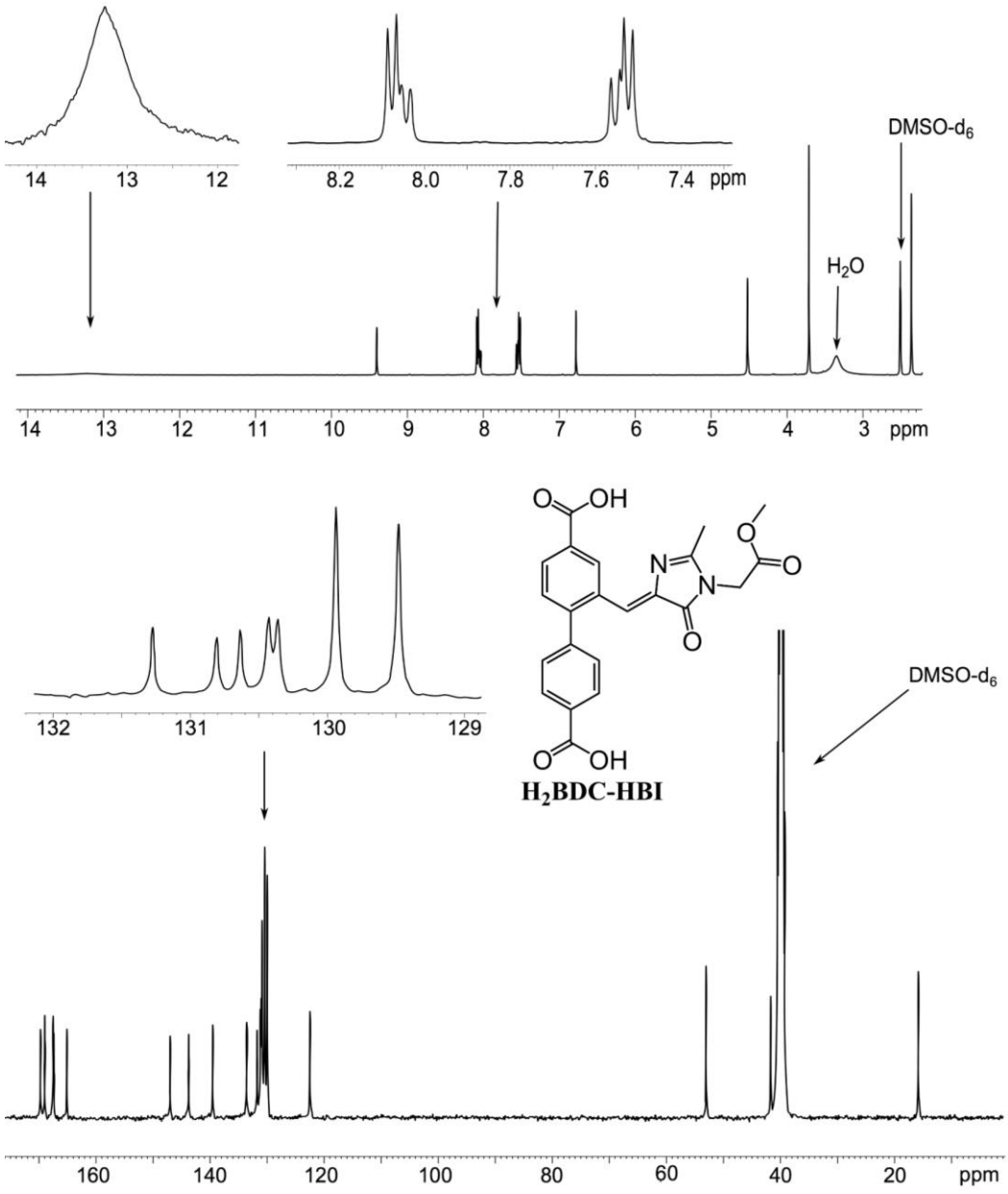

Figure 5.1. ^{1}H NMR (*top*) and ^{13}C NMR (*bottom*) spectra of H_2BDC-HBI.

5.2 Synthesis and Characterization of the 1, 2, and 2-PSM MOFs

Two methods were employed to incorporate the HBI chromophore into a MOF (i) post-synthetic modification of an aldehyde-containing parent framework with as-synthesized methyl-2-((1-ethoxyethylidene)amino)acetate (Scheme 5.3, route I), and (ii)

direct solvothermal MOF synthesis with an HBI-based MOF linker (Scheme 5.3, route II). Post-synthetic modification is defined as the chemical derivatization of MOFs after their formation.[33]

Synthesis and Characterization of $(Zn_4O(BDC\text{-}CHO)_3\cdot(DEF)_{6.2}\cdot(EtOH)_{0.6}$, $Zn_4C_{77.2}H_{95.8}N_{6.2}O_{22.8}$, ***1)***

The parent framework, **1**, was prepared using a modified literature procedure (Scheme 5.3a).[31] H_2BDC-CHO and $Zn(NO_3)_2\cdot 6H_2O$ were dissolved in DEF/ETOH, and subjected to solvothermal synthesis in an oven at 100 °C. After 24 h, the reaction was cooled to room temperature, and yellow cubic crystals of **1** were obtained in 55% yield. MOF **1** was characterized by single-crystal and powder X-ray diffractions (PXRD), ^{13}C CP-MAS NMR, FT-IR, diffuse reflectance, and fluorescence spectroscopies, as well as thermogravimetric analysis (TGA) (Figures 5.2, 5.5, 5.4, 5.18, 5.10, and 5.17, respectively).

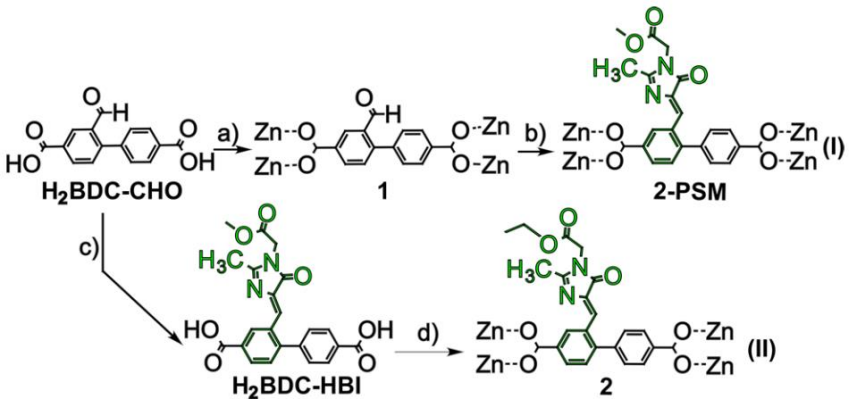

Scheme 5.3. Synthetic routes for H_2BDC-HBI immobilization and preparation of **2-PSM** (route I) and **2** (route II) using the following reagents and experimental conditions: (a) $Zn(NO_3)_2$, DEF/EtOH, 100 °C, 24 h; (b) methyl-2-((1-ethoxyethylidene)amino)acetate, room temperature, 3 days; (c) H_2BDC–HBI was synthesized according to Scheme S1; (d) $Zn(NO_3)_2$, DEF/EtOH, 100 °C, 24 h

As shown in Figure 5.2, aldehyde groups are present on the MOF linkers, which allows for in-situ post-synthetic modification with methyl-2-((1-ethoxyethylidene)amino)acetate. The internal pore aperture of **1** measured 15.5 Å along the a direction and 26.9 Å along the c direction, which is large enough for the diffusion of methyl-2-((1-ethoxyethylidene)amino)acetate (7.2 Å), necessary for post-synthetic modification. The PXRD pattern of bulk of **1** is in excellent agreement with the simulated data from the crystal structure (Figure 5.5).

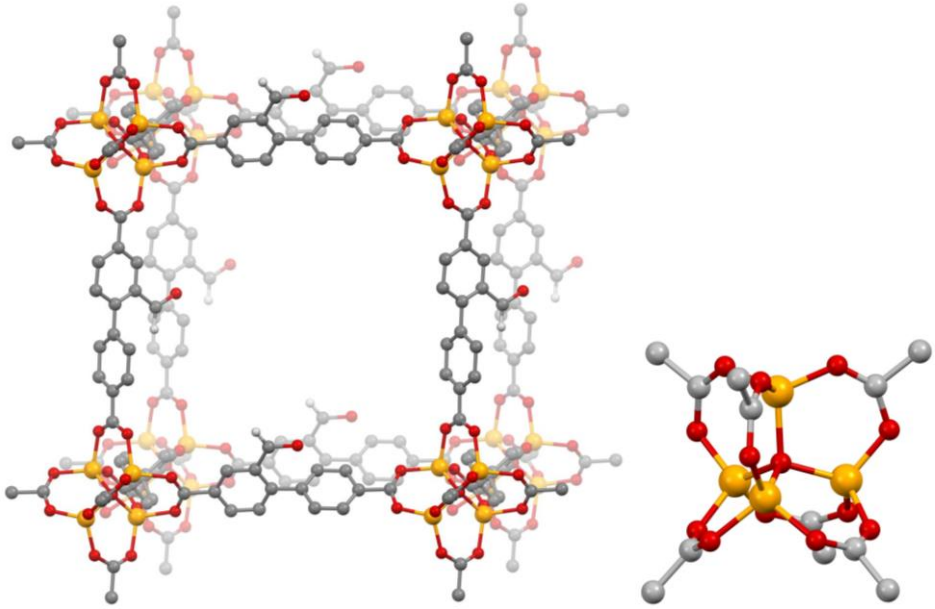

Figure 5.2. The single crystal X-ray structure of **1** (*left*) and an enlarged $Zn_4O(O_2C–)_6$ secondary building unit in **1** (*right*). Hydrogen atoms (except for the aldehyde groups) were removed for clarity. Orange, red, grey, and white spheres represent zinc, oxygen, carbon, and hydrogen atoms, respectively.

*Synthesis and Characterization of **2-PSM***

Post-synthetic modification of the parent scaffold, **1**, with methyl-2-((1-ethoxyethylidene)amino)acetate forms **2-PSM**, which contains the HBI-based

chromophore as part of the linker. The synthetic route of **2-PSM** is shown in Scheme 5.3, (route I).

Washed crystals of **1** were transferred to a 1 dram vial containing methyl-2-((1-ethoxyethylidene)amino)acetate, and soaked at room temperature for 72 h. Every 24 h, the supernatant was removed and replaced with fresh methyl-2-((1-ethoxyethylidene)amino)acetate (Scheme 5.3b). The resulting yellow crystals were washed several times with DMF to remove excess of methyl-2-((1-ethoxyethylidene)amino)acetate, and stored in fresh DMF. The **2-PSM** framework was comprehensively characterized using single-crystal and powder X-ray diffraction, FT-IR, ^{1}H NMR, and ^{13}C CP-MAS NMR spectroscopies (Figure 5.5, 5.18, 5.3, and 5.4, respectively), as well as mass spectrometry and TGA (Figures 5.3 and 5.17). Single-crystal X-ray data of **2-PSM** indicated a structure which was nearly identical to **1,** however the residual electron density within the pores could not be resolved due to partial occupancy

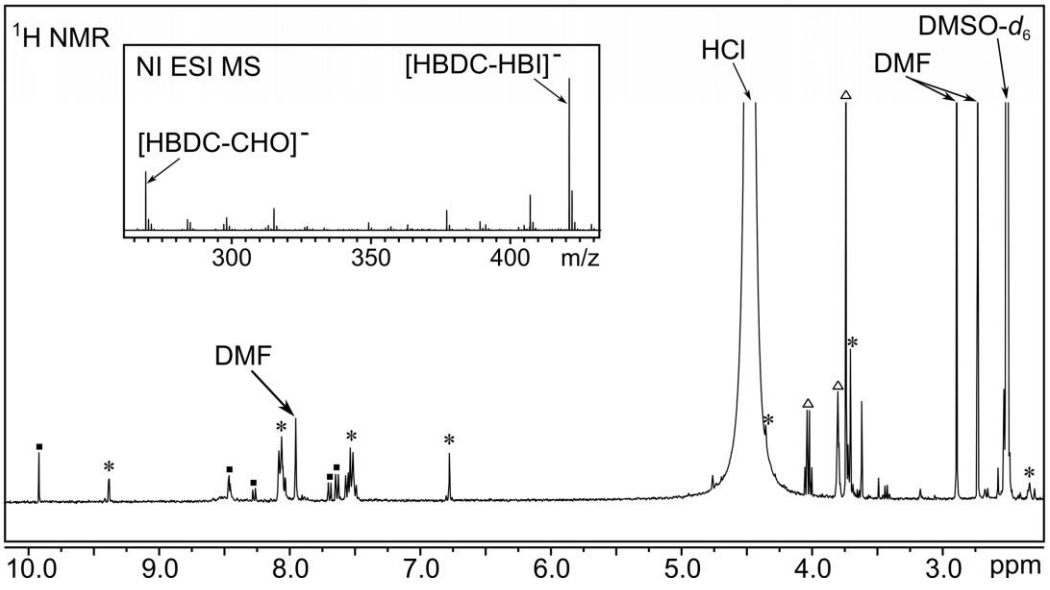

Figure 5.3. The ^{1}H NMR spectrum of digested **2-PSM** in DMSO-d_6. The inset shows the negative ion electrospray ionization mass spectrum of digested **2-PSM**. The peaks corresponding to H_2BDC-CHO (■), H_2BDC-HBI (⁎), and methyl-2-((1-ethoxyethylidene)amino)acetate (Δ) are labeled.

and disorder of the HBI chromophore. PXRD of **1** and **2-PSM** showed that integrity of the MOF was preserved during post-synthetic modification (Figure 5.5). To determine the percentage of BDC-HBI^{2-} incorporation, crystals of **2-PSM** were dried under vacuum, digested (destroyed in the presence of acid) by placing them into a one-dram vial containing 500 µL DMSO-d_6 and 3.5 µL HCl. We discovered that the digestion of the MOF in DCl resulted in the suppression of the methyl-2-((1-ethoxyethylidene)amino)acetate resonance at 2.4 ppm. We determined that an exchange of the methyl protons with deuterium in DCl had occurred which we supported with ^{2}H NMR spectroscopy. The digested solution was transferred to a 5 mm NMR tube and characterized using ^{1}H NMR spectroscopy, and with relative integrations, revealed that 64% of the BDC-CHO^{2-} linkers were converted to BDC-HBI^{2-} (Figure 5.3). For mass spectrometry, a similar digestion

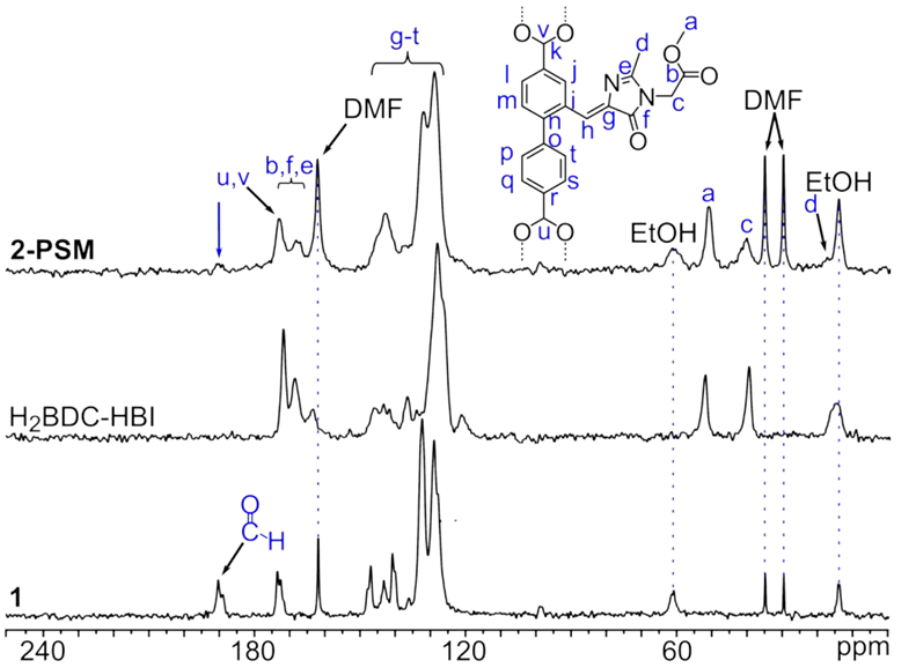

Figure 5.4. ^{13}C CP-MAS NMR spectrum of **1** (*bottom*), H_2BDC-HBI (*middle*), and **2-PSM** (*top*). The blue arrow indicates decrease of the peak corresponding to the –CHO group. The blue dashed lines indicate the peaks corresponding to solvents in **1** and **2-PSM**.

procedure was performed, however $CHCl_3$ was used instead of DMSO-d_6, so the solvent could be removed prior to analysis. The digested sample was evacuated under vacuum while heating (50 °C) for one day to remove trace acid and solvent from the mixture. Results from ESI MS of **2-PSM** showed the presence of both H_2BDC-CHO and H_2BDC-HBI (inset, Figure 5.3). To further assess the composition of **2-PSM** and confirm the post-synthetic modification success, ^{13}C CP-MAS NMR was used, which revealed the presence of both $[BDC\text{-}HBI]^{2-}$ and $[BDC\text{-}CHO]^{2-}$ (Figure 5.4).

*Synthesis of $Zn_4O(BDC\text{-}HBI')_3\cdot(DEF)_{3.07}\cdot EtOH\cdot(H_2O)_{3.13}$, $Zn_4C_{86.35}H_{100.03}N_{9.07}O_{29.2}$ **(2)***

A direct, solvothermal approach was used to prepare **2** (Scheme 5.3, route II) by heating a mixture of $Zn(NO_3)_2\cdot 6H_2O$ and H_2BDC-HBI in DEF/EtOH in a ramping oven at 100 °C (Scheme 5.3d). After 24 h of heating, the oven was cooled, and **2** was recovered as yellow crystals in 64% yield (full synthetic details in the experimental section). Despite having visually-promising crystals of **2**, they exhibited poor X-ray diffraction and no structural data could be extracted. Therefore, we relied on a combination of powder X-ray diffraction, ^{1}H NMR, ^{13}C CP-MAS NMR, heteronuclear multiple-bond correlation (^{1}H{^{13}C} HMBC) NMR, heteronuclear single-quantum correlation ({^{13}C} HSQC) NMR, and FT-IR spectroscopies, as well as MS to determine the composition of **2** (Figures 5.5, 5.7, 5.6, 5.8, 5.9, 5.19, and 5.7 inset, respectively).

The PXRD pattern of prepared **2** is in good agreement with the simulated and experimental patterns of **1** and **2-PSM** (Figure 5.5). From the PXRD, we can conclude that the structure of **2** is similar to that of **1**, which was solved with single-crystal X-ray diffraction. However further characterization was necessary to determine the composition. Figure 5.6 shows the ^{13}C CP-MAS NMR of **2**, and clearly indicates the presence of the

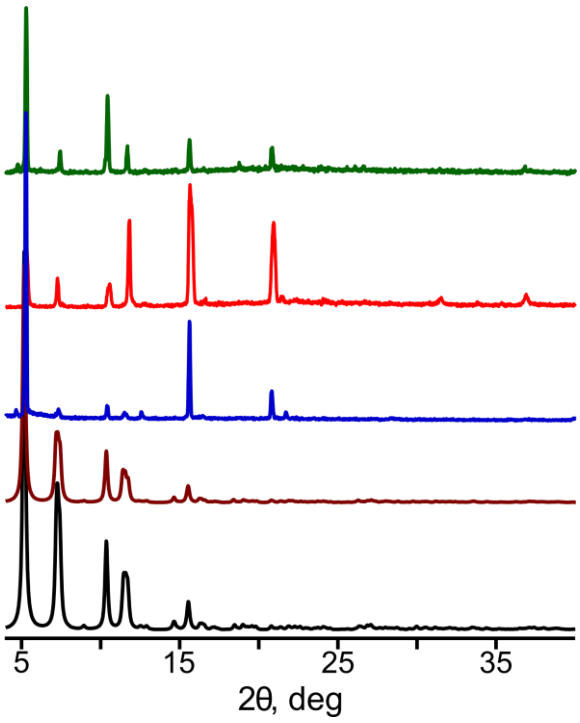

Figure 5.5. PXRD patterns of simulated **1** (black line), simulated **2-PSM** (brown line), as well as as-synthesized **1, 2-PSM**, and **2** (blue, red, and green line, respectively.)

HBI chromophore within the MOF, as well as the absence of the aldehyde peak which is present in **1** and **2-PSM** (Figure 5.4). It is important to note that we originally believed that the two resonances located at 15.1 ppm and 60.7 ppm were attributed to residual EtOH, but no amount of drying resulted in the suppression of the resonances. Moreover, the MS of digested **2** showed a large peak with a mass of 435, instead of 421, which we expected with the H_2BDC-HBI chromophore. Therefore, we performed additional NMR experiments, including ^{1}H, ^{13}C, ^{1}H{^{13}C} HMBC and ^{1}H{^{13}C} HSQC NMR spectroscopies to clarify the structural details, and results are shown in Figures 5.7, 5.8, and 5.9. Indeed, the ^{13}C NMR and ^{1}H NMR spectra of digested **2** indicate the presence of an ethyl group, which does not match the shifts expected for residual EtOH in the structure (Figure 5.7). Furthermore, the HSQC and HMBC NMR spectra show strong

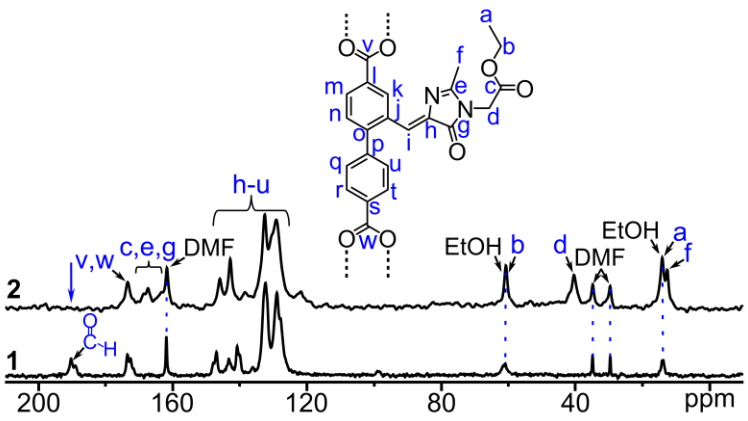

Figure 5.6. ^{13}C CP-MAS spectrum of **1** (*bottom*) and **2** (*top*). The blue arrow indicates the absence of the aldehyde from H_2BDC-CHO.

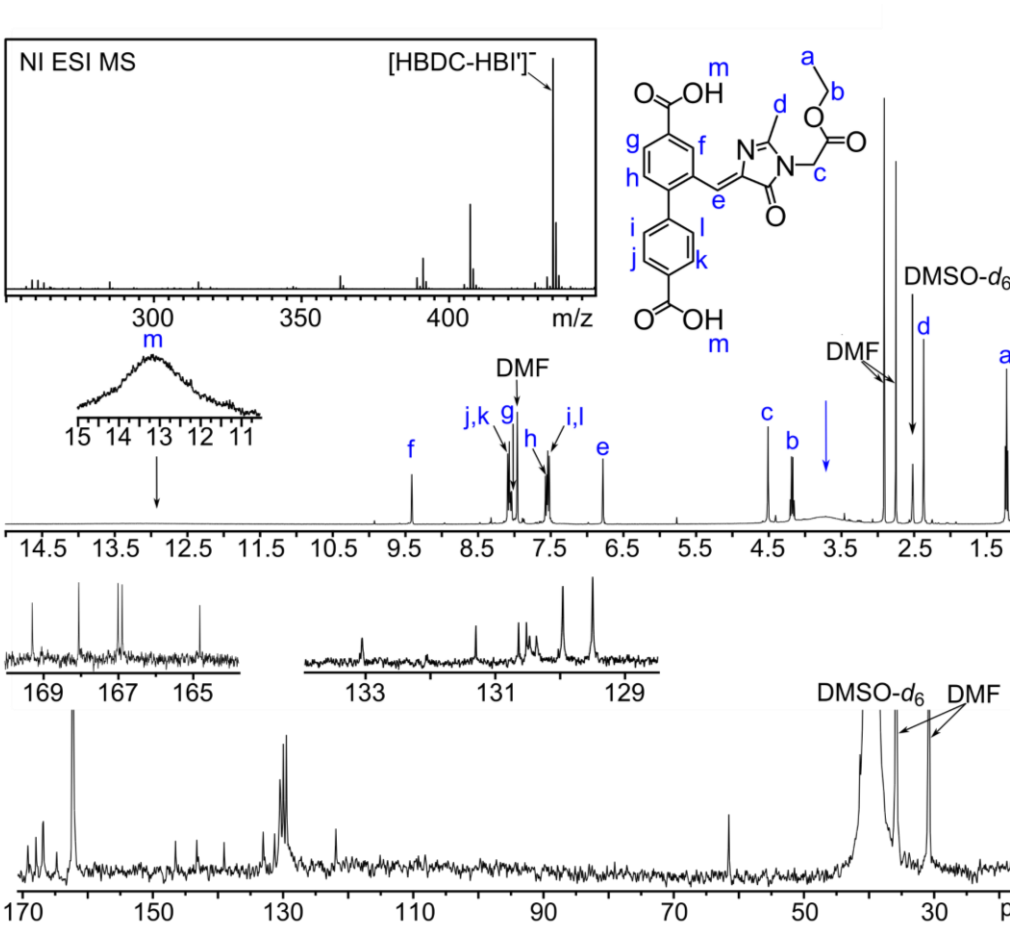

Figure 5.7. ^{1}H NMR (*top*) and ^{13}C (*bottom*) NMR of digested **2**. The inset shows the negative ion electrospray ionization mass spectrum. Each resonance from the ^{1}H NMR spectrum is identified on the structure of H_2BDC-HBI'. The blue arrow indicates the presence of HCl, which remained after MOF digestion.

resonance correlation from the "ethyl" protons to the ^{13}C O-CH_2 shift. With the combination of the NMR characterization techniques and MS, we confirmed that the H_2BDC-HBI chromophore had undergone a transesterification reaction *in-situ* in the presence of ethanol during solvothermal synthesis, which yielded the ethoxy-terminated chromophore, H_2BDC-HBI'.

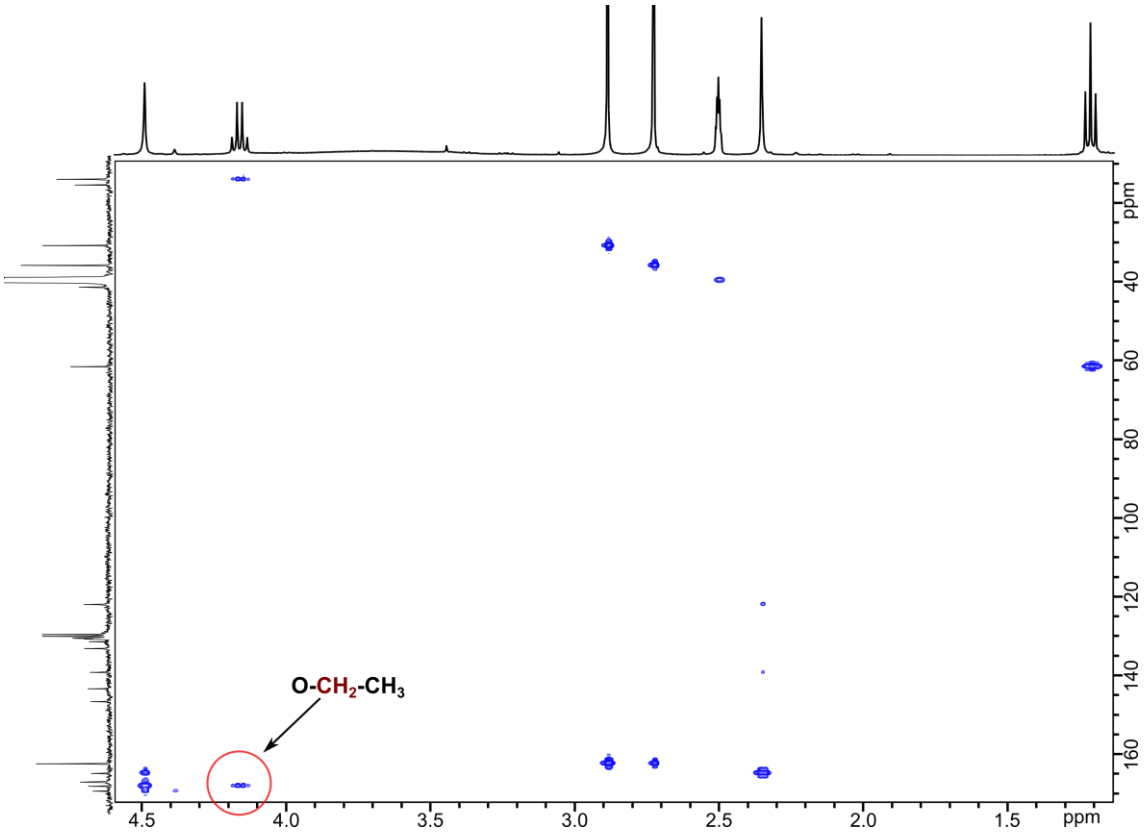

Figure 5.8. The $^{1}H\{^{13}C\}$ HMBC NMR spectrum of digested **2** (H_2BDC-HBI' ligand) demonstrating correlation of –OCH_2- with the carbonyl atom (depicted by the red circle). Formation of –OCH_2CH_3 group occurred due to a transesterification reaction (i.e., –OCH_3 $\rightarrow$ – OCH_2CH_3 conversion).

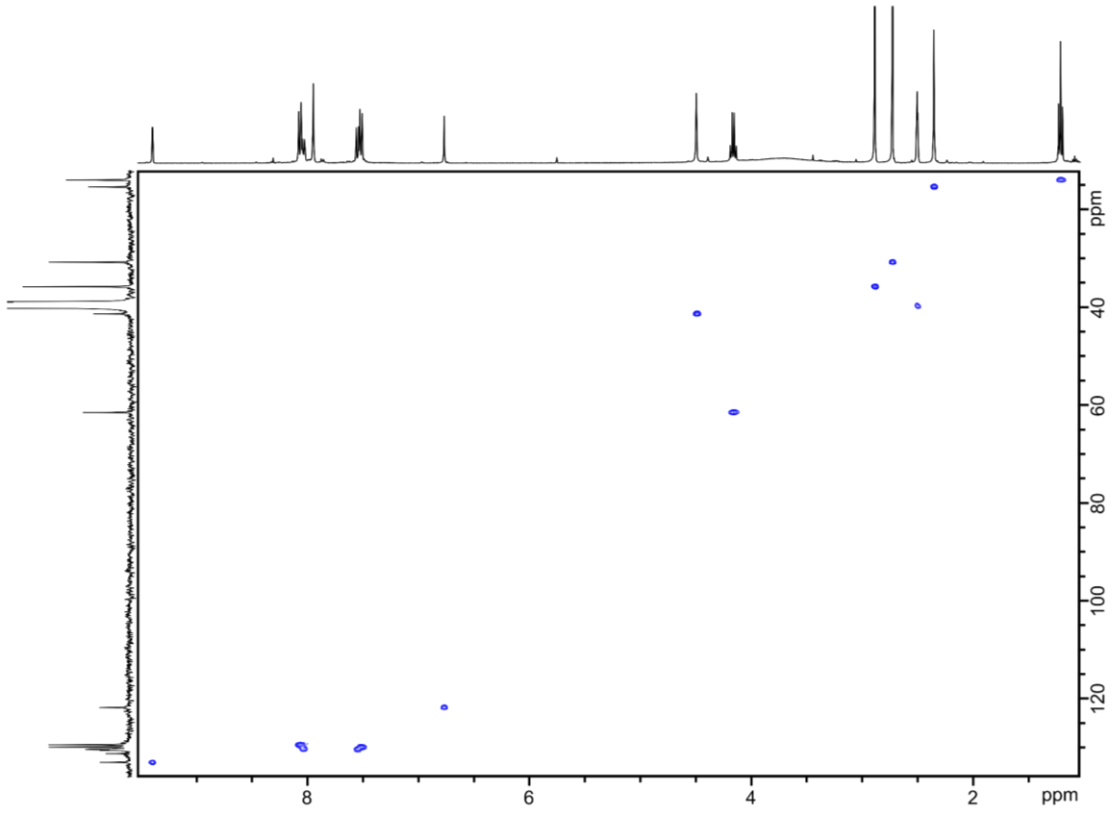

Figure 5.9. The $^{1}H\{^{13}C\}$ HSQC NMR spectrum of digested **2** (H_2BDC-HBI' ligand).

5.3. Analysis of the MOF Photophysical Properties and Chromophore Dynamics Inside the Framework

Photophysical properties of **1**, **2**, and **2-PSM** were studied by diffuse reflectance, as well as steady-state and time-resolved fluorescence spectroscopies. We determined that the diffuse reflectance profiles of **2** and **2-PSM** are bathochromically-shifted in respect to **1**, which could be attributed to the extended structure of $[BDC\text{-}HBI']^{2-}$ compared to $[BDC\text{-}HBI]^{2-}$. Also, the photoluminescence maxima are drastically shifted, from an emission max of 440 nm in **1**, to 516 nm in **2** and **2-PSM** (Figures 5.10 and 5.11), which is in line with the emission maxima of natural GFP and its mutants of ~510 nm.[34,35] Furthermore, the emission profile of **2-PSM** contains a shoulder at 440 nm, which can be attributed to the

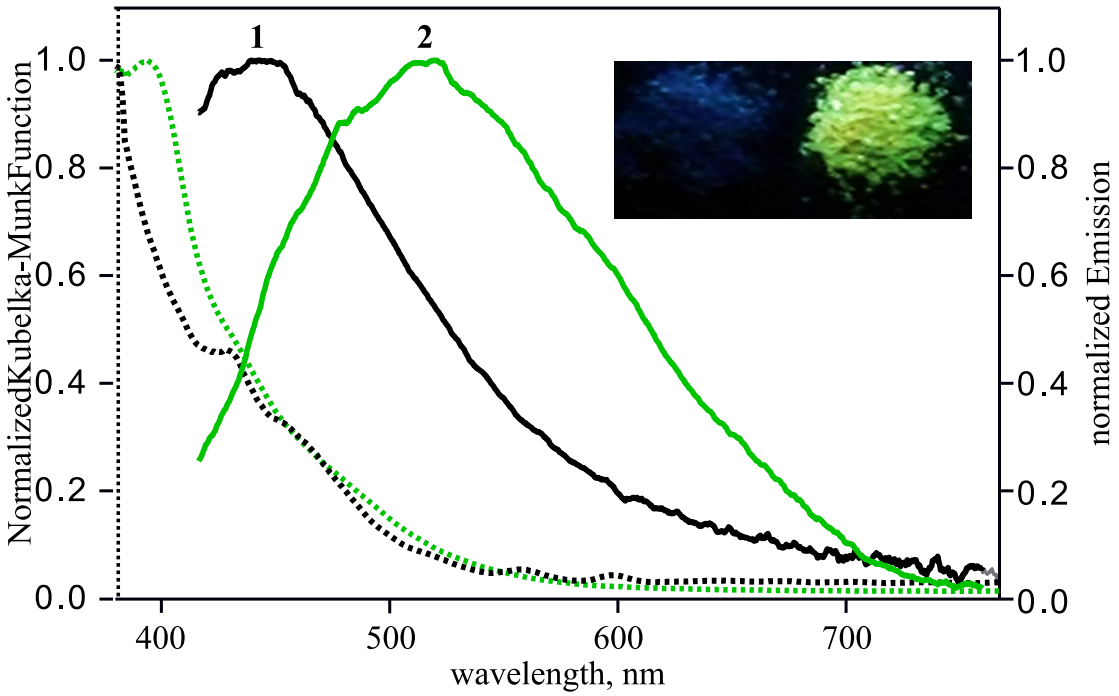

Figure 5.10. Diffuse reflectance (dotted lines) and fluorescence (solid lines) profiles of **1** and **2** (black and green lines, respectively). Inset shows a photograph of bulk **1** and **2**, demonstrating their respective emission (λ_{ex}=365 nm).

64% conversion of the MOF linkers from [BDC-CHO^{2-}] to [BDC-HBI^{2-}] (Figure 5.11). Time-resolved fluorescence lifetime measurements of **1**, **2**, and **2-PSM** were performed to measure their photoluminescence decays. Analysis of the time-resolved supported triexponential decays, which determined the intensity-weighted lifetime averages to be 4.23, 1.91, and 1.59 ns for **1**, **2-PSM**, and **2**, respectively (see the experimental section for equations and tables). As expected, the lifetime decay curve of **2-PSM** was located between those of **1** and **2**, which can be ascribed to the partial conversion of the linkers. Natural GFP systems have lifetime ranges between 2.7 and 3.4 ns, and the GFP mutants between 1.9 and 2.8 ns,[36] the latter being directly comparable with results obtained from **2-PSM**. Fluorescence lifetime and PL results indicate that the engineered GFP scaffolds, **2** and **2-PSM**, successfully mimic the photophysical behavior of the GFP β-barrel by restoring the emission of an HBI-based chromophore confined within the scaffold.

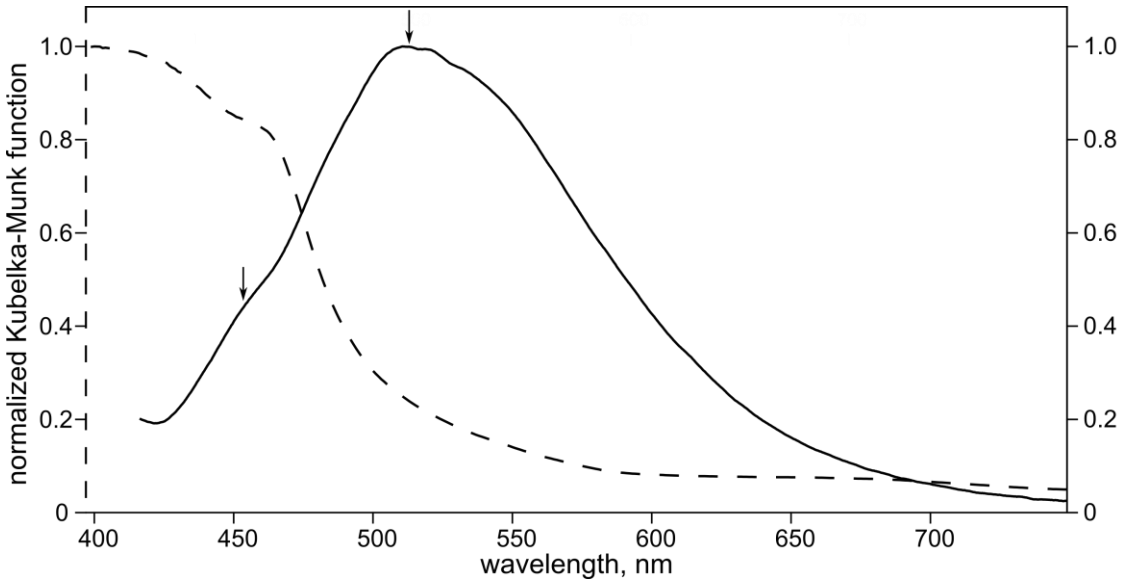

Figure 5.11. Diffuse reflectance (dotted line) and fluorescence (solid line) profiles of **2-PSM**. The black arrows indicate the fluorescence maxima (λ_{ex}=365 nm) corresponding to $[H_2BDC\text{-}CHO]^{2-}$ and $[H_2BDC\text{-}HBI]^{2-}$ (left and right arrows, respectively).

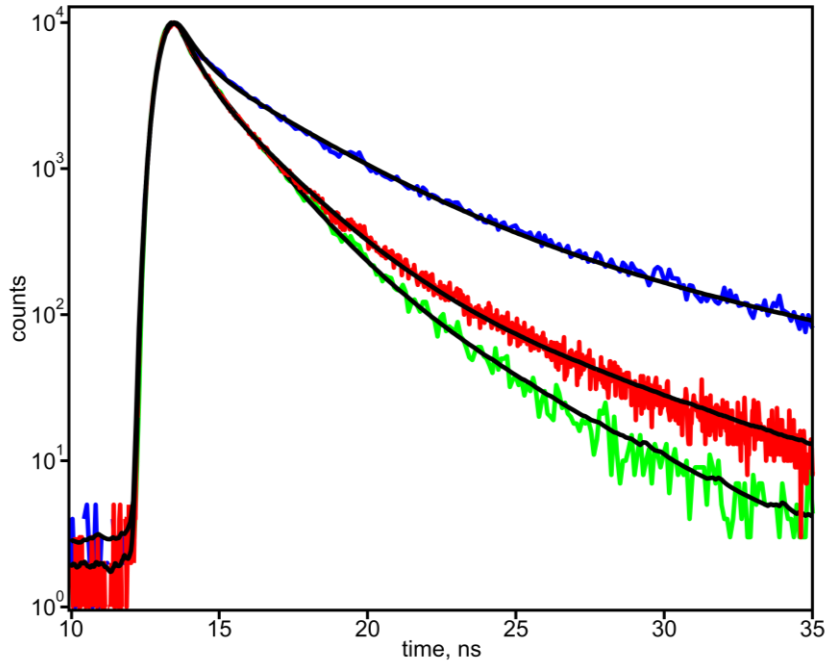

Figure 5.12. Fluorescence decays of **1** (blue line), **2-PSM** (red line) and **2** (green line). Black solid lines are fits of the decays.

Chromophore Dynamics

To understand the impact of the rigid scaffold on the dynamics of the confined H_2BDC-HBI chromophore, ^{2}H quadrupolar spin-echo NMR was used in conjunction with DFT calculations to model the rotational behavior of the chromophore *in-situ*. As previously mentioned, vibrational and rotational strains imposed on the chromophore can restrict the release of energy through a fluorescence response. These studies provided insight into the dynamics of the chromophore rotation within the MOF pores. To perform ^{2}H quadrupolar spin-echo NMR spectroscopy, H_2BDC-HBI was modified to contain a CD_3 group, which would allow us to observe the rotational behavior of the HBI group within

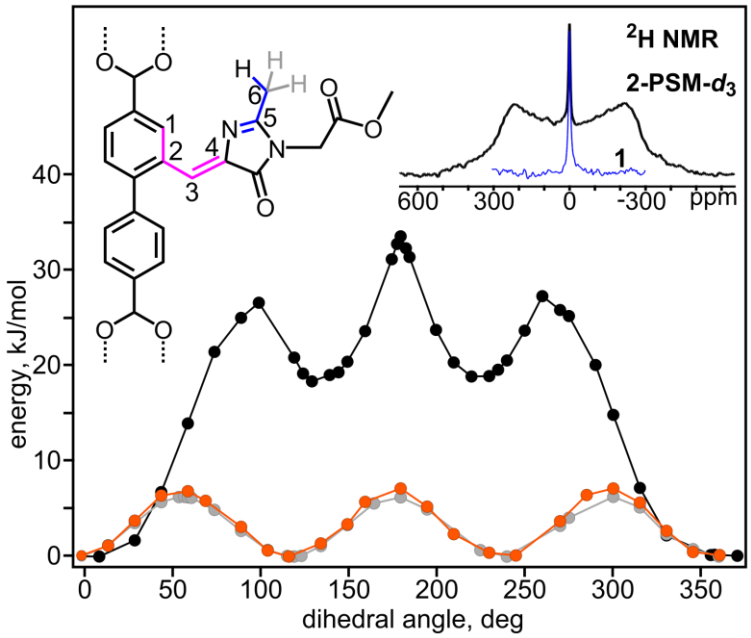

Figure 5.13. (*top left*) A diagram of [BDC-HBI]^2 with colored lines indicating the dihedral angles which were used to model the PES for the flipping of the CH_3 group. (*bottom*) The PES model for the motion of the C_2-C_3 flip (black line) and of the PES of the flipping of the CH_3 group in confined (grey) and unconfined (orange) environments. (*top right)* The ^{2}H spin-echo NMR spectrum of **2-PSM-*d*$_3$** and non-deuterated **1**.

the MOF pore. To incorporate the CD_3 tag into the framework, methyl-2-((1-ethoxyethylidene)amino)acetate-d_3 was prepared from imidoacetate-d_3 hydrochloride based on the synthesis reported for the protonated analog (Scheme 5.6).[32] The parent MOF, **1**, was post-synthetically modified using the same synthetic procedure (vide supra), which provided **2-PSM-*d*$_3$** as yellow crystals. Synthetic and characterization details of methyl-2-((1-ethoxyethylidene)amino)acetate-d_3 are provided in the experimental section. The H_2BDC-HBI-d_3 compound was also prepared from the cyclization reaction of H_2BDC-CHO with methyl-2-((1-ethoxyethylidene)amino)acetate-d_3, however, proton exchange occurred with DMF during solvothermal synthesis, which resulted in the absence of deuterium in the prepared scaffold.

The ^{2}H spin-echo NMR spectrum of **2-PSM-*d*$_3$** shows the classic Pake pattern with quadrupolar coupling C_Q = 52 Hz (Figure 5.13, inset). The Pake pattern can be attributed to the slow flipping of the $–CD_3$ group ($<10^4$ Hz), from which slow dynamics could be explained by restrictions imposed by the presence of solvent molecules inside the porous framework. The sharp isotropic peak can be attributed to the mobile solvent molecules within the framework, as confirmed by the ^{2}H spin-echo NMR response of non-deuterated **1**. We modeled the potential energy surfaces (PESs) of unbound versus restricted H_2BDC-HBI. For this purpose, four PESs were constructed to model the −CH3 group dynamics and single bond C_2−C_3 motions by varying the C_1−C_2−C_3═C_4 and N═C_5−C_6−H dihedral angles, respectively (Figure 5.13). The activation barrier for the methyl group in the confined and unrestricted situations were similar (6-7 kJ/mol), and are comparable with those in some natural proteins.[37] As expected, in the case of the C_2−C_3 bond flip, E_a values were significantly higher. For instance, we found that the E_a for the unrestricted

chromophore is 33 kJ/mol. Furthermore, when the chromophore was restricted, and the activation barrier calculated while restricting the movement of the two phenyl rings in the linker (as it is in the MOF), flipping around the C_2–C_3 bond was not possible without decomposition or destruction of the framework. This finding supports that the HBI-based chromophore rotation is restricted while immobilized in the MOF due to the rigidity of the framework. thereby inducing a fluorescence response. Figure 5.14 shows a representation of the H_2BDC-HBI rotation in confined versus unconfined environments. As shown in Figure 5.14, the coordinatively trapped chromophores could not, for instance, accommodate a 180°-conformation without scaffold/ligand decomposition. In contrast to the immobilized chromophore, the steric repulsion maximum could easily be avoided in the unbound H_2BDC-HBI due to the possibility of conformational deviation as shown in Figure 5.14.

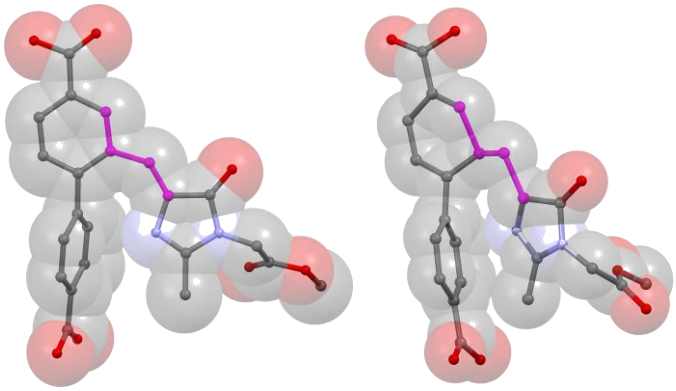

Figure 5.14. The DFT-calculated structures of the unbound (*left*) and confined (*right*) H_2BDC-HBI chromophore with fixed dihedral angles (depicted in pink), 180° and 175.9°, respectively. The right figure illustrates the distortion of the confined H_2BDC-HBI inside the rigid scaffold and demonstrates that a 180°-conformation of the chromophore could not be achieved without bending the scaffold. To minimize steric repulsion, the unbound H_2BDC-HBI could deviate as shown on the left structure. Grey, red, and blue spheres represent carbon, oxygen, and nitrogen atoms, respectively. The hydrogen atoms are omitted for clarity.

We've shown that **2** and **2-PSM** exhibit a PL and fluorescence decay response similar to that of natural GFP-based systems and its engineered mutants by trapping the HBI core within the MOF. The calculated PESs of the confined H_2BDC-HBI chromophore indicate that chromophore rotation is not possible without framework degradation, thereby inducing the observed fluorescence response in **2** and **2-PSM**.

Conclusion

We have demonstrated that the natural GFP system can be replicated by utilizing the porosity and rigidity of MOFs to inhibit the rotation of the benzylidene imidazolinone chromophore core, thus suppressing non-radiative, low-energy vibrational modes. The successful confinement of the HBI chromophore led to material emission which was similar to natural GFP-based systems. The results from ^{2}H quadrupolar spin-echo NMR spectroscopic studies, as well as theoretical DFT calculations showed the coordinative confinement of the HBI chromophore.

EXPERIMENTAL SECTION

Materials.

$Zn(NO_3)_2 \cdot 6H_2O$ (technical grade, Ward's Science), 4-bromo-3-methyl benzoic acid methyl ester (99.1%, Chem-Impex International Inc.), 4-carboxyphenylboronic acid (99.5%, Chem-Impex International Inc.), chromium(VI) oxide (99.9%, Sigma-Aldrich), sulfuric acid (ACS grade, Fischer Scientific), glacial acetic acid (ACS grade, BDH), ethanol (Decon Laboratories, Inc.), methanol (ACS grade, Fischer Scientific), *N,N*-diethylformamide (>99%, TCI America), *N,N*-dimethylformamide (ACS grade, BDH), trans-dichlorobis(triphenylphosphine)palladium(II) (99%, Strem Chemicals), ethyl

acetimidate hydrochloride (97%, Alfa Aesar), glycine methyl ester hydrochloride (98%, Acros Organics), potassium carbonate (ACS grade, BDH), sodium hydroxide (ACS grade, Macron Fine Chemicals), hexanes (ACS grade, Fischer Scientific), diethyl ether (ACS grade, J. T. Baker® Chemicals), ethyl acetate (HPLC grade, EMD Chemicals), tetrahydrofuran (ACS grade, EMD Chemicals), dichloromethane (ACS grade, BDH), chloroform-*d* (Cambridge Isotopes), acetonitrile-d_3 (Cambridge Isotopes), benzene-d_6 (Cambridge Isotopes), deuterium chloride (35 wt% in D_2O, Sigma-Aldrich), ethanol-d_6 (Cambridge Isotopes) and DMSO-d_6 (Cambridge Isotopes) were used as received.

Synthesis.

The compounds, 3-methylbenzoate (**L1**),[31] (2-bromo-5-(methoxycarbonyl)phenyl)methylene diacetate (**L2**),[31] methyl 4-bromo-3-formylbenzoate (**L3**),[31] and 4-bromo-3-formylbenzoic acid (**L4**),[31], and methyl-2-((1-ethoxyethylidene)amino)acetate[32] were synthesized according their reported procedures.

Synthesis of 2-formyl-[1,1'-biphenyl]-4,4'-dicarboxylic acid (H_2BDC-CHO)

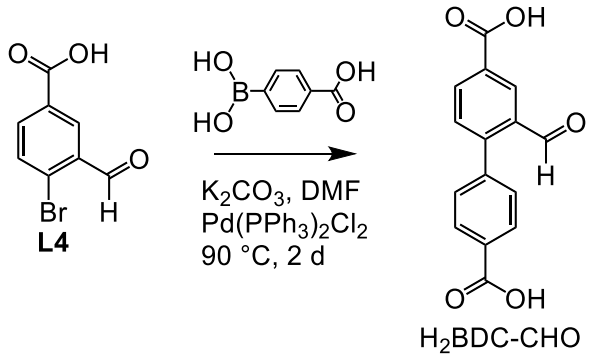

Scheme 5.4. Synthesis scheme of H_2BDC-CHO.

H_2BDC-CHO was synthesized according to a modified literature procedure.[31] In a 100 mL Schlenk flask, using air-sensitive technique, Na_2CO_3 (1.43 g, 13.5 mmol), 4-

carboxyphenylboronic acid (0.93 g, 5.6 mmol), $PdCl_2(PPh_3)_2$ (0.40 g, 0.57 mmol), and **L4** (1.03 g, 5.20 mmol) were added. Dry DMF (25 mL) was added via syringe, and the resulting mixture was heated at 90 °C for 72 h. After cooling, 10% NaOH (30 mL) was added and the resulting solution stirred an additional ten minutes. The aqueous layer was washed with ethyl acetate (3 × 100 mL), THF (2 × 50 mL). The aqueous layer was transferred to a 250 mL Erlenmeyer flask and the solution was acidified with concentrated HCl, which yielded a white precipitate. The precipitate was collected by filtration, washed with water, hexane, and dried under vacuum at 60 °C for 24 h, which yielded H_2BDC-CHO as a white powder (0.910 g, 3.37 mmol) in 80% yield. ^{1}H NMR (DMSO-d_6, ppm): δ = 7.63-7.65 (2H, d, J = 8.34), 7.68-7.71 (1H, d, J = 8.12), 8.07-8.10 (2H, d, J = 8.26), 8.26-8.29 (1H, d, J = 6.23), 8.47 (1H, s), 9.92 (1H, s), 13.29 (2H, s).

Synthesis of 2-((1-(2-methoxy-2-oxoethyl)-2-methyl-5-oxo-1,5-dihydro-4H-imidazol-4-ylidene)methyl)-[1,1'-biphenyl]-4,4'-dicarboxylic acid (H_2BDC-HBI)

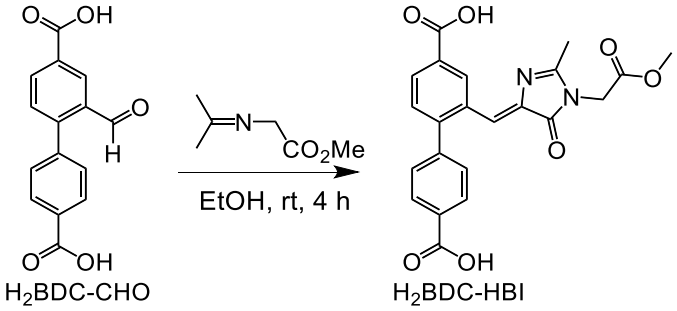

Scheme 5.5. Synthesis scheme of H_2BDC-HBI.

Methyl-2-((1-ethoxyethylidene)amino)acetate (1.43 g, 8.99 mmol) was added to a vial containing H_2BDC-CHO (1.00 g, 3.70 mmol) and EtOH (50 mL) and the resulting suspension was stirred vigorously for 4 h at room temperature. Distilled water (30 mL) was added to the flask and the solution was stirred for another 5 minutes. The suspension was

collected by filtration and washed with water, dichloromethane, and hexane. After drying under vacuum, H_2BDC-HBI (0.996 g, 2.36 mmol) was obtained as a pale-yellow powder in 64% yield. ^{1}H NMR (DMSO-d_6, ppm): δ = 2.36 (3H, s), 3.70 (3H, s), 4.51 (2H, s), 6.77 (1H, s), 7.51-7.53 (2H, d, J = 8.32 Hz), 7.53-7.56 (1H, d, J = 8.04 Hz), 8.02-8.05 (1H, dd, J = 8.00, 1.72 Hz), 8.05-8.08 (2H, d, J = 8.32 Hz), 9.39 (1H, d, J = 1.60 Hz), and 13.20 (2H, br). ^{13}C NMR (DMSO-d_6, ppm): δ = 15.46, 41.35, 52.69, 122.12, 129.62, 130.06, 130.51, 130.68, 130.82, 131.39, 133.22, 139.17, 139.83, 143.38, 146.64, 164.75, 167.03, 167.15, 168.63, and 169.38 ppm. IR (neat, cm^{-1}): 2958, 2547, 1815, 1721, 1688, 1604, 1562, 1418, 1371, 1292, 1227, 1149, 984, 908, 872, 846, 762, and 704. HRMS (NI-ESI, m/z) calculated for $C_{22}H_{17}N_2O_7$ [M-H]: 421.1036, found 421.1047.

Synthesis of Deuterated Methyl-2-((1-ethoxyethylidene)amino)acetate-d_3

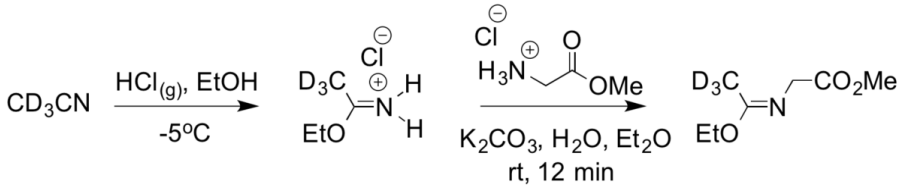

Scheme 5.6. Synthesis of methyl-2-((1-ethoxyethylidene)amino)acetate-d_3.

A mixture of K_2CO_3 (8.8 g, 63 mmol), glycine methyl ester hydrochloride (8.0 g, 63 mmol) and diethyl ether (250 mL) were suspended in a 500 mL separatory funnel. Distilled water (50 mL) and previously-synthesized ethyl imidoacetate-d_3 hydrochloride from deuterated acetonitrile (Scheme 5.6, 8.0 g, 63 mmol)[32] were added and the resulting mixture was shaken for six minutes. The organic layer was removed and the aqueous layer was extracted with diethyl ether (150 mL) for another six minutes. The combined organic layers were washed with water, brine, dried over magnesium sulfate, and the solvent removed under reduced pressure. The obtained pale yellow oil was distilled under vacuum,

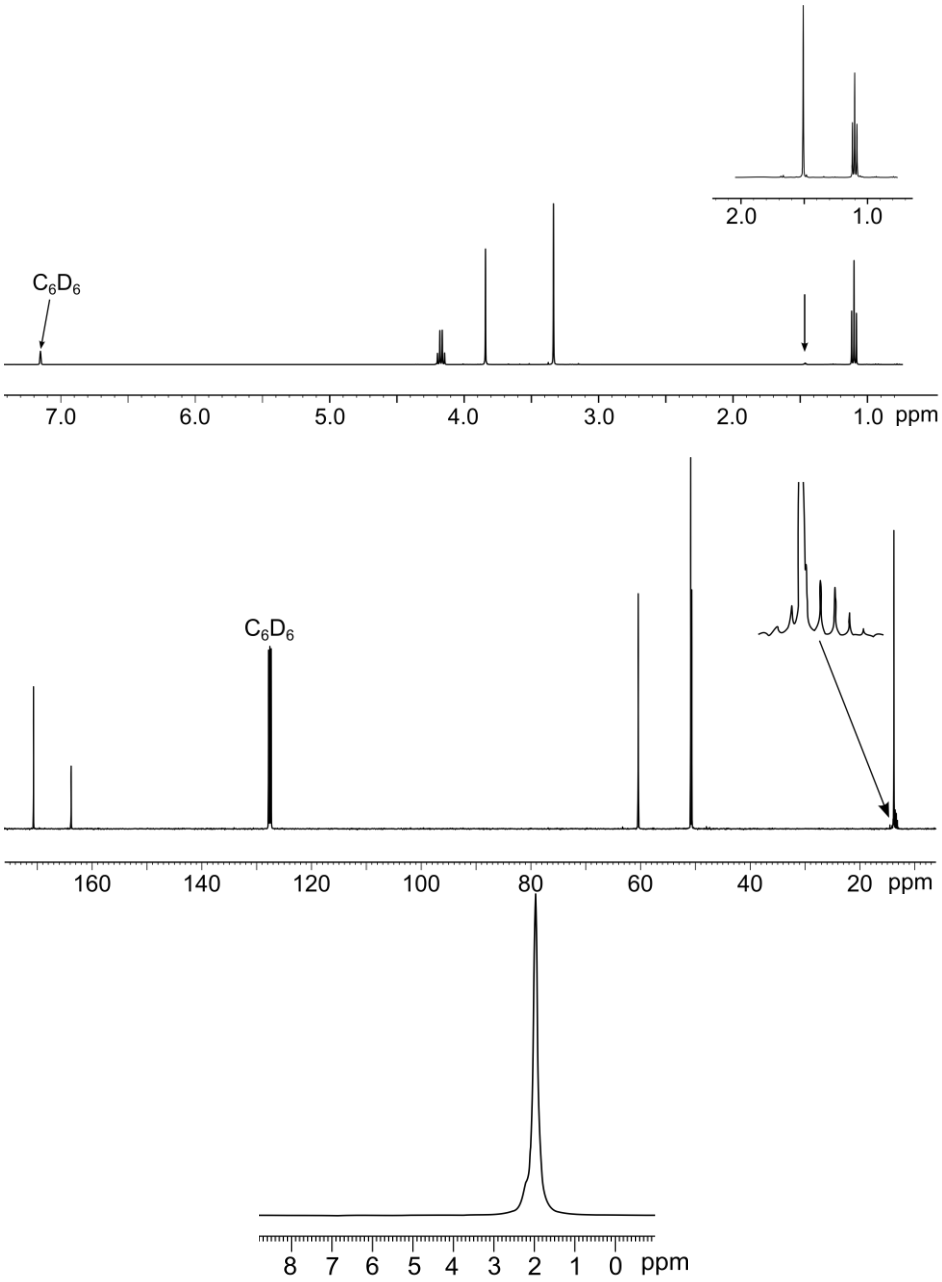

Figure 5.15. (*top*) The ^{1}H NMR spectrum of methyl-2-((1-ethoxyethylidene)amino)acetate-d_3 in C_6D_6. The inset shows the ^{1}H NMR spectrum of methyl-2-((1-ethoxyethylidene)amino)acetate in C_6D_6. The black arrow indicates a missing singlet due to CD_3 group inclusion. (*middle*) The ^{13}C NMR spectrum of methyl-2-((1-ethoxyethylidene)amino)acetate-d_3 in C_6D_6. The inset shows a septet due to the presence of the CD_3 group. (*bottom*) ^{2}H NMR spectrum of methyl-2-((1-ethoxyethylidene)amino)acetate-d_3 in $CHCl_3$.

and a colorless oil (3.6 g, 22 mmol) was isolated in 39% yield. ^{1}H NMR (C_6D_6, ppm): δ = 1.09-1.13 (3H, t, J = 7.16 Hz), 3.34 (3H, s), 3.85 (3H, s), and 4.15-4.21 (2H, q, J = 7.16 Hz) ppm. (Figure 5.15). ^{2}H NMR ($CHCl_3$, ppm): δ = 1.97 ppm (Figure 5.15). ^{13}C NMR (C_6D_6, ppm): δ = 14.58, 51.44, 51.64, 61.20, 164.61, 171.47 ppm (Figure 5.15). IR (neat, cm^{-1}): 1745, 1670, 1440, 1362, 1269, 1181, 1028, 971, 907, 792, and 715. HRMS (PI-ESI, m/z) calculated for $C_7H_{11}D_3NO_3$ $[M+H]^+$ 163.1162, found 163.1158.

*Synthesis of Zn4O(BDC-CHO)$_3$·(DEF)$_{6.2}$·(EtOH)$_{0.6}$, $Zn_4C_{77.2}H_{95.8}N_{6.2}O_{22.8}$ **(1)***

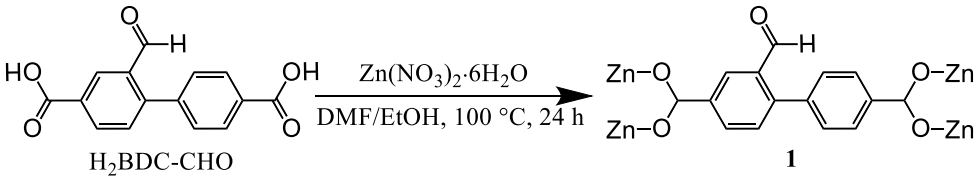

Scheme 5.7. Synthesis of **1**.

MOF **1** was prepared using a modified procedure[31] (Scheme 5.8). $Zn(NO_3)_2·6H_2O$ (6.2 mg, 21 μmol) and H_2BDC-CHO (5.0 mg, 19 μmol) were added to a one-dram vial containing 1.4 mL DEF and 0.6 mL EtOH. The resulting mixture was placed into a programmable isothermal oven after sonication, and heated to 100 °C at 0.2 °C/minute, and the temperature held for 24 h. The oven was cooled at a rate of 0.6 °C/minute and yellow cubic crystals of **1** (5.0 mg, 2.9 μmol) were isolated in 55% yield.

*Synthesis of **2-PSM** and **2-PSM-d$_3$**.*

DMF-washed crystals of **1** (10 mg, 5.8 μmol) were soaked with distilled methyl-2-((1-ethoxyethylidene)amino)acetate (0.30 g, 1.9 mmol) at 25 °C, refreshed daily, for 72 h. The resulting yellow crystals of **2-PSM** were washed thoroughly with DMF to remove excess methyl-2-((1-ethoxyethylidene)amino)acetate. IR (neat, cm^{-1}): 3294, 2936, 1984,

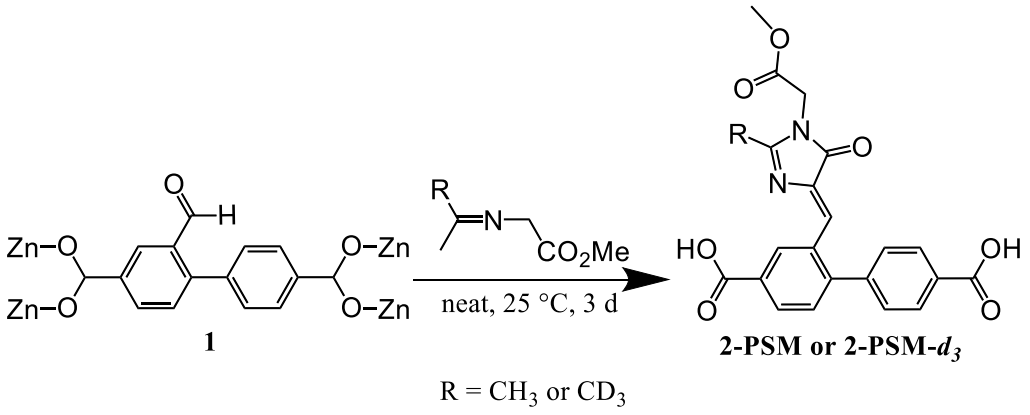

Scheme 5.8. Synthesis of **2-PSM** and **2-PSM-*d*$_3$**.

1838, 1742, 1659, 1603, 1383, 1211, 1095, 1005, 849, 779, 711, 679, and 661. The same procedure was used for the preparation of **2-PSM-*d*$_3$**, but methyl-2-((1-ethoxyethylidene)amino)acetate-*d*$_3$ was used instead.

*Synthesis of $Zn_4O(BDC\text{-}HBI')_3\cdot(DEF)_{3.07}\cdot EtOH\cdot(H_2O)_{3.13}$, $Zn_4C_{86.35}H_{100.03}N_{9.07}O_{29.2}$, (**2**).*

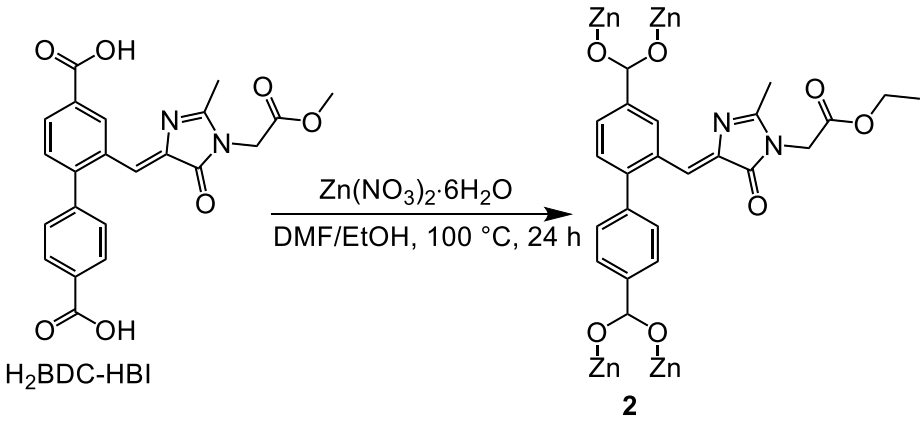

Scheme 5.9. Synthesis of **2-PSM** and **2-PSM-*d*$_3$**.

In a one-dram vial, $Zn(NO_3)_2\cdot 6H_2O$ (6.2 mg, 21 μmol) and H_2BDC-HBI (5.0 mg, 12 μmol) were dissolved in 1.4/0.6 mL DEF/EtOH mixture followed by sonication. The resulting solution was ramped over 6 h and remained at 100 °C for 24 h in an isothermal oven. After 24 h heating, the reaction mixture was cooled down to room temperature over 2 h. The yellow crystalline material of **2** (5.2 mg, 2.5 μmol) was isolated in 64% yield. IR

(neat, cm^{-1}): 3406, 2935, 1971, 1739, 1655, 1381, 1211, 1095, 1016, 854, and 775 (Figure 5.18).

Characterization Techniques.

Steady-state emission spectra were acquired on an Edinburgh FS5 fluorescence spectrometer equipped with a 150 W Continuous Wave Xenon Lamp source for excitation. Emission measurements on solid samples were collected on the powders of the appropriate materials placed inside a 0.5 mm quartz sample holder using the front-facing module.

The Ocean Optics JAZ spectrometer was also used to record the emission response. In this case, a mounted high-power 365 nm LED (M365L2, Thorlabs) was used as an excitation source.

Fluorescence lifetimes were measured using a Mini-τ lifetime spectrometer from Edinburgh Instruments equipped with a 365-nm picosecond-pulsed light-emitting diode (EPLED 365).

Fitting of Fluorescence Decays.

The fluorescence decays for **1, 2-PSM,** and **2** shown in Figure 5.12 were fit with the triexponential function (n = 3) shown in Equation 5.1 below:

$$I(t) = \int_0^t IRF(t')\,(C + \sum_{i=1}^{n}(B_i e^{\left[-\frac{t-t'}{\tau_i}\right]})dt' \qquad \textbf{Equation 5.1}$$

where τ_i and B_i are respective lifetimes and amplitudes of each component. The intensity-weighted average fluorescence lifetimes were calculated based on Equation 5.2:

$$\langle \tau_{av} \rangle = \frac{B_1\tau_1^2+B_2\tau_2^2+B_3\tau_3^2}{B_1\tau_1+B_2\tau_2+B_3\tau_3} \qquad \textbf{Equation 5.2}$$

Table 5.1. Lifetime data of **1**, **2**, and **2-PSM.**

	B_1	τ_1, ns	B_2	τ_2, ns	B_3	τ_3, ns	$\langle\tau_{av}\rangle$, ns
1	0.65	0.48	0.32	3.17	0.03	10.50	4.23
2	0.67	0.19	0.30	1.53	0.03	3.79	1.59
2-PSM	0.70	0.44	0.28	1.91	0.02	5.96	1.91

^{2}H and ^{13}C CP-MAS NMR Spectroscopy.

Two-dimensional HSQC and HMBC spectra were collected on a Bruker Avance III-HD 400 MHz spectrometer operating at 400.27 MHz for ^{1}H and 100.65 MHz for ^{13}C. Vendor supplied pulse sequences were used and processing was done with Bruker Topspin 3.2. All data were acquired with temperature controlled at 25 °C. The 2D HSQC spectrum (with pulsed field gradient coherence selection) was collected with spectral widths of 15 ppm and 165 ppm for ^{1}H and ^{13}C respectively. FIDs were acquired with 1024 points and 256 increments were collected in *t1*. The 2D HMBC spectrum (with pulsed field gradient coherence selection) was collected with spectral widths of 15 ppm and 220 ppm for ^{1}H and ^{13}C respectively. FIDs were acquired with 4096 points and 256 increments were collected in *t1*.

Single Crystal X-ray Data.

$Zn_4C_{42}H_{24.5}O_{13.25}$, ***1***.

X-ray intensity data from a yellow cube-shaped crystal were collected at 100(2) K using a Bruker SMART APEX diffractometer (Mo K_α radiation, $\lambda = 0.71073$ Å).[39] The raw area detector data frames were reduced and corrected for absorption effects using the SAINT+ and SADABS programs.[39] While strong diffraction was observed at low angles,

intensities dropped off rapidly with increasing θ and became unobservable at about 2θ = 42°. The dataset was truncated at that value. This is due to the extensive solvent disorder within the porous framework. Pronounced diffuse streaking between Bragg peaks was also observed in the area detector frames, another indication of local departures from the average structure described below. Final unit cell parameters were determined by least-squares refinement of 6516 reflections from the data set. The structure was solved by direct methods with SHELXS.[40] Subsequent difference Fourier calculations and full-matrix least-squares refinement against $F2$ were performed with SHELXL-2014[40] using OLEX2.[41]

The compound crystallizes in the monoclinic space group $C2/m$ as determined by the pattern of systematic absences in the intensity data and by obtaining a reasonable structural model despite crystal quality difficulties. The structure is afflicted by severe disorder, which drastically limits refinement precision. Known contents of the asymmetric unit consists of three zinc centers, two of which (Zn1 and Zn3) are located on mirror planes, a μ_4-oxo oxygen atom (O1), one complete ligand and half of another ligand also located on a mirror plane. One additional oxygen atom, also located on a mirror plane, was located near Zn3. It is presumably a water oxygen for charge balance reasons. Phenyl rings of the ligand {O2–O5, C1–C14} were refined as rigid hexagons, with additional planarity and distance restraints applied to this ligand. Some displacement parameters were restrained to approximate a spherical shape with SHELX ISOR instructions. No significant electron density was observed near any potential substitution sites on the ligands. The substituted groups are presumably partially populated and disordered over several sites. Because of uncertainty of the position and extent of ligand substitution, all carbon atoms were refined as fully occupied and an 'unsubstituted composition' reported. All non-hydrogen atoms

were refined with anisotropic displacement parameters except for the water oxygen O9 (isotropic). Hydrogen atoms bonded to carbon were placed in geometrically idealized positions and included as riding atoms. Disordered electron density between the framework could not be modeled and was accounted for using the Squeeze program.[42,43] Squeeze calculated a large solvent-accessible volume in the crystal of 6870 $Å^3$, (69% of the total unit cell volume) corresponding to 1223 electrons per unit cell. Note that the *F.W.*, *d*(calc), and *F*(000) values reflect framework atoms only due to uncertainty about the nature of the guest species. The refinement data is given in Table 5.2.

$Zn_4C_{42}H_{25}O_{13}$, **2-PSM**

X-ray intensity data from a yellow crystal of **2-PSM** were collected at 150 K on a D8 goniostat equipped with a Bruker PHOTON100 CMOS detector at Beamline 11.3.1 at the Advanced Light Source (Lawrence Berkeley National Laboratory) using synchrotron radiation tuned to λ = 1.0332 Å. Data collection frames were measured for a duration of 2 s at 0.5° intervals of ω. The data frames were collected using the program APEX2 and processed using the SAINT program routine within APEX2. The data were corrected for absorption and beam corrections based on the multi-scan technique as implemented in SADABS.[44] The structures were solved by direct methods using SHELXS[40] and refined against F^2 on all data by full-matrix least squares as implemented in SHELXL-97.[45] The Zn, C, and O atoms in **2-PSM** were refined anisotropically. Hydrogen atoms attached to the ligand were included in the model at geometrically calculated positions. Due to partial occupancy (64%) of $[BDC\text{-}HBI]^{2-}$ linkers and the disorder of the solvent molecules, which is very common in porous structures (e.g., MOFs), a large amount of spatially delocalized

electron density in the pores of the lattice was observed. The acceptable refinement values could not be obtained for this electron density, and therefore, the best residual indices were

Table 5.2. X-ray structure refinement data for **1**[a] and 2-**PSM**[b].

compound	**1**	**2-PSM**
formula	$C_{42}H_{24.5}O_{13.25}Zn_4$	$C_{42}H_{25}O_{13}Zn_4$
FW	1002.59	999.10
T, K	100(2)	150 (2)
crystal system	monoclinic	monoclinic
space group	C2/m	C2/m
Z	4	4
a, Å	24.117(2)	24.230(2)
b, Å	24.219(2)	24.193(2)
c, Å	17.0669(17)	17.0847(16)
α, °	90	90
β, °	92.381(2)	92.957(3)
γ, °	90	90
V, Å^3	9960.2(17)	10001.7(16)
$d_{calc,}$ g/cm^3	0.669	0.664
μ, mm^{-1}	0.979	2.606
F(000)	2010.0	2004.0
crystal size/mm^3	0.38 × 0.36 × 0.32	0.06 × 0.04 × 0.02
theta range	2.39 to 42.64	2.41 to 39.93
index ranges	-24 ≤ h ≤ 24 -24 ≤ k ≤ 24 -17 ≤ l ≤ 17	-29 ≤ h ≤ 29 -29 ≤ k ≤ 30 -20 ≤ l ≤ 20
refl. collected	26940	39167
data/restraints/parameters	5757/54/268	9993/289/0
GOF on F^2	0.958	0.816
Largest peak/hole, e/Å^3	0.49/–0.36	0.43/–0.32
R_1 (wR_2), %, [I ≥ 2sigma(I)][d]	6.56 (19.27)	5.33 (15.85)

[a] Mo-K$_\alpha$ (λ = 0.71073 Å) radiation;[b] synchrotron radiation (λ = 1.0332 Å)
[c] Formula is given based on single-crystal X-ray data and does not include disordered solvent molecules (complete formula was determined based on elemental analysis)
[d] $R_1 = \Sigma||F_o| - |F_c||/ \Sigma |F_o|$, $wR_2 = \{\Sigma [w(F_o^2-F_c^2)^2]/ \Sigma [w(F_o^2)^2]\}^{1/2}$

obtained from a model for which the Squeeze program[8] was used to account for the electron density in regions of high disorder. The refinement data are given in Table 5.2.

Computational Details.

Density functional theory (DFT) calculations were employed to model the potential energy surfaces (PESs) for the $–CH_3$ group and single bond dynamics for the unbound ligand and confined chromophore inside the engineered scaffold. To model chromophore behavior inside the framework, the oxygen atoms were fixed to mimic the rigidity imposed by the scaffold. Four PESs were constructed by varying the dihedral angles as shown in Figures 5.13 and 5.16. All theoretical calculations were performed using the SPARTAN 10 quantum chemistry program package. The B3LYP functional and 6–31G* basis set were employed to perform all DFT calculations.

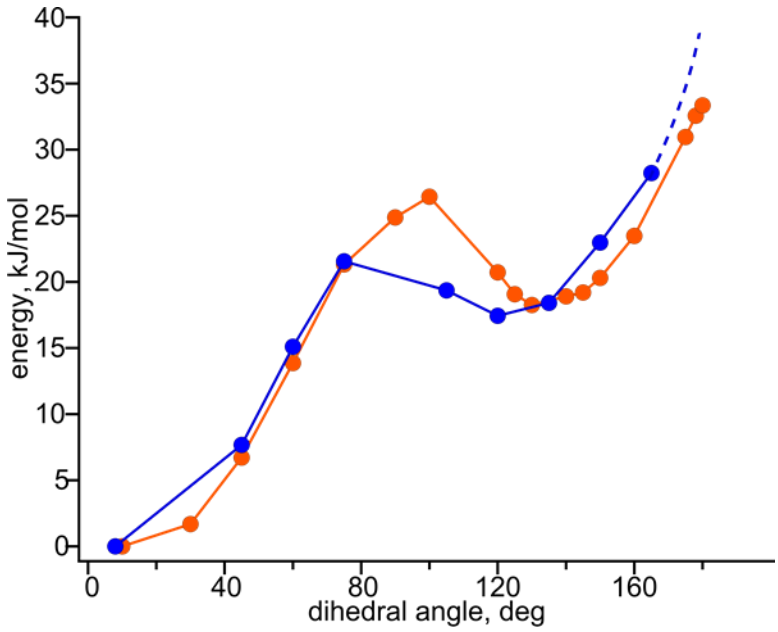

Figure 5.16. PES for a C_2–C_3 bond flip in the coordinatively trapped (orange solid line) and unbound (blue solid line) H_2BDC-HBI chromophores. The blue dashed line illustrates that a 180°-conformation could not be achieved in the case of the confined chromophore due to restriction imposed by the rigid scaffold.

Other Physical Measurements.

FT-IR spectra were obtained on a Perkin-Elmer Spectrum 100. NMR spectra were collected on Bruker Avance III-HD 300 and Bruker Avance III 400 MHz NMR spectrometers. ^{13}C NMR and ^{1}H NMR spectra were referenced to natural abundance ^{13}C peaks and residual ^{1}H peaks of deuterated solvents, respectively. Powder X-ray diffraction patterns were recorded on a Rigaku Miniflex II diffractometer with accelerating voltage and current of 30 kV and 15 mA, respectively. Thermogravimetric analysis was performed on a SDT Q600 Thermogravimetric Analyzer using an alumina boat as a sample holder. The Waters QTOF-I quadrupole time-of-flight and Thermo Scientific Orbitrap Velos Pro mass-spectrometers were used to record the mass-spectra of the prepared compounds. Diffuse reflectance spectra were collected on a Perkin Elmer Lambda 45 UV-vis spectrometer referenced to Spectralon®.

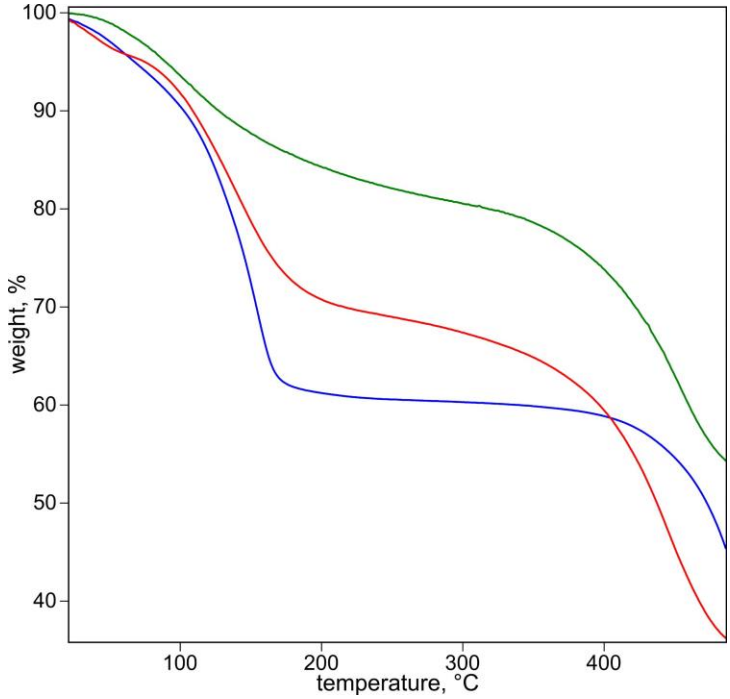

Figure 5.17. Thermogravimetric analysis plots of **1** (blue), **2** (green), and **2-PSM** (red).

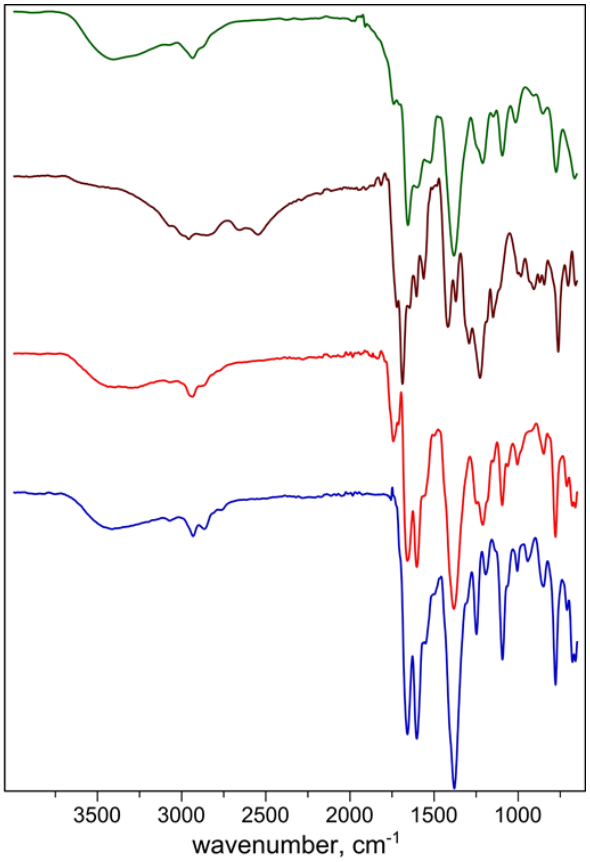

Figure 5.18. The FT-IR spectra of **2** (green), H_2BDC-HBI (brown), **2-PSM** (red), and **1** (blue).

REFERENCES

(1) Litvinenko, K. L.; Meech, S. R. *Phys Chem Chem Phys* **2004**, *6* (9), 2012–2014.

(2) Shu, X.; Kallio, K.; Shi, X.; Abbyad, P.; Kanchanawong, P.; Childs, W.; Boxer, S. G.; Remington, S. J. *Biochemistry* **2007**, *46* (43), 12005–12013.

(3) Zhao, Z.; Chen, S.; Deng, C.; Lam, J. W. Y.; Chan, C. Y. K.; Lu, P.; Wang, Z.; Hu, B.; Chen, X.; Lu, P.; Kwok, H. S.; Ma, Y.; Qiu, H.; Tang, B. Z. *J. Mater. Chem.* **2011**, *21* (29), 10949.

(4) Hughs, M.; Jimenez, M.; Khan, S.; Garcia-Garibay, M. A. *J. Org. Chem.* **2013**, *78* (11), 5293–5302.

(5) Hong, Y.; Lam, J. W. Y.; Tang, B. Z. *Chem. Soc. Rev.* **2011**, *40* (11), 5361.

(6) Liu, Y.; Tang, Y.; Barashkov, N. N.; Irgibaeva, I. S.; Lam, J. W. Y.; Hu, R.; Birimzhanova, D.; Yu, Y.; Tang, B. Z. *J. Am. Chem. Soc.* **2010**, *132* (40), 13951–13953.

(7) Yuan, W. Z.; Lu, P.; Chen, S.; Lam, J. W. Y.; Wang, Z.; Liu, Y.; Kwok, H. S.; Ma, Y.; Tang, B. Z. *Adv. Mater.* **2010**, *22* (19), 2159–2163.

(8) Pakhomov, A. a; Martynov, V. I. *Chem. Biol.* **2008**, *15* (8), 755–764.

(9) Tolbert, L. M.; Baldridge, A.; Kowalik, J.; Solntsev, K. M. *Acc. Chem. Res.* **2012**, *45* (2), 171–181.
(10) Meech, S. R. *Chem. Soc. Rev.* **2009**, *38* (10), 2922.
(11) Ormö, M.; Cubitt, A. B.; Kallio, K.; Gross, L. A.; Tsien, R. Y.; Remington, S. J. *Science (80-.).* **1996**, *273* (5280).
(12) Benelhadj, K.; Massue, J.; Retailleau, P.; Ulrich, G.; Ziessel, R. *Org. Lett.* **2013**, *15* (12), 2918–2921.
(13) Ge, S.; Deng, H.; Su, Y.; Zhu, X. *RSC Adv.* **2017**, *7* (29), 17980–17987.
(14) Padalkar, V. S.; Seki, S. *Chem. Soc. Rev.* **2016**, *45* (1), 169–202.
(15) Tolbert, L. M.; Baldridge, A.; Kowalik, J.; Solntsev, K. M. *Acc. Chem. Res.* **2012**, *45* (2), 171–181.
(16) Tozzini, V.; Bizzarri, A. R.; Pellegrini, V.; Nifosì, R.; Giannozzi, P.; Iuliano, A.; Cannistraro, S.; Beltram, F. *Chem. Phys.* **2003**, *287* (1–2), 33–42.
(17) Baranov, M. S.; Lukyanov, K. A.; Borissova, A. O.; Shamir, J.; Kosenkov, D.; Slipchenko, L. V.; Tolbert, L. M.; Yampolsky, I. V.; Solntsev, K. M. *J. Am. Chem. Soc.* **2012**, *134* (13), 6025–6032.
(18) Rafiq, S.; Rajbongshi, B. K.; Nair, N. N.; Sen, P.; Ramanathan, G. *J. Phys. Chem. A* **2011**, *115* (47), 13733–13742.
(19) Bahr, J. L.; Kodis, G.; de la Garza, L.; Lin, S.; Moore, A. L.; Moore, T. A.; Gust, D. *J. Am. Chem. Soc.* **2001**, *123* (29), 7124–7133.
(20) Baranov, M. S.; Solntsev, K. M.; Lukyanov, K. A.; Yampolsky, I. V. *Chem. Commun.* **2013**, *49* (51), 5778.
(21) Deng, H.; Zhu, Q.; Wang, D.; Tu, C.; Zhu, B.; Zhu, X. *Polym. Chem.* **2012**, *3* (8), 1975.
(22) Jung, S.; Kim, Y.; Kim, S.-J.; Kwon, T.-H.; Huh, S.; Park, S. *Chem. Commun.* **2011**, *47* (10), 2904.
(23) Sun, D.; Tham, F. S.; Reed, C. A.; Boyd, P. D. W. *Proc. Natl. Acad. Sci. U. S. A.* **2002**, *99* (8), 5088–5092.
(24) Deng, H.; Grunder, S.; Cordova, K. E.; Valente, C.; Furukawa, H.; Hmadeh, M.; Gandara, F.; Whalley, A. C.; Liu, Z.; Asahina, S.; Kazumori, H.; O'Keeffe, M.; Terasaki, O.; Stoddart, J. F.; Yaghi, O. M. *Science (80-.).* **2012**, *336*, 1018–1024.
(25) Li, H.; Eddaoudi, M.; O'Keeffe, M.; Yaghi, O. M. *Nature* **1999**, *402* (November), 276–279.
(26) Furukawa, H.; Cordova, K. E.; O'Keeffe, M.; Yaghi, O. M. *Science (80-.).* **2013**, *341* (6149), 1230444–1230444.
(27) Zhou, H.-C.; Long, J. R.; Yaghi, O. M. *Chem. Rev.* **2012**, *112* (2), 673–674.
(28) Chae, H. K.; Siberio-Pérez, D. Y.; Kim, J.; Go, Y.; Eddaoudi, M.; Matzger, A. J.; O'Keeffe, M.; Yaghi, O. M. *Nature* **2004**, *427* (6974), 523–527.
(29) Farha, O. K.; Yazaydın, A. Ö.; Eryazici, I.; Malliakas, C. D.; Hauser, B. G.; Kanatzidis, M. G.; Nguyen, S. T.; Snurr, R. Q.; Hupp, J. T. *Nat. Chem.* **2010**, *2* (11), 944–948.
(30) Wang, Z.; Cohen, S. M. *J. Am. Chem. Soc.* **2007**, *129* (41), 12368–12369.
(31) Burrows, A. D.; Frost, C. G.; Mahon, M. F.; Richardson, C. *Angew. Chem. Int. Ed. Engl.* **2008**, *47* (44), 8482–8486.
(32) Lerestif, J. M.; Perrocheau, J.; Tonnard, F.; Bazureaul, J. P.; Hamelin, J. *Tetrahedron* **1995**, *51* (24), 6757–6774.

(33) Wang, Z.; Cohen, S. M. *Chem. Soc. Rev.* **2009**, *38* (5), 1315.
(34) Heim, R.; Cubitt, A. B.; Tsien, R. Y. *Nature* **1995**, *373* (6516), 663–664.
(35) Follenius-Wund, A.; Bourotte, M.; Schmitt, M.; Iyice, F.; Lami, H.; Bourguignon, J.-J.; Haiech, J.; Pigault, C. *Biophys. J.* **2003**, *85* (3), 1839–1850.
(36) Allan W. Scruggs, ‡; Carole L. Flores, §; Rebekka Wachter, ‖ and; Neal W. Woodbury*, §. **2005**.
(37) Struts, A. V; Salgado, G. F. J.; Martínez-Mayorga, K.; Brown, M. F. *Nat. Struct. Mol. Biol.* **2011**, *18* (3), 392–394.
(38) Dolgopolova, E. A.; Williams, D. E.; Greytak, A. B.; Rice, A. M.; Smith, M. D.; Krause, J. A.; Shustova, N. B. *Angew. Chemie Int. Ed.* **2015**, *54* (46), 13639–13643.
(39)
(40) Sheldrick, G. M. *Acta Crystallogr. A.* **2008**, *64* (Pt 1), 112–122.
(41) Oleg V. Dolomanov, Luc J. Bourhis, Richard J. Gildea, J. A. K. H. and; Puschmann, H. *J. Appl. Crystallogr.* **2009**, *42*, 339–341.
(42) van der Sluis, P.; Spek, A. L. *Acta Crystallogr. Sect. A Found. Crystallogr.* **1990**, *46* (3), 194–201.
(43) Spek, A. L. *J. Appl. Crystallogr.* **2003**, *36* (1), 7–13.
(44) Sheldrick, G. M. *SADABS —A Program for Area Detector Absorption Corrections*; 2004.
(45) Sheldrick, G. M. *Acta Crystallogr. Sect. A* **1990**, *46*, 467.

APPENDIX A – Copyright Permissions

JOHN WILEY AND SONS LICENSE
TERMS AND CONDITIONS

Oct 15, 2017

This Agreement between Derek E Williams ("You") and John Wiley and Sons ("John Wiley and Sons") consists of your license details and the terms and conditions provided by John Wiley and Sons and Copyright Clearance Center.

License Number	4210410853892
License date	Oct 15, 2017
Licensed Content Publisher	John Wiley and Sons
Licensed Content Publication	Chemistry - A European Journal
Licensed Content Title	Metal–Organic Frameworks as a Versatile Tool To Study and Model Energy Transfer Processes
Licensed Content Author	Derek E. Williams,Natalia B. Shustova
Licensed Content Date	Aug 27, 2015
Licensed Content Pages	6
Type of use	Dissertation/Thesis
Requestor type	Author of this Wiley article
Format	Print and electronic
Portion	Full article
Will you be translating?	No
Title of your thesis / dissertation	Metal-Organic Frameworks: A Versatile Platform for Light Harvesting and Energy Transfer
Expected completion date	Nov 2017
Expected size (number of pages)	150
Requestor Location	Derek E Williams 631 Sumter Street COLUMBIA, SC 29208 United States Attn: Derek E Williams
Publisher Tax ID	EU826007151

Title: Fulleretic Well-Defined Scaffolds: Donor–Fullerene Alignment Through Metal Coordination and Its Effect on Photophysics

Author: Derek E. Williams,Ekaterina A. Dolgopolova,Danielle C. Godfrey,Evgeniya D. Ermolaeva,Perry J. Pellechia,Andrew B. Greytak,Mark D. Smith,Stanislav M. Avdoshenko,Alexey A. Popov,Natalia B. Shustova

Publication: Angewandte Chemie International Edition

Publisher: John Wiley and Sons

Date: Jun 6, 2016

Open Access Article